

Structural Investigation of Zn²⁺ ions, FXII and Complement receptor gC1q-R interaction: Triggering the Contact activation System.

Bubacarr Gibril Kaira, MSc.

Thesis submitted to The University of Nottingham
for the degree of Doctor of Philosophy

April 2019

School of Pharmacy
University Of Nottingham

Abstract

The contact activation system or CAS, is an important process that contributes in immunity, inflammation and thrombosis. Contact activation is triggered when coagulation FXII (FXII) and High molecular weight kininogen (HK) bound to Prekallikrein (PK) dock on the surface of complement receptor gC1q-R. Binding of FXII and HK to gC1q-R is mediated by Zn^{2+} ions, and can trigger contact activation which ultimately leads to inflammation and plasma coagulation.

The aim of this PhD project is to mainly elucidate the binding of full-length FXII and Fibronectine type II (FnII) domain binding to gC1q-R and structure determination of FXII FnII binding to Zn^{2+} ions and also structure of FXII FnII bound to gC1q-R. Several FXII and gC1q-R constructs have been successfully subcloned into plasmid vectors for bacterial and insect (S2) cell expression. Expression and purification of FXII and gC1q-R constructs were successfully achieved.

Solution studies (size exclusion chromatography or gel filtration), Surface Plasmon Resonance (SPR) and X-ray crystallography successfully characterise FXII FnII interaction with gC1q-R. Furthermore, interaction of FXII and HK to gC1q-R in the presence of Zn^{2+} ions was investigated using gel filtration. The structural data reveals interesting molecular insight into how Zn^{2+} ions play a role in 3D structures of FXII FnII in isolation and FXII FnII bound to gC1q-R. The FXII FnII bound gC1q-R structure reports novel binding sites, in which FXII FnII bridges two gC1q-R trimers using Arg36 and Arg65 of FXII FnII to interact with G1 and G2 pockets of gC1q-R, respectively. Finally, recombinant gC1q-R was shown to shorten clotting time in plasma in a dose-dependent fashion. In summary, our structural, binding and functional assay are the first reported data shedding light into how Zn^{2+} induced conformational changes in FXII FnII and broadens our understanding of how contact factors (FXII and HK bound PK) assemble on gC1q-R to trigger contact activation.

Acknowledgments

I would like to thank my supervisors Prof Jonas Emsley and Dr Ingrid Dreveny at the University of Nottingham, for their guidance and support.

Prof Emsley, whom I have worked under as both a research assistant and a PhD student has been instrumental as both a colleague and supervisor. Prof Emsley's has been instrumental throughout my PhD project and I am therefore extremely appreciative of Prof Emsley.

I would like to say a big thank you to all my laboratory colleagues; Dr Monika Pathak, Dr Chan Li, Dr Alexander Slater and everybody in Crystallography group.

I would like to thank Dr Nicola Mutch and Sumya Ummay, at the University of Aberdeen, for their collaboration and contributions made on the clotting assays.

I would like to thanks the University of Nottingham for awarding me a 50% discount on my tuition fee.

A warm and heartfelt thanks to my parents, Pa Gibou Kaira and Mam-marie Jeng for their support and understanding throughout my existence – prior and post PhD studies.

Most sincere thank you with love must go to my special wife, Mariam Njie and my inquisitive and adorable son, Gibril Bubacarr Kaira, for their endless love, understanding and support throughout my PhD journey.

Table of contents

Abstract	ii
Acknowledgments	iii
Table of contents	iv
List of Figures	ix
Abbreviations	xiv
CHAPTER 1.0	1
INTRODUCTION	1
1.0 Introduction	2
1.1.0 The Vascular system	2
1.1.1 Haemostasis and Thrombosis	2
1.1.2 Blood Coagulation	3
1.1.2.1 Tissue Factor (Extrinsic) Pathway	4
1.1.2.2 Contact Factor (Intrinsic) Pathway	4
1.1.3 The fibrinolytic system (clot lysis)	8
1.4 Coagulation Factor Domain Structure - Comparison	9
1.4.1 Prekallikrein (PK) and Factor XI (FXI)	10
1.4.2 High Molecular Weight Kininogen (HK)	10
1.4.3 Factor XII (FXII) – history	11
1.5 Interactions between contact factors and pathogens	20
1.6 Cell interactions with contact factors	21
1.7 Human gC1q-R: the major endothelial cell receptor for FXII	24
1.7.1 Human gC1q-R protein subunit and structure	25
1.8 gC1q-R protein interaction with ligands	30
1.8.1 Interactions between rubella virus capsid protein and gC1q-R	30
1.8.2 Interactions between Histone 4 and gC1q-R.....	31
1.8.3 Interactions between lamin B receptor and gC1q-R.....	31
1.8.4 Interactions between LyP-1 and gC1q-R	32
1.8.5 Interactions between FXII and gC1q-R	32
1.9 Complement system, coagulation and inflammation	34
1.9.1 Proteins containing SRCR and LDL-R domains	35
1.10 Aims and Objectives of this PhD thesis	36
CHAPTER 2.0	38
MATERIALS AND METHODS	38
2.1.0 Materials and Methods	39
2.1.1 Preparation of FXII and gC1q-R cDNA for expression	39
2.1.2 Amplification of DNA fragments using Polymerase Chain Reaction (PCR)	39
2.1.3 Restriction double digest, Plasmid vector dephosphorylation, ligation and gel electrophoresis	40
2.1.4 Site directed mutagenesis (SDM) of recombinant FXII and gC1q-R	41
2.1.5 Bacterial transformation	42

2.1.6 DNA quantification at wavelength 260 nm	42
2.2.0 Protein expression	43
2.2.1 <i>Escherichia coli</i> (<i>E. coli</i>)	43
2.2.2 <i>Drosophila Schneider 2</i> (<i>S2</i>) cells	43
2.3.0 Protein Purification	44
2.3.1 Purification of FXII by Ion exchange chromatography	44
2.3.2 Purification of FXII by Ni ²⁺ affinity chromatography	46
2.3.3 Purification of HisTrx-FXII FnII by affinity (Ni ²⁺ and Zn ²⁺) chromatography	46
2.3.4 Purification by size exclusion chromatography (gel filtration)	47
2.4 Sodium Dodecyl Sulfate-Polyacrylamide gel electrophoresis (SDS-PAGE) to confirm overexpressed protein	48
2.5 Western blot to detect mouse FXII and human FXII FnII	49
2.6 Protein quantification at a wavelength of 280 nm	50
2.7.0 Analytical gel filtration for isolating FXII bound gC1q-R	51
2.7.1 Mouse FXII (mFXII) bound gC1q-R in the presence of Zn ²⁺	51
2.7.2 FXII FnII-EGF1 bound gC1q-R in the presence of Zn ²⁺	51
2.7.3 FXII FnII bound gC1q-R in the presence of low and high Zn ²⁺ concentrations	52
2.8.0 Surface Plasmon Resonance (SPR)	53
2.8.1 Immobilisation of ligands on the sensor chip surface	53
2.8.2 Measuring the gC1q-R interaction with FXII	54
2.9.0 Crystallisation of FXII, FXII FnII and bound FXII FnII-EGF1 in the presence of gC1q-R	55
2.9.1 Crystallisation of full length mouse FXII	55
2.9.2 Crystallisation of untagged and tagged human FXII FnII-EGF1	56
2.9.3 Crystallisation of untagged human FXII FnII	57
2.9.4 Crystallisation of FXII FnII or FXII FnII-EGF1 in complex with gC1q-R	58
2.9.5 Crystallisation of gC1q-R and peptides	58
2.10. Structure determination, refinement and validation of untagged human FXII FnII in the presence of Zn ²⁺	59
2.11 Structure determination, refinement and validation of gC1q-R-FXII FnII-EGF1 complex	60
2.12 Contact activation assay using chromogenic substrates	61
CHAPTER 3.0	62
TECHNIQUES	62
3.0 Techniques	63
3.1.0 Chromatographic techniques	63
3.1.1 Ion Exchange Chromatography (IEX)	64
3.1.2 Affinity chromatography	65
3.1.3 Size exclusion chromatography (SEC)	66
3.2.0 Background on Surface Plasmon Resonance (SPR)	69
3.2.1 SPR Instrument and Sensor chip	71
3.2.2 Immobilisation of proteins on the sensor chip surface	74

3.2.3 Pre-concentration	74
3.2.4 Ligand immobilisation	75
3.2.5 Studying biomolecular interactions	77
3.2.6 Multiple binding sites	81
3.3.0 Introduction to protein X-ray crystallography	83
3.3.1 Protein Crystallogenesis	84
3.3.2 Harvesting and Cryocooling of crystals for X-ray diffraction experiment	87
3.3.3 Protein crystal and symmetry	88
3.3.4 X-ray generation	90
3.3.5 X-ray diffraction beginning with 'history'	91
3.3.6 X-ray detectors	95
3.4.0 Processing X-ray diffraction data	96
3.4.1 Indexing, Integration and Scaling of data	96
3.4.2 Structure factors and the phase problem	97
3.4.3 Structure refinement and model building	99
CHAPTER 4.0	102
STRUCTURAL STUDIES OF THE FXII FnII DOMAIN	102
4.1 Structural determination of human FXII FnII	103
4.1.1 Preparation of FXII constructs for expression in bacteria and insect cells	103
4.1.2 Expression and purification of untagged human FXII FnII-EGF1 and FXII FnII in drosophila S2 cells (insect cells)	106
4.1.3 Expression and purification of WT HisTrx-FXII FnII in Rosetta-gami2	110
4.1.4 Expression and purification of HisTrx-FXII FnII mutants	114
4.2.0 Crystallisation of human FXII FnII in the presence of Zn ²⁺	116
4.2.1 Crystallisation of human FXII FnII	116
4.2.2 Crystal structure of FXII FnII bound to Zn ²⁺	120
4.2.3 Crystallisation of human FXII FnII in the presence of Dextran sulfate	125
4.2.4 Crystal structure of FXII FnII bound to 1 Zn ²⁺ (form 3)	128
4.3.0 Structural comparison of the FXII FnII and FnII homologues	131
4.4.0 Discussion	140
4.4.1 Expression and purification of FXII FnII	140
4.4.2 Structural effect of Zn ²⁺ on FXII FnII	140
4.4.3 Structural similarities and differences in FXII FnII and FnII homologues	141
4.4.4 FXII FnII Cysteine 34 (Cys34) and Tenri deficiency	143
CHAPTER 5.0	145
STRUCTURAL STUDIES OF THE FXII FnII IN COMPLEX WITH gC1q-R	145
5.1.0 Structural determination of human FXII FnII in complex with complement receptor gC1q-R	146
5.1.1 Interaction between gC1q-R and FXII FnII	146
5.1.2 Implications of gC1q-R bound to FXII FnII	146

5.2.0 Crystallisation of gC1q-R with FXII FnII domain	152
5.2.1 Crystallisation of gel filtrated gC1q-R-FXII FnII-EGF1 or gC1q-R-FXII FnII ...	152
5.3.0 Crystal structure of gC1q-R bound to FXII FnII-EGF1	154
5.4.0 Bridging of FXII FnII to two gC1q-R trimers	161
5.5.0 Expression and purification of gC1q-R mutants	162
5.5.0 Binding studies of FXII and gC1q-R	163
5.5.1 Binding kinetics between FXII FnII (or FXII FnII-EGF1) and gC1q-R.....	164
5.5.2 Binding kinetics between HisTrx-FXII FnII and gC1q-R	168
5.5.3 Binding kinetics between full-length FXII and gC1q-R	170
5.6.0 Binding kinetics between FXII and other substrates (PK and FXI).....	172
5.7.0 Discussion	175
5.7.1 FXII binding to gC1q-R in the presence of Zn ²⁺ using gel filtration	175
5.7.2 Crystal structure of FXII FnII bound to gC1q-R	176
5.7.3 Binding studies of FXII FnII and gC1q-R.....	179
5.7.4 Binding studies of FXII to WT gC1q-R and gC1q-R mutants.....	180
5.7.5 FXII and substrates Prekallikrein (PK) and Factor XI (FXI)	181
CHAPTER 6.0	183
BINDING AND FUNCTIONAL STUDIES OF FXII, HK AND gC1q-R IN THE PRESENCE OF Zn ²⁺ IONS	183
6.1.0 Interaction of FXII (or FXII and HK) to gC1q-R	184
6.1.1 Interaction between gC1q-R and mFXII in solution	184
6.1.2 Interaction of human FXII and human HK to gC1q-R	186
6.1.3 Interaction of mFXII and human HK to gC1q-R	187
6.2.0 Contact activation assay for FXII and HK bound PK	191
6.3.0 Competition of FXII with FXII FnII in a contact activation assay	192
6.4.0 Contact activation assay using low and high molecular weight gC1q-R	192
6.5.0 Contact activation assay in plasma with WT gC1q-R	195
6.6.0 Discussion	197
6.6.1 Molecular assembly of the contact factors on gC1q-R.....	197
6.7.0 Conclusion	197
6.8.0 Future prospects	198
CHAPTER 7.0	199
STUDIES OF FXII FnII DIMERISATION IN THE PRESENCE OF Zn ²⁺ IONS	199
7.1.0 Zn ²⁺ mediated FXII FnII packing in the crystal lattice	200
7.2.0 Dimerisation of FXII using Gel filtration	201
7.3.0 Binding analysis of FXII self-interaction in the presence of Zn ²⁺	203
7.4.0 SPR analysis of FXII FnII interaction with full length FXII	204
7.5.0 Discussion	209
7.6.0 Conclusion	210
7.7.0 Future prospects	211
CHAPTER 8.0	212

CRYSTALLISATION OF MOUSE FXII (mFXII)	212
8.1.0 Cloning of FXII for expression and purification	213
8.2.0 Expression and purification of mFXII in drosophila S2 cells	213
8.3.0 Mouse FXII S526A in the presence of Corn trypsin inhibitor (CTI)	215
8.4.0 Crystallisation of WT mFXII in the presence of Dextran sulfate	218
8.5.0 Crystallisation of gC1q-R in the presence of WT mFXII	221
8.6.0 Crystallisation of HK domain 5 (HKD5) in the presence of gC1q-R	223
8.7.0 Crystallisation of gC1q-R in the presence of peptides	224
8.8.0 Discussion	226
8.9.0 Conclusion	226
CHAPTER 9.0	228
Co-purification of mFXII and Graal₈₆₃₋₁₁₅₀	228
9.1.0 Mouse FXII co-purification with Graal₈₆₃₋₁₁₅₀	229
9.2.0 Preparation and expression of Graal₈₆₃₋₁₁₅₀ in S2 insect cells	233
9.3.0 Binding analysis of Graal₈₆₃₋₁₁₅₀ and mFXII using SPR	237
9.3.1 Binding kinetics of Graal₈₆₃₋₁₁₅₀ to immobilised FXII	239
9.4.0 Binding kinetics of CFI to immobilised FXII	241
9.5.0 Plasma FXII activation in the presence of CFI	242
9.6.0 Graal1 homologues and Molecular docking	244
9.7.0 Molecular docking of SRCR and FXII FnII	244
9.10 Discussion	248
9.10.1 Graal1 and CFI binding to FXII	248
9.10.2 FXII activity assay in the presence of CFI	249
9.10.3 Binding of FXII FnII to SRCR domains	249
9.11.0 Conclusion	250
9.12.0 Future prospects	250
10.0 Appendices	252
11.0 Reference:	259

List of figures

Figure 1.1: Schematic representation showing the contact Factor and tissue factor pathways.

Figure 1.2: Diagrammatic representation showing the enzymatic degradation of the fibrin mesh.

Figure 1.3: Diagram showing domain organisation and different forms of human FXII.

Figure 1.4: Crystal structures of β -Factor XII and β -Factor XIIIa.

Figure 1.5: Structure of FXII Fnl-EGF2-like tandem domain.

Figure 1.6: Multiple sequence alignment of Fnl domains from various proteins including FXII Fnl.

Figure 1.7: Schematic overview showing receptor and contact factor mediated interactions.

Figure 1.8: Phylogram showing evolutionary relatedness of gC1q-R sequences in different species.

Figure 1.9: Cartoon diagram of the crystal structure of gC1q-R.

Figure 1.10: Electrostatic surface charge representation of gC1q-R.

Figure 1.11: HK bound PK and FXII assembly on gC1q-R surface with Zn^{2+} on the endothelial cell membrane.

Figure 3.1: ÄKTA pure instrument showing attached size exclusion column to the ÄKTA instrument.

Figure 3.2. Diagram showing a typical chromatogram from beginning (left) to end (right).

Figure 3.3: Excitation of surface plasmons and reflection from incidence beam.

Figure 3.4. Sensor CM5 chip showing the dust jacket sheath (outer part) and the gold surface sitting on a white plastic.

Figure 3.5: Amine coupling of ligand using EDC/NHS.

Figure 3.6: Analyte binding to immobilised ligand on the sensor surface (Gold surface).

Figure 3.7: Heterogenous ligand model.

Figure 3.8: Phase diagram and vapour diffusion method.

Figure 3.9: Crystal lattice made up of unit cells.

Figure 3.10: Radiation spectrum from a copper (Cu) source.

Figure 3.11: Description of Bragg's law in real space.

Figure 3.12: Ewalds sphere construction describing Bragg's law in reciprocal space.

Figure 4.1: Agarose gel electrophoresis of FXII constructs after PCR amplification.

Figure 4.2: Agarose gel electrophoresis of restriction double digest of expression plasmid vectors containing FXII FnlI and FXII FnlI-EGF1.

Figure 4.3: Affinity (Ni^{2+}) chromatography and SDS-PAGE gel analysis of FXII FnlI-EGF1.

Figure 4.4: Size exclusion chromatographic and SDS-PAGE gel analysis of FXII FnlI-EGF1.

Figure 4.5: Chromatographic and SDS-PAGE gel analysis of FXII FnlI.

Figure 4.6: SDS-PAGE gel analysis of WT HisTrx-FXII FnlI cleavage assay using HRV 3C enzyme.

Figure 4.7: SDS-PAGE gel (20 %) analysis of WT HisTrx-FXII FnlI.

Figure 4.8: WT HisTrx-FXII FnlI purification following HRV 3C cleavage.

Figure 4.9: HisTrx-FXII FnlI mutant purification following HRV 3C cleavage.

Figure 4.10: FXII FnlI crystals and diffraction pattern.

Figure 4.11: FXII FnlI bound Zn^{2+} crystal structure.

Figure 4.12 Zn^{2+} sites on FXII FnlI.

Figure 4.13: Electrostatic surface potential of FXII FnlI.

Figure 4.14: Electrostatic Isocontour of FXII FnlI.

Figure 4.15: Overlay of the tryptophan pocket (Trp-Trp) in FXII FnlI form 1 and form 2.

Figure 4.16: Crystals of FXII FnlI (form 3) in the presence of dextran sulfate 5 crystals.

Figure 4.17: FXII FnlI structure (form 3).

Figure 4.18: FXII FnlI form 3 and form 1.

Figure 4.19: Trp-Trp pocket of FXII FnlI (form 3).

Figure 4.20: Overlay of Trp53-Trp66 pocket of FXII FnlI form 1 and form 3.

Figure 4.21: Amino acid sequence alignment of FXII FnlI and FnlI homologues.

Figure 4.22: Structural overlay of FnlI in FXII and FnlI homologues

Figure 4.23: Disulfide bonds in FXII FnlI form 1 with loop 2 and Trp53-Trp66.

Figure 4.24: Structural overlay of FXII FnlI structures (form 1 and form 3).

Figure 4.25: Conformational changes in loop 2 of FXII FnlI form 1 and form 3.

Figure 4.26: Structural overlay of FnlI in FXII and FnlI in Pro-MMP2 (plus Prodomain).

Figure 4.27: Structural overlay of FnlI in FXII and FnlI in Fibronectin.

Figure 4.28: Loop 2 in PDC109 and FXII FnlI (form 1).

Figure 4.29: Stick representation of Trp-Trp pocket in PDC109 and FXII FnlI (form 1).

Figure 4.24: FXII Tenri deficiency as a result of amino acid mutation in Tyr34 to Cys34.

Figure 5.1: Interaction between gC1q-R and FXII FnlI in 10 μM and 50 μM Zn^{2+} .

Figure 5.2: Interaction between gC1q-R and FXII FnII.

Figure 5.3: Interaction between gC1q-R and FXII FnII-EGF1 in the presence of 50 μM Zn^{2+} .

Figure 5.4: Interaction between gC1q-R and WT HisTrx-FXII FnII in the presence of 50 μM Zn^{2+} .

Figure 5.5: Oligomerisation of gC1q-R and FXII FnII.

Figure 5.6: Crystals of gC1q-R bound FXII protein domains in the presence of Zn^{2+} .

Figure 5.7: Crystal structure of gC1q-R bound to FXII FnII.

Figure 5.8: gC1q-R chain C showing 190-loop and Zn^{2+} site.

Figure 5.9: Crystal structure of bound and unbound FXII FnII to gC1q-R.

Figure 5.10: FXII FnII bound to gC1q-R (form 4) showing anionic 190-loop and G1 pocket.

Figure 5.11: FXII FnII bridging two gC1q-R trimers.

Figure 5.12: Expression of human WT-gC1q-R and gC1q-R mutants.

Figure 5.13: Sensogram of FXII FnII binding to immobilised gC1q-R.

Figure 5.14: Sensogram of OneStep injection of FXII (FnII or FnII-EGF1) on immobilised gC1q-R.

Figure 5.15: Sensogram of OneStep of FXII FnII.

Figure 5.16: Sensogram of OneStep of HisTrx-FXII FnII and HisTrx (Control).

Figure 5.17: The effect of HisTrx-FXII FnII (Asp₆₃Ala-Gln₆₄Ala-Arg₆₅Ala) mutant in binding to G2 pocket of gc1q-R.

Figure 5.18: Binding of gC1q-R and immobilised FXII.

Figure 5.19: FXII binding to PK.

Figure 5.20: FXII binding to PK.

Figure 6.1: Complex formation of mFXII-gC1q-R in the presence of Zn^{2+} .

Figure 6.2: gC1q-R interaction with mFXII/mFXIIa mixture.

Figure 6.3: FXII-HK-gC1q-R complex formation in solution with Zn^{2+} added.

Figure 6.4: Complex formation of mFXII-HK-gC1q-R in solution in the presence Zn^{2+} .

Figure 6.5: HK-gC1q-R complex formation in solution with Zn^{2+} added.

Figure 6.6: Contact activation assay.

Figure 6.7: Displacement of FXII or HK binding to gC1q-R by FXII FnII or HKD5.

Figure 6.8: Forms of WT gC1q-R (oligomer and trimer).

Figure 6.9: Contact activation assay for WT gC1q-R oligomer and gC1q-R trimer.

Figure 6.10: Plasma-based contact activation using WT gC1q-R as an activator.

Figure 6.11: Clot formation using gC1q-R as an activator.

Figure 7.1: FXII FnII crystal packing with Zn^{2+} 1 and 2 in the interface.

Figure 7.2: Zn²⁺-induced FXII F_{nl} dimer formation in solution.

Figure 7.3: FXII and FXII F_{nl} binding to immobilised FXII on CM5 chip.

Figure 7.4: Binding studies showing FXII interacting to itself.

Figure 7.5: Fitting of FXII F_{nl} (with or without Zn²⁺) binding models.

Figure 8.1: Agarose gel analysis of mFXII. A

Figure 8.2: SDS-PAGE gel analysis of mFXII purification.

Figure 8.3: mFXII S526A in the presence of CTI.

Figure 8.5: 15 % reducing SDS-PAGE gel showing mFXII S526A deglycosylation.

Figure 8.6: Crystals of WT mFXII in the presence of dextran sulfate 5 with and without Zn²⁺.

Figure 8.7: Diffraction of WT mFXII crystals.

Figure 8.8: Crystals of mFXII in the presence of gC1q-R.

Figure 8.9: Crystals of gel filtrated gC1q-R in the presence of HK domain 5.

Figure 8.10: Crystals of gC1q-R in the presence of peptides (RCP, H4 or LBP).

Figure 9.1: SDS-PAGE gel of mFXII expressed in S2 cells.

Figure 9.2: Analytical size exclusion chromatography and SDS-PAGE gel of mFXII expressed in S2 cells.

Figure 9.3: Ion-exchange chromatography and SDS-PAGE gel of mFXII expressed in S2 cells.

Figure 9.4: Amino acid sequence and domain organisation of Graal1.

Figure 9.5: 1 % agarose gel analysis of double digested pMT-PURO- Graal₈₆₃₋₁₁₅₀ gene.

Figure 9.6: Graal₈₆₃₋₁₁₅₀ protein identification via western blot from insect media.

Figure 9.10: Size exclusion chromatography and SDS-PAGE gel analysis of Graal₈₆₃₋₁₁₅₀.

Figure 9.11: Binding analysis of immobilised mFXII S526A to Graal₈₆₃₋₁₁₅₀ and CFI.

Figure 9.12: FXII binding to immobilised Graal₈₆₃₋₁₁₅₀ on CM5 sensor chip surface.

Figure 9.13: SPR binding analysis of CFI to immobilised human FXIIa in the presence and absence of Ca²⁺.

Figure 9.14: Binding curves of Graal₈₆₃₋₁₁₅₀ to immobilised mFXII S526A.

Figure 9.15: Binding curves of Graal₈₆₃₋₁₁₅₀ to immobilised human FXIIa.

Figure 9.16: Binding curves of CFI to immobilised human FXIIa.

Figure 9.17: FXII cleavage of chromogenic substrate S-2302.

Figure 9.18: Prediction of Graal1 SRCR domain homologues using Phyre2.

Figure 9.19: Molecular docking of FXII F_{nl} to SRCR domain in CFI, mMARCO and Hepsin.

Abbreviation

aa- Amino acid

Abs- absorbance

CAS- contact activation system

CCD- Charged Coupled Device

CuSO₄- copper sulfate

dNTP- Deoxyribonucleotide triphosphate

E. coli- *Escherichia coli*

g- gram

GP1b- Glycoprotein 1 b

EDTA- Ethylenediaminetetraacetic acid

HEPES- 4-(2-hydroxyethyl)-1-piperazineethanesulfonic acid

IPTG- Isopropyl β-D-1-thiogalactopyranoside

kDa- Kilo Dalton

L.B- Luria Broth

L- Litre

mAU- milli absorbance unit

MES- d 2-(N-morpholino)ethanesulfonic acid

nm-nanometer

PVDF- Polyvinylidene difluoride

rpm- revolution per minutes

RMSD- Squared Root of Mean Deviation

RT- room temperature

SDS-PAGE- Sodium Dodecyl sulfate - Polyacrylamide gel electrophoresis (SDS-PAGE)

TEMED- Tetramethylethylenediamine

Tris- Tris(hydroxymethyl)aminomethane

UV- ultraviolet

2D SDS-PAGE- 2 dimensional Sodium Dodecyl sulfate - Polyacrylamide gel electrophoresis
(SDS-PAGE)

CHAPTER 1.0

INTRODUCTION

1.0 Introduction

1.1.0 The Vascular system

The vascular system, also called the circulatory system (or cardiovascular system) is made up of extensive networks of arteries, capillaries, veins or vessels that carry blood and lymph through the body. The vascular system delivers oxygen and nutrients to tissues, removes cellular and metabolic waste products, fights infections, temperature and pH control and maintains vessel integrity upon blood vessel injury. This therefore contributes significantly in maintaining homeostasis ⁽¹⁾. Haemostasis plays an integral part in maintaining the integrity of the vascular system ⁽²⁾.

1.1.1 Haemostasis and Thrombosis

Haemostasis is an important physiological process that aims to maintain normal blood fluidity and integrity within the vascular system ⁽³⁾ upon injury to prevent excessive blood loss by forming a blood clot. Thrombosis, on the other hand, is the pathogenesis of clot formation as a result of unregulated haemostasis without injury or damage to the blood vessel and can also cause numerous thrombosis-associated diseases ^(4, 5). To avoid excessive bleeding (haemorrhaging) and tissue infection ⁽⁶⁾ from sites of blood vessel injury, the primary mechanism of the haemostatic response involves recruiting platelets to the site of injury to adhere to components of the subendothelium within the vasculature. Platelets utilise receptors including glycoprotein Ib alpha (GPIb α) to interact with the A1 domain of Von Willebrand factor (VWF) expressed by endothelial cells ⁽⁷⁻⁹⁾. Also, sub-endothelial matrix proteins including fibrinogen, VWF, collagen, fibronectin and vitronectin promote platelet adhesion and aggregation by interacting with platelet integrins such as α IIb β 3 to form a provisional haemostatic plug (clot) ^(10, 11). The secondary mechanism of haemostasis through

insoluble fibrin (via blood coagulation) reinforces the primary haemostasis (plug formation) primarily formed by platelets ^(12, 13) and cells including leukocytes ⁽¹⁴⁾ with trapped erythrocytes as platelet aggregates and insoluble fibrin together contribute in forming a stable haemostatic plug. Tight regulation of haemostasis is paramount to avoid states of hypocoagulability or hypercoagulability. Deficiency in or imbalance between procoagulation and anticoagulation can lead to states of hypocoagulability or hypercoagulability ^(15, 16). Thrombosis can arise from the imbalance between procoagulation and anticoagulation, by which arteries or veins are occluded by a pathological thrombi (clot), in the heart or brain, causing arterial thrombosis that can lead to cardiovascular diseases (i.e. heart attack) or stroke, ⁽¹⁷⁾ respectively. In the veins, venous thrombosis leads to venous thromboembolism such as deep vein thrombosis in the legs and pulmonary embolism in the lungs ⁽¹⁸⁾. Research interest is increasing in the field of thrombosis as death from thrombosis and/or thrombosis related diseases each year is on the rise ^(19, 20). The need to diagnose, treat and prevent thrombosis through a multidisciplinary approach ⁽²¹⁾ has proven invaluable, although a lot more needs to be done to tackle thrombosis. Understanding the fundamental molecular mechanisms involved in blood coagulation, inflammation, atherogenesis and their regulation is of huge importance in the design and development of biomarkers ⁽²²⁻²⁵⁾ and medicines to treat and manage thrombosis ^(26, 27).

1.1.2 Blood Coagulation

The secondary mechanism of haemostasis, also referred to as blood coagulation, is a concept dating back to the 1960's, when Davie, Ratnoff and Macfarlane described the "cascade-waterfall" hypotheses, ⁽²⁸⁾ outlining how proteolytically cleaved and activated proenzymes

became enzymes and subsequently leading to the activation of other proenzymes downstream of the cascade ⁽²⁹⁾. This ultimately leads to haemostasis or cessation of bleeding. Blood coagulation is made up of two pathways; tissue factor (extrinsic) and contact factor (intrinsic) pathway. Both pathways converge to make up the common pathway via FXa to ultimately form a clot architecture characterised by platelet aggregates and an insoluble fibrin mesh ⁽²⁹⁾ (Figure 1.1).

1.1.2.1 Tissue Factor (Extrinsic) Pathway

The tissue factor pathway, also known as the extrinsic pathway operates through a cell surface glycoprotein tissue factor (TF; cofactor) on leukocytes (monocytes and neutrophils) ⁽³⁰⁾ and the subendothelial tissues. The tissue factor pathway is initiated when constitutively expressed TF forms a complex with zymogen FVII; TF-FVII ⁽³¹⁾ upon mechanical or chemical damage of the vascular wall ⁽³²⁾. TF-FVII is subsequently activated by FXa to produce TF-FVIIa, which in turn activates FX to FXa ⁽³³⁾ and FIX to FIXa. This thereby serves as a bridge between the tissue factor and contact factor pathway, ⁽³⁴⁾ for FXa production to cleave and activate prothrombin to thrombin with fibrin formation from precursor fibrinogen by thrombin.

1.1.2.2 Contact Factor (Intrinsic) Pathway

The contact factor pathway, also referred to as the intrinsic pathway, has been termed the contact activation system (CAS), which includes serine proteases factor XII (FXII), plasma prekallikrein (PK), coagulation factor XI (FXI), and cofactor high molecular weight kininogen (HK), a non-enzymatic cofactor of PK and FXI ^(35, 36). CAS is considered an ancient and conserved arm of the innate immune system, ⁽³⁷⁾ implicated in various physiological responses

(38, 39) including blood coagulation, (40) fibrinolysis, (41) inflammation (42, 43) and angiogenesis (44). As the name indicates, contact factors (FXII, HK bound PK or HK bound FXI) in the CAS have a requirement to come in contact with physiological (45, 46) or non-physiological negatively charged surfaces (47) for activation. A wealth of knowledge on the biochemistry of contact activation pertaining the activation of contact factors by non-physiologically relevant negatively charged surfaces (kaolin, ellagic acid, dextran sulfate and biomaterial surfaces in biomedical devices etc.) has been well studied *in vitro* (35, 48). Recently, physiologically relevant negatively charged surfaces including polyphosphate (49-51) and gC1q-R (52, 53) have been reported to be potential biomolecules that may provide the appropriate surface for the initiation of the CAS.

Contact activation has been reported to have a role in thrombosis (54, 55) but not in haemostasis (56). However, thrombosis and haemostasis share a host of coagulation factors with the ultimate aim of forming a pathophysiological or physiologically relevant clot, respectively.

CAS has been recognised to have two branches; (i) the inflammatory branch and (ii) the plasma coagulation branch (57). In both branches, contact activation is initiated when FXIIa proteolytically cleaves HK bound PK or HK bound FXI upon assembly on a negatively charged surface mediated by Zn^{2+} . Zn^{2+} has been reported to bind and subject both FXII and HK to conformational changes required for binding to negatively charged surfaces, leading to zymogen autoactivation to generate trivial amounts of FXIIa (58, 59).

In the inflammatory branch, activated FXIIa on a negatively charged surface and in close proximity to HK bound PK cleaves PK to PKa, then PKa in turn reciprocally cleaves and activates FXII to FXIIa (60) in a positive feedback loop. Subsequently, PKa ends up cleaving and releasing the inflammatory mediator peptide, bradykinin (BK) (61) from domain 4 of cofactor

HK⁽⁶²⁾. The BK peptide binds to its receptors (B₁ and B₂)^(63, 64) expressed on the surface of endothelial cells within the blood vessels. BK binding to its receptor induces the activation of several pro-inflammatory signalling pathways leading to vasodilation, pain, and neutrophil chemotaxis^(65, 66).

Activated FXIIa in the plasma coagulation branch activates FXI through proteolytic cleavage on the surface of platelets with no reciprocal activation reported between FXII and FXI thus far, despite 58 % amino acid sequence homology between PK and FXI⁽⁶⁷⁾. However, FXI activation by thrombin in a positive feedback loop following tissue factor (extrinsic) pathway activation can result in contact activation mediated via FXI bound HK *in vitro* but not in plasma⁽⁶⁸⁻⁷¹⁾. Activated FXI (FXIa) in the contact factor (intrinsic) pathway results in further cleavages further down the serine protease cascade, in which activated FIX (FIXa) by FXIa⁽⁷²⁾ further cleaves and activates FX to FXa,⁽⁷³⁻⁷⁵⁾ which subsequently generates thrombin from prothrombin. Fibrin generation from fibrinogen via thrombin cleavage is the end point of the pathway to ensure that the haemostatic plug (clot) initiated by the primary haemostasis is mechanically stable⁽⁷⁶⁾. Additional mechanisms relating activated fibrin stabilizing factor, (thrombin-activated transglutaminase, FXIIIa)⁽⁷⁷⁾ and FXII⁽⁷⁸⁾ have been described to contribute in modulating the mechanical stability of the formed clot. FXII has been reported to make the clot denser with thicker fibrin fibres⁽⁷⁹⁾.

FXII-mediated contact activation in the presence of a negatively charged surface provides a mechanistic basis for diagnostic coagulation tests in the hospitals or clinics using activated partial thromboplastin time (aPTT) assay. The importance of the contact factors in animal models have shown that injury-induced thrombus formation in FXI, FXII, PK and HK deficient mice models manifest an anti-thrombotic phenotype, thus raising an interesting possibility for use in the development of safer anti-thrombotic drugs or therapeutics⁽⁸⁰⁻⁸⁴⁾.

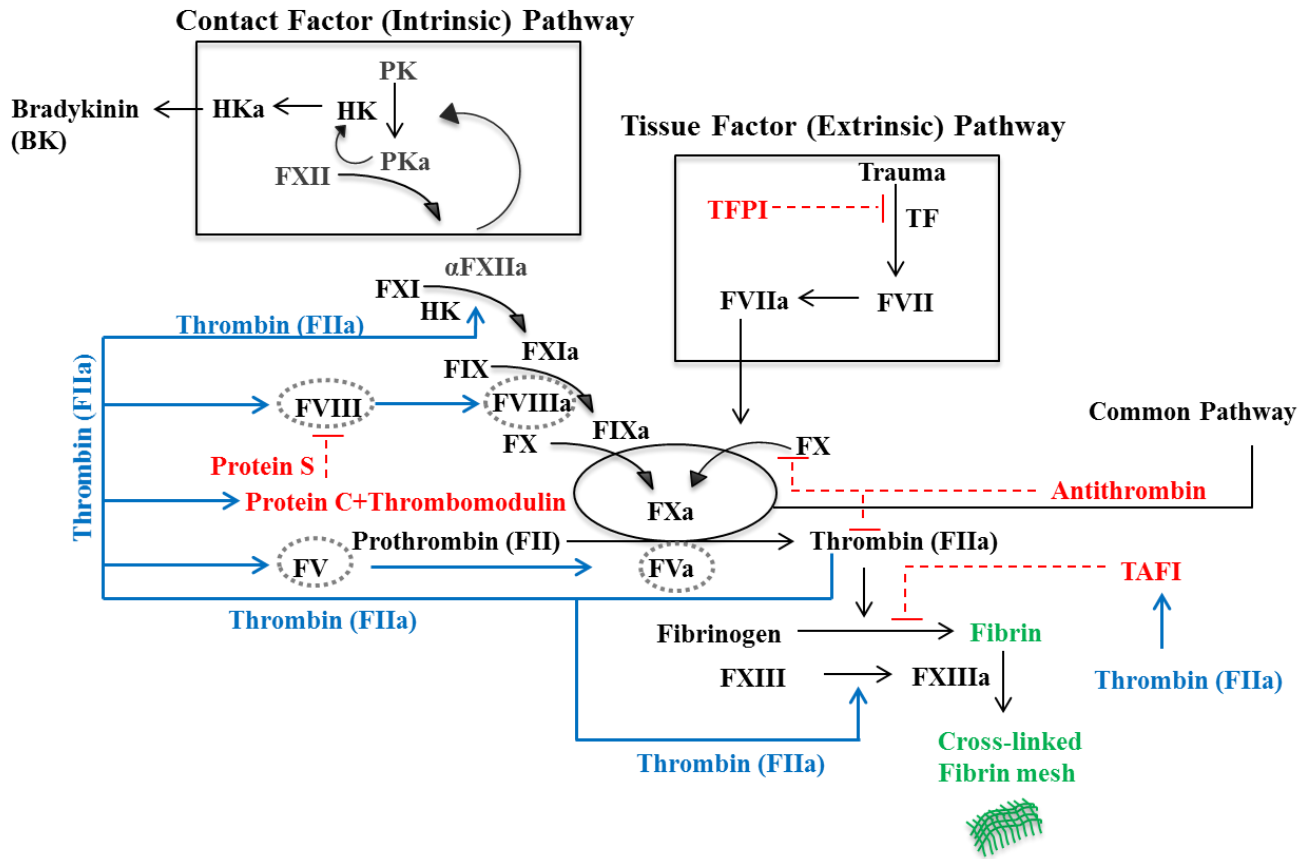


Figure 1.1: Schematic representation showing the contact Factor and tissue factor pathways. The tissue factor (extrinsic) pathway is initiated when cell surface tissue factor (TF) forms a complex with FVII to TF:FVII, leading to TF:FVIIa which ultimately contributes to fibrin formation (green) via FXa. FXa is where both the tissue factor and contact factor pathway converge to form the common pathway. The contact factor (Intrinsic) pathway is triggered upon FXII binding to a negatively charged surface in the presence of HK, PK and Zn^{2+} , ultimately resulting in fibrin formation. Inhibitors regulating the pathways are shown in red and the blue arrows show which proteins thrombin cleaves. Dashed black arrows represent activation, while red dash shows inhibition. The blue arrows signify the role thrombin has in activating proteins and protease to ultimately lead to fibrin formation.

1.1.3 The fibrinolytic system (clot lysis)

Proenzymes such as plasminogen bind to fibrin and are subsequently converted to plasmin by tissue plasminogen activator (tPA) and urokinase plasminogen activator (uPA) to promote clot degradation via the fibrinolytic (clot lysis) system ⁽⁸⁵⁾. FXII and tPA have some degree of homology and FXIIa has been demonstrated to contribute in fibrin degradation by converting plasminogen to plasmin. Plasminogen is adsorbed and concentrated on the haemostatic plug (clot) where it also binds to fibrin to facilitate the formation of plasmin when necessary for fibrin degradation (clot lysis) as shown in Figure 1.2 ^(79, 86).

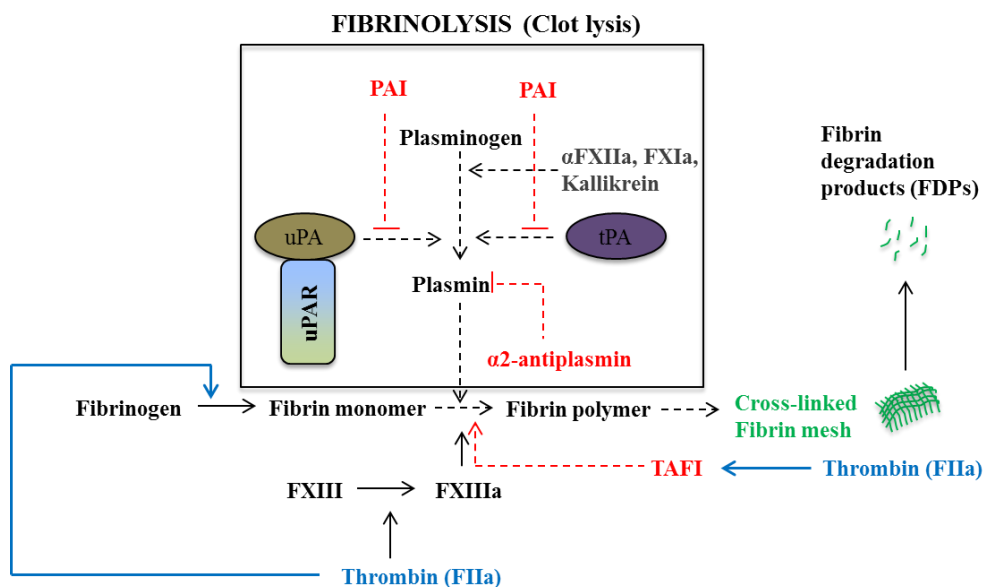


Figure 1.2: Diagrammatic representation showing the enzymatic degradation of the fibrin mesh. The zymogen plasminogen is converted to plasmin by uPA or tPA. Other enzymes such as αFXIIa, FXIa and Kallikrein (grey) are suggested to convert plasminogen to plasmin. Bound Plasmin to fibrin degrades the fibrin into fibrin degradation products (FDPs) as shown in green. Fibrinolysis is tightly regulated as Plasminogen activating inhibitor or PAI (red) inhibit fibrinolysis by preventing uPA or tPA (in red) from converting plasminogen to plasmin. Also, α2-antiplasmin (red) and Thrombin-activatable fibrinolysis inhibitor (TAFI) help to regulate fibrinolysis. Dashed black arrows denotes activation while red dashed represents inhibition.

Fibrinolysis promotes the initiation of wound healing of the injured blood vessel, in which proteolysis of fibrin (dissolved fibrin) gives rise to soluble fibrin degradation products (FDPs), which is reported to have a degree of immunomodulatory and chemotactic functions ⁽⁸⁷⁻⁸⁹⁾. Fibrinolysis is tightly regulated, as α 2-antiplasmin (α 2-AP) prevents free plasma plasmin from activating plasminogen while plasminogen activator inhibitor (PAI) type-1 and PAI-2 control the activity of uPA and tPA ⁽⁹⁰⁾.

1.4 Coagulation Factor Domain Structure - Comparison

Vitamin K-dependent (VKD) plasma proteins including factor X contain a γ -carboxyglutamic acid (Gla) rich domain at the N-terminus, through which they bind to externalised phosphatidylserine (PS) on activated cell membranes in a Ca^{2+} dependent manner to facilitate the localisation of the prothrombinase (FXa and cofactor FVa) and tenase (FIXa and cofactor FVIIIa) complexes on membrane surfaces for proteolysis ⁽⁹¹⁾. This is reminiscent of what is observed in FXII contact activation. However, instead of utilising Gla domains, contact factors (FXII, PK, FXI and HK) bind negatively charged surfaces through key modules of fibronectin for FXII, apple domains for PK and FXI, while HKD5 is used for HK ^(92, 93). Although PK and FXI contain apple domains and are reported to be involved in protein-protein interaction with other proteins, both serine proteases are mostly bound to HK in plasma and shown to localise on surfaces through cofactor HK. In contrast to Ca^{2+} ions facilitating Gla domains binding to PS, contact factors FXII and HK in the CAS utilise Zn^{2+} ions to mediate their binding to negatively charged surfaces.

1.4.1 Prekallikrein (PK) and Factor XI (FXI)

Prekallikrein (PK), also known as Fletcher factor, is a single chain glycoprotein serine protease existing in two molecular weight variants of M_r 88,000 and M_r 85,000, due to different glycosylation forms. PK circulates in plasma as a zymogen at a concentration of 50 $\mu\text{g/mL}$ (490 nM), with most of PK bound non-covalently to HK ⁽⁹⁴⁾. Limited proteolysis of PK to PKa generates two chains consisting of an NH_2 -terminal heavy chain at 52 kDa and two light chain variants around 33-36 kDa linked by a disulphide bond. Further cleavages have been reported ⁽⁹⁵⁻⁹⁷⁾.

Unlike PK, FXI is a dimer of 80 kDa monomer subunit (607 amino acid) ⁽⁹⁸⁾ with 58% sequence identity to PK and shares the same ancestral predecessor which, through duplication of the PK gene in mammalian evolution. Both PKa and FXIa have in the heavy chain 4 apple domains (A1-4) and a catalytic domain in the light chain. The FXI zymogen circulates in plasma at a concentration of 5 $\mu\text{g/mL}$ (30 nM) tightly bound to HK in a similar manner to PK ^(99, 100).

1.4.2 High Molecular Weight Kininogen (HK)

Williams-Fitzgerald factor, ⁽¹⁰¹⁾ commonly known as HK, ⁽¹⁰²⁾ is a single-chain non-enzymatic glycoprotein with a molecular weight of 120 kDa ⁽¹⁰³⁾ and is abundant at a plasma concentration of 80 $\mu\text{g/mL}$ (670 nM). HK consists of 6 domains (D1-6) in which the heavy chain is made up of domains 1, 2 and 3, with domains 5 and 6 from the light chain, while domain 4 links the heavy and light chain together to form a globular structure ⁽¹⁰⁴⁾. Domain 6 of HK is the PK and FXI binding site, ^(94, 105, 106) while domain 5 has been reported to bind to negatively charged surfaces on platelets and various cell types including neutrophils ⁽¹⁰⁷⁾ and endothelial cells ⁽¹⁰⁸⁾ to mediate the recruitment of PK and FXI to surfaces for proteolysis.

Zn²⁺ has been implicated in binding to domain 5 of HK to induce a conformational change within HK and as a result facilitates HK binding to negatively charged surfaces ⁽¹⁰⁹⁾. This can subsequently lead to HK cleavage by PKa to generate HKa; producing a disulphide linked two-chain HKa consisting of a heavy chain (D1–D3; 64 kDa) and a light chain (D5–D6; 56 kDa), releasing the short proinflammatory mediator BK peptide (D4) ⁽¹⁰⁴⁾. *In vitro*, HK has also been demonstrated to undergo proteolysis by FXIa at a much slower rate in comparison to PKa and contrary to HK bound PK involvement in contact activation, HK bound FXI appears to inhibit contact activation by degrading domains 5 and 6 in HK ⁽¹¹⁰⁾.

1.4.3 Factor XII (FXII) – history

Factor XII (FXII), also referred to as Hageman factor, was discovered in 1955 by the haematologist, Oscar Ratnoff and colleagues as a clotting factor lacking in plasma ⁽¹¹¹⁾ of a patient called John Hageman through routine pre-operative screening to have a prolonged clotting time in his activated partial thromboplastin time (aPTT) results ⁽¹¹²⁾.

Neither John Hageman nor his family had any bleeding tendency thus asymptomatic for any bleeding disorder. However, he died from pulmonary embolism ^(113, 114). Oscar Ratnoff, alongside Earl Davie and other investigators including Robert G MacFarlane, identified FXII acting at the initial phase of blood clotting. FXII binding to negative charged surfaces initiates the “Waterfall or Cascade” model of coagulation leading to sequential activation of FXI, FIX and FX, culminating in thrombin production and fibrin formation, thereby contributing to clot formation.

Lack of FXII in humans and the prolongation in the aPTT assay do not correlate. However, FXII has been reported to have no role in haemostasis but demonstrated to play a significant role

in thrombosis as mouse knockouts in the FXII gene or FXII targeted monoclonal antibodies showed thrombo-protective phenotypes with either no or reduced thrombi formed, respectively ⁽¹¹⁵⁾.

1.4.3.1 Factor XII (FXII) protein and domain structure

The factor XII gene is a 12-kb DNA consisting of 13 introns and 14 exons located on the tip of the long arm of the fifth chromosome (5q33-qter) and is transcriptionally processed down to a 2-kb mRNA for translation into protein ⁽¹¹⁶⁾. The protein is transcribed and translated in hepatocytes in the liver ⁽¹¹⁷⁾ under the control of transcription factor, hepatocyte nuclear factor (HNF) α and/or estrogen ⁽¹¹⁸⁾ and secreted into the plasma ⁽¹¹⁹⁾.

Factor XII (FXII), is a single chain 80 kDa glycoprotein serine protease, ⁽¹²⁰⁾ circulating in plasma as a zymogen, at a concentration of 40 $\mu\text{g}/\text{mL}$ (375 nM) ⁽¹²¹⁾. FXII has been associated with Zn^{2+} binding to induce a conformational rearrangement, ^(122, 123) thereby facilitating FXII binding to negatively charged surfaces such as Neutrophil Extracellular Traps (NETs), ⁽¹²⁴⁾ platelet polyphosphates, endothelium exposed collagen, ⁽¹²⁵⁾ mast cell derived heparin, ⁽¹²⁶⁾ externalised phosphatidylserine on apoptotic cells, ⁽¹²⁷⁾ extracellular RNA, ⁽¹²⁸⁾ amyloid β protein (of Alzheimer's disease) and bacterial derived polyphosphate ⁽¹²⁹⁾ resulting in FXII autoactivation ⁽¹³⁰⁾. This results in reciprocal activation of FXII and PK to PKa and FXIIa by FXIIa and PKa, respectively ⁽¹³¹⁾. FXIIa is the active form of FXII, which has undergone proteolysis by PKa cleaving between Arg353-Val354. Subsequent cleavages on FXII have been reported between Arg334-Asn335 and Arg343-Asn344 producing β -Factor XIIa fragments with a portion of the heavy chain remnant attached to its N-terminus.

FXIIa consists of two chains; N-terminal 52 kDa heavy chain and C-terminal 28 kDa light chain, linked by a disulphide bond between Cys340 and Cys467 ⁽¹³²⁾. The heavy chain is made up of

the N-terminal fibronectin type-II domain (FnII), an epidermal growth factor like domain (EGF1), a fibronectin type-I domain (FnI), a second EGF-like domain (EGF2), a kringle domain, and a distinctive proline-rich domain, while the protease (catalytic) domain is confined to the light chain ⁽¹³³⁾ (Figure 1.3). Both chains have glycosylation sites, with a glycosylation defect reported in hereditary angioedema III (HAEIII) patients suffering from an inherited swelling disorder due to increased contact activation-driven microvascular leakage as a result of a point mutation in Thr309 to Lys309 (or Arg309) ^(134, 135). This makes FXII hyperactive, which as a result increases BK release from HK by PKa cleaved FXIIa. HAE type I and II have also been reported in unregulated FXII and PK activity manifesting episodes of swelling in patients, as a result of defective serpin C1 esterase inhibitor (C1-INH), natural inhibitor for FXII and PK ⁽¹³⁶⁻¹³⁸⁾.

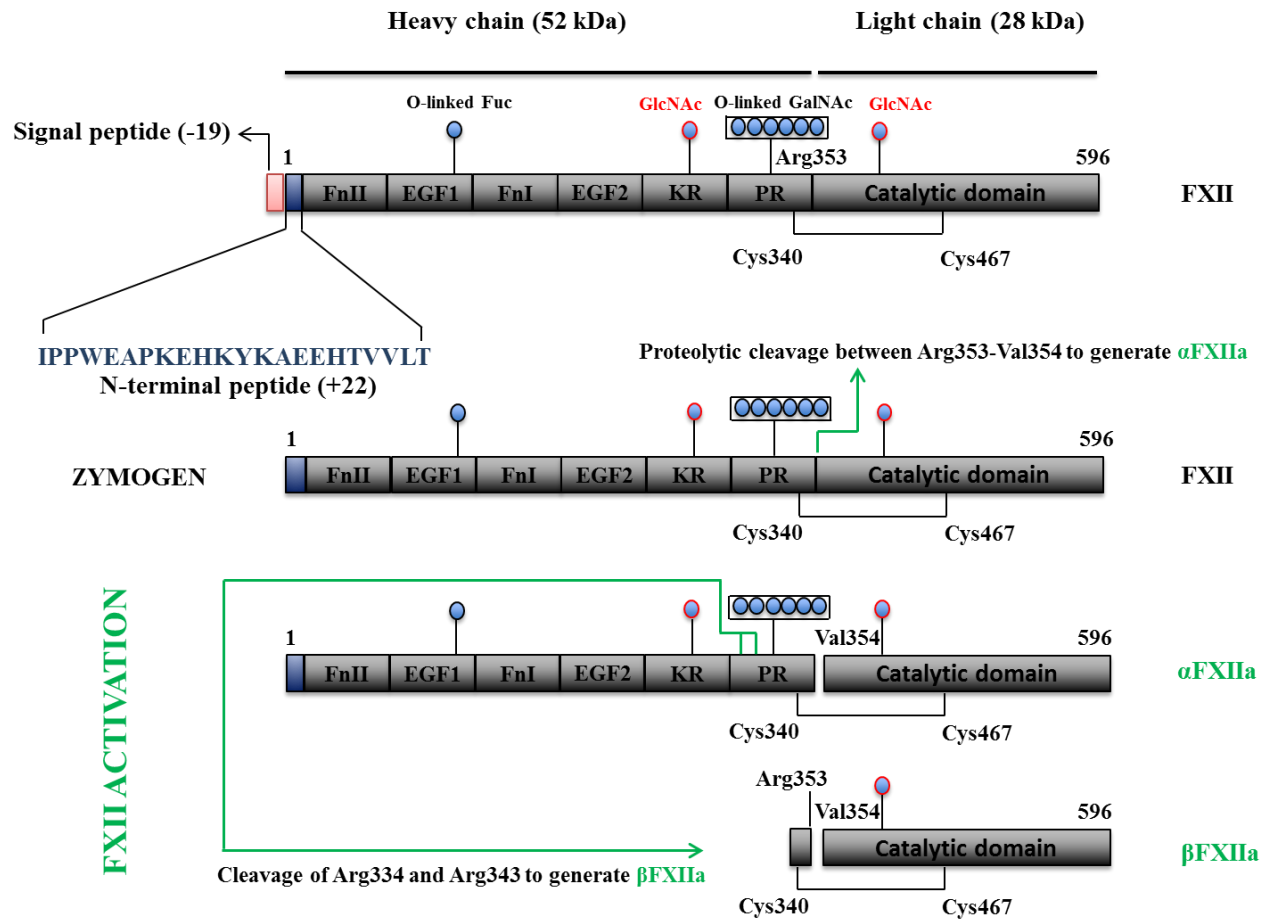


Figure 1.3: Diagram showing domain organisation and different forms of human FXII. FXII is comprised of two chains; a 52 kDa heavy and a 28 kDa light chain. The heavy chain contains a 22-residue N-terminal peptide, two Fibronectin type (Fn) domains (FnII and FnI), two Epidermal growth factor (EGF) domains (EGF1 and EGF2) and a kringle (KR) domain followed by a unique proline-rich (PR) region. The zymogen FXII is converted to α FXIIa by PKa or α FXIIa by proteolysis between Arg353-Val354. Subsequent cleavages of Arg334 and Arg343 generates β FXIIa. The catalytic domain and the heavy of chain are held together by a disulphide bond consisting of Cys340 and Cys467. The heavy chain is both N and O-linked glycosylated while the light chain is only N-linked glycosylated (close blue circles).

1.4.3.2 Structure of the β -Factor XIIa protease domain

The ability of FXII to cleave substrates or bind to inhibitors targeting the active site lies within the light chain of FXII, commonly referred to as β -Factor XIIa protease domain (or catalytic domain). The 28 kDa β -Factor XIIa protease domain is disulphide bonded to a 2 kDa heavy chain remnant from the Proline-rich (PR) region of the heavy of FXII ⁽¹³⁹⁾ when subjected to further cleavages between residues Arg334-Asn335 and Arg343-Asn335; ⁽¹⁴⁰⁾ ultimately losing almost all the domains from the heavy chain of FXII.

β -Factor XIIa has 6 intramolecular disulphide bonds and one intermolecular disulphide bond with the heavy chain remnant within the Proline-rich (PR) of the heavy chain of FXII ⁽¹⁴¹⁾. The enzymatic activity of β -Factor XIIa in the active site is performed by the catalytic triad His393, Asp442, and Ser544 ⁽¹²⁰⁾ when substrates including PK and FXI occupy substrate binding sites or pockets prior to cleavage of the activation loop.

A zymogen-like recombinant β -Factor XII 3D crystal structure (Figure 1.4A) was solved in 2015 by Pathak *et al.* describing the first structural basis for understanding FXII substrate recognition and zymogen activation. Furthermore, Alexey Dementiev *et al* 2018 revealed the first active β -Factor XIIa cocrystallized with inhibitors (figure 1.4B). An MBP fused β -Factor XIIa in complex with inhibitor PPACK and β -Factor XIIa alone crystal structures describing expression in insect cells and kinetics of β -Factor XIIa in an article, authored by Dr Monika Pathak and Dr Rosa Manna is published in Acta Crystallographica section D.

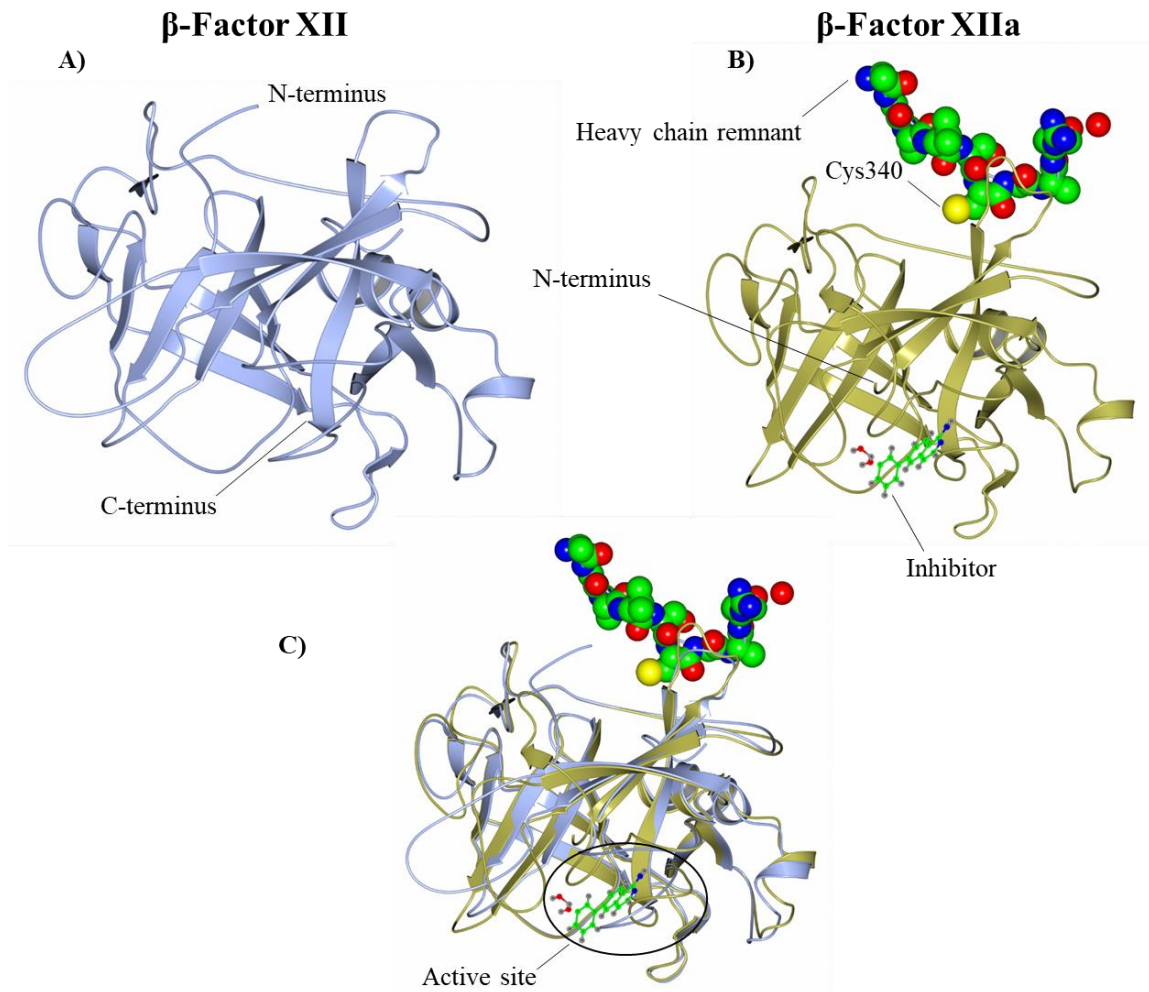


Figure 1.4: Crystal structures of β -Factor XII and β -Factor XIIa. A) β -Factor XII 3D structure showing solvent exposed N-terminus while in B) β -Factor XIIa the N-terminus is positioned around the active. Cys340 is disulphide bonded with Cys467 (not shown) thus linking the heavy chain remnant (in sphere) to the light chain of FXII. C) Shows an overlay of β -Factor XII and β -Factor XIIa structures showing differences in regions including the N-terminus with no heavy chain remnant in β -Factor XII. PDB codes = 4XDE for β -Factor XII and 6B77 for β -Factor XIIa.

1.4.3.3 The function of the heavy chain of FXII

The N-terminal 52 kDa heavy chain of FXII comprises of 6 domains, ⁽¹⁴²⁾ and the KOK5 antibody directed against the heavy chain has been shown to inhibit FXII binding to kaolin. Furthermore, other monoclonal antibodies (B7C9 and P5-2-1) against the heavy chain have also been reported to inhibit FXII activation by negatively charged surfaces ⁽¹⁴³⁾. Domains within the heavy chain such as fibronectin type II and type I domain, the kringle domain and the second EGF-like domain have all been suggested to bind to negatively charged surfaces ^(139, 142, 144, 145). A crystal structure of the FXII Fnl-EGF2 domains (Figure 1.5) was solved in 2013 showing the surface charged potential with predominantly positively charged patches displayed on its surface ⁽¹⁴⁶⁾.

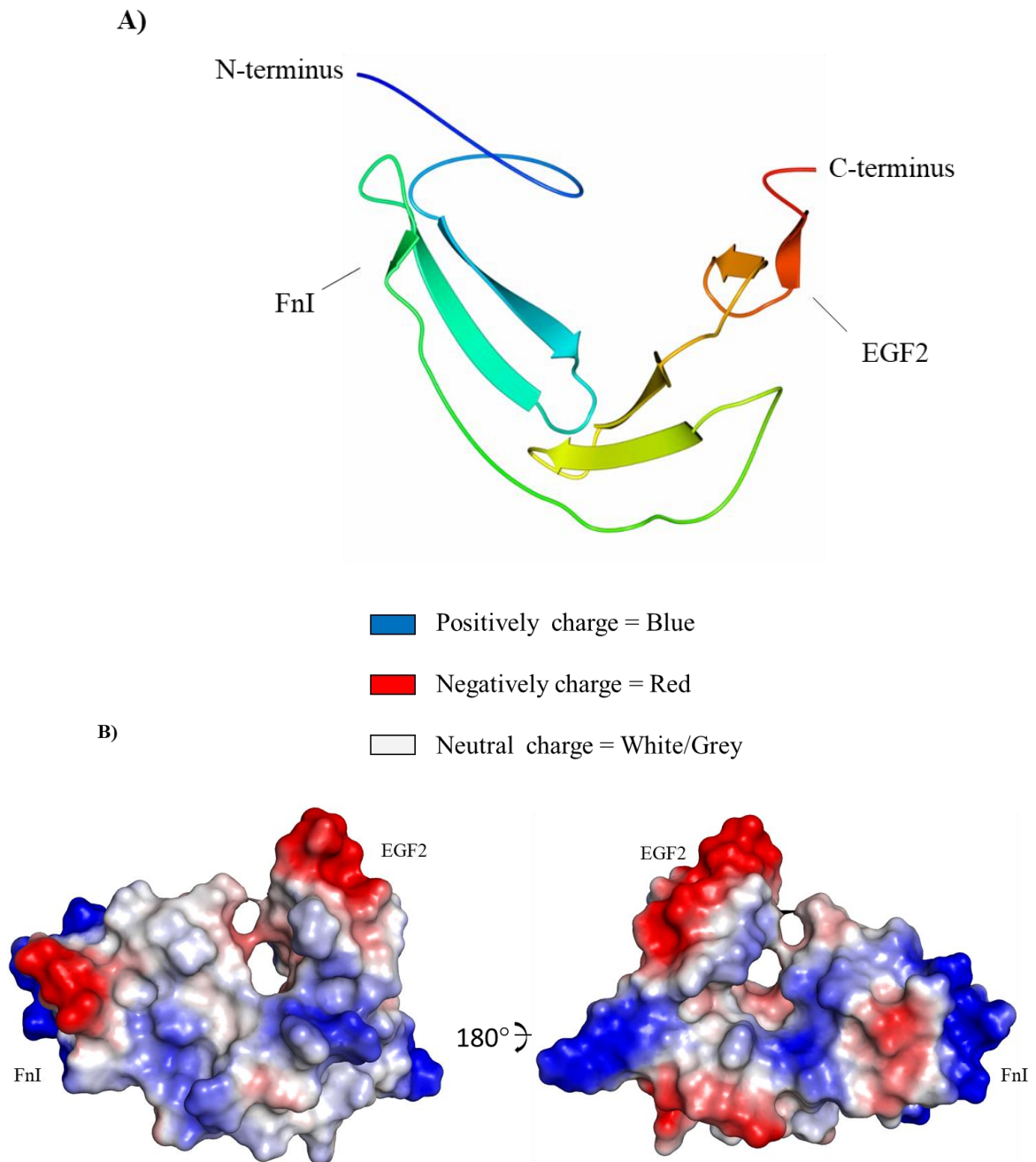


Figure 1.5: Structure of FXII Fnl-EGF2-like tandem domain. A) A rainbow coloured ribbon showing the 3D structure of FXII Fnl-EGF2 tandem domain with Fnl on the N-terminus and EGF2 on the C-terminus. B) Electrostatic surface potential showing the charged surface of the FXII Fnl-EGF2 structure with charged residues represented in colour – Red (negative), Blue (positive) and White/Grey (neutral). PDB code = 4BDX.

FXII heavy chain natural inhibitors such as Anophensin and hamdarin in mosquito saliva, isolated from *Anopheles* species including *An. Stephensi* and *An. Gambiae* have been characterised to display inhibitory effects on surface mediated activation of FXII. Furthermore, prolongation of the aPTT assay relative to PT assay in plasma has been reported in the presence of anophensin and the FXII FnII is demonstrated to bind to anophensin in a Zn²⁺ dependent manner ⁽¹⁴⁷⁾.

1.4.3.4 The fibronectin type II domain (FnII) in FXII and homologues

Fibronectin is composed of multiples repeats of fibronectin domains; fibronectin type I (FnI), fibronectin type II (FnII) and fibronectin type III (FnIII) ⁽¹⁴⁸⁻¹⁵⁰⁾. FnII domains are also found in other proteins including Hepatocyte Growth Factor Activator (HGFA), ⁽¹⁵¹⁾ Matrix metalloprotease 2 (MMP2), ^(152, 153) Matrix metalloprotease 9 (MMP9) ⁽¹⁵⁴⁾ and bull seminal plasma protein PDC109, ^(155, 156) with PDC109 having a similar structural homology to FXII FnII. The FXII FnII domain is 71-amino acids in length and contains four conserved cysteines involved in disulphide bond formation. A 22 amino acid N-terminal peptide is located upstream of the FnII domain unique to FXII. Apart from the four conserved cysteines involved in disulphide bond formation in FnII domains, other residues including Trp53 in FXII are conserved within the FnII domains. Arg47 in FXII is not conserved in PCD109 and is replaced by a serine at the same position in comparison to other FnII domains including FXII FnII as shown in the multiple sequence alignment (Figure 1.6).

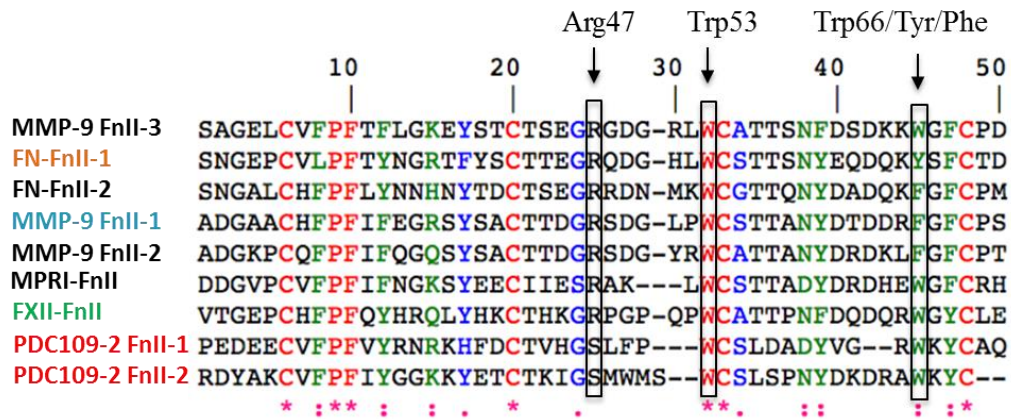


Figure 1.6: Multiple sequence alignment of FnlI domains from various proteins including FXII FnlI. Cysteines (in red) in all sequences are conserved. Also, residues corresponding to FXII Arg47 and Trp53 are all conserved in other FnlI domains, except in PDC109, FXII Arg47 is replaced with a serine. Trp66 in FXII is conserved in MMP9 FnlI-3, MPRI, FXII FnlI and PDC109. Asterisk indicates conserve in the all residues in the sequence.

Peptides from FXII FnlI have been demonstrated to outcompete full-length FXII for binding to gC1q-R on human vascular endothelial cells (HUVEC), therefore implicating and strengthening the hypothesis of FXII FnlI binding to artificially charged surfaces. Residues 39-47, 30-33 and 57-60 of FXII FnlI have been predicted from homology modelling to be surface exposed and contribute to the conformational changes required for binding to negatively charged surfaces (157).

1.5 Interactions between contact factors and pathogens

Bacterial and viral infections in clinical conditions such as sepsis lead to the activation of both the immune and coagulation systems (via contact factor or tissue factor pathway) for host defense, (158). However, uncontrolled activation can lead to bacteremia and viremia with major tissue damaging effects leading to disseminated intravascular coagulation (DIC), (159, 160)

microvascular thrombosis–induced hypoxia that contributes to multiple organ failure, septic shock, and ultimately death ⁽¹⁶¹⁾. Contact factors (FXII and HK bound PK) interact with a host of gram negative bacteria such as *Moraxella catarrhalis*, *Salmonella typhimurium*, *Salmonella enteritidis*, *Porphyromonas gingivalis*, *Klebsiella pneumoniae*, *Haemophilus influenza*, *Yersinia enterocolitica*, *Escherichia coli* and gram positive bacteria including *Streptococcus pyogenes*, *Streptococcus pneumoniae*, *Staphylococcus aureus*, ⁽¹⁶²⁾ as well as viruses (i.e. Hantavirus and Herpes simplex 1 virus). Pathogens have been reported to have the ability to provide on their surface negatively charged biomolecules to induce contact activation ⁽¹⁶³⁾. Bacterial derived negatively charged lipopolysaccharide (LPS) ⁽¹⁶⁰⁾ or surface associated negatively charged teichoic acids from *S. aureus* ⁽¹⁶⁴⁾ and long chain polyphosphate, ⁽¹⁶⁵⁾ curli ⁽¹⁶⁶⁾ or fimbriae ⁽¹⁶⁷⁾ from *E.coli* have all been demonstrated to induce contact activation and bradykinin release from HK ⁽¹⁶⁸⁾ thereby contributing to the host-defence reactions by activating the complement cascade ⁽³⁹⁾.

1.6 Cell interactions with contact factors

The interaction of contact factors HK ^(169, 170) and FXII with platelets, leukocytes and endothelial cells ^(52, 171) are likely to contribute to the innate immunity. Furthermore, Platelet-leukocyte-endothelial cell interactions ⁽¹⁷²⁾ and FXII activation in the presence of HK bound PK or HK bound FXI to collectively contribute to arterial thrombosis and deep vein thrombosis (DVT) in animal models have shed light on some of the roles contact activation can play *in vivo*.

The containment and destruction of pathogens through immune cells and plasma factors including FXII and FXIII provide an intravascular scaffold for protecting and maintaining vascular/host integrity ^(173, 174). Platelets are a key regulator of immunothrombosis, and serves

to bridge coagulation and inflammation via platelet-mediated contact activation on platelet surfaces. Platelet adhesion receptors including GPIb-IX-V complex and GP Iba α bind to contact factors (FXII, FXI and HK) ^(175, 176) and also facilitate NETosis (the process of forming neutrophil extracellular traps or NETs) by engaging neutrophils ⁽¹⁷⁷⁾. Platelet activation by thrombin in complex with the GPIba receptor has been reported to be regulated *in vivo* by the co-localisation of FXII and HK ^(178, 179). Furthermore, HK has been implicated in serving as a molecular bridge in the interplay between leukocytes and platelets, as GPIba on platelets is engaged by HK through domain 3 ⁽¹⁸⁰⁾ and domain 5 of HK on the other hand, binds in unison to MAC-1 on leukocytes ⁽¹⁸¹⁾. Contact factors (FXII, FXI, PK and HK) assembly on circulating neutrophil surface during inflammation has been proposed to enhance the release of granule contents at site of infection or blood vessel injury ⁽¹⁸²⁾.

Although, FXII deficiency is not associated with a defect in haemostasis; it has been reported to decrease migration of inflammatory cells into skin windows ⁽¹⁸³⁾ and has an important role in neutrophil aggregation in human plasma as it has been found to be present on neutrophil surfaces ^(184, 185).

Other proinflammatory mediators such as Bradykinin (BK) localise to the endothelial cell surface as a result of HK cleavage to release BK by FXII-mediated PKa via the CAS is important as BK receptors are expressed and localised on endothelial cell surfaces for signalling. A wealth of evidence has proven that the contact factor proteins FXII and HK can assemble along the surface of HUVEC in a Zn²⁺ dependent fashion and one of the major endothelial cell receptors demonstrated to interact with HK and FXII is the ubiquitously expressed gC1q-R (a receptor for the complement protein C1q) ⁽¹⁸⁶⁾.

Figure 1.7 gives an overview of contact factors and cell-mediated interactions in thrombosis and inflammation.

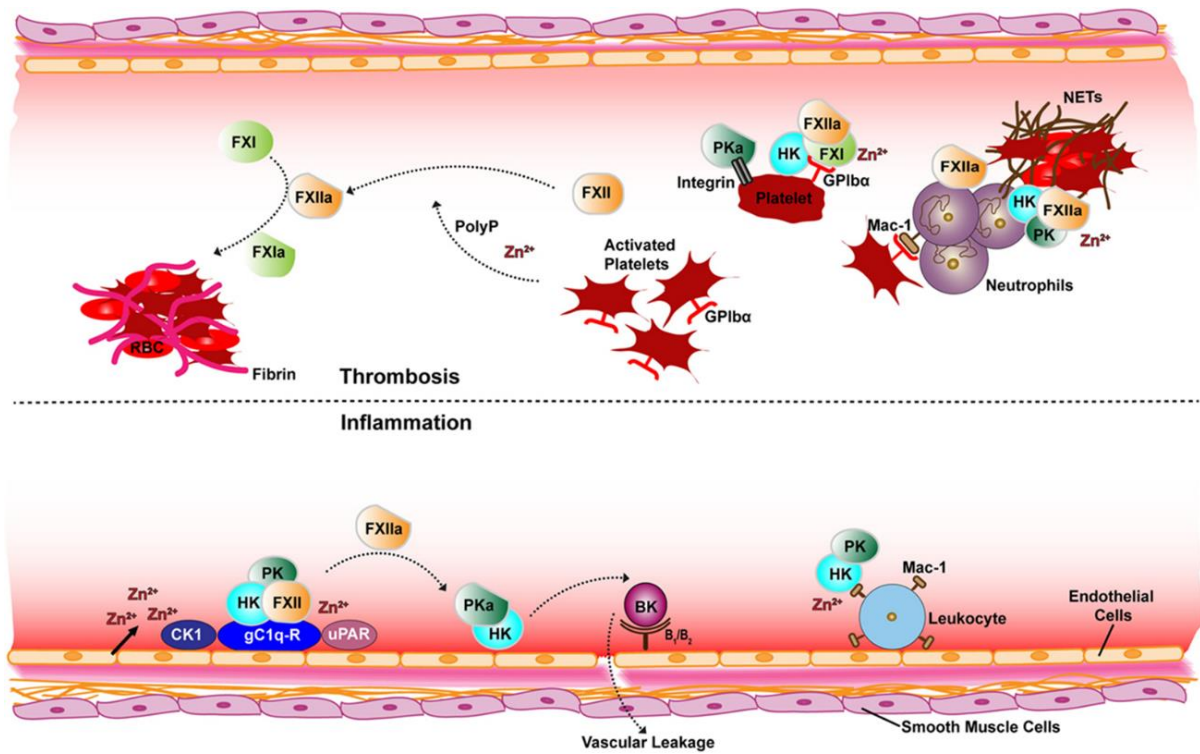


Figure 1.7: Schematic overview showing receptor and contact factor mediated interactions. Schematic overview of receptor and cofactor interactions of the contact factors for thrombotic (top) and inflammatory (bottom) pathways. Assembly of the contact system via gC1q-R (with elevated Zn^{2+}) generates PKa, FXIIa, and BK is produced on the surface of endothelial cells (bottom). Also shown is the FXII and HK interactions with the uPAR receptor and CK1. FXIIa activates plasma coagulation cascades via FXI on the surface of platelets (top). The platelet GP1b-IX receptor GP1b α chain interaction with FXI–HK and PKa binding to the activated platelet integrin α IIb β 3 is also depicted. Neutrophils are also depicted releasing NETs known to associate with contact proteins. Abbreviations: FXII, factor XII; FXIIa, activated FXII; PK, prekallikrein; PKa, activated PK; FXI, factor XI; FXIa, activated FXI; HK, high molecular-weight kininogen; BK, bradykinin; uPAR, urokinase receptor; GPIb α , platelet glycoprotein Ib; CK1, cytoke­ratin 1; gC1q-R, receptor for complement protein C1q; Mac-1, macrophage-1 antigen receptor; PolyP, polyphosphate; RBC, red blood cells; NETs, neutrophil extracellular traps. This image is adapted from a review paper I co-authored ⁽¹⁸⁷⁾.

1.7 Human gC1q-R: the major endothelial cell receptor for FXII

Endothelial cells play a crucial role in regulating the molecular and cellular events within the vasculature under normal conditions and also in the event of thrombosis and inflammation. Upregulation of gC1q-R has been reported in breast, prostate, liver, lung and colon tumours, ⁽¹⁸⁸⁾ by inflammatory mediators including interferon-gamma and tumor necrosis factor-alpha and *E.coli* LPS ⁽¹⁸⁹⁾. Other roles of gC1q-R are reported in thrombosis, ⁽¹⁹⁰⁾ regulation of RNA splicing, ⁽¹⁹¹⁾ adipogenesis and insulin signalling ⁽¹⁹²⁾.

Overexpressed and secreted soluble gC1q-R (sgC1q-R) from activated endothelial cells at site of inflammation has been shown to bind to endothelial cells in an autocrine/paracrine manner thus enhancing vascular permeability by upregulating the bradykinin receptor (B1R) ⁽¹⁹³⁾. A plethora of evidence have demonstrated gC1q-R localisation on the mitochondria and cell membrane ⁽¹⁹⁴⁾ with earlier studies suggesting gC1q-R expression in B cells, mast cells, neutrophils, and platelets ⁽¹⁹⁵⁻¹⁹⁸⁾.

Human gC1q-R was first isolated from membrane preparations of Raji cells, then originally identified as a receptor that has a high binding specificity for the globular “head” Complement component 1q, C1q ($K_d = 15-50$ nM) ⁽¹⁹⁹⁾ and been reported to bind to diverse ligands including thrombin, ⁽²⁰⁰⁾ cC1q-R (calreticulin), ⁽²⁰¹⁾ vitronectin, ⁽²⁰²⁾ HK ($K_d = 0.8$ nM) ⁽²⁰³⁾ and FXII ⁽²⁰⁴⁾. A body of evidence have shown that contact factors HK and FXII assembly on the gC1q-R surface with Zn^{2+} to induce contact activation and subsequently release BK. gC1q-R is an ancient and conserved glycoprotein across species and is also found in freshwater prawn. The freshwater prawn has no adaptive immune response and depends on the innate immune system upon pathogen invasion ⁽²⁰⁵⁾. Figure 1.8 shows a phylogenetic tree of gC1q-R from different species.

Phylogenetic tree of gC1q-R (Phylogram)

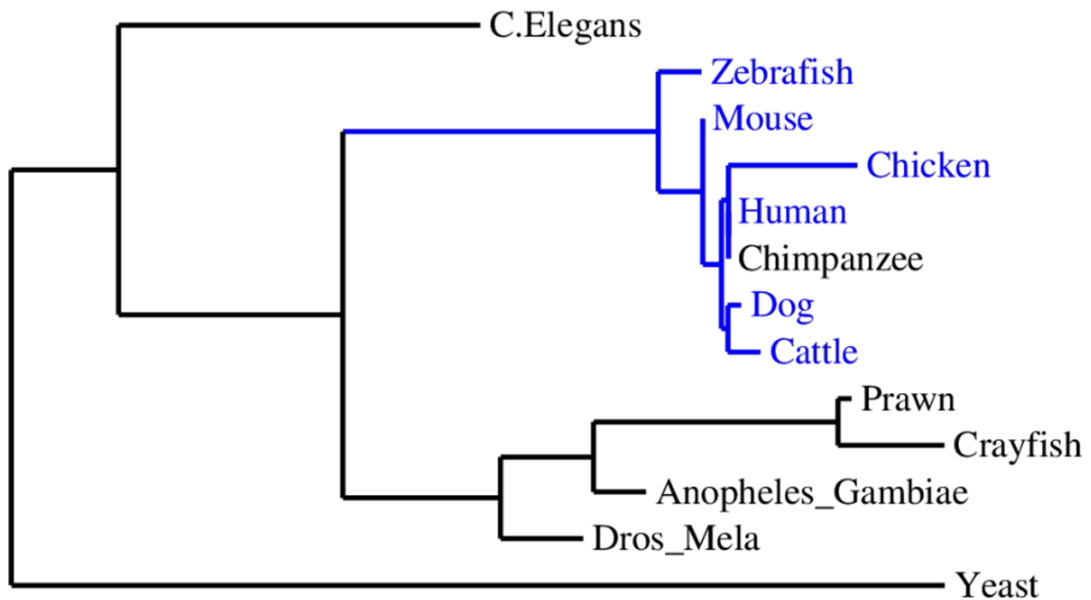


Figure 1.8: Phylogram showing evolutionary relatedness of gC1q-R sequences in different species. gC1q-R in species including Drosophila melanogaster (Dros_Mela) and Caenorhabditis elegans (C.Elegans) are also shown.

A gC1q-R homologue from Trypanosoma brucei (*T.brucei*), called p22 has been reported to exist as a tightly bound trimer but lacks the 140-loop, 190-loop, part of the reported HK binding site (aa 204-218) on human gC1q-R. Furthermore, 220-loop on gC1q-R is not conserved in p22 ⁽²⁰⁶⁾.

1.7.1 Human gC1q-R protein subunit and structure

Human gC1q-R, also referred to as p33, p32, C1Qbp is a multi-compartmental (nucleus, endoplasmic reticulum, mitochondria and cell membrane) and multi-functional protein with 282 amino acids in length, and the N-terminus (aa 1-73) is cleaved off to generate a mature

gC1q-R. The first N-terminal 73 amino acid sequence is used to target gC1q-R on the mitochondrial membrane or secretory pathway.

Human gC1q-R migrates as a monomer at around 33-kDa on a reducing and nonreducing SDS-PAGE gel, but found as a trimer in solution. Furthermore, the 3D crystal structure of gC1q-R (aa 74-282, with Leu74 substituted to Met74) solved at 2.25 Å resolution, describes the symmetrical, homotrimeric gC1q-R ring structure. The gC1q-R structure forms a doughnut-shaped quaternary structure held together by noncovalent intermolecular interactions with a central cavity of an average inner diameter of approximately 20 Å. All monomers have a similar conformation, with each monomer consisting of seven consecutive β-strands (β1-β7) forming twisted antiparallel β-sheets and three α-helices (αA, αB and αC) located within the N and C terminus⁽²⁰⁷⁾ (Figure 1.9).

The αA helix in the N terminus (aa 74-96) has been mapped to contain the C1q binding site as deletion negates binding to C1q. Mature gC1q-R has one buried cysteine at position 186 (Cys186) in each monomer and forms no inter-or-intramolecular disulphide bond. Posttranslational modifications such as N-glycosylation sites at residues 114, 136, and 223,⁽²⁰⁸⁾ phosphorylation site at residue 207 and a myristylation site at position 252 have been reported, although the solved gC1q-R crystal structure was expressed in *E.coli*.

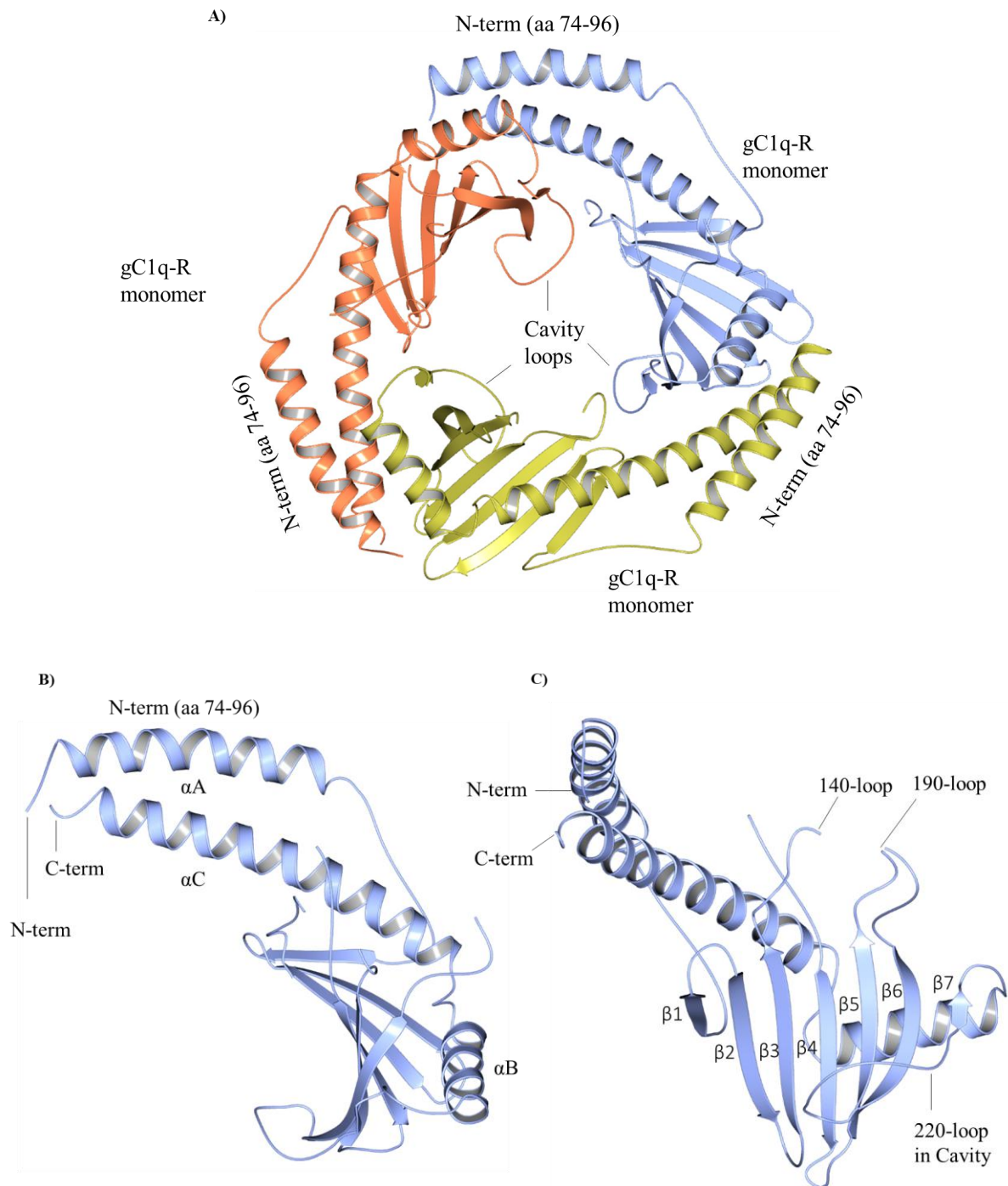


Figure 1.9: Cartoon diagram of the crystal structure of gC1q-R. A) gC1q-R trimer (in ice blue, gold and coral) showing three homologous monomers held together by intermolecular non-covalent interactions. The N-terminal helix (aa 74-96) is also shown. B-C) The gC1q-R monomer and its secondary structure is shown in ice blue, labelled with three α -helices (α A, α B and α C), 7 β -strands and loops (140, 190 and 220). This image was made from QtMG using gC1q-R structure (PDB code: 1P32). The gC1q-R structure was crystallised in its trimeric form.

Human gC1q-R is highly acidic (Figure 1.10) with a calculated pI of 4.1 and is negatively charged on one face (soluble face, S-face), while predominantly positively charged on the opposite face (membrane face, M-face). The S-face has been reported to bind to HK and FXII. However, how gC1q-R gets anchored on endothelial cells is unclear as its amino acid sequence does not predict the presence of a transmembrane segment or a consensus site for a glycosylphosphatidylinositol (GPI) anchor. Recent evidence has suggested that gC1q-R can be anchored to transduce signalling by glycosaminoglycans in the presence of β 1 integrin receptors ^(194, 209). The notion of gC1q-R recruiting signalling partners with transmembrane domains has also been proposed, by which bound C1q to gC1q-R can associate with DC-SIGN (membrane-spanning molecule) on dendritic cells where gC1q-R uses DC-SIGN as a transmembrane partner ⁽²¹⁰⁾.

Urokinase plasminogen activated receptor (uPAR), which has a GPI anchor, and cytokeratin 1 (CK1) together with gC1q-R have been demonstrated to be on the surface of HUVEC cells in close proximity binding to both HK and FXII. Although, preference in binding of HK by gC1q-R than FXII and FXII by uPAR than HK, there are no *in vivo* studies characterising binding of gC1q-R or uPAR to HK and FXII. Human uPAR is involved in cell signalling, proteolysis and cell-extracellular matrix (ECM) interaction and has also been linked to angiogenesis and cancer.

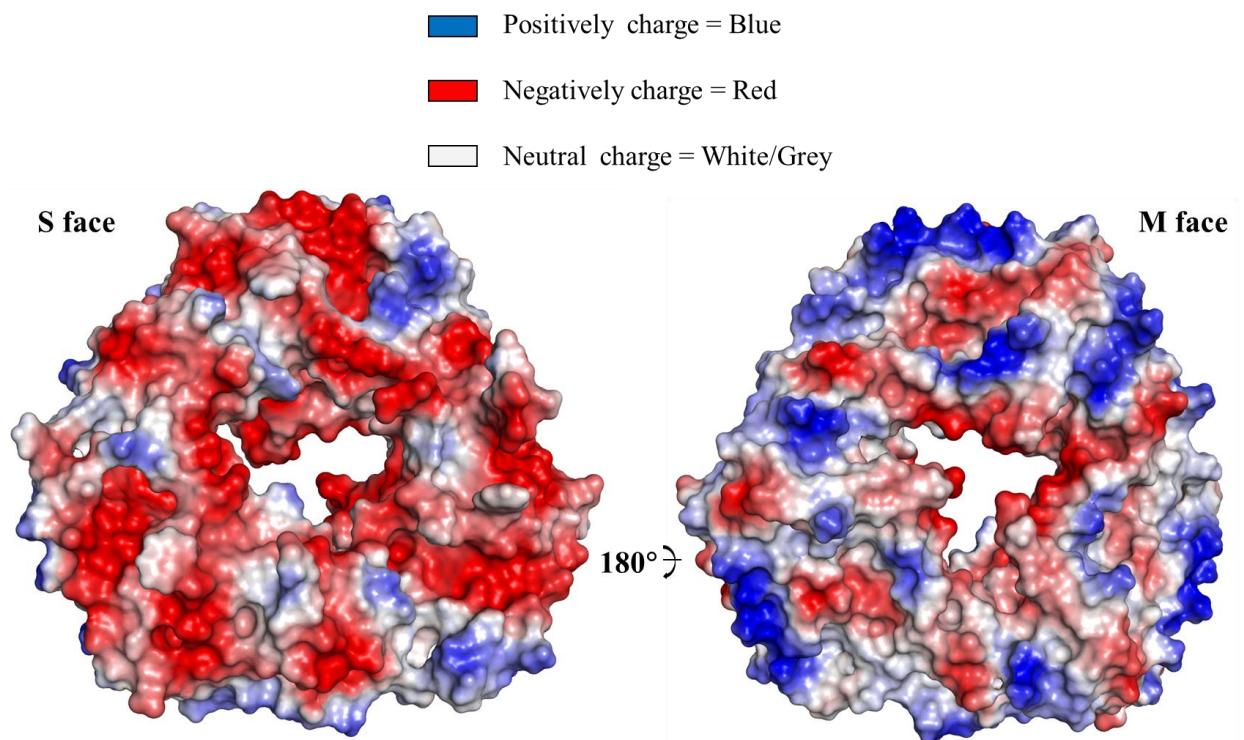


Figure 1.10: Electrostatic surface charge representation of gC1q-R. The colour representation shows areas that are negatively, positively and neutral charge in red, blue and white/neutral, respectively. The S face is predominately negatively charge while the M face is a mixture of positive and neutral charge with less negatively charge residues compared to the S face. This image was made from PyMOL using the gC1q-R structure (PDB code: 1P32).

1.8 gC1q-R protein interaction with ligands

Human gC1q-R has been shown to interact with a number of ligands ranging from pathogens (bacteria, virus and Plasmodium falciparum) to fibrinogen and basic charged peptides. Some of these basic peptides are derived from Rubella Capsid Protein (RCP), Histone 4 (H4), Lamin B receptor and a tumor homing peptide called LyP-1.

1.8.1 Interactions between rubella virus capsid protein and gC1q-R

The rubella viral capsid protein has been shown to form a stable interaction with gC1q-R, in which two clusters of arginine residues within the capsid protein play an important role in the binding to gC1q-R. This ultimately enables the virus to regulate its nucleocapsid assembly and also causes reorganization of the mitochondria during infection ^(211, 212). Viral proteins including Epstein–Barr virus (EBV) EBNA I protein, adenovirus polypeptide V, hepatitis C virus (HCV) core protein, herpes simplex virus type-1 (HSV-1) IE63 protein and the human immunodeficiency virus (HIV-1) proteins Rev and Tat use gC1q-R to regulate mRNA splicing, protein trafficking, or down regulating the immune responses of the host cell being hijacked for survival ⁽²¹³⁻²¹⁷⁾.

The N-terminal conserved domain of the rubella viral capsid protein has been reported to interact with the C-terminal region of gC1q-R and up regulation of gC1q-R has been demonstrated to enhance the rubella virus infectivity in three independent cell lines ⁽²¹⁸⁾.

1.8.2 Interactions between Histone 4 and gC1q-R

Histones released from damaged endothelial cells have been reported to interact with gC1q-R *in vitro*. The interaction between gC1q-R and Histones reveals that gC1q-R has a neutralising effect on the pathological host responses caused by elevated extracellular histones in murine model and therefore making treatment with gC1q-R a promising therapeutic approach in severe infectious diseases ⁽²¹⁹⁾.

1.8.3 Interactions between lamin B receptor and gC1q-R

The lamin B receptor (LBR) or p58 is a transmembrane protein localised to the inner membrane of the nuclear envelope with its C-terminal end reported to be housed within the inner nuclear membrane ⁽²²⁰⁾. LBR interacts with Lamin B and heterochromatin through its nucleoplasmic amino-terminal domain and is phosphorylated throughout the cell cycle ⁽²²¹⁾. It has a key role in nuclear reassembly after mitosis, interphase nuclear envelope growth and compartmentalization of the nuclear architecture ⁽²²⁰⁾. Previous studies have shown that a short arginine/serine-rich (RS) domain within the LBR binds tightly to gC1q-R, therefore leading to gC1q-R preventing phosphorylation of LBR ⁽²²²⁾.

Furthermore, gC1q-R is believed to act as an adaptor protein in recruiting proteins including the Human cytomegalovirus (HCMV) protein kinase pUL97 to LBR in the nuclear lamina. Overexpression of gC1q-R has been reported in HCMV-infected cells, which as a result leads to increased efficiency of viral replication and thereby inducing a dissolution of the nuclear lamina to facilitate release of viral particles ⁽²²³⁾.

1.8.4 Interactions between LyP-1 and gC1q-R

Human gC1q-R overexpression has been reported in various tissues (breast, prostate, liver, lung, and colon) under pathological conditions such as cancer and the quest to find solutions to complement and enhance the conventional anti-cancer therapy is challenging ⁽²²⁴⁻²²⁶⁾. A tumor homing peptide, LyP-1 (CGNKRTRGC), has been found to selectively bind gC1q-R expressing tumor cells in the lymphatic vessels, acting as a marker with a potential for diagnosis and therapy in cancer ⁽²²⁷⁾. Recently, an improved LyP-1 mimicking peptide (TT1, CKRGARSTC) targeting gC1q-R was identified, in which a compound, TT1 was chemically attached to LyP-1 and tested *in vivo* against gC1q-R with interesting possibilities for strategy improvement to increase their therapeutic index ^(228, 229). The LyP-1 is similar to the lamin B receptor peptide sequence.

1.8.5 Interactions between FXII and gC1q-R

Previous studies using immunochemistry and sequencing analysis have demonstrated FXII and HK binding to endothelial cells and HUVEC with a Zn²⁺ requirement for both FXII and HK in binding to gC1q-R ^(121, 230). Other proteins also identified to interact with HK and FXII on endothelial cells in close proximity to gC1q-R are uPAR and cytokeratin-1 as shown in Figure 1.11.

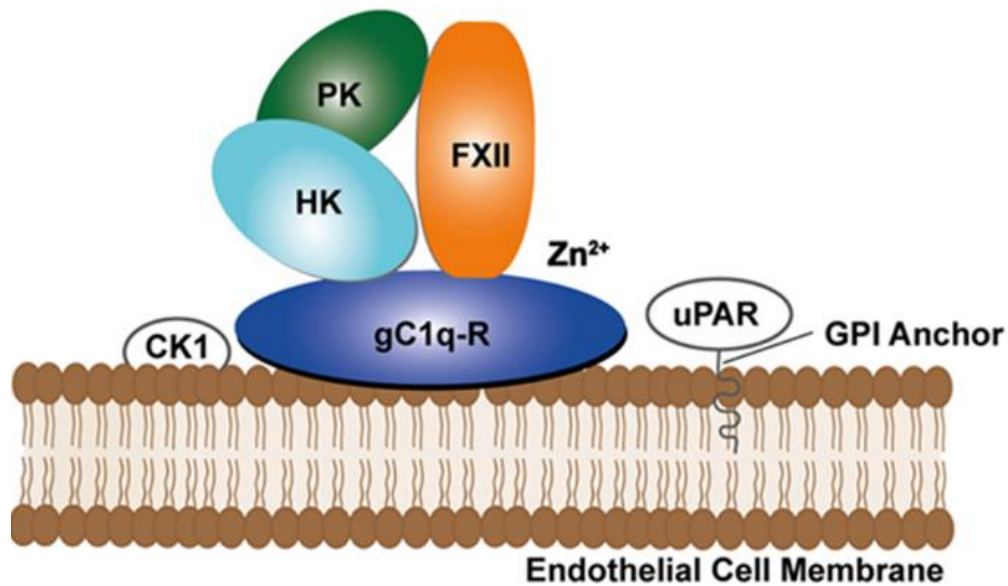


Figure 1.11: HK bound PK and FXII assembly on gC1q-R surface with Zn²⁺ on the endothelial cell membrane. gC1q-R (blue), HK bound PK in cyan and sea green, respectively and FXII in coral. Cytokeratin-1 (CK1) and uPAR with GPI anchor embedded into the endothelial cell membrane are shown. Adapted from a review article I co-authored ⁽¹⁸⁷⁾.

Deletion of gC1q-R amino acid residues 196-202 (190-loop) has been demonstrated to reduce FXII binding to gC1q-R. Furthermore, an amino acid substitution of Trp233 to Gly also showed significant reduction in FXII binding, suggesting that both the gC1q-R deletion mutant 196-202 and Trp233Gly are important in FXII binding. Berhane Ghebrehwet *et al*, in 2011 reported HK and FXII do not compete for the same site but rather have overlapping binding sites ⁽²³¹⁾. However, the gC1q-R deletion mutant described by Berhane Ghebrehwet and colleagues for the gC1q-R 204-218 (HK binding site) did not form a trimer but rather a monomer in solution and therefore showed no binding to HK. The 3D structure of proteins need to be carefully considered when making deletions as the protein fold can be disrupted thus affecting the structural integrity of the protein and can as a result affect how data is

interpreted from an experiment. Deletion of the gC1q-R N-terminal helix (aa 74-96) did not disrupt the trimer formation as demonstrated by the crystal structure (PDB code 3RPX).

Monoclonal antibodies 60.11 and 74.5.2 directed against the gC1q-R N-terminal helix (aa 74-96) and C-terminal amino acid 204-218, ⁽²³²⁾ respectively are used in various *in vitro* and *ex vivo* studies for mostly detection purposes. However, caution should be taken as gC1q-R is indispensable for foetal development and mitochondrial function reported for primary embryonic fibroblast isolated from gC1q-R-knockout embryos ⁽²³³⁾.

1.9 Complement system, coagulation and inflammation

Huber-Lang *et al.* 2006 reported a link between the complement (Classical, Lectin and Alternative pathways) and the coagulation pathway ⁽²³⁴⁾. Plasma proteases such as thrombin have been linked to the complement component 5a (C5a) generation ⁽²³⁵⁾. Thrombin can cleave C5 at positions R751 and R947 to generate C5 intermediate C5_T and C5b_T ⁽²³⁶⁾ and ultimately contributing in the membrane attack complex (MAC). In addition, plasma proteases such as FIXa, FXIa, FXa and plasmin have also been shown to promote C3 and C5 cleavage ⁽²³⁷⁾. PK activation to PKa has been demonstrated to cleave complement factor B ⁽²³⁸⁾ with its activity regulated by factor H when C3 is present in plasma upon contact system activation triggered by *Candida albican* (*C.albican*) ⁽²³⁹⁾. PKa has been reported to further cleave α -FXIIa to form β -FXIIa, and β -FXIIa is capable of activating the macromolecular C1qrs complex of the classical pathway leading to enzymatically active C1r and C1s ^(47, 240). C3 and C5 activation in FXII depleted plasma has been shown to be affected as reconstitution with purified FXII in plasma depleted FXII restored complement activity. Normal complement activity was not

affected, suggesting that upon contact activation induced by oversulfated chondroitin sulfate, FXIIa and PKa can promote C3 and C5 generation through plasmin generation ⁽²⁴¹⁾.

1.9.1 Proteins containing SRCR and LDL-R domains

Proteins such as plasma complement factor I (CFI), containing scavenger Receptor Cysteine-Rich (SRCR) domain, LDL-R, FIMAC and a protease domain play a key role in the alternative complement pathway. The complement system is a crucial component of the innate immune system. Human homologues of insect serine protease Graal1 containing SRCR domains are found in lysyl oxidase homolog 2 (LOXL2), complement factor I (CFI), macrophage receptor with collagenous structure (MARCO), cluster differentiation 5 and 6 (CD5 and CD6) on lymphocyte ⁽²⁴²⁾ and Hepsin (also known as TMPRSS1).

Membrane-associated hepsin has been linked to blood coagulation and can activate FVII on the surface, ultimately leading to thrombin generation ^(243, 244), while CFI is implicated in thrombocytopenia and Thrombotic Microangiopathy. Mutations causing CFI deficiency in CFI domains including SRCR and LDLRA2 as well as the protease domain have been reported in patients ^(245, 246).

MARCO has been associated with the innate antimicrobial immune system, where MARCO is reported to interact with both Gram-negative and Gram-positive bacteria via its scavenger receptor cysteine-rich (SRCR) domain ⁽²⁴⁷⁾. SRCR domains are highly conserved ⁽²⁴⁸⁾ and found in both secreted and cell surface proteins and have been subdivided into subtypes A and B, based primarily on the spacing between the cysteine residues and how the introns/exons are organised ⁽²⁴⁹⁾. The SRCR domain in Hepsin has an atypical cysteine residue pattern revealing third subtype of SRCR domain. The SRCR domain is usually 90-110 amino acids in length with 6–8 cysteine residues and are known to bind specific ligands having roles in host defence and

immune response ⁽²⁵⁰⁾. SRCR domains have been reported to be implicated in disease states, including autoimmune diseases, tumour development, atherosclerosis and Alzheimer's disease ^(251, 252).

1.10 Aims and Objectives of this PhD thesis

Although, there are 3D crystal structures of the FXII Fnl-EGF2 tandem domain and β -Factor XII (zymogen-like and active forms), crystal structures for full-length FXII and other domains within the heavy chain of Factor XII (FXII) such as FXII FnII has not yet been solved. The conversion of zymogen Factor XII to activated Factor XIIa has been reportedly demonstrated to rely on conformational changes induced by Zn^{2+} binding to the heavy chain of FXII. Zn^{2+} mediated binding of the heavy chain of FXII to negatively charged surfaces including polyphosphate and gC1q-R increases the rate of FXII activation to FXIIa. Although not proven yet, FXII FnII has been suggested to bind to negatively charged surfaces. So the aims of this project without limiting it to FXII alone are as follows:

- 1) To determine the 3D crystals structure of full length FXII
- 2) To determine the 3D crystal structure of FXII FnII bound to Zn^{2+}
- 3) To determine the 3D crystal structure of FXII FnII bound to gC1q-R
- 4) To determine the 3D crystal structure of HK domain 5 bound to gC1q-R
- 5) To determine the 3D crystal structure of gC1q-R and basic peptides (H4, RCP and LBP)
- 6) Use gel filtration to isolate oligomer of FXII-gC1q-R-HK in the presence of Zn^{2+}
- 7) Characterise Graal and CFI binding to FXII using SPR
- 8) Effect of clotting time in the presence of gC1q-R will be assessed in plasma in collaboration with Dr. Nicola Mutch (University of Aberdeen)

Macromolecular X-ray crystallography will be used to determine the 3D crystal structure while Surface Plasmon Resonance (SPR) will also be employed to characterise FXII binding to proteins including gC1q-R. Plasma based assay will also be conducted to understand gC1q-R function in plasma.

Structure-function relationship is crucial in finding solutions to proteins involved in disease states. 3D Structures of human gC1q-R in complex with FXII will certainly provide details in the molecular insight of gC1q-R and FXII interaction, therefore providing a suitable platform for designing appropriate inhibitors or be used as a biomarker by raising novel antibodies against key binding sites for thrombosis and thrombosis related diseases including cancer.

CHAPTER 2.0

MATERIALS AND METHODS

2.1.0 Materials and Methods

2.1.1 Preparation of FXII and gC1q-R cDNA for expression

2.1.2 Amplification of DNA fragments using Polymerase Chain Reaction (PCR)

Full-length mouse FXII (WT mFXII and active site mutant S526A) and various truncated human FXII cDNA fragments were amplified using the polymerase chain reaction (PCR). A PCR mixture of 10 μ L made up of phusion HF buffer (1x), 1 μ L of dNTPs (0.2 mM), 1 μ L of each primer (0.5 μ M), 1.5 μ L DMSO (3%), 10-50 ng of FXII cDNA (template), 0.5 μ L phusion DNA polymerase (0.5 -1 units) was prepared with 34.5 μ L of dH₂O added to make up a final volume of 50 μ L. The PCR mixture was then put into the PCR machine and ran with 35 cycles of 98 °C for 30 seconds (initial denaturation), 98 °C for 10 seconds (denaturation), a gradient between 50-60 °C for 30 seconds (annealing), 72 °C for 15 seconds (extension) and 72 °C for 10 minutes (final extension). A temperature at 55 °C has also been successfully used for the annealing to PCR amplify other constructs. As the PCR primers for FXII DNA were designed to introduce restriction enzyme sites on either end of 5'-3' primer end, the final PCR amplified FXII DNA should contain a restriction enzyme site designed for the cloning experiment.

Firstly, the PCR amplified FXII DNA was analysed using 1 – 1.3 % (w/v) agarose gel electrophoresis to confirm whether the PCR product of FXII DNA was amplified and that it migrated at the expected size on the agarose gel. The desired and expected PCR amplified FXII DNA band was identified and excised from the agarose gel and placed in an Eppendorf tube (Thermo Scientific) to be weighed in order to add the recommended volume of solubilisation solution to dissolve the DNA gel at 60 °C using a gel extraction kit (Sigma). The dissolved DNA gel with added binding buffer was captured onto a prepared spin column following centrifugation at more than 12 000 g for 30 seconds.

The flow through in the collection tube in which the spin column was inserted into was decanted. The old autoclaved Eppendorf tube was replaced with a clean autoclaved tube followed by addition of 50 μL of elution buffer to the centre of the silica membrane of the spin column and allowed to incubate for 1 minute prior to DNA recovery by centrifugation. The concentration of the recovered DNA was measured using a NanoDrop 1000 (Thermo Scientific) spectrophotometer at a wavelength of 260 prior to double digestion. All constructs and primers used in this thesis are listed in the appendix (chapter 10).

2.1.3 Restriction double digest, Plasmid vector dephosphorylation, ligation and gel electrophoresis

10-20 μg of gel extracted and purified FXII DNA (insert) and undigested plasmid vectors were digested by mixing solutions of 2.5 μL of each restriction enzyme (10 units), 1x BSA, 10 μL of 10x Buffer and dH_2O to make up a total volume of 50 μL . The reaction was left to incubate for 4 hours or overnight (in some cases) at 37 $^\circ\text{C}$ followed by heat inactivation of the restriction enzymes a 65 $^\circ\text{C}$ for 15 minutes prior to ligation of digested plasmid vector and insert. The plasmid vector underwent dephosphorylation using Antarctic phosphatase (NEB) to prevent self-ligation. Both insert and plasmid vector underwent a final purification step using PCR-clean-up kit (Sigma) followed by DNA concentration measurement using NanoDrop 1000. Then, a 3-fold molar excess of digested FXII insert to digested plasmid vector DNA were mixed well in a total volume of 10 μL , then added 10 μL 2x Quick ligation buffer (NEB) and 1 μL Quick T_4 DNA ligase (NEB). The mixture was briefly centrifuged and incubated at room temperature for 5 minutes to allow the formation of phosphodiester bond between the 5' and 3' end of each DNA fragments using the equation below:

$$\text{Insert (kb)} / \text{Vector (kb)} \times \text{vector (ng)} = \text{ng of insert needed for a 1:1 molar ratio}$$

The mixture was allowed to chill on ice before transformation. All DNA work were subjected to gel electrophoresis to analyse DNA. 100 mL of 1x TBE (Tris-Boric acid-EDTA) buffer was added to either 1 or 1.3g (1% or 1.3%) of agarose powder (Sigma) and then heated with mixing to completely dissolve the powder. This was allowed to cool before pouring into a gel casting chamber in which a comb (with teeth) was already inserted to produce wells to load DNA samples into. This was allowed to solidify at room temperature followed by filling the chamber with 1x TBE to cover the solidified gel.

5 μ L of 4x loading dye and 2 μ L Syber green or Nancy were added into 20 μ L of DNA sample and mixed well before loading into a well next to a DNA ladders of varying sizes (0.1-1 kb or 1-10 kb). The DNA ladders are used as a reference. The gel apparatus was closed and current applied to allow DNA to migrate and separate for 45-60 minutes at 100 V (voltage) followed by analysis under blue light.

2.1.4 Site directed mutagenesis (SDM) of recombinant FXII and gC1q-R

Plasmid vectors containing wild type templates of full-length mouse FXII (mFXII), HisTrx-FXII FnII or gC1q-R were used to introduce mutation/s in their DNA to generate full-length mouse active site mutant (S526A), HisTrx-FXII FnII mutants and gC1q-R mutants using an Agilent site-directed mutagenesis kit with primers design using the Agilent primer design software.

10-50 ng of template DNA was mixed with 10x Phusion buffer, 0.5 μ M primer each (forward and reverse primer) containing a mutation or mutations, dNTPs (0.2 mM), Phusion DNA polymerase (0.5-1 units) and centrifuge briefly prior to introducing mutation and amplifying the DNA sequence using PCR. The amplified PCR products were Dpn1 treated for 1 hour at 37 °C to get rid of the methylated parent DNA template and leaving the amplified unmethylated PCR mutant product. PCR amplification was followed by transformation, whereby 2-5 μ L of

the PCR amplified mutant product was mixed with thawed novablue cells to obtain sufficient DNA of the amplified PCR product for further analysis including DNA sequencing or protein expression experiments.

2.1.5 Bacterial transformation

For each transformation, 5-10 ng or 2 μ L of DNA was mixed into an aliquot of thawed 50 μ L *E.coli* cells and left to incubate for 20-30 minutes on ice. The mixture was then heat-shocked at 42 °C for 30-90 seconds and returned back on ice for 3-5 minutes followed by adding 500-900 μ L LB broth and allowed to incubate at 37 °C with shaking at 180 rpm for 1 hour. The broth was centrifuged at 13,000 g for 2-3 minutes after an hour and more than 200 μ L of LB discarded and the pellet re-suspended with the remaining LB prior to plating cells on an antibiotic resistance agar plate with overnight incubation at 37 °C.

A colony was picked the following day to grow a single colony in 5 mL LB broth (without agar) with the same antibiotics and temperature for an additional 16 hours, followed by harvesting and purifying DNA using mini-prep kit (Sigma). For insect cells expression, larger volumes (50-150 mL) of cultured novablue cells is needed to obtain μ g quantity of DNA for transfection.

2.1.6 DNA quantification at wavelength 260 nm

DNA concentration and quality was measured using ND-1000 Spectrophotometer NanoDrop (thermo fisher scientific, UK) at a wavelength of 260 nm. A 2-3 μ L of blank (usually water) was initially loaded and measured, then stored with absorbance reading of zero or flat baseline. After wiping both pedestals (measuring and arm), 2-3 μ L of DNA sample was loaded onto the measuring pedestal and pedestal arm lowered to measure DNA in the sample at 260 nm.

2.2.0 Protein expression

2.2.1 *Escherichia coli* (*E. coli*)

Constructs shown in were expressed in *E.coli* strains BL21 (DE3), Rosetta-2, Rosetta-gami-2 and Origami-2 cells following the transformation protocol described in the material and methods section 2.1.5 (bacterial transformation).

A colony following transformation on an agar plate was taken and grown overnight in 100 mL LB medium containing antibiotics at 37 °C and used as an inoculum for large scale expression in 0.8-3.2 L LB medium with antibiotics. This was grown to OD₆₀₀ between 0.6-0.8, followed by IPTG induction at a concentration between 0.3-0.8 mM at 18 °C overnight.

The following day the cell culture was spun to harvest cells by centrifugation at 4,600 g for 40 minutes to separate the cell pellet from the supernatant. The supernatant was discarded and the pellet re-suspended into a buffer (refer to appendix chapter 10.0) with added lysozyme and EDTA-free protease inhibitor prior to cell lysis by sonication on ice for 10-15 minutes with 30 seconds on and 30 seconds off. The sonicated mixture or lysate was then centrifuged at 15,000 g for 50 minutes at 4 °C and the supernatant from the centrifugation step was filtered using a 0.45 µm filter. The filtered sample containing expressed protein is subjected to protein purification as described in the protein purification section.

2.2.2 *Drosophila Schneider 2* (*S2*) cells

Solution A containing 36 µL of 2 M CaCl₂, 20 µg of recombinant plasmid DNA (i.e. pMT-PURO-FXII) with added tissue culture sterile water to bring the total volume to 300 µL was slowly added in a dropwise manner to 300 µL of solution B (2x HEPES Buffered Saline) with continuous mixing to allow the formation of fine precipitate necessary for efficient transfection.

The mixture was incubated for 30 minutes, mixed and added dropwise onto the drosophila S2 cells at a cell density of 1×10^6 cells/mL in 5 mL complete Schneider's Drosophila S2 medium with swirling to mix each drop before incubating overnight at 28 °C. On day 2, the old complete Schneider's Drosophila S2 medium was replaced by pelleting the cells at 1,000 g and the supernatant containing calcium phosphate from the transfection was discarded and pellet replaced with fresh and warm complete Schneider's Drosophila S2 medium.

Stable cell lines were generated with puromycin after few passaging of cells and allowed to grow between 2×10^6 - 4×10^6 cells /mL in ExpressFive media (reduced serum) prior to induction with 500 μ M CuSO₄. Protein sample from induced cells were collected from the media and tested for expression by western blot before scaling up to first and foremost confirm whether FXII was being expressed and secreted into the medium. Medium containing mFXII, FXII FnII, FXII FnII-EGF1 and Graal₈₆₃₋₁₁₅₀ were all spun, filtered and then subjected to protein purification. All purifications using columns were performed using the ÄKTA instrument.

2.3.0 Protein Purification

2.3.1 Purification of FXII by Ion exchange chromatography

Media collected from the insect cell expression were centrifuged at 4,600 g for 30 minutes to pellet S2 cells, followed by an additional centrifugation step at 15,000 g for 1 hour to clarify the media. The media was then filtered using 0.22 μ m filter (Millipore). Filtered media was diluted with equal volume of buffer that will keep the isoelectric point (pI) of the overexpressed protein below the pH for WT mFXII (full length) or pH below the pI for FXII domains (FXII FnII and FXII FnII-EGF1), thus rendering the protein capable of being captured on the ion-exchange column.

The diluted media was then loaded onto a pre-equilibrated ion-exchange column (Capto S or Capto Q) with the same buffer the media was diluted with without or reduced salt (NaCl) in the buffer to maximise binding to the column.

A gradient elution run was performed to elute bound FXII FnII and FXII FnII-EGF1 from the Capto-S column with buffer 50 mM MES, 1M NaCl pH 6.0, while both WT mFXII and mFXII S526A with pI less than 7 were captured on a Capto-Q column and eluted using a buffer containing 20 mM Tris-HCl, 1M NaCl pH 8.0.

Other media batches containing overexpressed FXII FnII and FXII FnII-EGF1 have also been subjected to ammonium sulfate precipitation with 90% ammonium sulfate added and incubated at 4 °C under stirring overnight, precipitated by centrifugation at 15,000g for 40 minutes. Whitish pellet is then resuspended in buffer A and then dialysed for an additional day. Fractions from the ion-exchange purification (Capto-Q or Capto-S) or dialysed ammonium sulfate precipitated samples were diluted 10x with buffer A and then loaded onto an equilibrated (with buffer A) 5 mL HiTrap Ni²⁺ column (Ni²⁺ affinity chromatography) purchased from GE healthcare.

Overexpressed untagged WT gC1q-R and its mutants were also subjected to ion-exchange chromatography using 5 mL HiTrap Q column (GE healthcare) after ammonium sulfate precipitation and dialysis (as described by Jiang et al. 1999 ⁽²⁰⁷⁾) with a strong Q exchanger (Resource Q from GE healthcare) used as a second purification step prior to size-exclusion chromatography.

2.3.2 Purification of FXII by Ni²⁺ affinity chromatography

Both WT mFXII and mFXII S526A had a His₆ engineered in their sequence at the C-terminus required for affinity purification while untagged human FXII FnII and FXII FnII-EGF1 capitalised on the capability of FXII FnII domain to bind to divalent metal ions including Zn²⁺ (130). Both immobilised Ni²⁺ and Zn²⁺ have been used. Eluted fractions from the Capto-S or Capto-Q purification or ammonium sulfate precipitated samples after dialysis were diluted with 50 mM Tris-HCl, 200 mM NaCl pH 8 (buffer A), then loaded onto the pre-equilibrated (with buffer A) 5 mL HiTrap Ni²⁺ column followed by a gradient run with 0-1 M imidazole concentration to elute FXII proteins.

Other proteins including Graal₈₆₃₋₁₁₅₀ were also subjected to similar purification procedure. All fractions from this stage of purification were analysed using SDS-PAGE gel and the desired peak fractions pooled and concentrated down using vivaspin 20 (Sartorius) with molecular weight cut-off (MWCO) of usually 3 kDa for FXII FnII and FXII FnIIEGF1, while 10 kDa used for mFXII and Graal₈₆₃₋₁₁₅₀ to prepare sample for a final purification step by Size exclusion chromatography.

2.3.3 Purification of HisTrx-FXII FnII by affinity (Ni²⁺ and Zn²⁺) chromatography

WT HisTrx-FXII FnII lysate was captured on a 5 mL Ni²⁺ affinity column (HisTrap) after having equilibrated the Ni²⁺ column with buffer A (20 mM HEPES pH 7.4, 140 mM NaCl, 20 mM Imidazole). This was followed by attaching the column to the AKTA Prime instrument and then commanded the instrument to wash the column with 25-30 mL of just buffer A to remove nonspecifically unbound contaminants. WT HisTrx-FXII FnII was eluted from the gradient (0-0.5 M) run, in which both buffer A and buffer B (20 mM HEPES pH 7.4, 140 mM NaCl, 500 mM Imidazole) were used.

Eluted WT HisTrx-FXII FnII fractions from the Ni²⁺ affinity column purification were pooled and concentrated, then loaded onto an equilibrated S200 16/60 size exclusion column in buffer without imidazole (20 mM HEPES pH 7.4, 140 mM NaCl). Samples were collected in collection tubes during elution and each fraction tube collected was subjected to SDS-PAGE gel analysis prior to pooling and concentrating pure protein together.

As HisTrx-FXII FnII is a fusion with HisTrx as a tag, the tag was cleaved off with protease 3C human Rhinovirus (3C HRV – made inhouse by Dr Philiipe). Different cleavage trials were performed at different amount of 3C HRV protease relative to HisTrx-FXII FnII in weights of 1:100, 1:200 and 1:500 in which 100, 200 and 500 times less 3C HRV protease was used. A time course of the mixture of HisTrx-FXII FnII and 3C HRV protease was incubated for hour/s 1, 2, 3, 4, 8, and overnight (O/N). Samples taken at different time points were analysed on SDS-PAGE gel in the presence of HisTrx-FXII FnII alone as an uncleaved control. All other cleavages were performed with either 1:200 or 1:500 for larger scale expression of WT HisTrx-FXII FnII. HisTrx-FXII FnII mutants were also subjected to the same purification and 3C HRV cleavage procedures as WT HisTrx-FXII FnII.

2.3.4 Purification by size exclusion chromatography (gel filtration)

All protein samples were concentrated to desired volumes and spun in an autoclaved Eppendorf tube, then loaded into a sample loop and subsequently injected into the pre-equilibrated size exclusion column with constant buffer flow (i.e. 0.5 mL/min) to allow migration of injected proteins down the column for separation.

Both HiLoad Superdex™ 75 16/60 and HiLoad Superdex™, 200 16/60 columns from GE healthcare were used as preparatory purification step throughout this project with the following buffers; (50 mM Tris-HCl, 100 mM NaCl pH 8.0), (20 mM HEPES, 100 mM NaCl pH 8.0), (20 mM HEPES, 140 mM NaCl pH 8.0) and (1x Phospahe buffered saline or PBS) used.

Apart from PBS all the other buffers have been used for crystallisation with caution taken as high salt or phosphate concentration can readily form salt crystals. SDS-PAGE gel analysis, western blot followed by protein concentration quantification and mass spectrometry were performed on a number of proteins including WT mFXII and human FXII F_nII to verify the identity and purify of the overexpressed FXII proteins before performing any characterisation and structural studies.

2.4 Sodium Dodecyl Sulfate-Polyacrylamide gel electrophoresis (SDS-PAGE) to confirm overexpressed protein

Protein fractions after each purification step from ion-exchange to Affinity (Ni²⁺) to size-exclusion chromatography were subjected to SDS-PAGE gel analysis with an appropriate gel percentage (10%, 12%, 15% and 20 %) depending on the protein size for better resolution to confirm the expected protein size using a molecular weight marker of known sizes as a reference. Also, protein purity is assessed.

Running an SDS-PAGE gel will determine what step to take next. 1 volume 4x LDS or SDS loading dye is added to 10-15 μ L of protein sample and mixed well, followed by heating using a heat block at 95 °C for 10 minutes to denature and coat protein with SDS. This is important for separating all proteins in the sample by size when current is applied to the SDS-PAGE gel. 1x SDS running buffer was poured into the gel tank in which a casted SDS-PAGE gel (0.75 or 1.5 mm thickness) was inserted and fixed. 10 μ L of protein sample and 5 μ L of marker (Novagen) were loaded into individual wells and current applied at 200 V for 60 minutes to allow protein separation. After running the SDS-PAGE gel, proteins on the gel were visualised by staining the gel with either coomassie brilliant blue or instant blue followed by de-staining with de-staining solution (10 % (v/v) isopropanol, 10 % (v/v) acetic acid) or dH₂O, respectively.

2.5 Western blot to detect mouse FXII and human FXII FnII

Full length mouse FXII and FXII FnII were subjected to western blotting to identify and confirm their expression from insect cells and that the correct protein was being synthesised. An SDS-PAGE gel was ran first, then the proteins in the unstained SDS-PAGE gel were transferred onto either a nitrocellulose or PVDF membrane (Thermo Fisher Scientific) by a semi dry transfer method using iblot (Invitrogen) for 7 minutes.

A blocking solution consisting of 5 % (w/v) semi-skimmed milk in PBS with added 0.05% tween20 (PBS-T) was added to cover the blotted membrane and allowed to incubate at room temperature with rocking for 1 hour to reduce background and weak non-specific binding of antibodies to the membrane surface. The blocking solution was discarded following incubation. A B7C9 monoclonal mouse antibody (Abcam) against the FXII heavy chain diluted in PBS-T (1:1000) was added to cover the membrane surface for 1 hour at room temperature with rocking. The antibody solution was removed and the membrane was washed 3 times with PBS-T for 5 minutes, then discarded the wash solution and added a secondary anti-mouse IgG antibody (HRP-conjugate) solution diluted 1:2000 in PBS-T to the membrane.

This was left to incubate for 2 hours, then washed 3 times for 5 minutes before discarding the solution containing the secondary antibody and adding a developing solution (22 μ L of 90 mM p-coumaric acid, 50 μ L of 250 mM luminol and 3 μ L H_2O_2 in 0.1 M Tris-OH pH 8.5) for 1-2 minutes. The signal for FXII-B7C9 antibody complex is enhanced by anti-B7C9 antibody when Horseradish Peroxidase (HRP) catalyses the oxidation of luminol in the developing solution when hydrogen peroxide (H_2O_2) is added to produce a colour change. This sensitive method is referred to as Enhanced chemiluminescence (ECL).

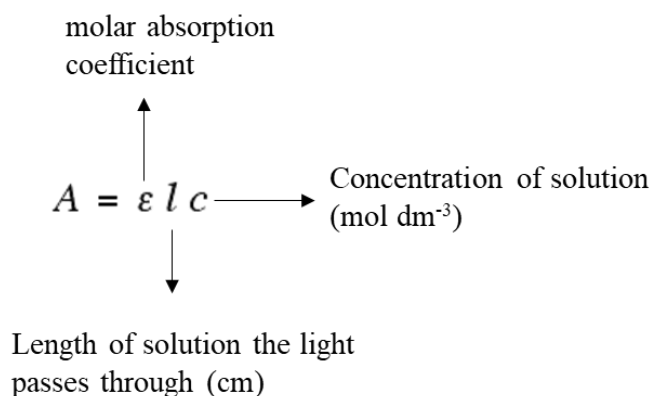
Mass spectrometry analysis from excised protein bands from the SDS-PAGE gel further confirmed the expression of both mouse FXII and human FXII FnII in the MALDI peptide

fingerprinting analysis (performed by the Biopolymer synthesis and analysis unit, QMC, Nottingham).

2.6 Protein quantification at a wavelength of 280 nm

Purified proteins exhibiting absorbance at 280 nm with no need for a standard curve were measured using ND-1000 Spectrophotometer NanoDrop (thermo fisher scientific, UK).

The value obtained from this measurement was used to calculate the true protein concentration, as the general reference setting on the instrument is based on a 0.1% (1 mg/mL) protein solution producing an absorbance at 280 nm of 1.0 Abs. The equation from the beer-lambert law was used to calculate the protein concentration using the molar extinction coefficients (ϵ) calculated from protparam (ExpASy Server) by putting in the primary amino acid sequence.

$$A = \epsilon l c$$


The diagram shows the equation $A = \epsilon l c$ with three arrows pointing to its components: an upward arrow from ϵ to "molar absorption coefficient", a rightward arrow from c to "Concentration of solution (mol dm⁻³)", and a downward arrow from l to "Length of solution the light passes through (cm)".

The Absorbance value obtained from the nanodrop was divided by the extinction coefficients of the protein to give a true corrected protein concentration for that particular protein as the correction factor can be different for each protein sequence analysed. All proteins described and discussed in this thesis were analysed using ND-1000 Spectrophotometer NanoDrop. All

proteins used and described in this thesis were concentrated using vivaspin20 or vivaspin500 concentrators (Sartorius).

2.7.0 Analytical gel filtration for isolating FXII bound gC1q-R

2.7.1 Mouse FXII (mFXII) bound gC1q-R in the presence of Zn²⁺

A 1:1 molar ratio of pure mFXII and gC1q-R were mixed well in buffer (20 mM HEPES pH 7.4, 140 mM NaCl and 50 μ M Zn²⁺) and incubated on ice for 30 minutes. The sample was then spun at 17 000 g at 4 °C for 10 minutes and loaded into the sample loop (maximum volume capacity of 500 μ L), followed by injection of sample into the pre-equilibrated analytical gel filtration (Superose 6, S6) column. Buffer containing 20 mM HEPES pH 7.4, 140 mM NaCl and 50 μ M Zn²⁺ was used to equilibrate the S6 column at a flow rate of 0.5 μ L/min for 1 column volume before loading sample into the loop.

The fractions from the isolated peak/peaks containing mFXII and gC1q-R were ran on a 15% SDS-PAGE gel to confirm complex peak and which fractions under the peak to pool together and concentrated using vivaspin20 MWCO 10 kDa. The complex peak containing mFXII and gC1q-R was concentrated down to 6.6 mg/mL. All other constructs including FXII FnII-EGF1, FXII FnII and gC1q-R and complexes were subjected to gel filtration purification as a final purification step for characterisation and crystallisation.

2.7.2 FXII FnII-EGF1 bound gC1q-R in the presence of Zn²⁺

A similar preparation to full-length mFXII was made for human FXII FnII-EGF1 to form a complex with gC1q-R. The same buffer (20 mM HEPES pH 7.4, 140 mM NaCl and 50 μ M Zn²⁺) was also used with twice the amount of FXII FnII-EGF1 protein added relative to gC1q-R to give a molar ratio of 2:1.

The mixture was incubated overnight in the fridge, then spun at 17 000 g at 4 °C for 10 minutes and ran on an S6 column at a flow rate of 0.5 µL/min for 1 column volume. A peak corresponding to FXII FnII-EGF1 bound gC1q-R from the chromatograph and confirmed by a 15 % SDS-PAGE gel was pooled and concentrated down to 5.6 mg/mL.

2.7.3 FXII FnII bound gC1q-R in the presence of low and high Zn²⁺ concentrations

To confirm whether FXII FnII is able to interact with gC1q-R in the presence of low and high Zn²⁺ concentration; Zn²⁺ concentration of 10 µM was initially added in the buffer containing 20 mM HEPES pH 7.4, 140 mM NaCl. A mixture of FXII FnII and gC1q-R at a molar ratio of 2:1 was incubated on ice for 30 minutes, then subjected to S6 column purification with no apparent complex formed as confirmed by both the gel filtration peak profiles and the SDS-PAGE gel.

The two distinct peaks for FXII FnII and gC1q-R were both pooled together in one tube, then concentrated and buffer exchanged with 20 mM HEPES pH 7.4, 140 mM NaCl and 50 µM Zn²⁺ using the vivaspin500 concentrator (Satorius). The concentrated sample of 100 µL total volume was incubated on ice for 30 minutes and spun at 17 000 g at 4 °C for 10 minutes prior to rerunning sample on the same S6 column after pre-equilibration with buffer (20 mM HEPES pH 7.4, 140 mM NaCl and 50 µM Zn²⁺). The S6 column was ran at a flow rate of 0.5 µL/min for 1 column volume. An elution peak for FXII FnII and gC1q-R complex was formed in the presence of 50 µM Zn²⁺ with a small peak for FXII FnII excess observed. A 15% SDS-PAGE gel was ran to analyse fraction peaks. The FXII FnII and gC1q-R complex peak was pooled and concentrated down to 2.6 mg/mL.

2.8.0 Surface Plasmon Resonance (SPR)

2.8.1 Immobilisation of ligands on the sensor chip surface

SPR experiments were performed with both BIAcore 3000 (GE healthcare) and SensiQ Pioneer instrument (Pall ForteBio). An amine coupling kit (GE healthcare) was used to immobilise the ligand. Ligands immobilised on sensor chips in this project are FXII, gC1q-R, PK and FXI. Frozen aliquots of 200 μ L of 0.09M N-Hydroxysuccinimide (NHS) and 0.4M 1-Ethyl-3-(3-dimethylaminopropyl) carbodiimide (EDC) were thawed and spun, then a 1:1 (v/v) mixture of each were presented to the docked sensor chip surface. This will activate the carboxymethyl groups on a dextran-coated chip with the command of the surface preparation wizard from the BIAcontrol software (GE healthcare).

The surface preparation wizard application was programmed to immobilise (amine couple) amine groups of the lysine on the ligand to the activated sensor chip surface for covalent bonding with the activated reactive ester groups on the sensor chip surface. For the immobilisation, 10-30 μ g/mL of the ligand was diluted into 50 mM Na-acetate with a pH ranging from 3.58 to 4.5 used throughout this study for various ligands including gC1q-R, FXII, FXI and PK to couple to a sensor chip surface. A reference surface was also prepared in the same manner, except all carboxyl groups including the ones in which a ligand is immobilised were blocked with 1M Ethanolamine hydrochloric acid pH 8.5 to deactivate the surface. No ligand (blank surface) was added for the reference surface. A running buffer consisting of 20 mM HEPES pH 7.4, 140 mM NaCl and 0.005% P20 in the presence of 50 μ M Zn^{2+} (or Ca^{2+}) or EDTA was used throughout the immobilisation experiment with a reduced flow rate (<30 μ L/min). A flow rate of 30 μ L/min following immobilisation was initially used to allow the sensor chip surface to stabilise prior to scouting for a suitable regeneration solution. It's important for the regeneration solution to be mild and not harsh for the immobilised ligand

as all needed is to allow the baseline to return back to normal after removing remaining bound analyte on the sensor chip surface before performing the next analyte injection. In my case the surface was usually regenerated with 20 mM EDTA and 1M NaCl for gC1q-R binding to FXII and 1 M NaCl for any other interaction that do not require Zn²⁺ in HEPES buffer.

2.8.2 Measuring the gC1q-R interaction with FXII

Both FXII and gC1q-R were used as analytes depending on which ligand was immobilised on the sensor chip surface. Using FXII or FXII domains (FXII FnII or FXII FnII-EGF1) as analyte on the BIAcore 3000 instrument, a concentration series of minimum 5 different concentrations are usually prepared using running buffer (20 mM HEPES pH 7.4, 140 mM NaCl, 0.005 % P20 and 50 µM Zn²⁺) for the kinetics experiment. A sample without protein or just the running buffer is also prepared as a control, which should ideally not give any response unit (RU) and can therefore be subtracted from the data curves during data processing.

250 µL centrifugated (10 minutes at 17,000 g at 4 °C) analyte samples at different concentrations, buffer control (no analyte) and regeneration solution in microcentrifuge tubes were all transferred into SPR plastic vials. All samples in SPR plastic vials were then placed on the rack of the BIAcore 3000 instrument and a running buffer in a glass bottle already in position to provide constant flow of buffer during the experiment. All samples were made up from this running buffer.

The kinetics experiment was performed using the BIAcontrol kinetic wizard application within the BIAcore 3000 control software. A flow rate of 30 µL/min (or 50 µL/min) and a regeneration step with injection volume of 50 µL for 50 seconds after each protein analyte injection were used. All other protein analytes including gC1q-R, Graal₈₆₃₋₁₁₅₀ and CFI followed

a similar process as described above to obtain binding data for kinetics parameter determination.

Another SPR instrument used in this project is the SensiqPioneer, which can perform both analyte concentration series and a single concentrated protein analyte injection compared to BIAcore 3000 which does not have an updated software to perform a single injection. The newer BIAcore instrument should have this function in their software.

After performing a kinetics experiment, raw data from both BIAcore 3000 and SensiqPioneer were processed using the BIAevaluation or Qdat software, respectively. The association and dissociation phase on the curves are used for the kinetic analysis to fit the data into binding models, which ultimately gives a best fit with kinetic parameters (k_a , k_d and K_D etc.).

2.9.0 Crystallisation of FXII, FXII FnII and bound FXII FnII-EGF1 in the presence of gC1q-R

2.9.1 Crystallisation of full length mouse FXII

Gel filtrated fractions of WT mouse FXII and active site mutant S526A FXII (mFXII S526A) were pooled and concentrated down to 18.6 mg/mL and 24.6 mg/mL, respectively in 20 mM Tris-HCl, 50 mM NaCl pH 8.0 buffer using a vivaspin20 (Sartorius) 10 kDa MWCO.

A pre-crystallisation test (PCT) was performed using the PCT reagents and a 24-well plate. The test involves dispensing equal volume of protein and PCT solution (Hampton Research), usually around 0.5 μ L to 1.0 μ L on a 24-well plate with 500 μ L PCT solution in the reservoir, then sealed with a transparent adhesive tape and left to incubate at room temperature for 30 minutes or more.

Both Matrix Hydra II (Thermo Scientific) and Mosquito robots (TTP Labtech) were used to dispense smaller volumes of around 0.2 μ L of FXII protein (WT and mutant) and 0.2 μ L of

crystallisation solution in a 96-well MRC plate (Molecular Dimensions) using a sitting drop vapour diffusion method. Just like the PCT experiment on the 24-well plate, the 96-well MRC plate was also sealed and incubated at 20 °C and 10 °C to allow crystal growth. A single crystal of mFXII S526A mutant was observed but with no diffraction. Crystallisation experiments with more mFXII S526A mutant at concentrations 12.3 mg/mL, 9.5 mg/mL, 6.15 mg/mL, 5 mg/mL, 4.8 mg/mL, 2.5 mg/mL, 1.9 mg/mL and 1.25 mg/mL were also set with no crystals observed in various crystallisation screens including Classic I, PEG I, AmSO₄, PACT and Morpheus from Qiagen, Molecular Dimensions or Hampton Research.

Fresh batch of WT mFXII and mFXII S526A purified from yeast by our collaborator Prof David Gailani (Vanderbilt University Medical Center) at concentrations 2.5 mg/mL and 1.98 mg/mL, respectively were further concentrated using vivaspin500 to 14.83 mg/mL for WT mFXII and 28.1 mg/mL for mFXII S526A. WT FXII was mixed in the presence of dextran sulfate in a molar ratio of 1:3 with 50 mM Zn²⁺ added prior to crystallisation. Crystallisation was performed for both in which 0.3 µL of mFXII and 0.3 µL crystallisation solution are placed on a 96-well plate to form a drop and 80 µL of crystallisation solution in the reservoir. This was sealed using a transparent adhesive tape and incubated at 10 °C and 19 °C.

2.9.2 Crystallisation of untagged and tagged human FXII FnII-EGF1

Fractions of untagged FXII FnII-EGF1 from the size exclusion chromatographic or gel filtration (HiLoad SuperdexTM 200 16/60) experiment were pooled and concentrated down to 5.4 mg/mL in 50 mM Tris-HCl, 100 mM NaCl pH 8.0 buffer using vivaspin20 (Sartorius) 3kDa MWCO. Apart from the FXII Fni-EGF2 and the protease domain of FXII, structure for the full length FXII or its N-terminal domains have not been determined yet; FXII FnII-EGF1 was made to be crystallised and characterised accordingly. MBP-FXII FnII-EGF1 fusion and FXII FnII-EGF1

were subjected to crystallisation in the same way described for full-length mFXIII. Although, no crystals were observed for FXII FnII-EGF1 alone, MBP-FXII FnII-EGF1 produced crystals. MBP-FXII FnII-EGF1 crystals were cryo-cooled to preserve the crystal for the transport as well as radiation damage when exposed to X-ray beam at the Diamond Light Source (DLS).

2.9.3 Crystallisation of untagged human FXII FnII

Pooled gel filtrated and concentrated FXII FnII (expressed in S2 cells) down to 6.0 mg/mL using vivaspin20 (Sartorius) were set for crystallisation using a 96-well MRC plate with initial volumes of 0.3 μ L FXII FnII and 0.3 μ L crystallisation solution on the well and 80 μ L crystallisation solution in the reservoir using the sitting drop vapour diffusion method. Crystallisation screens Pi-PEG, JCSG+ and PACT were used for the crystallisation trial and the 96-well MRC plate sealed with a transparent adhesive tape and incubated at 19 °C. Crystals appeared within 48 hours from the PACT and JCSG+ screens.

To test the crystals for diffraction; a crystal was cryo-protected with 30% glycerol added to the mother liquor in which the crystal grew in, followed by fishing with a suitable nylon loop size. The fished crystal is then flash cooled in liquid nitrogen and the loop containing the crystal mounted on the home source goniometer (Rigaku Mibromax-007 X-ray generator). The mounted crystal was exposed to a dose of X-ray to record diffraction confirming whether the crystal is protein or salt. The diffraction pattern recoded was of both low and high-resolution reflections confirming crystal to be protein.

A similar cryo-cooling preparation aforementioned was made with more crystals and transported to the Oxford synchrotron facility at Diamond Light Source (DLS) beamline I04 and subsequently to the European Synchrotron Research Facility (ESRF).

2.9.4 Crystallisation of FXII FnII or FXII FnII-EGF1 in complex with gC1q-R

Gel filtrated gC1q-R-FXII FnII (2.6 mg/mL) or gC1q-R-FXII FnII-EGF1 (5.4 mg/mL) in 20 mM HEPES pH 7.4, 140 mM NaCl and 50 μM Zn^{2+} from S6 10/300 column. For the gC1q-R-FXII FnII complex (2.6 mg/mL), PCT was performed first, followed by crystallisation with screens JCSG+ and Pi-PEG on a 96-well MRC plate, while for gC1q-R-FXII FnII-EGF1 (5.4 mg/mL) crystallisation screens PACT, JCSG+ and PEG were used and set on a 96-well MRC plate. All liquids were handled by the Mosquito dispensing instrument for the 96-well MRC and sealed with a transparent adhesive tape plates for both complexes and incubated 19 °C and 10 °C.

Crystals for gC1q-R-FXII FnII-EGF1 (5.4 mg/mL) grew from the crystal trial within 24 hours and were optimised from the crystal trial. The crystal trial was optimised by changing the pH range (5.3-5.9) PEG 4000 and by substituting calcium acetate with sodium acetate. These two crystal forms for gC1q-R-FXII FnII-EGF1 will be henceforth termed form 3A and 3B for crystal trial and optimised, respectively. Form 3A diffracted to 3.16 Å, while form 3B diffracted to 3.14 Å.

2.9.5 Crystallisation of gC1q-R and peptides

Human gC1q-R isolated from S200 16/60 column was incubated on ice with peptides; gC1q-R-RCP, gC1q-R-H4 or gC1q-R-LBP in a 1:5 or 1:10 molar ratio with or without metal ions such as Mg^{2+} or Zn^{2+} in 20 mM HEPES pH 7.4, 140 mM NaCl.

Human gC1q-R was also prepared by mixing a 1:2 molar ratio of gC1q-R to HK domain (HKD5) and incubated on ice for 30 minutes, followed by isolation from S200 increase 10/300 column. The complex peak was pooled and concentrated in 20 mM HEPES pH 7.4, 140 mM NaCl and 25 μM Zn^{2+} and subjected to crystallisation trials with hits observed for all

complexes. Crystals were cryo-cooled and exposed to X-ray beam at the Diamond Light Source (DLS) was used to test the crystals for diffraction.

2.10. Structure determination, refinement and validation of untagged human FXII F_nII in the presence of Zn²⁺

Datasets collected from the diffracted FXII F_nII crystals were initially indexed by adding all the images using the 'add images' window in iMOSFLM or MOSFLM within the CCP4 suite. A separate window will automatically be displayed when the images are open. The displayed image was prepared by masking the circular backstop shadow by clicking the green box icon, which will show a green circle in the centre of the diffraction image. Furthermore, a spot finding radius (red box icon) and resolution limit (blue box icon) for the displayed diffraction image was selected.

The Autoindexing selection was chosen, which allows the software to automatically pick spots on the diffraction images and the spots (recorded reflections) identified are shown in yellow crosses. Finding the spots allow the assignment of integer numbers (h, k, l = Miller Indices) for the planes as this is crucial for obtaining the correct geometry for integrating the intensities from the reflections. Cell refinement and then integration is also performed iMOSFLM by clicking on the buttons on the left hand side displaying the icons in the session. This generates an *.mtz output file, which is further used to to combine all the integrated values from the reflections in all images into one structure factor and normalised using Aimless. The output logfile generated after Scala or Aimless provided diagnostics on data quality before moving on to Phasing, model building and refinement of the model.

For phasing using molecular replacement, Mr Bump (automated scheme for Molecular Replacement) was initially giving the FXII F_nII amin acid sequence and experimental structure

factors to create a suitable FnII template. The FnII template (PDB coordinates), FXII FnII amino acid sequence and the *.mtz from Aimless were put into the Phaser (CCP4 and PHENIX) and the program ran. A solution for FXII FnII was found to solve the structure. FXII FnII bound to Zn²⁺ model (form 1 and form 2) were built using Coot (Emsley and Cowtan 2004) with rounds of refinement (with restrains and constrains) using REFMAC 5.0 (Murshudov *et al.*, 1997) in CCP4 and phenix.refine in PHENIX with each refinement run validated.

FXII FnII Form 1 and Form 2 structures were validated using validation programmes including PROCHECK in CCP4 and MOLPROBITY in PHENIX and wwPDB Validation Service for final validation before submitting structures to the protein databank (PDB). PyMOL and QtMG (CCP4) were used to visualise the FXII FnII structures (Form 1 and Form 2) and figures made for this thesis using both programs.

2.11 Structure determination, refinement and validation of gC1q-R-FXII FnII-EGF1 complex

Diffraction images for gC1q-R-FXII FnII-EGF1 were autoindexed, cell refined and integrated in iMOSFLM in a similar manner to what has already been mentioned for FXII FnII in the presence of Zn²⁺ (subsection 2.10). The output *.mtz file generated from the integration job run was scaled in Aimless and the output *.mtz file generated was used for the molecular replacement.

After careful inspection of the data collection statistics for gC1q-R-FXII FnII-EGF1 from the logfile after Aimless, the *.mtz file from Aimless was used as an input file in Phaser alongside the PDB coordinates for FXII FnII (unpublished) mentioned in subsection 2.10 and the gC1q-R (PDB ID 1P32) . An amino acid sequence for gC1q-R and FXII FnII in one file was also put in Phaser and then ran the program. A solution was found for the gC1q-R-FXII FnII-EGF1 to solve

the structure. Coot (Emsley and Cowtan 2004) was used for model building gC1q-R-FXII FnII-EGF1 with rounds of refinement (with restrains and constrains) using REFMAC 5.0 (Murshudov *et al.*, 1997) in CCP4 followed by validation using MOLPROBITY. The gC1q-R-FXII FnII-EGF1 structure was visualised in both PyMOL and QtMG (CCP4) and figures made using both programs.

2.12 Contact activation assay using chromogenic substrates

Contact factors FXII (50 nM), HK (10 nM), PK (10 nM) and negatively WT gC1q-R (100 nM) in the presence of 50 μ M Zn²⁺ were mixed well and incubated in a 96-well nunc plate (Thermo Fisher Scientific) at 37 °C for 15 minutes. After the mixture chromogenic substrate S-2302 (0.4 mM) were added and mixed well using a shaker.

Parallel experiments consisting of FXII (50 nM) and gC1q-R (100 nM) with Zn²⁺ or HK (10 nM), PK (10 nM) and gC1q-R (100 nM) with Zn²⁺ incubated at 37 °C for 15 minutes, then added chromogenic substrate S-2302 (0.4 mM) were also performed to determine whether contact activation is triggered in the absence of a contact factor. The data were normalised by subtracting the buffer from the test absorbance, analysed and figures produced using GRAPHPAD PRISM 7 Software.

CHAPTER 3.0

TECHNIQUES

3.0 Techniques

3.1.0 Chromatographic techniques

Understanding the biophysical and chemical properties of proteins is useful when considering to use any chromatographic technique including ion exchange, affinity and size exclusion chromatography. Rational design of a construct before expressing the protein of interest (POI) is important, as this may help in upstream and downstream processing of proteins. Proper protein folding and purification needs careful considerations when designing constructs and choosing expression systems as this can aid protein expression, increased yield and produce functional protein. In structural biology, especially X-ray crystallography, protein purity and yield are important for obtaining crystals. In other words, protein purification with desired quantity and purity is vital for characterising protein structure, function and understanding the biological role of proteins ⁽²⁵³⁾. In this PhD project, the ÄKTA system (Prime, Purifier and Pure) (Figure 3.1) were used to perform all purifications and analysis.

ÄKTA pure protein purification system

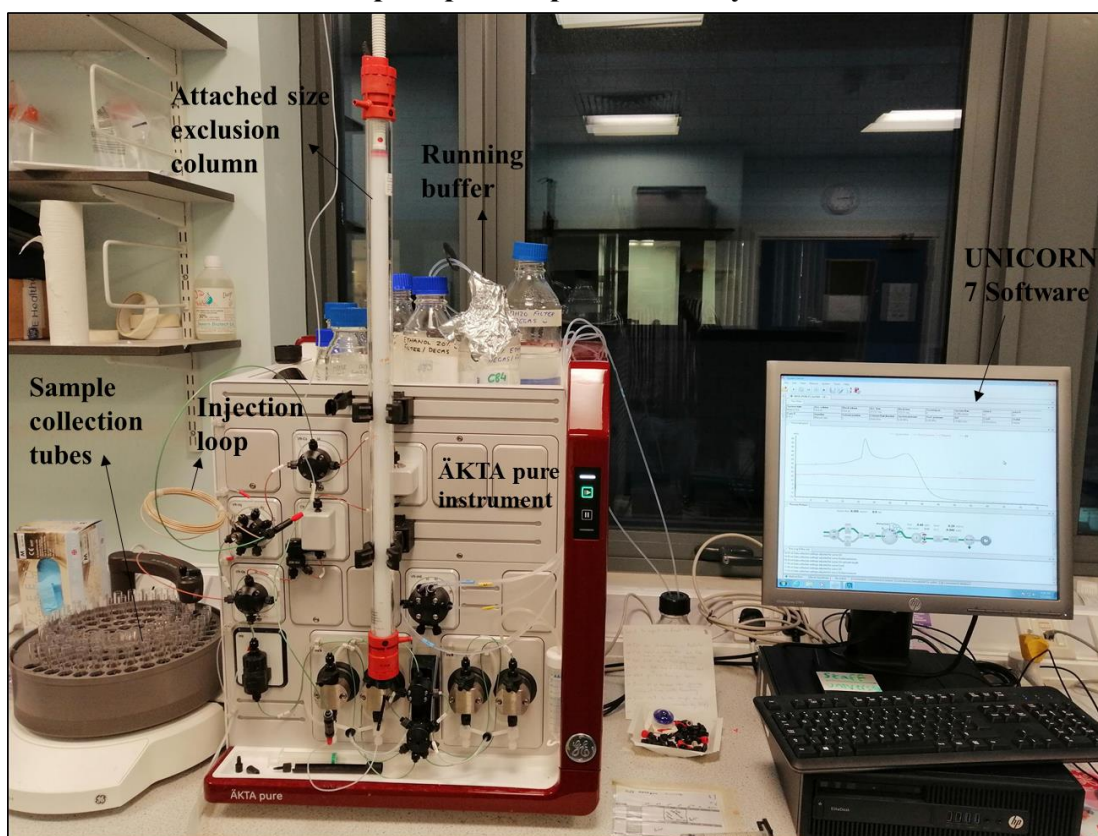


Figure 3.1: ÄKTA pure instrument showing attached size exclusion column to the ÄKTA instrument. The UNICORN 7 software was used to run the ÄKTA instrument. Samples are loaded and injected from the injection loop to the attached column and followed by elution in which samples are collected on the sample collection tubes.

3.1.1 Ion Exchange Chromatography (IEX)

Ion Exchange Chromatography (IEX) is a popular method and the principle of this method involves allowing the separation of ionisable ions and polar molecules/biomolecules (i.e. proteins, peptides, amino acids or nucleotides) based on their total charge depending on the pH. The total charge of the molecule is referred to as the isoelectric point, or pI , in which the molecule has no net charge, neither a net positive charge nor net negative charge. The theoretical pI of proteins can be calculated using the primary amino acid sequence using

Expaty protpatram online or calculated using 2D SDS-PAGE gel or mass spectrometry. Ionisable ions and polar molecules have an affinity for the ion exchanger depending on what type of exchanger one decides to use. There are two types of ion exchangers; cationic and anionic exchangers, whereby the solid matrix containing a negatively or positively charged group for cationic (Carboxymethyl cellulose) and anionic (DEAE cellulose) exchangers bind to positively and negatively charged proteins, respectively. In other words, a protein in buffer with a pH above its pI will bind to positively charged anion exchanger, while a negatively charged anion exchanger will bind to proteins when the pH is less than the protein's pI. Buffer pH and salt concentration are crucial for both binding and elution of biomolecules in IEX. To elute bound biomolecules on the immobile exchanger, high salt - NaCl can be used to compete for binding to the exchanger in a concentration dependent fashion and ultimately eluting the biomolecules of interest ⁽²⁵⁴⁾.

3.1.2 Affinity chromatography

Affinity chromatography, also called affinity purification is a unique purification technique used to separate biomolecules (i.e. from DNA to proteins) on the basis of reversible interaction between biomolecules and a specific ligand immobilised to a chromatography matrix (solid support) offering high specificity, resolution and high capacity for the biomolecule of interest. This purification technique is quick, reliable and cheap. This technique relies on interactions between biomolecules and the ligand coupled to the chromatography matrix. Fusion proteins with polyhistidine tag (His-tag) bind to a number of transition metal ions (Ni^{2+} , Zn^{2+} , Co^{2+} and Cu^{2+}) thus serving as a good and reliable immobilized metal affinity chromatography (IMAC) method. Other methods for fusion protein purification include Glutathione S Transferase (GST) or Mannose Binding Protein (MBP) binding to

glutathione or Dextrin Sepharose™ immobilised columns or resins, respectively. Other tags including FLAG and thioredoxin (Trx) are also available for use. Alternatively, commercially available activated affinity supports can be used to covalently immobilise a ligand of interest such as a peptide known to bind to a protein including antibodies or nanobodies for instance⁽²⁵⁵⁾. Captured proteins on immobilised ligand in a column matrix under physiological pH and ionic strength such as phosphate buffered saline (PBS) and other buffer types are usually used, followed by a wash step to remove non-specifically unbound components from the column with no effect on the bound sample. Adding low levels of detergent, ionic strength or salt concentration might help in both binding of protein of interest and easily washing out unbound prior to the final elution. Finally, an elution buffer is used to disrupt the protein of interest and ligand interaction thus causing dissociation of the protein of interest, which is collected with a collection tube. Fusion proteins with His-tagged are eluted with an elution buffer containing high imidazole concentration, which displaces the bound His-tagged protein. Purified fusion proteins (e.g. His tagged) after elution usually require additional purification to ensure that purer sample is obtained. In protein crystallography, a homogeneous and monodisperse protein sample is required for increasing the chances of crystal formation and growth. This can be achieved using size exclusion chromatography⁽²⁵⁶⁻²⁵⁸⁾.

3.1.3 Size exclusion chromatography (SEC)

Size exclusion chromatography (SEC), generally known as gel filtration separates molecules in solution on the basis of size and shape using a porous matrix with a distinct pore size made up of cross linked dextran (Sephadex), agarose (Sepharose) or polyacrylamide (Sephacryl or BioGel P) to separate molecules of various molecular weights. Fractionation experiment from

a gel filtration column starts when a sample (i.e. protein) loaded in a loop is injected into a column. Proteins then migrate through the column in a running buffer aided by a purification instrument such as an ÄKTA system controlled by the Unicorn software. Proteins with higher molecular weight penetrates and elutes earlier than low molecular weight proteins, as intermediate and lower molecular weight proteins enter the pores of the cross linked gels, therefore taking longer to elute as shown in Figure 3.2. Bigger proteins outside the column separation range elute in the void volume (V_0) and are therefore not separated. Gel filtration was performed throughout this project to either obtain pure protein after affinity or ion exchange chromatography or to confirm the state of the protein in solution before any downstream experiment. Additionally, macromolecular complexes including gC1q-R bound FXII FnII were isolated using analytical gel filtration prior to crystallisation. Eluted samples are always subjected to SDS-PAGE gel analysis to confirm purity of protein of interest and also, whether protein complexes are formed relative to individual controls.

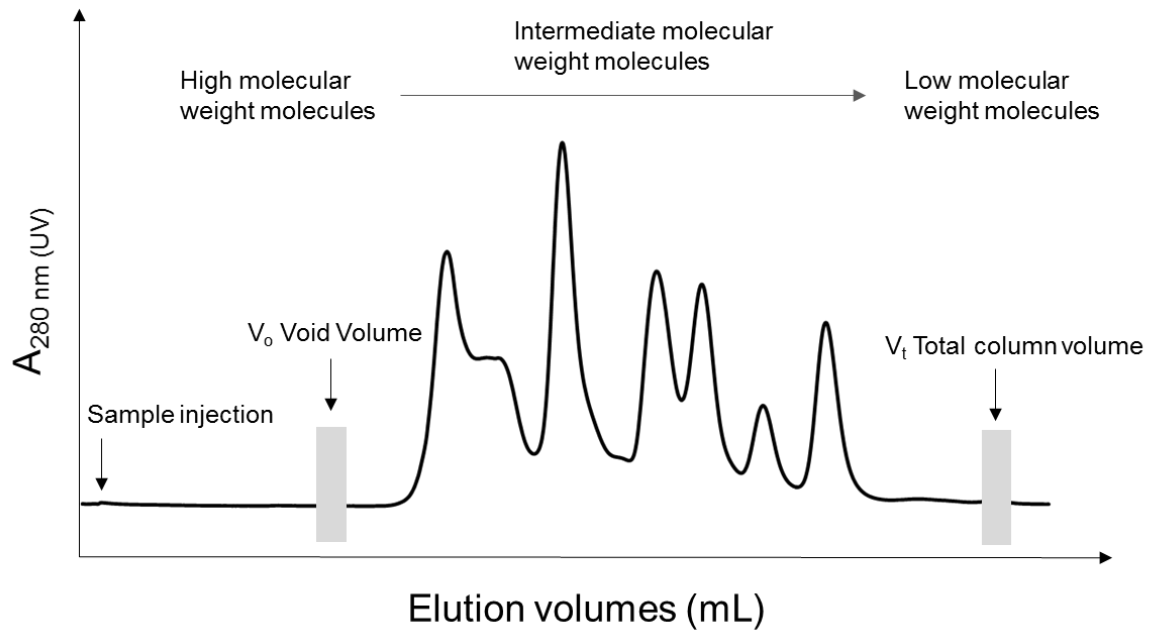


Figure 3.2: Diagram showing a typical chromatogram from beginning (left) to end (right). Injected sample migrates through the gel in the column to be separated by size and shape in a running buffer. Proteins with aromatic residues absorb at a wavelength of 280 nm to produce a peaks with varying height. Bigger proteins elute earlier than smaller proteins and bigger proteins outside of the column separation range elute first and are present in the void volume (V_0). A total column volume (V_t) is achieved when a solution (i.e running buffer) runs through the whole column once.

Approximation of the molecular weight of proteins or macromolecular complexes isolated from a gel filtration experiment can be calculated using commercially available protein standards of varying molecular weights from companies such as Sigma. The elution volume (V_e) correlating to the hydrodynamic radius of the protein of interest can be used to calculate the K_{av} from the defined equation below.

$$K_{av} = (V_e - V_0) / (V_t - V_0)$$

A plot of scatter graph produced by plotting the calculated K_{av} against the log molecular weight (MW) of the protein standards allows the calculation of unknown protein molecular weight from the linear regression equation derived from the scatter plot ⁽²⁵⁹⁻²⁶¹⁾.

3.2.0 Background on Surface Plasmon Resonance (SPR)

The first anomalies of polarised light shone on metal film surface producing dark and light bands in the reflected light were observed by R.M. Wood between 1902 and 1912, while the theoretical behaviour of the anomalies was described by Lord Rayleigh in 1907 ⁽²⁶²⁾. This subsequently gave way for scientists including Otto and Kretschmann in the late sixties and early seventies, respectively to demonstrate how incident beam of polarized light undergoes reflection using a prism and the relationship this has with optical excitation of electrically conducting gold layer at the interface of a glass sensor and an external liquid medium ^(263, 264) (Figure 3.3).

The smallest change detected at the interface due to changes in refractive index of the medium adjacent to the metal surface will lead to a change in SPR signal which allows precise measurements in real-time. Ligands including proteins immobilised on functionalised gold coated glass results to change in refractive index in comparison to no ligand immobilised. Furthermore, analytes added in the medium can absorb the incident light during interaction with the immobilised ligand on the gold surface resulting into a shift in the resonance angle and the intensity of light reflected in real-time. A shift in the resonance angle can also occur when subtle change as a result of components in the running buffer absorb light and must therefore be subtracted from the reference cell to reduce noise and increase the signal (Figure 3.2A-B) ⁽²⁶⁵⁾.

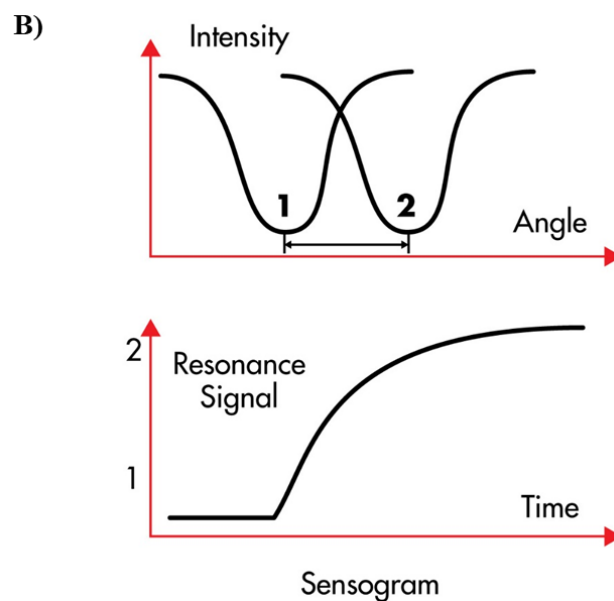
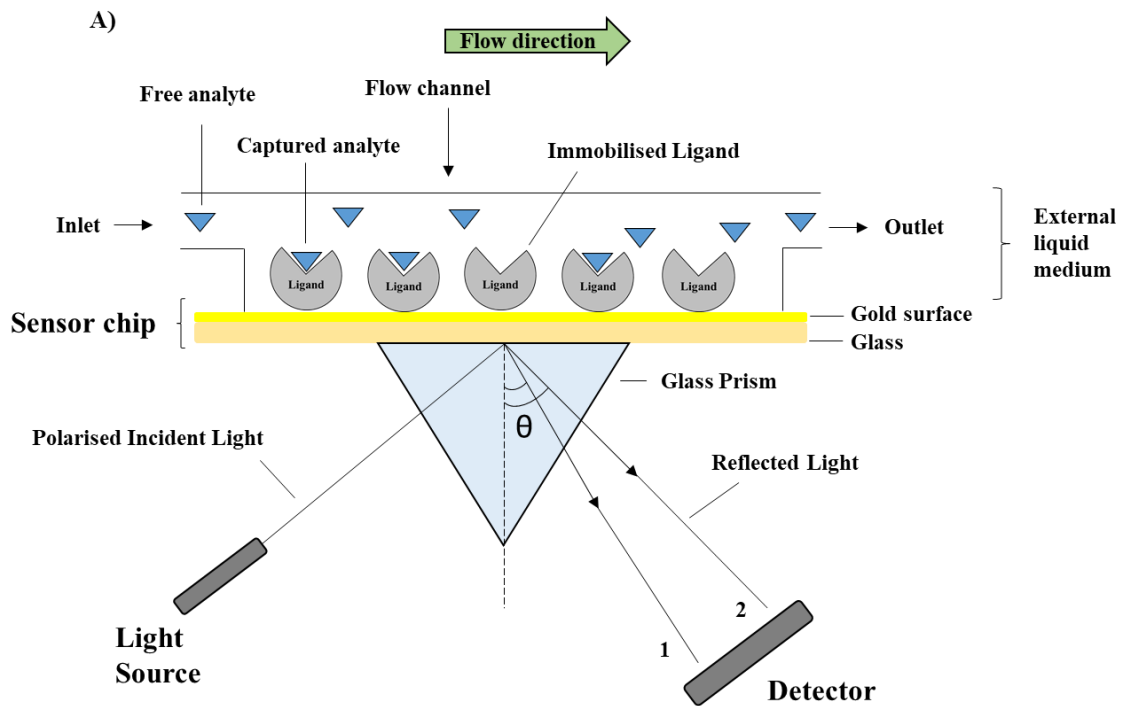


Figure 3.3: Excitation of surface plasmons and reflection from incidence beam. A) The incident (incoming light) at an incidence angle (SPR angle) perturbs the mobile electrons on the gold surface and causes a change in the surface plasmon wave. B) As analytes bind to the immobilised ligand a shift in SPR angle is observed and this is represented as a sensogram. Dapted from the following link: <https://www.ifm.liu.se/applphys/molphys/equipment/spr/>.

3.2.1 SPR Instrument and Sensor chip

Metals such as copper, aluminium, indium, silver and gold are used for SPR sensor chips as the metal surface can be utilised to generate surface plasmon resonance from their electrons following excitation of light at a suitable wavelength ⁽²⁶⁶⁾.

Gold surfaces are commonly used, as it is inert to chemical reactions. Two instruments were used throughout this project; BIAcore 3000 system (GE Healthcare) and SensiQ Pioneer and Pioneer FE systems (Pall ForteBio) and the general principle is the same for both instruments. However, the SensiQ Pioneer instrument is newer with functionalities such as OneStep kinetics injection option, more sensitive in detecting smaller analytes (70-100 Daltons) and has an updated Evaluation software (Qdat). For both systems, when the gold sensor surface is altered by ligand immobilisation or analyte bound to immobilised ligand, the SPR signal from changes in the refractive index within the system is recorded by the detector and relayed to the control software ⁽²⁶⁷⁾.

There exist many different types of sensor chips with different surface chemistries and modifications depending on the application. I throughout this project used a sensor chip CM5 for the BIAcore3000 and other sensor chip series including COOHV, COOH1 and COOH2 for the SensiQ Pioneer. The sensor chip CM5 is generally used for biomolecular analysis and has a carboxymethylated dextran covalently attached to a gold surface and extends 100 nm from the gold surface. The depth of dextran can vary from none for C1 and 30 nm for CM3. The gold surface for the CM5 chip is fixed on a plastic support and is protected by a dust jacket sheath as shown in Figure 3.4C.

BIAcore 3000 Instrument

A)

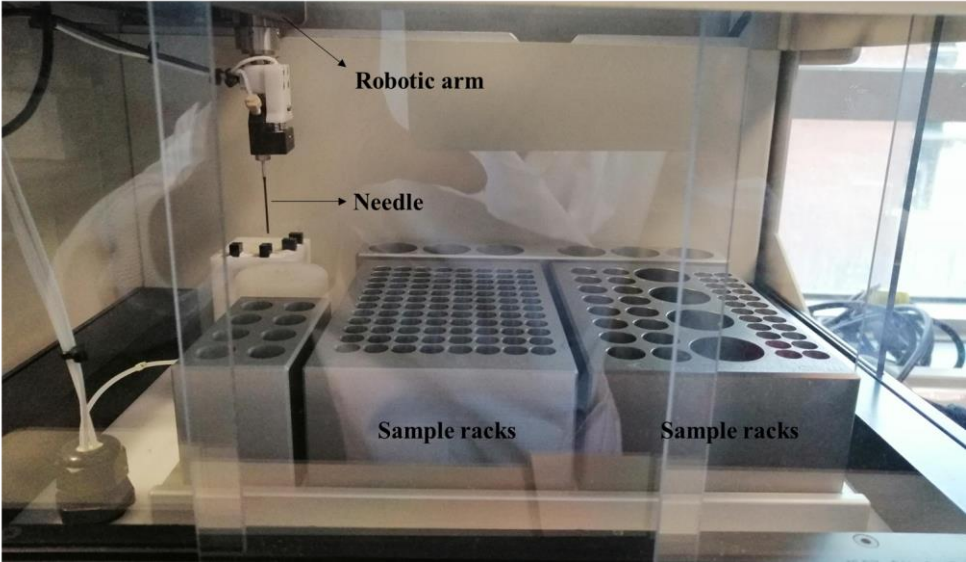


Waste bottle

Running buffer

B)

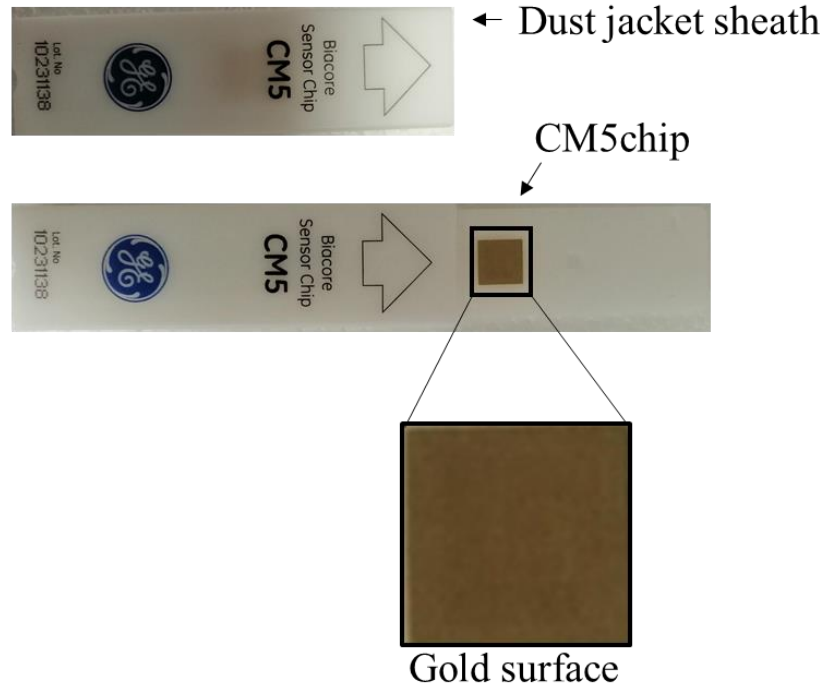
Autosampling compartment for BIAcore 3000



Dust jacket sheath with sensor chip inside

CM5 chip for BIAcore 3000

c)



SensiQ Pioneer Instrument

D)



E) Sensor chips for SensiQ Pioneer

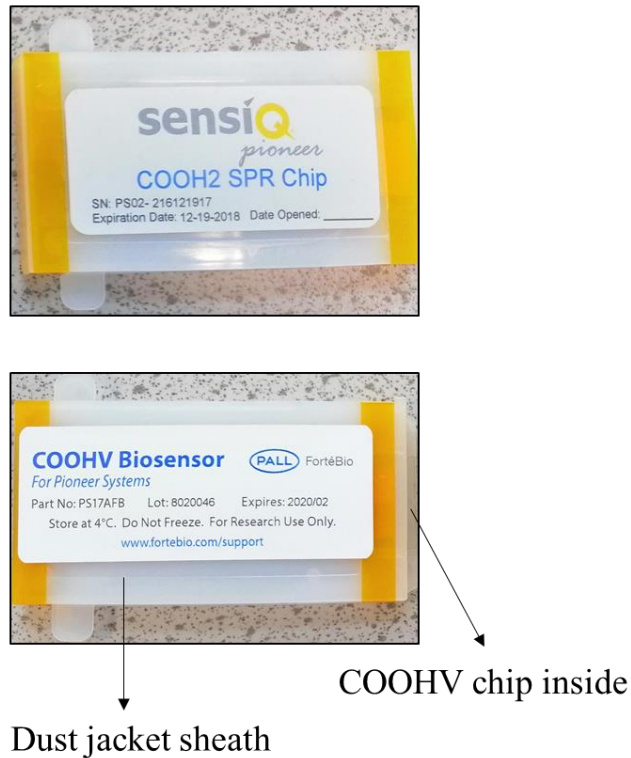


Figure 3.4: Sensor CM5 chip showing the dust jacket sheath (outer part) and the gold surface sitting on a white plastic. A-B) BIAcore 3000 instrument showing different parts. C) CM5 chip for BIAcore 3000. D) SensiQ Pioneer instrument and E) Sensor chips (COOH2 and COOHV) for SensiQ Pioneer.

3.2.2 Immobilisation of proteins on the sensor chip surface

3.2.3 Pre-concentration

Before activating the dextran sensor chip surface and immobilising the protein, the protein in low ionic strength buffer (10 mM Sodium acetate) with pH range of 6.0 to 4.0 is tested for binding to the inactivated surface first. This is used to make the protein positively charged, as this will allow the electrostatic attraction between the negatively charged dextran surface

layer and protein to form. The electrostatic interaction occurs when the protein pI is above the pH and the pH above the pI of the carboxymethylated dextran layer (pI -3.5).

Pre-concentration at a pH lower than 3.0 will result into the carboxymethylated dextran layer to lose its capacity to attract injected protein on its surface. Pre-concentration is a useful step as the relative response unit (RU) produced in a sensogram readout in real-time can reveal how much of the protein is being injected and attracted to the negatively charged dextran surface in different pH (5.5, 5.0, 4.5 or 4.0) and can also indicate protein stability (or denaturation) from the sensogram ^(268, 269).

3.2.4 Ligand immobilisation

The amount of ligand to immobilise is important depending on what type of experiment is being conducted; binding analysis or kinetic analysis. A high ligand amount is immobilised in binding analysis but much less in kinetics analysis to avoid mass transport limitation.

The concentration of the ligand to be immobilised is important in determining the rate of pre-concentration and it is generally recommended to use a concentrations between 5 and 50 µg/mL for protein depending on protein molecular weight.

As the buffer (i.e. salt concentration, Tris etc.) can have undesired effects on the immobilisation of the ligand on the dextran surface, it is highly recommended to prepare the protein ligand dilutions from a high concentrated stock in buffer with low ionic strength.

For kinetics experiments, it is recommended to achieve a maximum theoretical response (R_{max}) of 50-150 response unit (RU) assuming in theory that 100 % of the immobilised ligand is active and capable of interacting with the injected analyte on the sensor surface. The equation below describes how the R_{max} can be calculated; the R_{max} is the ratio of the analyte molecular weight over the ligand molecular weight multiplied by the amount of ligand

immobilised (R_L) and the stoichiometry (S_M) of the binding as shown in the equation expressed below ⁽²⁶⁹⁾.

$$R_{max} = \frac{\text{analyte MW}}{\text{ligand MW}} \times R_L \times S_M$$

Following the calculation, if a 1:1 binding of ligand to analyte is considered, in which S_M will be 1, then the value obtained from dividing the molecular weights of the analyte and ligand, multiplied by 100 is the amount needed in RU terms for reasonable kinetics experiments. The method is programmed in such a way that the desired calculated RU for ligand immobilisation is entered in the method for the programme to inject the ligand until the desired level is reached. For the actual immobilisation experiment, the protein ligand stock is diluted down using immobilisation buffer (10 mM Sodium acetate, pH 4.5) and centrifuged alongside the amine coupling reagents 1-Ethyl-3-(3 dimethylaminopropyl carbodiimide (EDC) and N-Hydroxysuccinimide (NHS) at 17,000 g at 8 ° C for 20 minutes. Amine coupling is a common method in which the sensor chip i.e CM5 is inserted and docked onto a docking unit in the SPR instrument (whether BIAcore 3000 or SensiQ Pioneer) exposing the gold sensor surface layer over the liquid handling system or IFC for BIAcore 3000.

The IFC (liquid handling system or microfluidic system) delivers the samples; ligand to be immobilised or analyte to bind to the immobilised ligand on the docked sensor chip surface. Activation of the carboxymethylated dextran layer on the sensor chip surface is achieved by injecting a mixture of EDC and NHS onto the chosen flow cell at a flow rate of 5 μ L/min for 7 minutes to create reactive succinimide ester groups that will react with primary amine groups from the ligand (i.e protein) or any nucleophilic group.

The final step of the immobilisation method involves capping or deactivating the reactive ester groups unbound to ligand with 1M-ethanolamine pH 8.5 (Figure 3.5). As a stable baseline is required, the running buffer is usually flown onto the sensor chip surface following successful immobilisation of the ligand at usually a flow rate of 30 $\mu\text{L}/\text{min}$ with time (sometimes hours). This can help in preventing baseline drifting during the biomolecular interactions thus giving a much more reliable data to fit the model ^(268, 270).

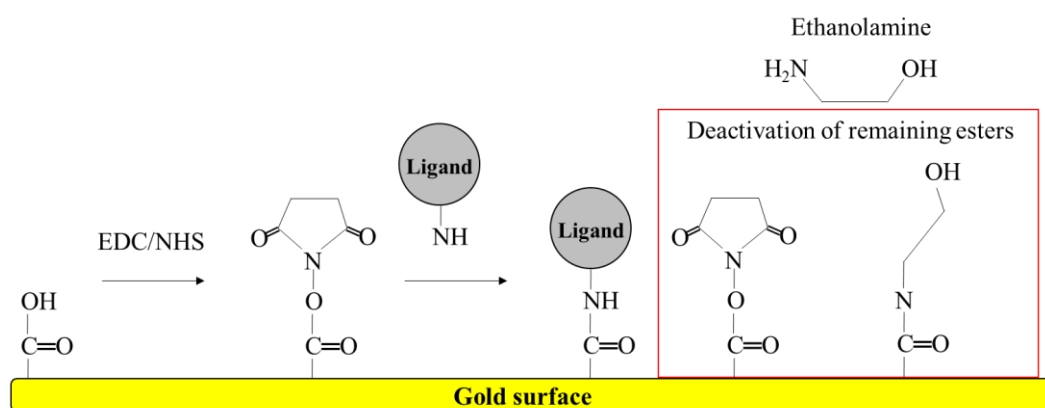


Figure 3.5: Amine coupling of ligand using EDC/NHS. The carboxyl groups of the dextran layer on the gold surface are activated to create reactive ester groups, followed by covalent attachment of the primary amine on ligand by. The remaining esters are then deactivated with ethanolamine as highlighted in the red box.

3.2.5 Studying biomolecular interactions

Interaction between the immobilised ligand and the injected analyte is defined by an association phase and a dissociation phase, in which, bonds are formed during the association phase and broken with time for the dissociation phase. For a concentration series (low to high concentration), a suitable regeneration solution is injected onto the sensor chip surface to remove the remaining bound analyte after each dissociation phase of every injected analyte before the next analyte injection. As some analytes dissociate very slowly without returning to

baseline, it is important to regenerate the surface and return to baseline before the next analyte injection ^(269, 271) (Figure 3.6).

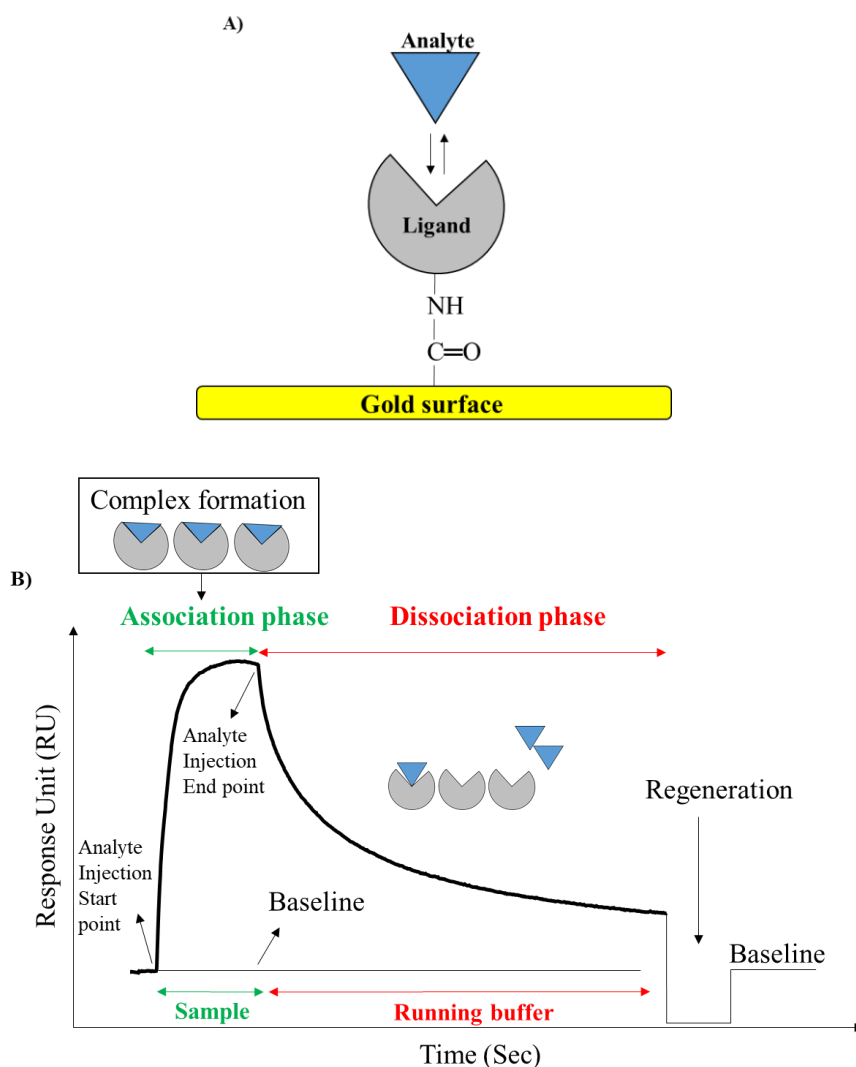
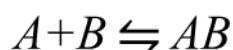


Figure 3.6: Analyte binding to immobilised ligand on the sensor surface (Gold surface). **A)** shows amine coupled ligand (immobilised ligand) on the gold surface (yellow) and analyte in blue with arrows for both forward and reverse reaction (association and dissociation). **B)** shows the forward reaction in which ligand (A) interacts with analyte (B) to form a complex of ligand:analyte (AB) for the association phase, while the reverse reaction when running buffer is flown on the sensor surface causes analyte to come off the ligand thus dissociating with time. At the end a regeneration solution is injected to allow the system to return back to baseline for more analyte injections.

The simplest interaction to fit a ligand and an analyte assumes a 1:1 binding, in which a ligand (A) with one binding site has an affinity for the injected analyte (B) to form a complex of AB (269, 272, 273).



The steady state or equilibrium is reached when equal number of bonds formed from the association phase is the same for the number of bonds being broken in the dissociation phase. This is usually observed when the system manifests a saturation behaviour and can be useful to extrapolate the values at equilibrium to obtain a binding constant from a hill plot in Prism. From the equation above, two important constants can be derived for the binding. The affinity the analyte has for the immobilised ligand can be expressed by rearranging the equation above to give the following expression:

$$\frac{[AB]}{[A][B]} = K_A$$

The ratio of bound AB complex and unbound A or B is where the association constant K_A with unit of M^{-1} is derived and gives an indication of how strong the binding between the ligand (A) and analyte (B) is when the K_A is high. On the other hand, the dissociation constants defined by the K_D with the unit of M describes the amount of unbound analyte over the amount of bound ligand (A) and analyte (B) and its reciprocal expression can therefore be derived from the following expression: (269, 272)

$$\frac{[A][B]}{[AB]} = K_D$$

As molecules A and B prefer to be in the bound state, AB, this therefore reflects on how tightly A and B bind to each other and if the K_D is smaller in its unit, then, this indicates a tight binding. In other words, K_D values ranging from femtomolar (fM) to millimolar (mM) implies tight binding in the fM range and weak binding for mM. K_A and K_D are inversely related and can therefore be expressed as:

$$K_A = \frac{1}{K_D} \quad K_D = \frac{1}{K_A}$$

Both the association phase and dissociation phase of the sensogram has a rate constant that defines K_A and K_D . The association phase defined by A and B colliding via diffusion to form a complex of AB has a rate constant of association (k_a) with unit in S^{-1} , while the rate constant of dissociation (k_d) with unit in $M^{-1} S^{-1}$ for AB describes how long it takes the analyte to unbind the ligand. The equation for both rates (association and dissociation) are expressed as:

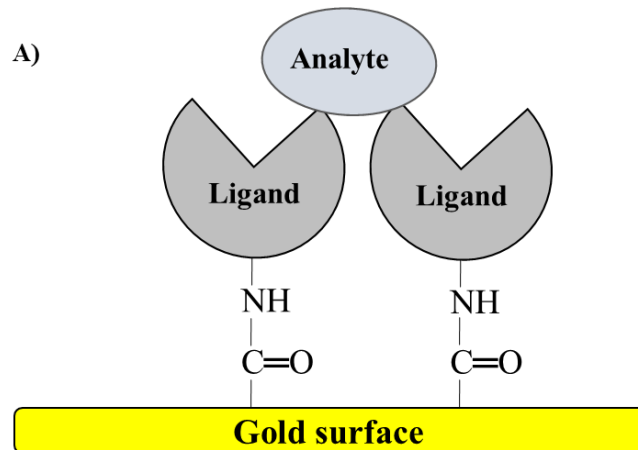
Rate of association	Rate of dissociation
$[A] \times [B] \times k_a$	$[AB] \times k_d$

At equilibrium, the rate of association and the rate of dissociation of the biomolecular interaction is equal. Furthermore, the rate constants k_a and k_d have a relationship with the association and dissociation constants K_A and K_D , respectively and can therefore be expressed as:

$$K_A = \frac{k_a}{k_d} \quad K_D = \frac{k_d}{k_a}$$

3.2.6 Multiple binding sites

Some analytes such as antibodies have two binding sites, in which the first site on the immobilised ligand is occupied thus making the other free binding site available for binding. The flexibility and closeness of both the ligand and analyte is important for binding to the second site. In the BIAcore3000 evaluation software, the Langmuir (1:1) model is recommended to use first, and if data does not fit the Langmuir (1:1) model, then there are other models to derive the kinetics parameters from; heterogeneous ligand model and a bivalent analyte model for instance. The heterogeneous ligand model accounts for the presence of two species of immobilised ligand that independently bind to the injected analyte. The immobilised ligand for this model can also mean that two molecules of the same ligand on the surface of the sensor chip can have two different binding sites for the analyte. This ultimately gives the following expression, whereby two sets of bonds are formed for AB_1 and AB_2 (Figure 3.7).



B)

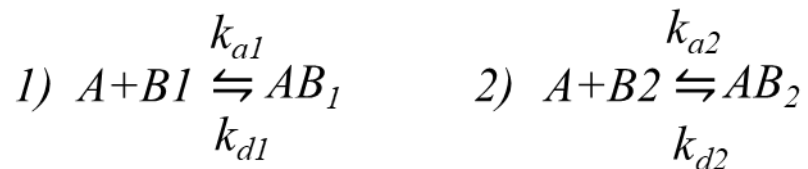
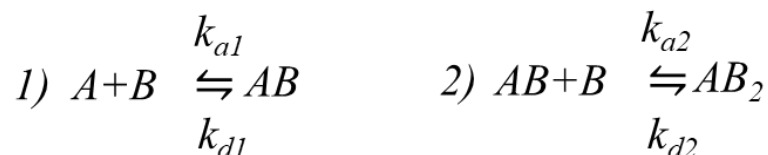


Figure 3.7: Heterogenous ligand model. This model shows one analyte binding to two immobilised ligands at two independent bonding sites. A) Diagrammatic representation and B) equation of the binding kinetics.

This model assumes that there are two association rate constants of K_{a1} and K_{a2} for complex AB_1 and AB_2 , respectively, with dissociation rate constant K_{d1} and K_{d2} .

For the bivalent analyte model ⁽²⁷⁴⁾, as the name indicates, has two regions within the analyte that can bind to one immobilised ligand on the sensor chip surface, therefore strengthening the overall binding compared to 1:1 Langmuir binding. The bivalent analyte equation to fit the model is expressed below.



The evaluation software Qdat for SensiQ Pioneer can fit data to different sites and you can chose whether the binding is 1:1, 1:2 or 1:3 for the simple (k_a , k_d) model.

3.3.0 Introduction to protein X-ray crystallography

Structural biology techniques including Nuclear Magnetic Resonance (NMR), Small Angle X-ray Scattering (SAXS), Cryonic-electron microscopy (Cryo-EM) and X-ray crystallography aim to understand the biological roles and function of macromolecules (primarily nucleic acids, polysaccharides and proteins) by determining 3D structures, shapes and dynamism of macromolecules ⁽²⁷⁵⁾.

For X-ray crystallography, crystals are required to determine structures. X-ray crystallography is a powerful technique that enables crystallographers and non-crystallographers to investigate and determine the 3D atomic and molecular structure of a crystal ⁽²⁷⁶⁾. A crystal is needed in X-ray crystallography, as diffraction from a single molecule would be too weak to be measured, while a crystal having millions or billions ⁽²⁷⁷⁾ of periodically arranged molecules would amplify the diffraction signal. A monochromatic (single wavelength) X-ray beam from a home source or most commonly synchrotron radiation (high energy electron beam) is used to expose a rotating crystal to produce diffraction patterns on a series of images recorded by X-ray detectors. The diffraction pattern from the detector are shown as arrays of spots from the diffracted X-ray beam by the crystal, and is also referred to as reflections, which have different intensities ⁽²⁷⁸⁾.

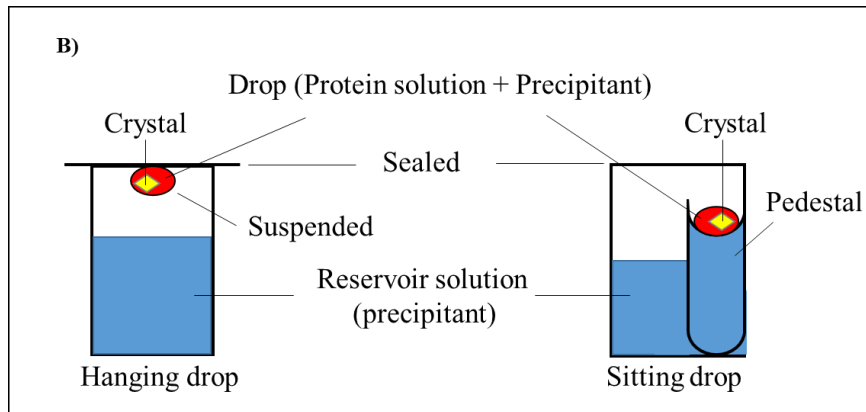
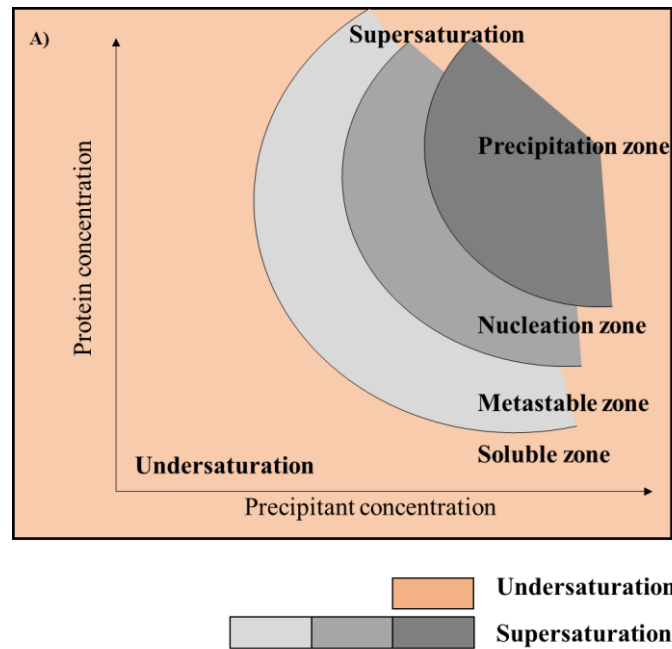
3.3.1 Protein Crystallogenesi

Crystallisation has been referred to as dark art (or dark science) as the physiochemical dictates of crystal growth are not well understood and crystal growth is to a certain extent therefore, a matter of trial and error. However, a rational approach in which a set of commercially available screening conditions for initial trial, also referred to as Sparse Matrix Screens have been formulated and developed based on previously grown crystals in various conditions. In other words, identification of the chemical, biochemical and physical conditions coupled with systematic alteration (optimisation of screening conditions) can help to yield some crystalline material ⁽²⁷⁹⁾. First and foremost, a homogeneous and properly folded protein sample in sufficient quantity (usually 2-50 mg/mL) is needed to start the crystallisation experiment. For protein crystallisation experiments, the vapour diffusion method is commonly employed and can be performed in two formats; either sitting-drop or hanging-drop format. The principle is the same for both formats and entails the use of plates such as a polystyrene MRC 2-drop plate (96-well format), in which a drop of protein solution (sample) and crystallisation solution (precipitant) in ratio of 1:1 is added onto a pedestal (or well) in the sitting-drop format. For the hanging-drop format, both protein solution and crystallisation solution on a coverslip or a transparent sealant (with a non-stick zone for the drop) is inverted thus suspended above the reservoir. Also, a reservoir solution in a chamber on the plate is filled with the crystallisation solution, which is next to the well for the sitting-drop vapour diffusion method and below for the hanging-drop.

The plate is sealed with a transparent sealant or glued coverslip to the plate in the hanging drop and subjected to temperature incubation at usually 4 °C to 20 °C to allow equilibration ⁽²⁸⁰⁾. Incubation allows vapour to diffuse out of the droplet, thereby increasing both the protein and precipitant concentration in the drop. Water diffusion from the reservoir occurs

at a slower rate. This continues till the system reaches equilibrium with no net movement of water out of the droplet and can potentially create small nuclei in the nucleation zone. For this to happen, the protein and precipitant concentrations need to be at the right level to facilitate and provide surface tension energy for protein-protein contact or nucleation ⁽²⁸¹⁾. Nuclei formation allows more protein in the drop solution to build on the already formed nuclei to allow crystal growth and ultimately lowering the protein concentration in solution during the course of crystal growth in the metastable zone ⁽²⁸²⁾ (Figure 3.8).

High protein or/and precipitant concentration coupled with incubation with high temperature can speed up the rate of diffusion and can therefore result to precipitation (precipitation zone). And the reverse is true with low protein concentrations in unfavourable crystallisation conditions that keeps the system in the clear zone (undersaturation) with no precipitate or crystal. Increasing or lowering the protein concentration can be considered when the drop (protein solution + precipitant) is clear (undersaturation) or precipitated (supersaturation), respectively ^(279, 283).



Vapour diffusion method

Figure 3.8: Phase diagram and vapour diffusion method. A) Phase diagram depicting the effect protein concentration (Y-axis) and precipitant concentration (X-axis) have on all the zones (precipitation, nucleation, metastable and soluble) as a function of time and temperature. **B)** Vapour diffusion methods (Hanging drop and sitting drop) showing a sealed system in which water diffuses into the reservoir to reach equilibrium and subsequently initiating nuclei formation (nucleation zone) and crystal (yellow diamond) growth in the metastable zone.

Ideally, nucleation cessation is preferred when crystal growth begins to prevent too many nuclei formation in the droplet with many small crystals as opposed to formation of larger and single crystals with good quality when in the metastable zone ⁽²⁷⁹⁾.

When a crystalline material is produced from the initial screening, optimisation is usually required. Optimisation is achieved in different ways and can include altering the diffusion rate by temperature, or by varying components in the crystallisation solution (pH, MPD, PEG, Salt etc.) or even adding additives to the initial condition the crystal grew in, in the hope of obtaining better quality crystal. Other variables to change during optimisation are the droplet size (protein solution + precipitant solution), protein concentration and performing seeding as all have been demonstrated to help in improving the crystal packing or crystal size thus helping in improving data quality during X-ray measurement ⁽²⁸⁴⁾. Nowadays, robotic handling for crystallisation is a common practice because it is quick and can support nanolitre volume dispensing with less error compared to pipetting smaller volumes by hand. Other crystallisation methods reported are the Microbatch, Microdialysis ⁽²⁸³⁾ and Free-interface diffusion ⁽²⁸⁵⁾. None of these three methods were used in my PhD project.

3.3.2 Harvesting and Cryocooling of crystals for X-ray diffraction experiment

Cryocooling is a well-established method that offers extension of crystal lifetime when exposed to X-ray source by greatly reducing radiation damage thus preventing degradation of data-quality ^(286, 287) by slowing down free radicals, when a crystal is cooled typically over 100 K ⁽²⁸⁸⁾. Cryocooling itself can often affect crystal data quality as a result of ice crystal formation, but adding cryoprotectant (anti-freeze agent) can suppress the formation of ice while collecting diffraction data ⁽²⁸⁹⁾. Cryoprotectants range from small polyols including

Glycerol, ethylene glycol and 2-methyl-2, 4-pentanediol (MPD) to Low-molecular-weight PEGs, is commonly used.

Glycerol (20-30%) is generally used and seem to work most of the time. Generally, the chosen cryoprotectant is added to the mother liquor the crystal grew in, allowing the crystal to be soaked into the solution prior to fishing the crystal out. A mounted nylon CryoLoop (Hampton Research Corp.) with the desired loop diameter (0.025 - 1.0 mm) is used to carefully 'fish' the crystal out and plunged it into liquid nitrogen containing a precooled metal container for transport to house the CryoLoop prior to mounting on a goniometer for X-ray beam exposure (286, 290).

3.3.3 Protein crystal and symmetry

Crystals formed by organic, inorganic compounds or proteins are regular 3D arrays of identical repeating units of molecules or molecular complexes, in which equivalent molecules interact identically with their neighbours. The basic building block or unit of the periodic arrangement of a crystal lattice is called a unit cell, which is characterised by its axes a , b , c , expressed in terms of Å and the angles (α , β , γ) between them and can be translated in 3D to generate the entire crystal lattice ⁽²⁹¹⁾. The dimensions that define a single unit cell can be used to estimate the volume of its content by calculating atoms or molecules contained in the unit cell using the Mathews coefficient program within the CCP4 suite. The fraction of a unit cell volume containing an atom, a molecule (one or more copies) or part of a molecule to generate the entire unit cell and the whole crystal lattice by applying crystallographic symmetry operations of the space group is called the asymmetric unit, which has no symmetry.

Its space group defines symmetry of a crystal lattice and the space group has an intrinsic relationship with the unit cell. The repetitive nature of the unit cell possesses symmetry within the lattice of the crystal (Figure 3.9).

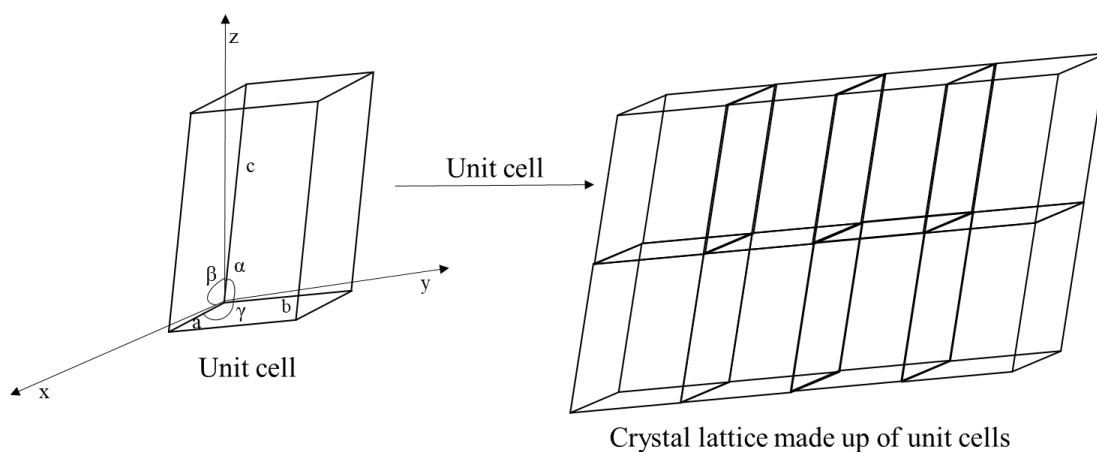


Figure 3.9: Crystal lattice made up of unit cells. Unit cell length is a , b and c with their respective angles α , β , γ . The coordinates (x,y,z) are also shown.

The conventions for choosing a crystal symmetry depending on unit cell dimensions (length of cell edges and its angles) define the 7 crystal systems (or lattice system): Triclinic, Monoclinic, Orthorhombic, Trigonal, Tetragonal, Hexagonal and Cubic. The 7 crystal systems are grouped based on their lattice system and as a result produce 14 Bravais lattices, formed by a combination of primitive lattice points and translational centering. There are 32 crystallographic point groups in the crystal lattice obtained from constraints defined by rotational symmetry operation. A combination of rotational and translational restraint for a unit cell within the crystal lattice leads to 65 chiral space groups used in crystallography ⁽²⁹¹⁾.

3.3.4 X-ray generation

X-rays have a spectrum range between 0.01 to 10 nanometers (0.1 to 100 Å) and were discovered by the German scientist, Wilhelm Conrad Röntgen, in 1895 ⁽²⁹²⁾ and has undergone significant advancements including higher brilliance. X-Ray photons for crystallography are high frequency electromagnetic rays with wavelengths typically in the range 0.5 – 4 Å.

In Crystallography, X-rays are used to characterise 3D structures of molecules or macromolecules. To generate X-rays, heated cathode filament producing electrons accelerate in a vacuum towards a rotating metal anode (i.e copper) resulting into collision with electrons on the metal anode. This causes electrons to transit from an L-shell or an M-shell to a K-shell, producing a continuous spectrum called bremsstrahlung, giving $K\alpha$ and $K\beta$ characteristic peaks at wavelengths of 0.139 nm (1.39 Å) and 0.154 nm (1.54 Å), respectively, thereby emitting electromagnetic radiation in a form of X-rays ⁽²⁹³⁾ (Figure 3.10).

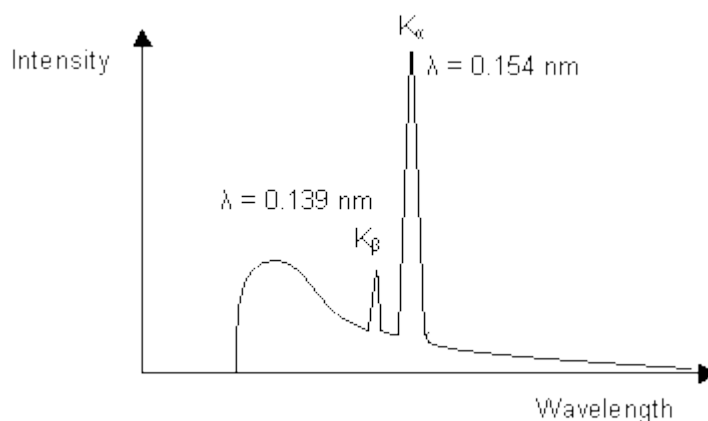


Figure 3.10: Radiation spectrum from a copper (Cu) source. Two radiation peaks at wavelengths 0.154 nm (1.54 Å) and 0.139 nm (1.39 Å) for $K\alpha$ and $K\beta$, respectively are shown as a result of copper transiting from an L-shell or an M-shell, to a K-shell. Adapted from <https://www.doitpoms.ac.uk/tlplib/xray-diffraction/production.php?printable=1>.

X-ray source from our home source (Rigaku Micromax-007) in the centre for Biomolecular Science, at the University of Nottingham has been used to test for protein diffraction and is mostly, followed by sending protein crystals to the synchrotron at usually the Diamond Light Source (DLS) in Oxford. Although, the Rigaku Micromax-007 (which has an X-ray generator) uses a microfocus rotating anode to produce a high brilliance X-ray beam, and can be used for crystal structure determination, the synchrotron radiation produces a much more intense X-ray beam and has better optical devices and software for X-ray diffraction experiments.

3.3.5 X-ray diffraction beginning with ‘history’

X-ray crystallography from which X-ray diffraction is obtain was discovered in 1914 by Max von Laue (a Nobel Prize winner in Physics) using crystalline materials. Laue developed the Laue method (used to determine the orientation of single crystals) for crystal structure analysis. A new method for looking at Laue’s method was introduced by Paul Peter Ewald in 1921 and conceived the Ewald’s sphere construction ⁽²⁹¹⁾.

William H Bragg and William L Bragg, father and son went on to solve the first X-ray crystal structure of NaCl in 1913, winning them a Nobel Prize in Physics in 1915. However, protein crystals were not solved and published by X-ray diffraction till 1958 for myoglobin (a blood protein) structure solved using a method found by Max Perutz. Max Perutz used normal crystals and heavy metal derivatives to calculate the phases of the structure factors by visualising the differences in the diffraction patterns ⁽²⁹⁴⁾.

X-rays are a form of electromagnetic waves with higher energy and can be described as a periodic function using values such as amplitude, wave velocity, phase, and wavelength.

X-ray source is needed to perform a diffraction experiment on a crystalline substance (i.e. protein crystal). Crystal diffraction is when the molecule under investigation scatters

electromagnetic radiation upon interaction with the incidence monochromatic X-ray beam. The incoming photons from the X-ray beam interact with the electrons within an atom that form the crystal, and therefore results in the electron oscillating with the same frequency as the incoming beam of X-ray. Energy is release in the form of radiation in many directions by the electrons when it returns to its ground state following electron oscillation and has the same wavelength as the initial incoming photon.

Each unit (unit cell) within the crystal lattice scatters upon photon exposure and can only diffract when scattered rays from each unit or miller planes (introduced by William Hallowes Miller in 1839) are in phase or interfere constructively to produce a strong reflection, recorded by a detector. Destructive interference on the other hand, produces no diffraction, as the scattered rays from the crystal are not on parallel planes (hkl) in a crystal lattice, thus “out of phase” to produce a reflection. The condition that must apply as defined by Bragg’s law states that scattered rays by atoms from a set of parallel planes (hkl) with interplanar lattice distance (d_{hkl}) within the crystal lattice can diffract an incoming X-ray of wavelength (λ) at an angle (θ) if the path difference $2d \sin \theta$ between reflected beam 1(R1) and 2 (R2) equal to a number of wavelengths λ (n is an integer) to produce a reflection on the detector ⁽²⁹¹⁾. X-ray diffraction can only be observed when Bragg’s law is obeyed as summarised in the following equation shown below:

$$n\lambda=2d_{hkl}\sin\theta$$

In real space, the distance (d_{hkl}) between the lattice planes, which is inversely related to the angle of the incoming incident beam is key in producing a diffraction spot (reflection) thus demonstrating Bragg’s law being satisfied ⁽²⁹¹⁾ (Figure 3.11).

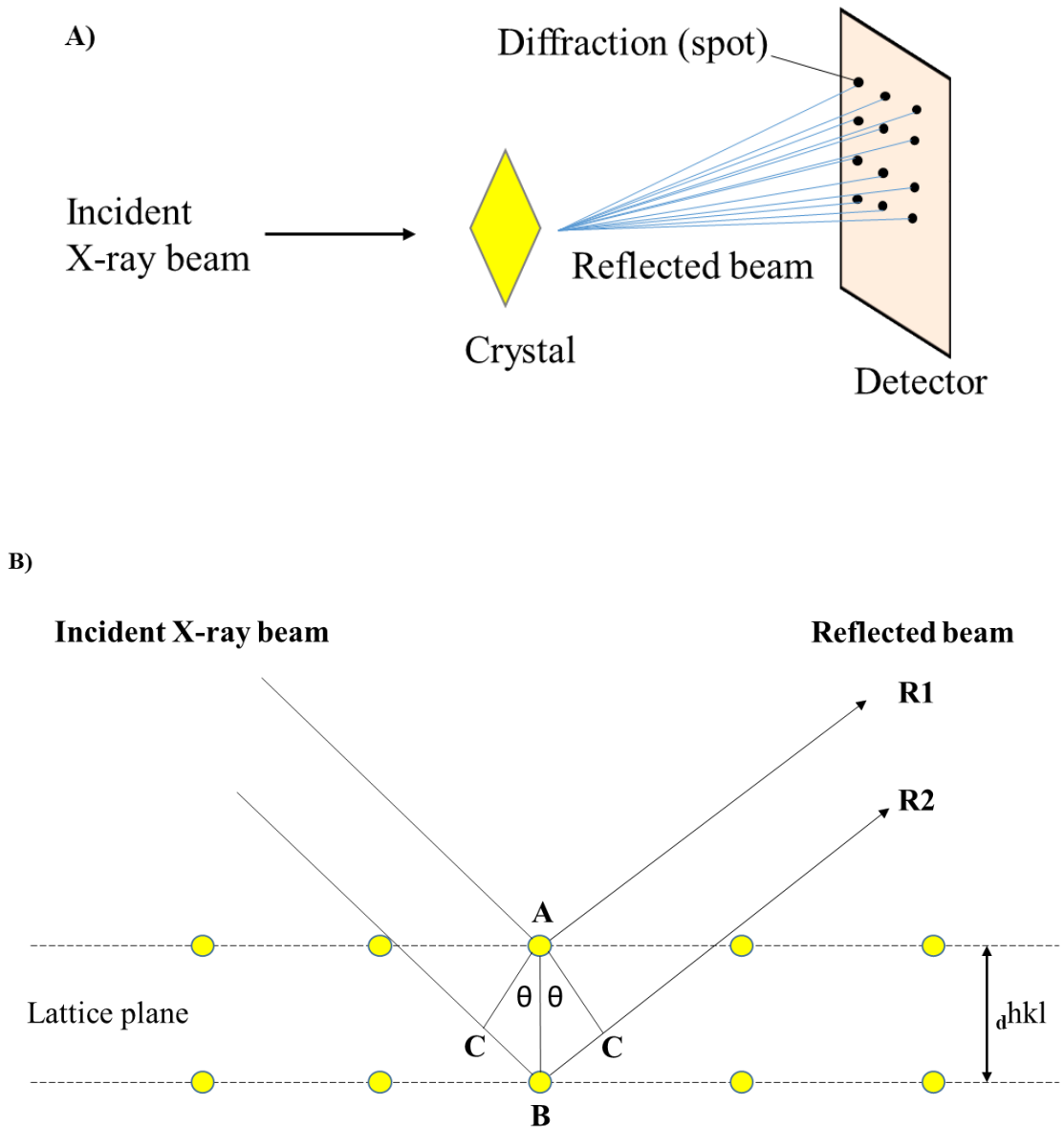


Figure 3.11: Description of Bragg's law in real space. A) Crystal (yellow) exposed to incident X-ray beam showing reflection of the X-ray beam to produce diffraction pattern (spots) recorded by the detector. B) Two sets of lattice planes are separated by an interplaner distance d_{hkl} in dashed black line parallel to each other. For diffraction to occur X-ray R2 must travel a longer distance relative to R1 to be in phase and satisfy Bragg's law ($n\lambda = 2d_{hkl}\sin\theta$).

This geometric description of Bragg's law demonstrates the relationship the lattice planes have with respect to the incident angle of the incoming X-ray beam to satisfy Bragg's law in real space. Therefore, rotating the crystal leads to Bragg's law being satisfied manifold, as the angle of the incident beam is changed when the crystal is rotated during measurement. Applying trigonometric conditions from the Ewald sphere construction can be used to consider Bragg diffraction for the reciprocal lattice for all corresponding reciprocal lattice points by applying diffraction conditions upon rotating the crystal (Figure 3.12). The real unit cell parameters can be calculated from the reciprocal cell parameters and can be determined during indexing of the diffraction pattern containing the reflections ⁽²⁹¹⁾.

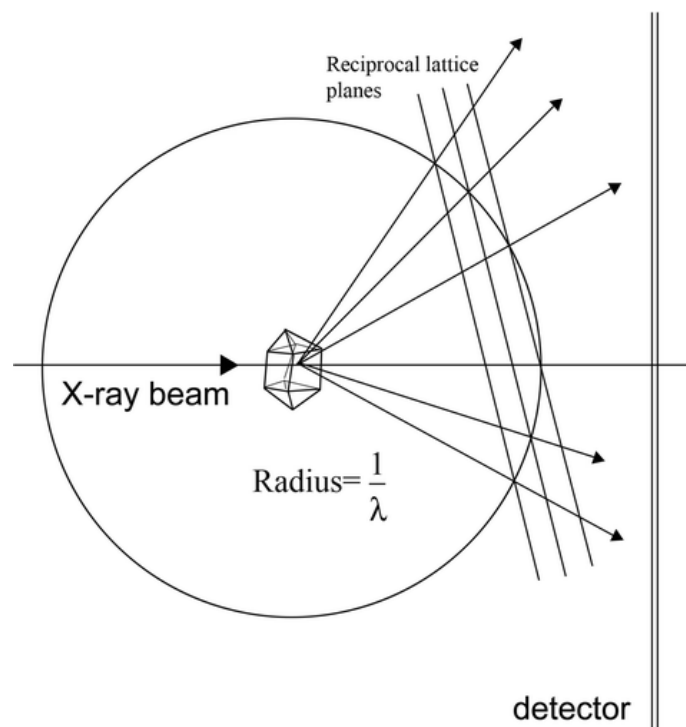


Figure 3.12: Ewalds sphere construction describing Bragg's law in reciprocal space. Adapted from ⁽²⁹¹⁾.

3.3.6 X-ray detectors

An X-ray detector records X-ray diffraction in many specific directions when a crystal is subject to a beam of incidence X-ray. The detector detects the energy of the diffracted beam from the crystal and records the relative intensity and position of every reflection in the diffraction images. Before the late 1980s and beginning of 1990s, photographic films (X-ray films) were used, but had its challenges; time consuming and slow. Although, the detectors at this time were sensitive and recorded high-resolution reflections, new detectors were needed to cope with the fast and efficient recording of reflections and data transfer. Electronically controlled imaging plates and charge-coupled devices (CCD) sped up the data-collection process, making software for data-handling, data processing and structure determination much easier. Image plates including MAR345, produced by MAR Research, and R-AXIS IV⁺⁺, developed by Rigaku were popular with time as a home-source and at synchrotron beamlines, although relatively slow readout of the plate by the scanning laser was experienced by users ⁽²⁹³⁾.

The image-plate detectors contain photosensitive material that creates colour upon exposure to X-rays, thus allowing readout as a digital image in a scanning mode with a laser. At the end of data collection with the CCD detector the diffraction data is recorded and read as electronic data by the computer to generate the diffraction pattern. CCD detectors have shorter readout of diffraction pattern compared to image plates ⁽²⁹⁵⁾. Other detectors such as the PILATUS detector are currently in use at the synchrotron such as Diamond Light Source (DLS) and has an advantage over CCD detectors due to its high speed for collecting data, short readout time of 3-5 milliseconds (ms) and good signal to noise ratio. The PILATUS detector is usually employed at synchrotron sources ⁽²⁹¹⁾.

3.4.0 Processing X-ray diffraction data

3.4.1 Indexing, Integration and Scaling of data

The diffraction images containing the geometric arrangement (crystals lattice and symmetry of the crystal) of the reflections and the intensities (content of the lattice) of the reflections, lacking the phases is indexed. A number of programs including MOSFLM or iMOSFLM (GUI version of MOSFLM) ⁽²⁹⁶⁾ within the CCP4 (Collaborative Computational Project, number 4) suite ⁽²⁹⁷⁾ is used to find the spots on the diffraction images and assign integer numbers (h, k, l = Miller Indices) with accurate crystal geometric determination for accurate integration of the intensities from the reflections⁽²⁹⁶⁾. This ultimately determines the unit cell parameters and can subsequently lead to the assignment of the Bravais lattice, using a Fast Fourier transform (FFT) of the reciprocal-space vectors in 3-dimensions ⁽²⁹⁸⁾. Following indexing, all refined and accurate determination of the unit cell parameters; the dataset (intensities of the reflections) is integrated in MOSFLM or iMOSFLM, although other programs such as XDS can also perform a similar task. Finally, downstream computer programs can be used to process the saved integrated intensities in an *.mtz output file. As the intensities in different images are not on a common scale and that potential errors can occur during data collection, scaling is performed. To improve internal consistency and maximise sufficient accurate measurements for further data processing, all the integrated values from different images (diffraction data) are combined and average into one set of structure factor and normalised using SCALA or AIMLESS programs (scaling programs) within the CCP4 suite ⁽²⁹⁹⁾.

Scaling provides useful information on the data such as the signal to noise ratio (I/σ) and associated errors in the intensities and data quality after the application of all necessary corrections ⁽³⁰⁰⁾. Furthermore, the SCALA or AIMLESS report or log file is useful to review before moving on to finding solutions for the phase problem (phase information). Values such

as the R_{merge} (known also as R_{sym}), R_{meas} (known also as R_{pim}), correlation coefficient $CC_{(1/2)}$, mean $(\langle I \rangle / \langle \sigma \rangle)$ and completeness give indications of data quality ^(293, 301).

3.4.2 Structure factors and the phase problem

During data collection, the X-ray detector can record the intensities of the reflections but not the phase. The structure factor or reflection on the images recorded can easily calculate the amplitude (related to the experimental intensity) by taking the square root of the intensity, with no phase information, as the phase is systematically lost (lost information) during the process of measurement (data collection) ⁽³⁰²⁾. The main purpose of X-ray crystallography is to determine the 3D structure of molecules or macromolecules and if the phases are known, the electron density at a position in real space $\rho(xyz)$ for the molecule in the unit cell can be calculated and reconstructed using Fourier transform (FT) on all the structure factors $F(hkl)$ ⁽²⁹¹⁾. The Patterson function introduced by Arthur Lindo Patterson, can be calculated from modifications introduced in the electron density function of the structure factor by replacing the amplitudes $[F(hkl)]$ and phases $\Phi(hkl)$ with squared amplitude as this is proportional to the intensities from the diffraction.

$$\rho(xyz) = \frac{1}{V} \sum_{hkl} |F(hkl)| \exp[-2\pi i(hx + ky + lz) + i\alpha(hkl)]$$

Each atom in the unit cell contributes to the final structure factor. The structure factor provides information that can be represented as a vector with amplitude $|F(hkl)|$ and phase $\phi(hkl)$ of a diffracted wave. To recover the lost phase information (phase problem) during the data collection, a number of methods have been developed and are instrumental in solving

the phase problem in X-ray crystallography. These methods include Isomorphous Replacement Method such as Single Isomorphous Replacement (SIR) and Multiple Isomorphous Replacement (MIR), in which heavy atoms (such as Mercury, Platinum etc.) are soaked in the crystal (i.e. protein crystal) to interact with the solvent channels for instance, without distorting the unit cell in the crystal lattice and its packing; hence, they need to be isomorphic. Max Perutz and John Kendrew applied this method in the 1960s, in which significantly higher atomic scattering factor than the carbon, oxygen or nitrogen in the protein crystal was measured. Location of the heavy atoms (i.e. Fe^{2+} , Zn^{2+}) intrinsic to proteins can also be taken advantage of to find the phases to solve the phase problem using anomalous dispersion (including single wavelength anomalous dispersion (SAD) or multiple-wavelength anomalous dispersion (MAD)). The carbon, nitrogen, and oxygen in the protein do not contribute to the anomalous dispersion when the wavelength used is closed to the absorption edge of the heavy atom. Isomorphous Replacement and anomalous dispersion methods are experimentally used to solve the phase-problem. A non-experimental approach to solve the phase problem is by Molecular replacement (MR) ^(291, 302).

Molecular replacement was developed by Michael Rossmann and David Mervyn Blow in 1962 and is a commonly used method to solve the phase problem in X-ray crystallography. This method relies on previously solved structures (i.e. nucleic acid or protein) deposited in the protein data bank (PDB) to solve the unknown crystal structure. This method takes advantage of the initial estimates of the phases from the calculated phases of the known structure (from the PDB), provided there is reasonable homology at the amino acid level between the unknown structure to be solved and the known solved structure ⁽³⁰³⁾. The PDB model used as a template to find the initial phases for the unknown structure should typically be identical (greater than 30%) in amino acid sequence to the unknown. MR works by

performing a rotational and translational function of the known structural model to find phases for the unknown crystal structure, thus providing some degree of alignment between them, depending on atom positions and orientation. Furthermore, Phaser uses the known phases from the model (known structure) in addition to the amplitudes from the diffraction of the target structure to produce an initial electron density using the equation expressed below:

$$\rho(xyz) = \frac{1}{V} \sum_{hkl} |F(hkl)_{target}| \exp[-2\pi i(hx + ky + lz) + i\alpha(hkl)_{model}]$$

Programs such as Phaser in CCP4 or in PHENIX can be used to either perform MR or experimental phasing. To run Phaser, an *.mtz output file containing the structure factor amplitudes from AIMLESS (or SCALA), amino acid sequence of the target macromolecule under examination and also the coordinates of the model or solved structure (from the PDB) are loaded in to the Phaser program. When Phaser finishes the run, it gives a solution after performing a rotational and translational function to provide a log-likelihood gain (LLG) and translation function Z score (TFZ score) values for best search of the model. The LLG gives the best match between the observed (target) and the calculated (model) values. The LLG value should be positive and the higher the better. TFZ score is recommended to be above 8, as this indicates whether the structure can be solved or not ^(304, 305).

3.4.3 Structure refinement and model building

The initial phases obtained for the crystallographic model from the molecular replacement are just an approximation of the actual phase angles, as the similarities in structure factor between initial model and the observed data may be low. Therefore, refinement of the initial

model and building (adjusting) into the electron density map to give a better convergence between the observed and calculated model is paramount to structure determination ⁽²⁹³⁾. After Phaser, followed by usually rigid body refinement, the atomic model and electron density map can be displayed for visualisation and manipulation in Coot (Crystallographic Object-Oriented Toolkit). Firstly, making sure that the protein backbone fits into the electron density map is important. Resolution and electron density map quality dictate how much detail Coot can display. Model building can be performed automatically (to build model into electron density map) using the autobuilding programs in CCP4 or PHENIX and works well for small proteins with reasonable resolution. Autobuilding can also be performed for big proteins as long as the resolution is within the limit of what the program can take. Manual building in Coot is useful and important as one can visually alter the atomic structure and refine the structure in PHENIX or use Refmac5 in CCP4 ⁽³⁰⁶⁾. The refinement uses restraints and constraints to allow adjustments of the model made to subsequently optimise the agreement between observed structure factors $|F_{obs}|$ and calculated structure factors $|F_{calc}|$. The equation below describes the agreement between the structure factors.

$$R_{factor} = \frac{\sum_{hkl} ||F_{obs}| - |F_{calc}||}{\sum_{hkl} |F_{obs}|}$$

A total agreement or perfect fit between the observed structure factors $|F_{obs}|$ and calculated structure factors $|F_{calc}|$ would have a value of 0, while a random set of atoms used as a search model will give an R -value of about 0.60. Usually, a typical model that has been completely solved will have a final value ranging between 0.16 - 0.25, depending on

data quality and resolution. Although, the R factor provides a measure of quality of a structure, it can over fit thus decreasing the R factor and as a result introduces bias in the model. To avoid this another set of R value, known as R free is used and has proved to be an indicator for unbiasedness in the refinement process. For this, 5-10 % of the reflection data (experimental data) is used as a test set, which is not included in the refinement process at all (293).

$$R_{free} = \frac{\sum_{hkl} |F_{obs}| - |F_{calc}|}{\sum_{hkl} |F_{obs}|}$$

Both R -values (R factor and R free) are used to assess the quality of the data under examination during the refinement process (291). Other indicators used to validate structural models include the use of the Ramachandran plot (developed by Gopalasamudram Ramachandran in 1963) for checking the stereochemistry of the main chain. The Ramachandran plot validates based on geometric condition by focusing on dihedral angles ψ against ϕ of amino acid residues in protein structures (307, 308).

CHAPTER 4.0

STRUCTURAL STUDIES OF THE FXII F_nII DOMAIN

4.1 Structural determination of human FXII FnII

4.1.1 Preparation of FXII constructs for expression in bacteria and insect cells

Genes for human FXII FnII-EGF1 and human FXII FnII were PCR amplified to contain restriction enzyme sites (REs), BglII and MluI, giving a product size of 0.327 and 0.213 kb, respectively as shown in the agarose gel (Figure 4.1A). Additionally, XbaI and HindIII REs in FXII FnII-EGF1 and FXII FnII (Figure 4.1B) were also produced and subsequently cloned into the pMALX (E)-MBP plasmid vector, while FXII FnII-EGF1 and FXII FnII containing BglII and MluI REs were cloned into the pMT-PURO plasmid vector.

A FXII FnII fusion protein designated HisTrx-FXII FnII in pOPINTRX plasmid vector, made by Pascal Wilmann (Ex-Postdoc in Prof. Emsley's lab) at the Oxford Protein Production Facility (OPPF), UK, was also used for expression in Rosetta-gami2 cells. This *E.coli* strain is reported to enhance protein expression and aid in disulfide bond formation compared to other *E.coli* strains such as BL21.

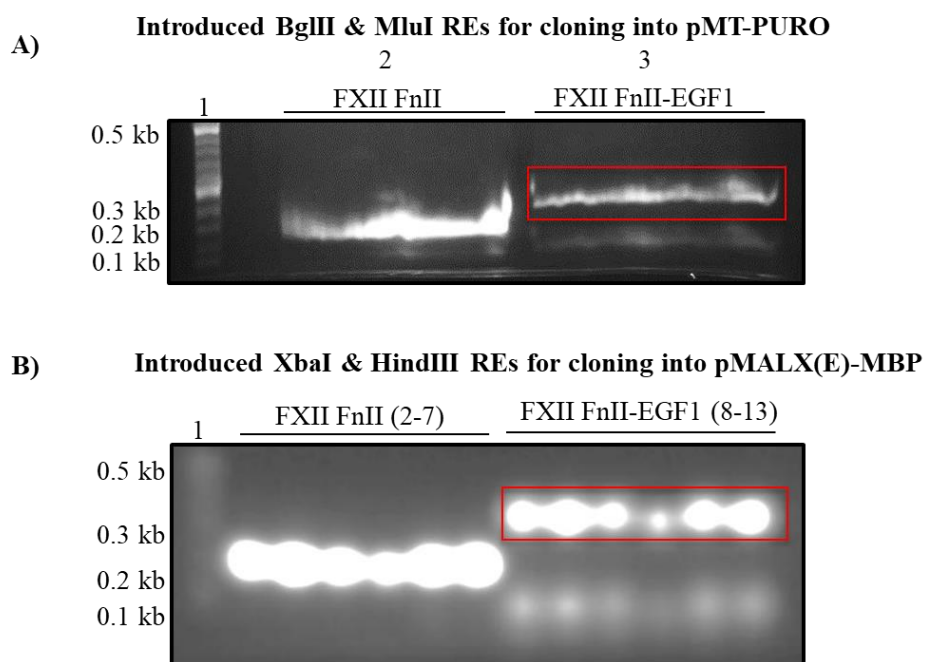


Figure 4.1: Agarose gel electrophoresis of FXII constructs after PCR amplification. A) Amplified human FXII fragments (FXII FnII and FXII FnII-EGF1) with BglII and MluI REs in lanes 2 and 3 using pCI-neo-FXII template. This produced DNA fragment sizes of 0.213 and 0.327 kb for FXII FnII and FXII FnII-EGF1, respectively. **B)** Introduction of XbaI and HindIII REs in FXII FnII and FXII FnII-EGF1 DNA sequence in lanes 2-7 and 8-13, respectively. Ladder size range from 0.1 -0.5 kb.

All recombinant plasmids of FXII and plasmid vectors (appendix chapter 10.0) described in Figure 4.2 were analysed by agarose gel electrophoresis following restriction double enzyme digest to generate a linearised plasmid vector (pMALX (E)-MBP or pMT-PURO) and insert (FXII FnII-EGF1 or FXII FnII), shown in Figure 4.2A-B. Figure 4.2 shows bands of FXII FnII-EGF1 and FXII FnII to migrate around 0.327 kb and 0.213 kb, respectively thus confirming successful cloning of FXII constructs. Furthermore, DNA sequencing confirmed all FXII inserts were successful ligated into their respective plasmid vectors and this was in conformity with the double bands for plasmid vector and insert shown on the agarose gel electrophoresis analysis in Figure 4.2A and 4.2B.

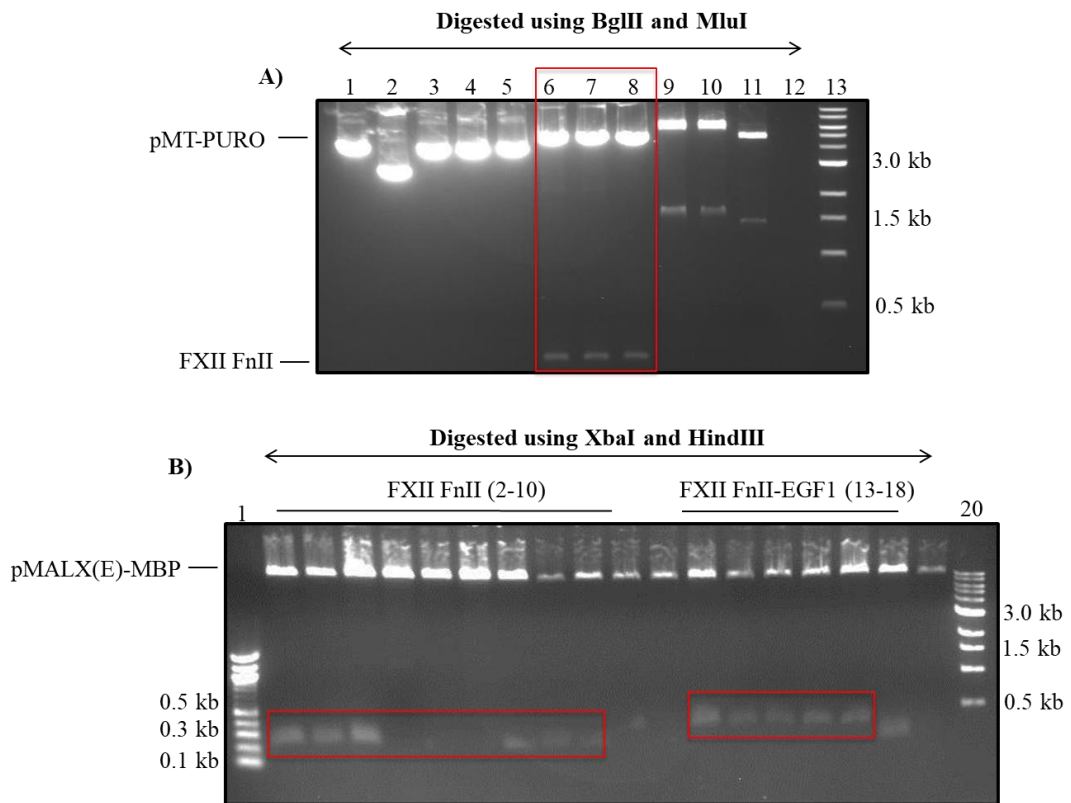


Figure 4.2: Agarose gel electrophoresis of restriction double digest of expression plasmid vectors containing FXII FnII and FXII FnII-EGF1. **A)** FXII FnII in lanes 6, 7 and 8 migrated around 0.213 kb. **B)** DNA fragments corresponding to sizes 0.213 for FXII FnII (lanes 2-10) and 0.327 kb for FXII FnII-EGF1 (lanes 13-18) digested with XbaI and HindIII are shown highlighted with a red box. A high molecular weight band corresponding to plasmid vectors pMT-PURO and pMALX(E)-MBP are also shown.

4.1.2 Expression and purification of untagged human FXII FnII-EGF1 and FXII FnII in drosophila S2 cells (insect cells)

Untagged human FXII FnII-EGF1 (residues 1-109) and FXII FnII (residues 1-71) transfected and expressed in drosophila S2 cells were successfully captured and eluted on an Affinity (Ni^{2+}) chromatography column following ammonium sulfate (AmSO_4) precipitated. Figure 4.3A displays peaks 1 and 2 following elution with Imidazole.

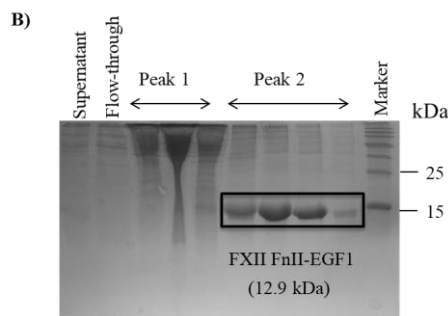
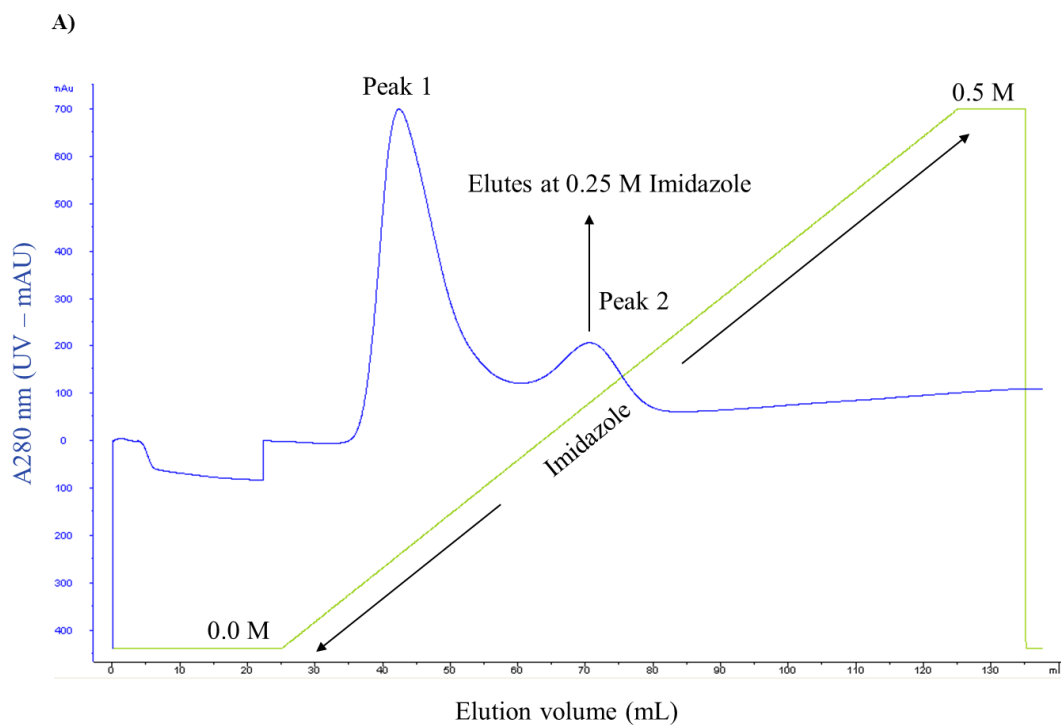


Figure 4.3: Affinity (Ni^{2+}) chromatography and SDS-PAGE gel analysis of FXII FnII-EGF1. A) Shows the affinity (Ni^{2+}) chromatographic profile with peaks 1 and 2 from the Imidazole elution and subjected to B) SDS-PAGE gel from peak 2 identifies FXII FnII-EGF1 which migrated at a molecular weight of around 12.9 kDa.

FXII FnII-EGF1 was eluted with 0-1 M Imidazole gradient concentration. Peaks 1 and 2 are analysed on an SDS-PAGE gel showing the FXII FnII-EGF1 band to migrate close to the 15 kDa marker band. FXII FnII-EGF1 has a molecular weight of 12.9 kDa when calculated using the FXII FnII-EGF1 amino acid sequence in ExPasy protparam. Next, a homogeneous and pure sample of FXII FnII-EGF1 was obtained from size exclusion chromatography showing 2 distinct peaks (peak 1 and peak 2). Figure 4.4A shows proteins in peak 1 to elute in the void (47 mL), while peak 2 elutes at a volume of 82 mL thus separating FXII FnII-EGF1 from the higher molecular weight bands to produce monodisperse peak (peak 2) as shown in Figure 4.4A. The SDS-PAGE gel for peak 2 from the size exclusion chromatography showed a pure FXII FnII-EGF1 band (Figure 4.4B). Pooled fractions under peak 2 from the size exclusion chromatography yielded a protein concentration of 5.4 mg/mL for FXII FnII-EGF1.

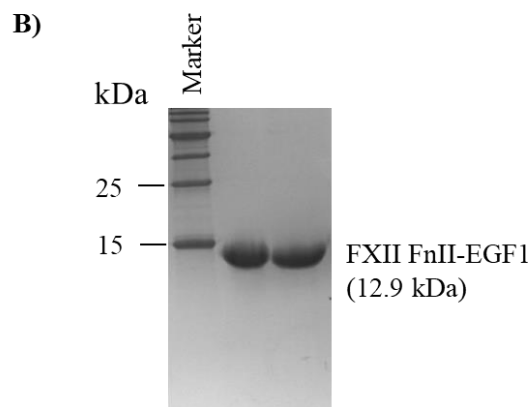
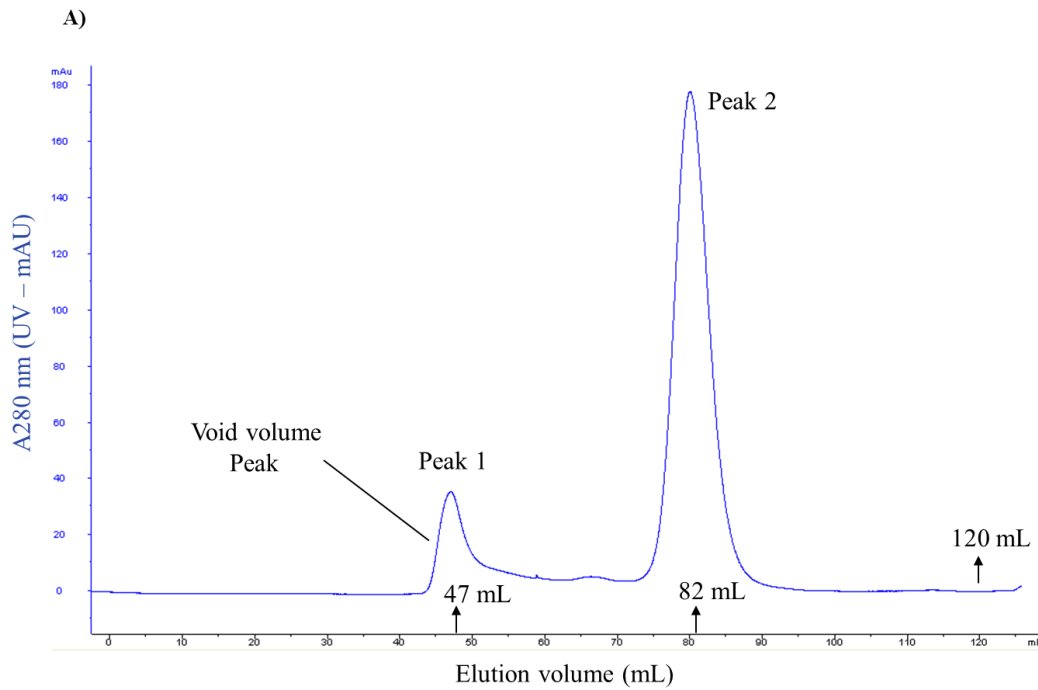


Figure 4.4: Size exclusion chromatographic and SDS-PAGE gel analysis of FXII FnII-EGF1. **A)** Peak 2 from the affinity (Ni^{2+}) chromatographic pooled and concentrated fractions was isolated using size exclusion chromatography as shown in peak 1 for the void and peak 2 for FXII FnII-EGF1 eluting as a monodisperse around 82 mL. **B)** Fractions from peak 2 in figure A was run on 20 % SDS-PAGE gel showing a pure band.

For FXII FnII, only 1 broad peak was shown to be eluting from the Affinity (Ni^{2+}) chromatography column and analysed on SDS-PAGE gel, although overloaded with protein, shows FXII FnII protein to be overexpressed (Figure 4.5A). Similar to FXII FnII-EGF1, FXII FnII

purity was achieved following size exclusion chromatography and shows a monodisperse peak eluting around 92 mL (Figure 4.5B). The FXII FnII migrates on the SDS-PAGE gel close to 10 kDa (Figure 4.5B), although calculated from ExPASy protparam to have a molecular weight of 8.5 kDa from its amino acid sequence.

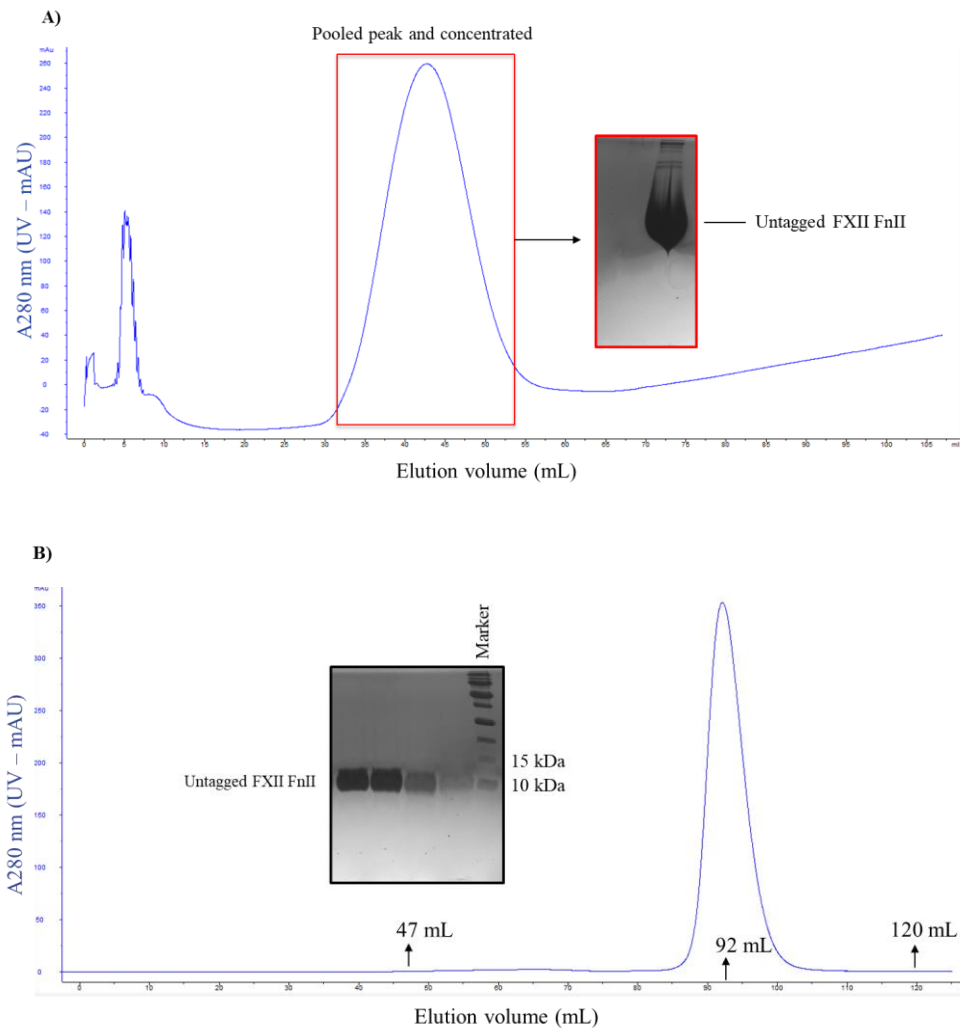


Figure 4.5: Chromatographic and SDS-PAGE gel analysis of FXII FnII. A) A broad peak from the Affinity (Ni^{2+}) chromatography was pooled and concentrated followed by SDS-PAGE gel analysis which showed an overexpressed FXII FnII band with higher molecular weight bands (contaminants). Further purification was performed using size exclusion B) in which a single monodisperse peak eluting around 92 mL is shown as a pure FXII FnII band on SDS-PAGE gel.

4.1.3 Expression and purification of WT HisTrx-FXII FnII in Rosetta-gami2

From the trial expression, WT HisTrx-FXII FnII gave a better yield than WT HisTrx-FXII FnII-EGF1 in Rosetta-gami2 cells and a decision was made to continue and express WT HisTrx-FXII FnII instead. Soluble and pure WT HisTrx-FXII FnII was obtained following purification and to explore whether FXII FnII can be separated from the HisTrx tag, trial cleavage with 3C HRV enzyme was performed. Figure 4.6 demonstrates successful cleavage of WT HisTrx-FXII FnII in 3 different ratios of 3C HRV enzyme by cleaving the following sequence (Leu-Glu-Val-Leu-Phe-Gln*Gly-Pro) linking HisTrx and FXII FnII. Figure 4.6A-B shows ratios 1:100 and 1:200 to completely cleave the cleavage sequence of WT HisTrx-FXII FnII after 1 hour of treatment, while reducing the amount of 3C HRV enzyme in the reaction to give a ratio of 1:500 achieved complete cleavage after almost 3 hours of treatment (Figure 4.6C).

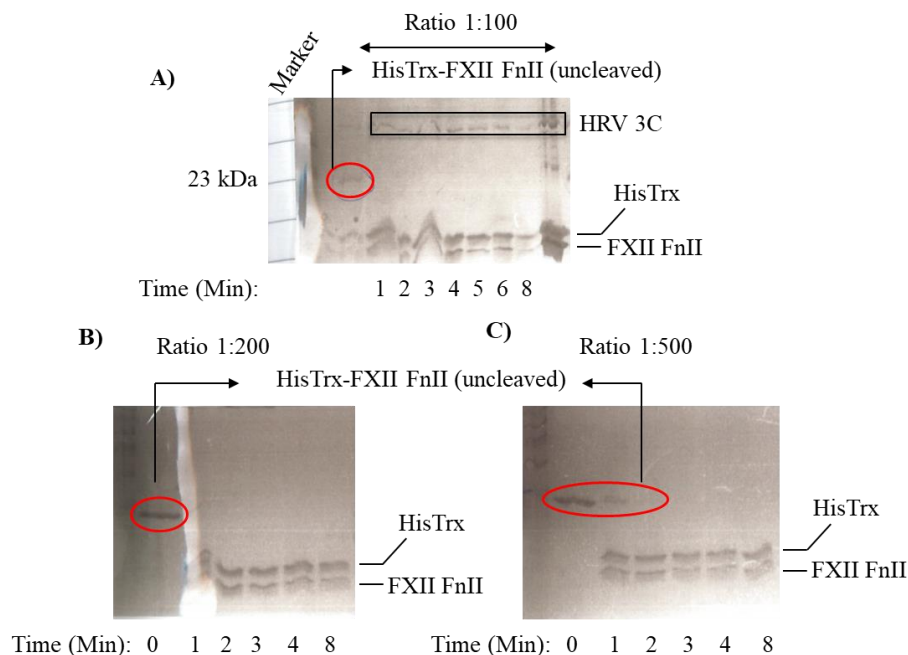


Figure 4.6: SDS-PAGE gel analysis of WT HisTrx-FXII FnII cleavage assay using HRV 3C enzyme. Weight for weight ratios of HRV 3C protease and HisTrx-FXII FnII for **A)** 1:100, **B)** 1:200 and **C)** 1:500) following a time course (0-8 hours) produced two protein bands corresponding to HisTrx (12.5 kDa) and FXII FnII (8.5 kDa) compared to uncleaved at time 0.

Establishing WT HisTrx-FXII FnII cleavage by 3C HRV allowed for all future cleavages of large-scale expression WT HisTrx-FXII FnII to be performed with ratios between 1:200 and 1:500. Figure 4.7 shows the large-scale expression of WT HisTrx-FXII FnII in affinity (Ni^{2+}) chromatography (Figure 4.7A) and size exclusion chromatography (Figure 4.7B). Cleavage of WT HisTrx-FXII FnII is shown in Figure 4.7C and was further separated using ion-exchanger chromatography (Resource S) showing bands of FXII FnII (8.5 kDa) and HisTrx (12.5) as shown in Figure 4.7D.

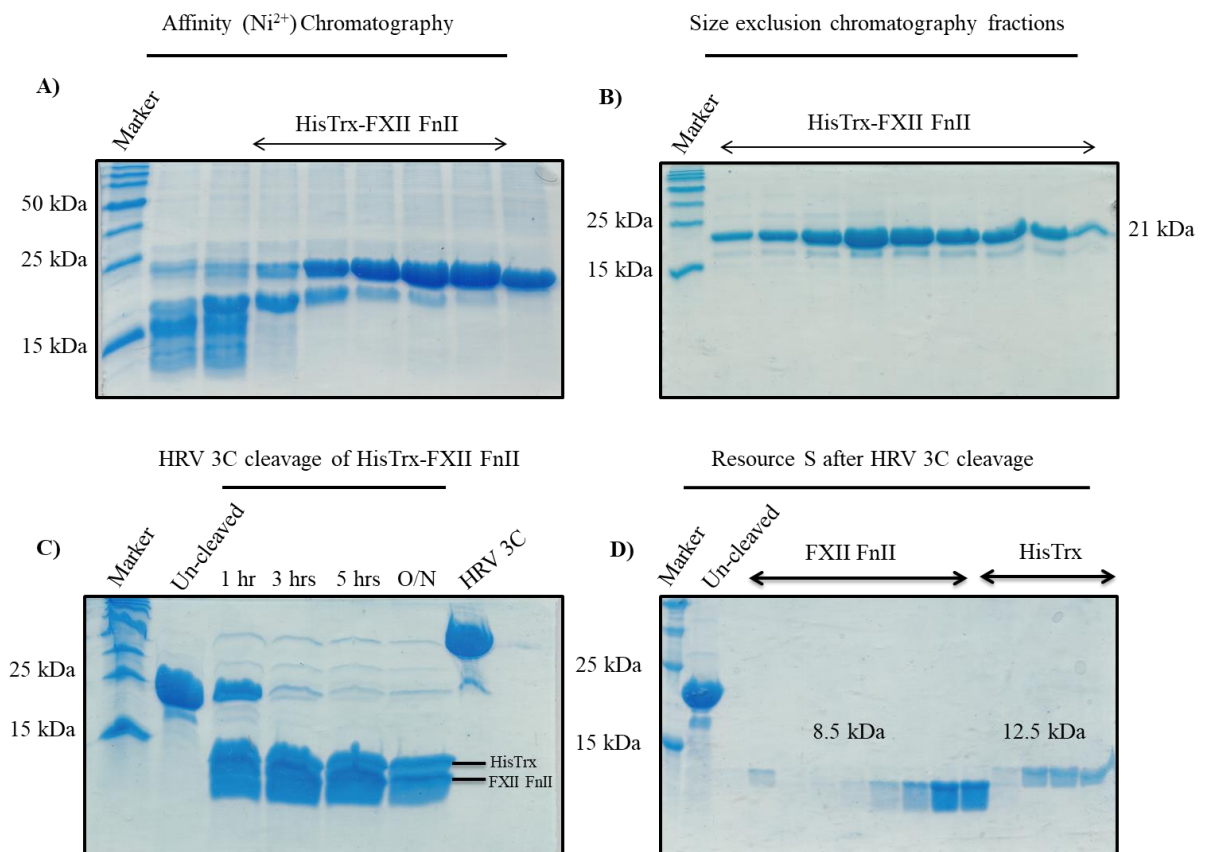


Figure 4.7: SDS-PAGE gel (20 %) analysis of WT HisTrx-FXII FnII. HisTrx-FXII FnII purification from **A)** Affinity (Ni^{2+}) chromatography, **B)** Size exclusion chromatography. **C)** WT HisTrx-FXII FnII was subjected to HRV 3C protease cleavage at a ratio of 1:250 HRV 3C and HisTrx-FXII FnII. **D)** Cleaved HisTrx-FXII FnII was separated using ion-exchange chromatography (Resource S).

As untagged FXII F_{NI} was successfully captured and purified using Affinity (Ni²⁺) chromatography, as shown in Figure 4.5A and FXII F_{NI} suggested in the literature to bind to Zn²⁺, the captured cleaved HisTrx and FXII F_{NI} sample from WT HisTrx-FXII F_{NI} on the Affinity (Zn²⁺) chromatography produced 2 peaks (peak 1 and peak 2) following elution (Figure 4.8A). Figure 4.8B shows loaded fractions from peak 1 and peak 2 of the Affinity (Ni²⁺) chromatography on an SDS-PAGE gel. Bands for peak 1 corresponds to FXII F_{NI}, while bands from peak 2 corresponds to HisTrx. This therefore demonstrates that Affinity (Zn²⁺) chromatography can separate the cleaved HisTrx-FXII F_{NI} mixture. The FXII F_{NI} from peak 1 was demonstrated to be soluble and folded as it eluted at the correct elution volume as the insect expressed untagged FXII F_{NI} on size exclusion chromatography.

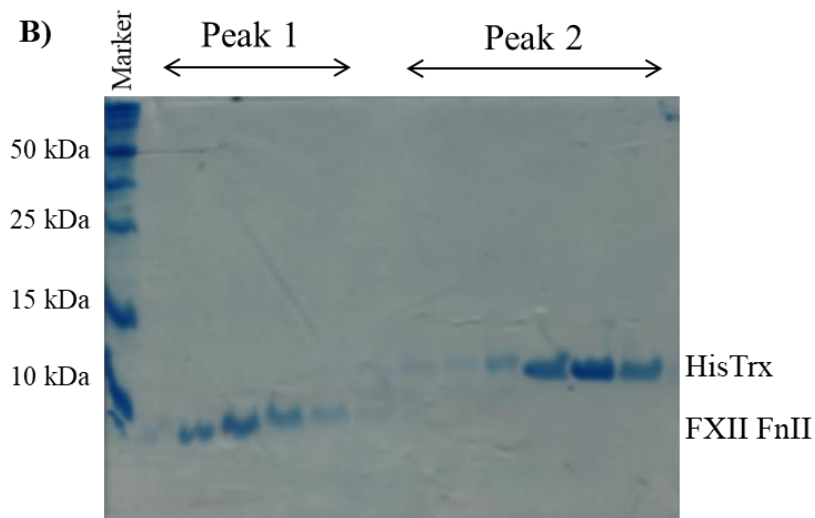
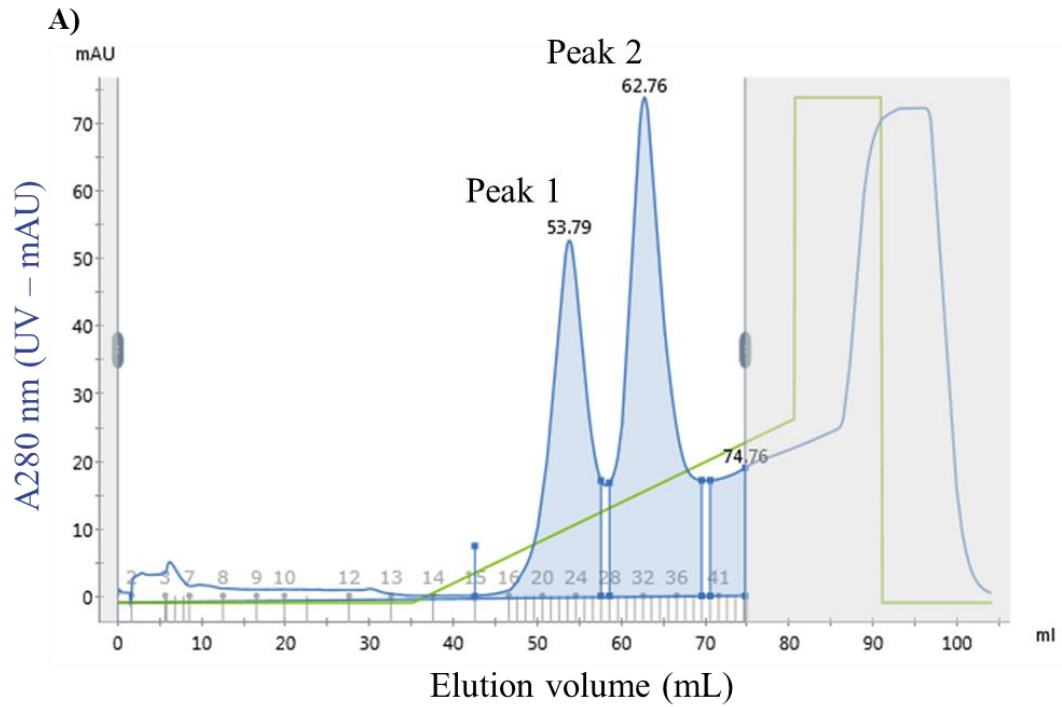


Figure 4.8: WT HisTrx-FXII FnII purification following HRV 3C cleavage. **A)** Peaks 1 and 2 from the Affinity (Zn^{2+}) chromatography purification were subjected to **B)** SDS-PAGE gel with peak 1 migrating around 8.5 kDa for FXII FnII and peak 2 for HisTrx (12.5 kDa) having a slighter higher molecular weight than FXII FnII.

4.1.4 Expression and purification of HisTrx-FXII FnII mutants

As it is quicker to express FXII FnII with two intramolecular disulphide bonds for correct folding in rosetta-gami2 cells in comparison to insect cells, a number of FXII FnII mutants were generated using the WT HisTrx-FXII FnII as a template. All mutants were made based on the crystal structure of FXII FnII bound gC1q-R and were to be tested for binding to gC1q-R using SPR.

All HisTrx-FXII FnII mutants were successfully sequenced thus identifying desired changes in the DNA sequence prior to expression. Similar to WT HisTrx-FXII FnII, Figures 4.9 shows successful 3C HRV enzyme cleavage analysed on SDS-PAGE gels for HisTrx-FXII FnII Arg65Ala, HisTrx-FXII FnII Arg36Ala and HisTrx-FXII FnII Asp63Ala/Gln64Ala/Arg65Ala following affinity (Zn^{2+}) chromatography. Two peaks (peak 1 and peak 2) were produced for all mutants and analysed on SDS-PAGE gel, demonstrating separation of FXII FnII variants and HisTrx from cleaved HisTrx-FXII FnII mixture.

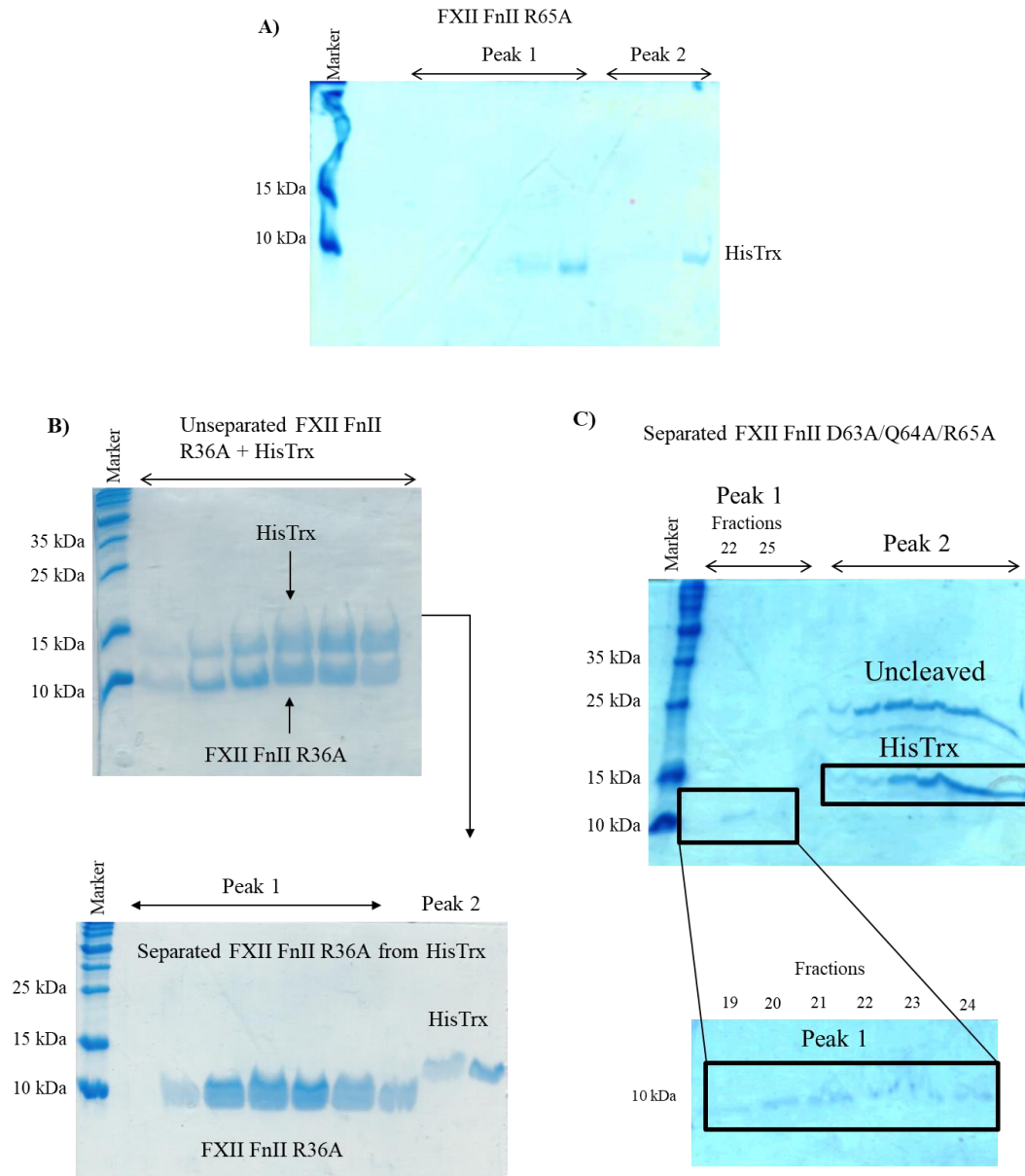


Figure 4.9: Mutant HisTrx-FXII FnlI purification following HRV 3C cleavage. **A)** Cleavage of HisTrx-FXII FnlI Arg65Ala to HisTrx and FXII FnlI Arg65Ala shown in peaks 1 and 2, respectively. **B)** Cleaved fragments from HisTrx-FXII FnlI Arg36Ala were unable to be separated on an affinity (Ni^{2+}) column and was subsequently loaded onto an affinity (Zn^{2+}) column instead. FXII FnlI Arg36Ala was successfully separated as shown in the peaks 1 and 2 on the SDS-PAGE gel. **C)** HisTrx-FXII FnlI Asp63Ala/Gln64Ala/Arg65Ala mutant cleavage did not go to completion as shown in the upper band (labelled uncleaved) in peak 2. Incomplete cleavage of FXII FnlI Asp63Ala/Gln64Ala/Arg65Ala is shown in peak 1 and to further confirm this, samples in peak 1 were rerun on SDS-PAGE gel as indicated in the highlighted black box from fractions 19-24.

4.2.0 Crystallisation of human FXII FnII in the presence of Zn²⁺

4.2.1 Crystallisation of human FXII FnII

As there is no 3D structure of FXII FnII in isolation or bound to Zn²⁺, initial crystallisation experiments for untagged FXII FnII (aa 1-71) and FXII FnII-EGF1 (aa 1-109) proteins at concentrations of 6.06 mg/mL and 5.4 mg/mL for FXII FnII and FXII FnII-EGF1, respectively produced both single plate and clustered needle-like crystals (Figure 4.10A-D). These crystals grew in the JCSG+, Pi-PEG and PACT screens with crystals from the PACT screen producing bragg diffraction (Figure 4.10E) when tested on the home source (*Rigaku Mibromax-007 X-ray generator*).

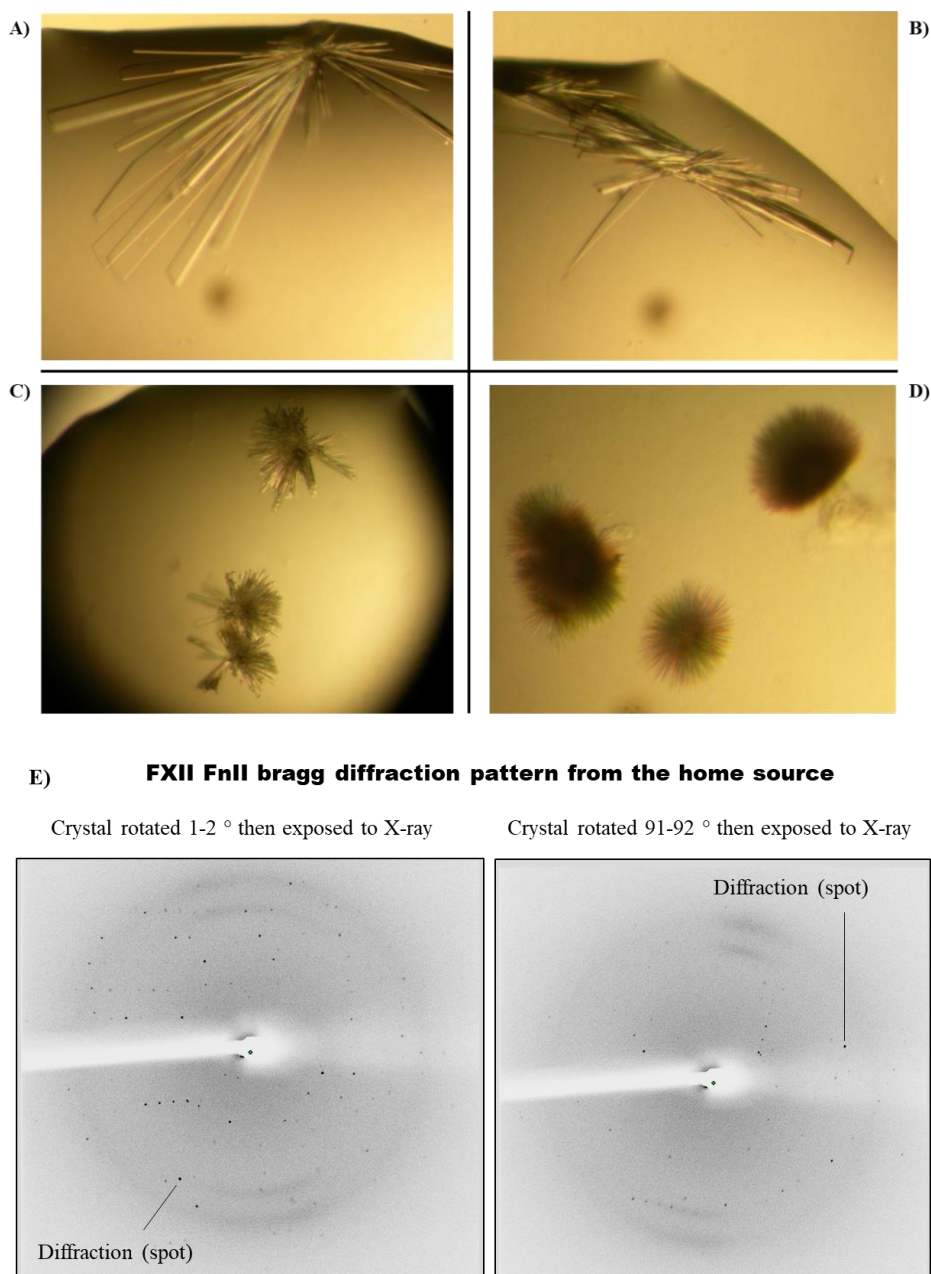


Figure 4.10: FXII FnlI crystals and diffraction pattern. **A)** Plate crystals obtain from the PACT screen in 0.01 M Zn^{2+} , 0.1 M Sodium acetate pH 5.0, 20 % (w/v) PEG 6000. **B)** Plate like crystals were also observed in the JCSG+ screen in 0.2 M $Zn(CH_3CO_2)_2$, 0.1M Sodium acetate pH 4.5, 1M di-ammonium hydrogen phosphate. **C)** More crystal growth from the JCSG+ screen in a condition with 0.2 M $Zn(CH_3CO_2)_2$, 0.1 M Sodium cacodylate pH 6.5, 10 % (v/v) 2-propanol is shown and **D)** no Zn^{2+} in the Pi-PEG screen produced needle-like crystal clusters in 0.05 M MES pH 6.0, 40 % PEG MME 350. **E)** Diffraction pattern of FXII FnlI from the home source (Rigaku Mibromax-007 X-ray generator) at different angles (1-2 ° and 91-92 °).

Crystals with a plate-like morphology were observed for the JCSG+ and PACT screens, while clustered needles-like crystals from the Pi-PEG screen. Crystals from the PACT and JCSG+ screens in conditions highlighted in the Figure 4.10 were sent to both the DLS and ESRF, with the crystals from the PACT screen producing high-resolution data at 1 Å (data cut down to 1.2 Å). The table below (Table 4.1) presents data collection statistics for FXII F_{hII} crystals from PACT and JCSG+ following data reduction (diffraction data processing). Henceforth, form 1 will represent FXII F_{hII} from the PACT condition, while form 2 for FXII F_{hII} from the JCSG+ condition.

Table 4.1. Crystallographic data collection statistics.

Sample	<i>FXII-Zn²⁺ (form 1)</i>	<i>FXII-Zn²⁺ (form 2)</i>
Data collection		
<i>Space group</i>	P2 ₁ 2 ₁ 2 ₁	P2 ₁ 2 ₁ 2 ₁
<i>Cell dimensions a, b, c (Å)</i>	26.3, 40.8, 45.3	26.2, 40.7, 45.2
<i>α, β, γ (°)</i>	90, 90, 90	90, 90, 90
<i>Resolution (Å)*</i>	30.36-1.2	30.27-2.0
<i>R_{merge} † (%)*</i>	12.1(39.5)	11.6(24.6)
<i>Mean I / sigI*</i>	7.13 (4.09)	5.68 (2.95)
<i>Completeness (%)*</i>	97.46 (96.51)	95.03 (97.41)
<i>Redundancy*</i>	4.5(4.6)	3.5(3.7)
<i>CC1/2 †</i>	0.993(0.822)	0.988(0.944)

**Values in parentheses are for highest-resolution shell.*

The data collection statistics show the unit cell parameters for an orthorhombic space group with a screw axis (P2₁2₁2₁) as well as other important statistics including the CC_{1/2}, Mean $|I|/\sigma|I|$ and redundancy values for crystal forms 1 and form 2.

To solve the phase problem following data reduction, molecular replacement was performed and for form 1 a top LLG value of 2455.4 and TFZ score of 33 was reported, while form 2 gave a solution of 1280.9 for the LLG and a TFZ score of 8.9. The pdb and mtz output files generated from the Phaser program were built and refined to acceptable bond lengths and angles with no outliers and more than 98 % of FXII F_{II} amino acid residues in the favoured regions as shown in the refinement statistics table 4.2.

Table 4.2. Crystallographic refinement statistics.

Sample	FXII-Zn ²⁺ (form 1)	FXII-Zn ²⁺ (form 2)
Refinement		
<i>Number of reflections</i>	70131	11953
<i>R_{work} / R_{free}</i>	17.3/22.5	017.2/19.7
<i>B-factors (Å²)</i>		
<i>Protein</i>	14.5	23.4
<i>Ligands</i>	21.0	48.6
<i>R.m.s. deviations</i>		
<i>Bond lengths (Å)</i>	0.0076	0.0079
<i>Bond angles (°)</i>	1.073	1.030
<i>Ramachandran plot</i>		
<i>Favoured (%)</i>	98.11	98.1
<i>Outliers (%)</i>	0	0

$R_{work} = \text{Sum}(h) \left| |F_o|/h - |F_c|/h \right| / \text{Sum}(h)|F_o|/h$, where F_o and F_c are the observed and calculated structure factors, respectively. R_{free} computed as in R_{work} , but only for (5%) randomly selected reflections, which were omitted in refinement, calculated using PHENIX.

4.2.2 Crystal structure of FXII FnII bound to Zn²⁺

Figure 4.11 shows 3 Zn²⁺ ions bound to both forms (form 1 and form 2) of the FXII FnII crystal structure, despite 10 mM of Zn²⁺ present in the crystallisation conditions for the PACT condition in form 1 and 200 mM Zn²⁺ for the JCSG+ condition in form 2. The 3D crystal structures for form 1 and form 2 of FXII FnII are identical as shown in the overlay with the RMSD value. The FXII FnII structure displays two anti-parallel β -sheets while an additional anti-parallel β -sheet is formed by a β -sheet from the FXII FnII and part of the N-terminal peptide upstream of the FXII FnII domain.

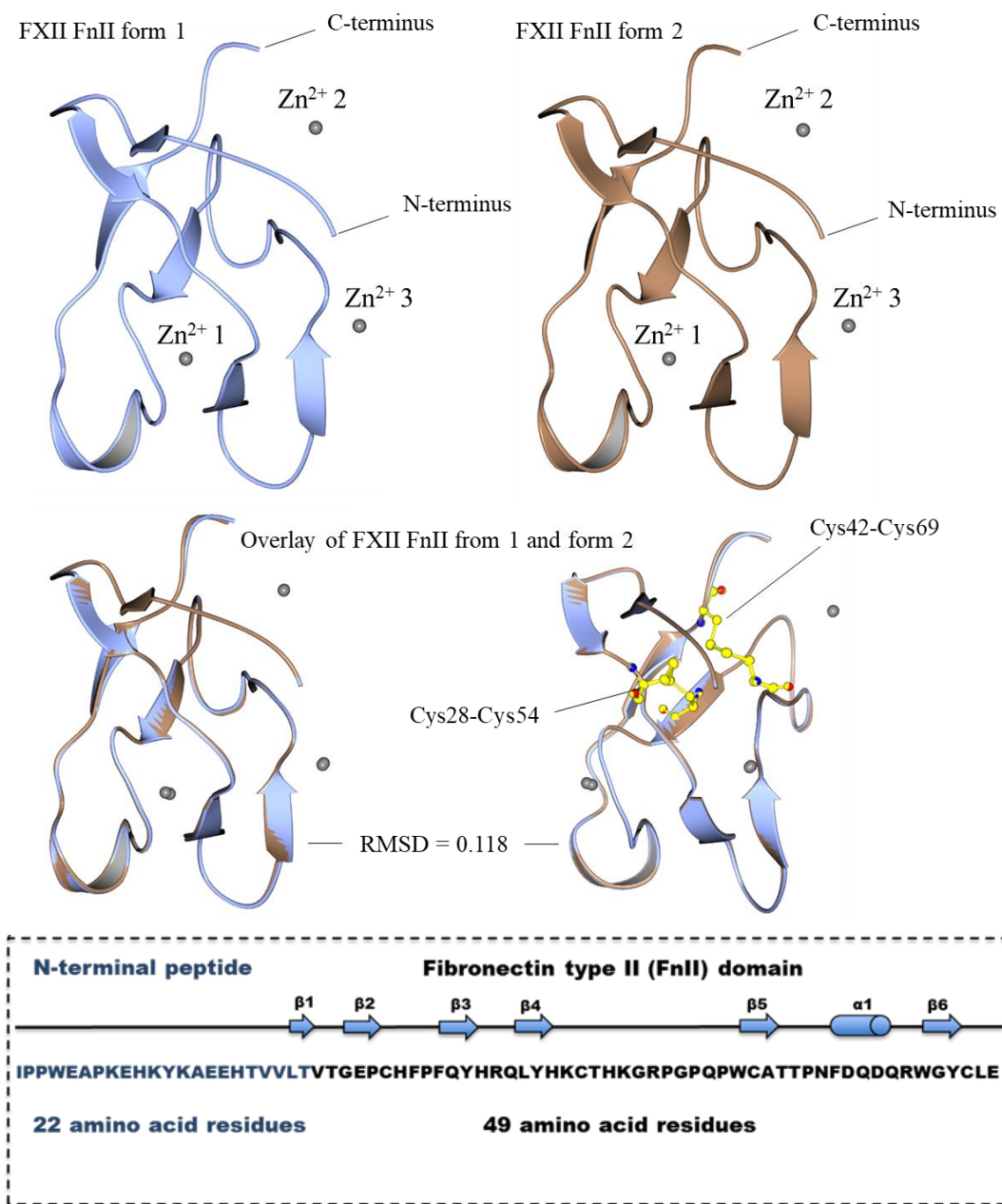


Figure 4.11: FXII FnlI bound Zn²⁺ crystal structure. Crystal structures from conditions in the PACT (Ice blue) and JCSG+ (Pale brown) screens. Both structures are bound to three Zn²⁺ (Grey) and the structural superposition (overlay) in the bottom structure shows that the two structures are the same with Zn²⁺ ions (Grey) at a similar position too. Disulphide bonds (balls and stick) are shown in yellow between Cys28-Cys54 and Cys42-Cys69. A secondary structure of the human FXII FnlI with N-terminal (22 residues) is also shown.

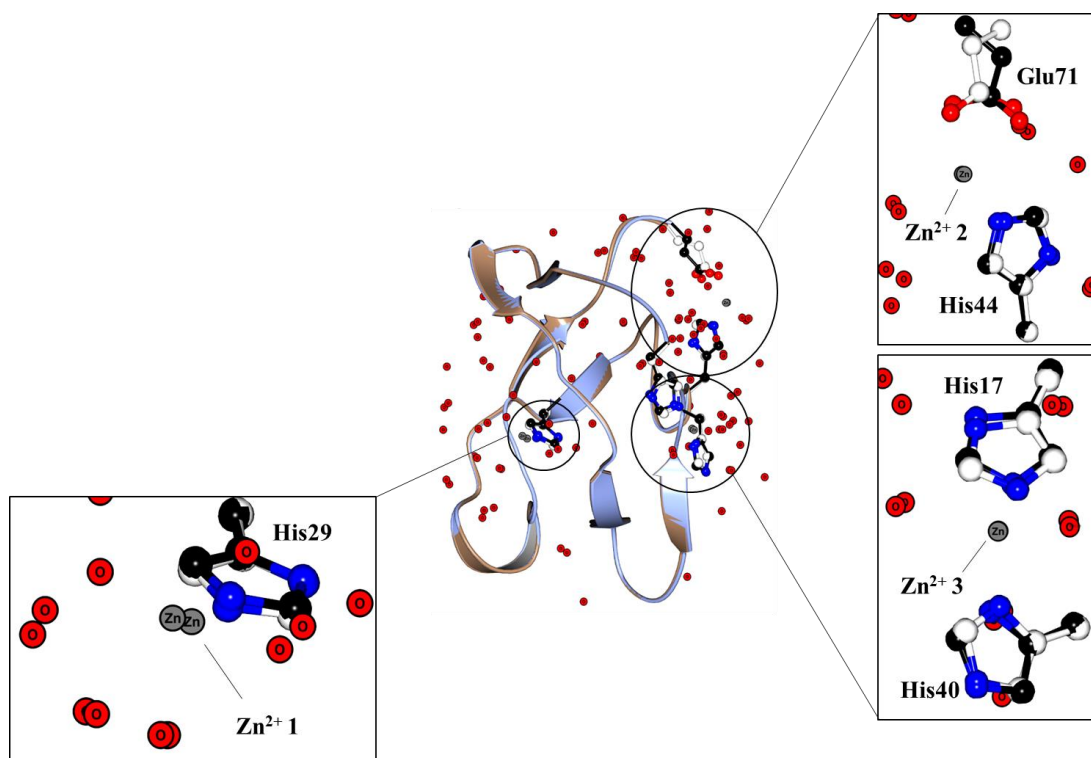


Figure 4.12: Zn^{2+} sites on FXII FnlI. Residues involved in Zn^{2+} (Grey) coordination are also shown in ball and stick overlaid FXII FnlI (form 1) in ice blue and FXII FnlI (form 2) in pale brown with solvent showing water molecules displayed in spheres of oxygen labelled by o. Images were made using QtMG.

Zn^{2+} is located on the same FXII FnlI site for both structures (form 1 and 2) with the same amino acid residues engaged in the coordination plus the solvent contributing in satisfying the minimum requirement for Zn^{2+} coordination. His29 coordinates Zn^{2+} 1, while His44 and Glu71 coordinate Zn^{2+} 2. Zn^{2+} 3 is coordinated by His17 and His40 (Figure 4.12). All the Zn^{2+} sites have water molecules present to satisfy the coordination. FXII FnlI has a pI above 7 and is predicted to contain positively charged residues important for binding to negatively charged surfaces or activators. Displayed in Figure 4.13 and Figure 4.14 are the surface charge potential and the isocontour of FXII FnlI (bound and unbound to Zn^{2+}), respectively.

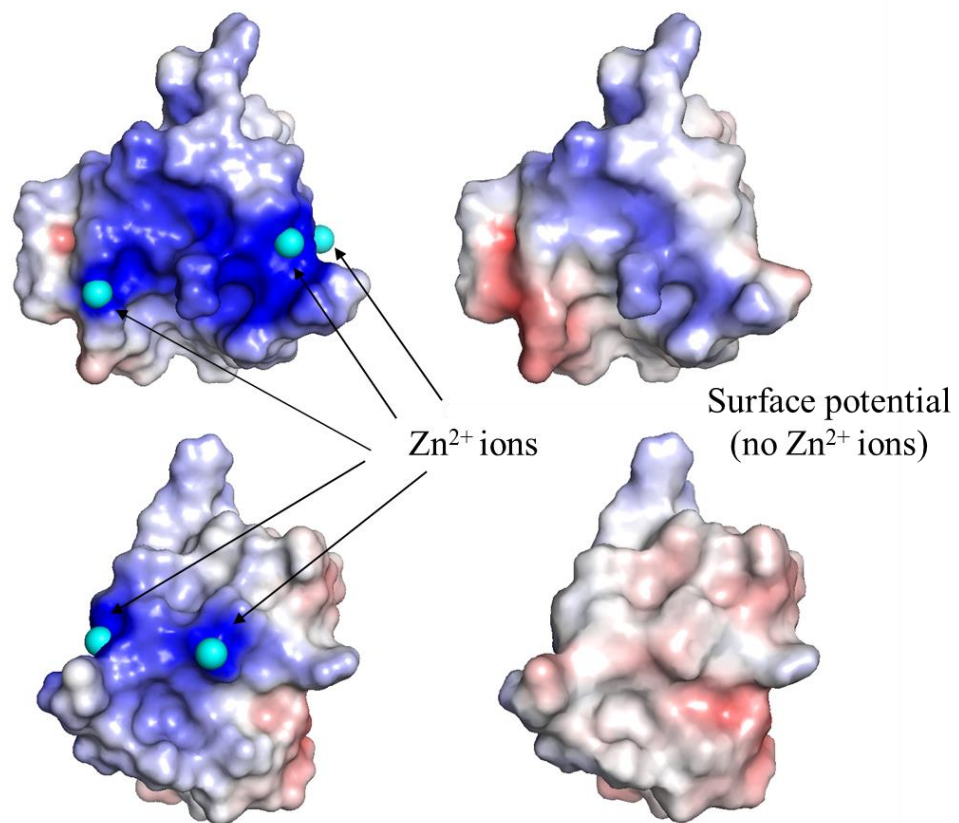


Figure 4.13: Electrostatic surface potential of FXII FnII. Electrostatic surface potential represented with and without Zn²⁺ (Cyan). Blue = positive charge, Red = negative charge and White/Grey = neutral.

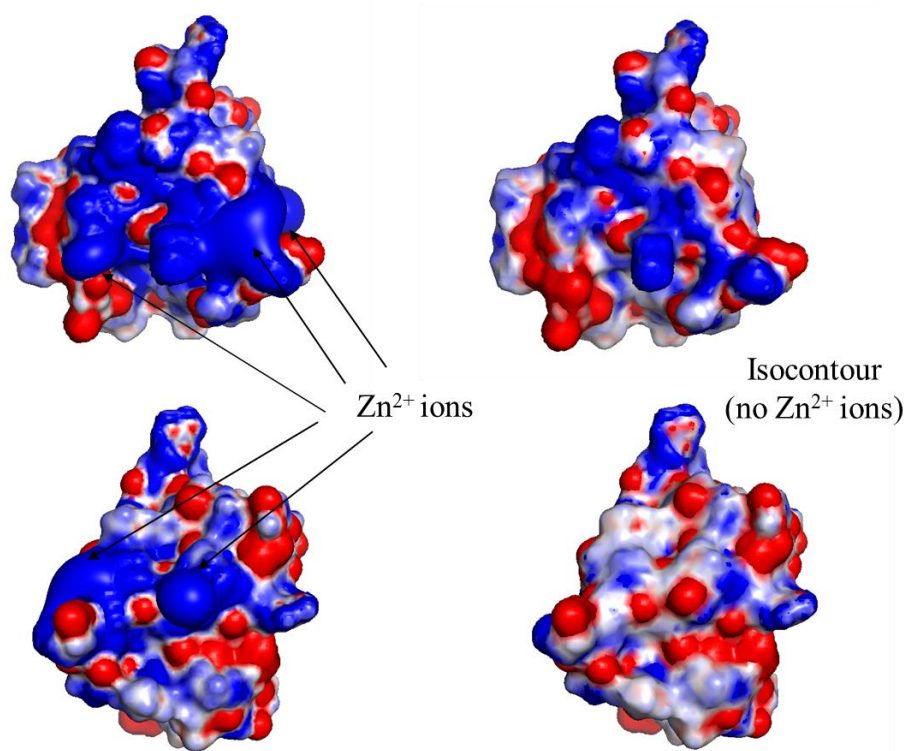


Figure 4.14: Electrostatic Isocontour of FXII FnII.

Furthermore, rotating the FXII FnII structure by 180 degrees for both form 1 and form 2, shows an overlay in ball and stick of two conserved tryptophans, Trp53 and Trp66 accommodating Arg47, thus forming a cation- π interaction with Trp66. Other residues such as Tyr34, Phe60 and Tyr68 are observed in contributing in the creation of the solvent exposed hydrophobic pocket as shown in Figure 4.15. FXII FnII form 1 is shown in black ball and tick, while in white is form 2.

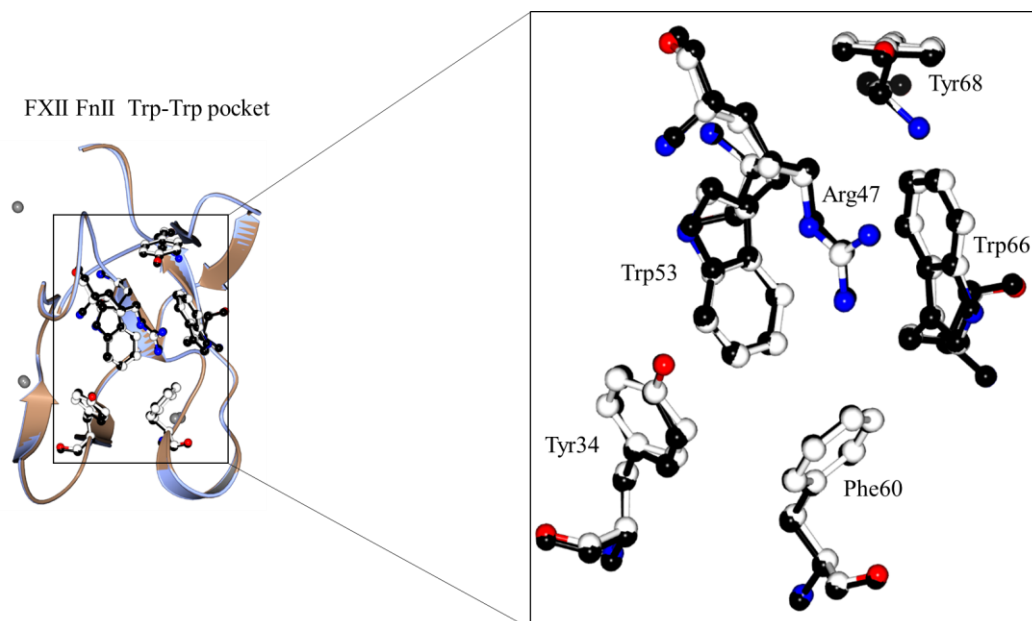


Figure 4.15: Overlay of the tryptophan pocket (Trp-Trp) in FXII FnII form 1 and form 2. Hydrophobic residues such as Tyr34, Trp53, Phe60, Trp66 and Tyr68 are also involved in forming the solvent expose hydrophobic pocket. Arg47 is inserted in the Trp-Trp pocket and forms a cation- π interaction with Trp66. FXII FnII form 1 is shown in black and in white is form 2.

4.2.3 Crystallisation of human FXII FnII in the presence of Dextran sulfate

FXII has been reported in the literature by many groups to interact with dextran sulfate and as there is no structure available yet to elucidate the molecular mechanism of the interaction, dextran sulfate in the presence of $50 \mu\text{M Zn}^{2+}$ was added in the crystallisation experiment. From this, crystals were observed after few days and showed single diamond-like morphology in conditions from the procomplex (Figure 4.16A) and PACT screens (Figure 4.16B). This crystal form for FXII FnII will be called form 3, as it is a different crystal form from FXII FnII form 1 and form 2. The data collection statistics presented in Table 4.3 following data

reduction provides a reports on how good the data is and therefore gives an indication of decisions to make for further data processing downstream.

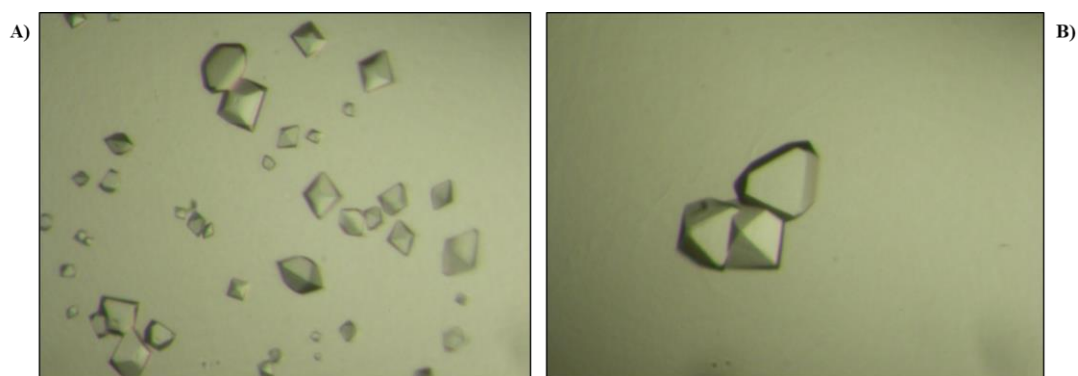


Figure 4.16: Crystals of FXII FnlI (form 3) in the presence of dextran sulfate 5 crystals. FXII FnlI crystals in the presence of dextran sulfate 5 were observed in the following crystallisation screens; **A)** 0.1 M Sodium Cacodylate pH 5.5, 25 % (w/v) PEG 4000 and **B)** 0.2 M Sodium Chloride, 0.1 M MES pH 6.0, 20 % (w/v) PEG 6000.

Table 4.3. Crystallographic data collection statistics.

Sample	FXII FnlI (form 3)
Data collection	
Space group	P4 ₁ 2 ₁ 2
Cell dimensions	
a, b, c (Å)	45.8, 45.8, 53.5
α, β, γ (°)	90, 90, 90
Resolution (Å)*	34.80-1.64
R _{merge} † (%)*	4.6(13.9)
Mean I / sigI*	26.6 (8.2)
Completeness (%)*	100.0 (99.8)
Redundancy*	10.2(7.0)
CC1/2 †	0.998(0.977)

*Values in parentheses are for highest-resolution shell.

The data collection statistics after data reduction were of good quality with high resolution cut-limit down to 1.64 Å. The MR solution values were 3091 for the LLG value and 30.5 for the TFZ score. However, under careful inspection no extra electron density map for dextran sulfate 5 was found, leaving an electron density map of just FXII FnII bound to 1 Zn²⁺ ion alone, as shown in Figure 4.17.

FXII FnII (Yellow stick) with symmetry mates of FXII FnII (Pink stick)

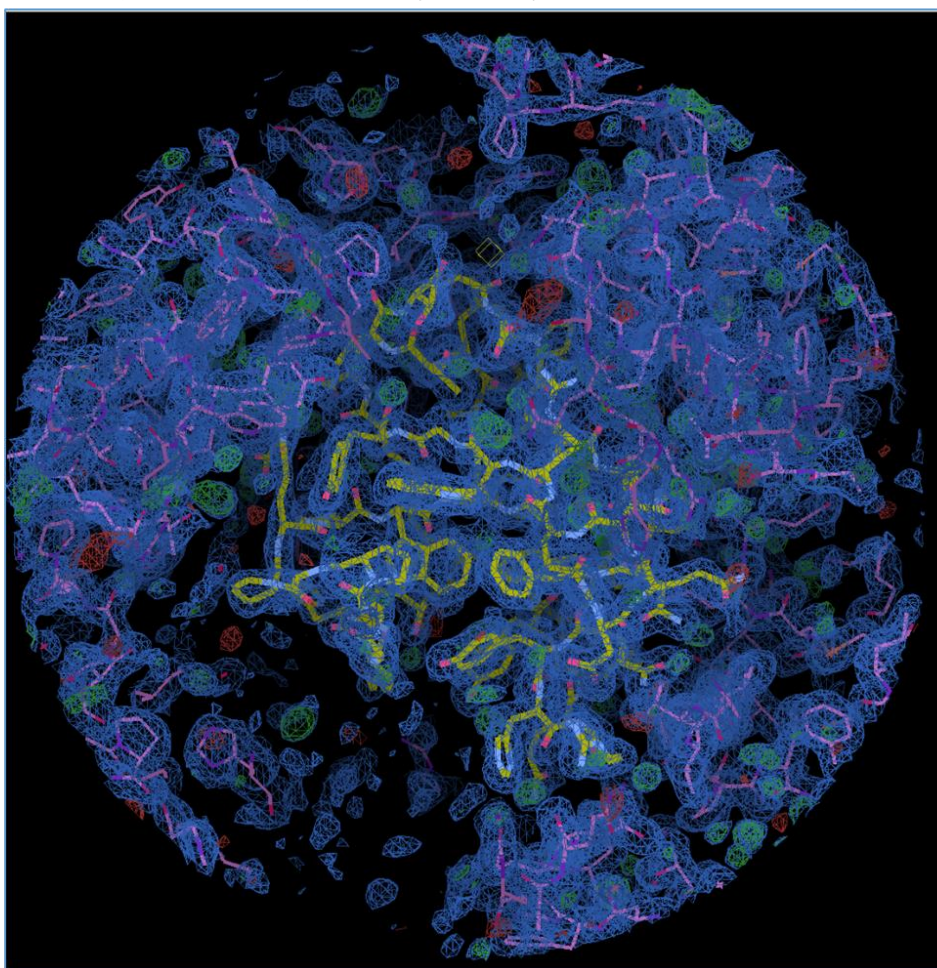


Figure 4.17: FXII FnII structure (form 3). No extra electron density for dextran sulfate was observed. Small green electron densities for water molecules and Zn²⁺ ions are also shown. FXII FnII (Yellow stick) is fitted into the blue electron density while the symmetry mates (copy of FXII FnII) is shown in pink stick.

4.2.4 Crystal structure of FXII FnII bound to 1 Zn²⁺ (form 3)

The 3D crystal structure of FXII FnII bound to 1 Zn²⁺ (form 3) has some similarities to the FXII FnII structure bound to 3 Zn²⁺ (form 1). However, interesting differences are shown displayed in loops 1 and 2 of the overlay between form 3 (magenta) and form 1 (ice blue) of FXII FnII. The RMSD value is also displayed to indicate closeness in the overlay and the bigger the value, the more dissimilar the structures are to each other (Figure 4.18).

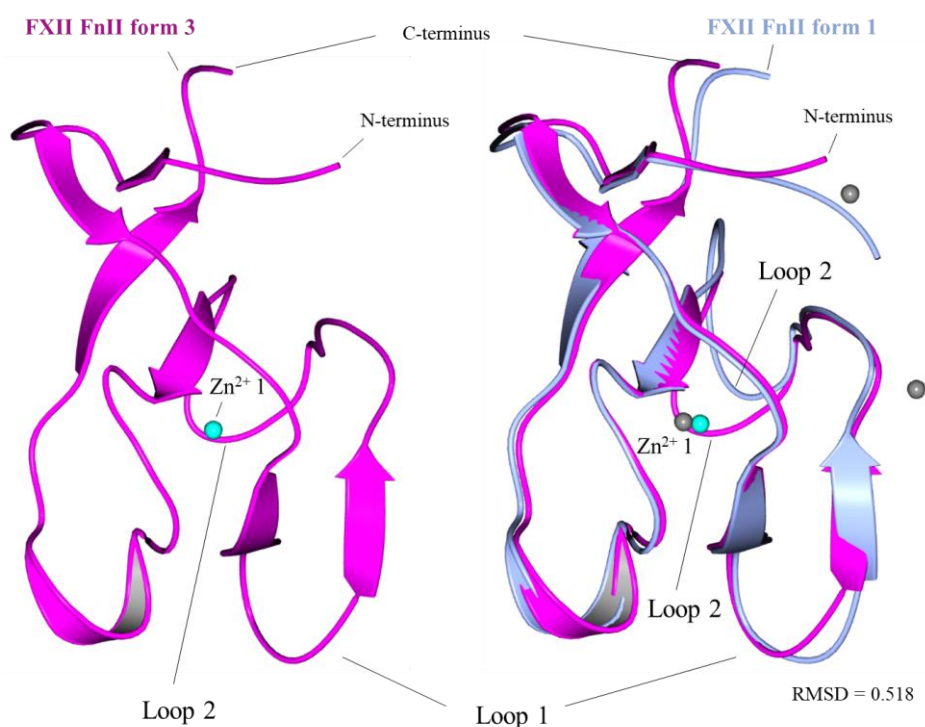


Figure 4.18: FXII FnII form 3 and form 1. In magenta, FXII FnII form 3 is shown bound to 1 Zn²⁺. A similar fold is observed upon comparison with FXII FnII form 1 (bound to 3 Zn²⁺), but clear differences in loops 1 and 2 are shown in the overlay between form 3 (magenta) and form 1 (ice blue). Zn²⁺ is coloured in grey for form 1 and cyan for form 3.

Similar to the FXII F_nII structures form 1 and form 2, form 3 also forms the Trp53-Trp66 pocket and shows many similarities, as shown in the structural overlay in Figure 4.18. However, the difference observed in loop 2 between form 1 and form 3 reveals a rearrangement of FXII F_nII Pro48-Gly49-Pro50 amino acid sequence causing Arg47 to move out of the Trp53-Trp66 pocket for form 3 (Figure 4.19).

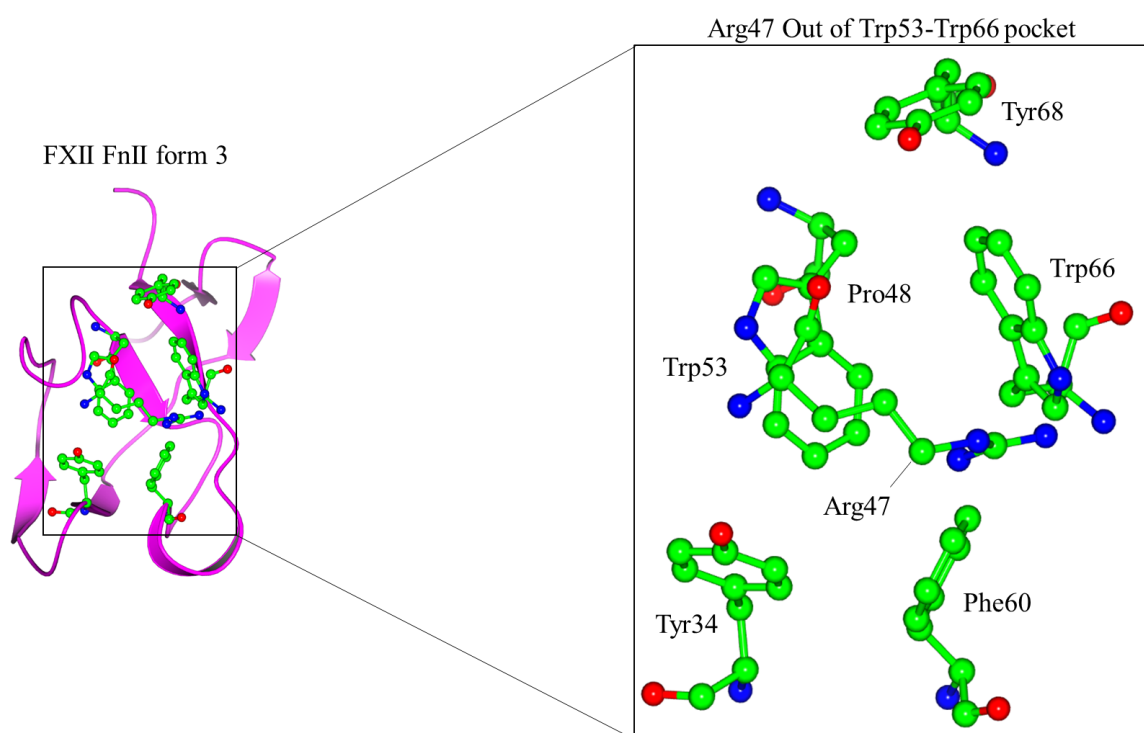


Figure 4.19: Trp-Trp pocket of FXII F_nII (form 3). Shows the solvent exposed hydrophobic pocket with Arg47 out and Pro48 inserted into the Trp53-Trp66 pocket as represented in ball and stick for FXII F_nII form 3.

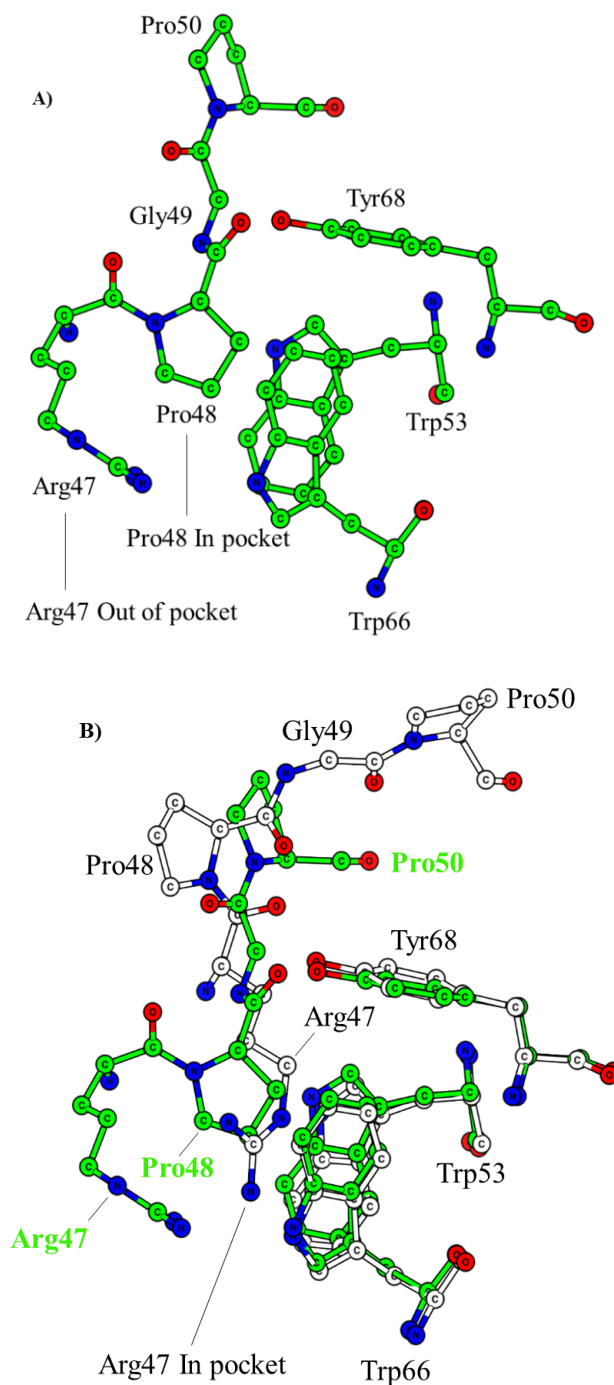


Figure 4.20: Overlay of Trp53-Trp66 pocket of FXII FnlI form 1 and form 3. A) Circle representation of FXII FnlI form 3 in green showing the amino acid sequence Pro48-Gly49-Pro50 with Pro48 accommodated into the Trp53-Trp66 pocket. B) In the overlay, FXII FnlI form 1 (white circle representation) is displayed showing Arg47 of FXII FnlI form 1 to occupy the Trp53-Trp66 pocket, while Arg47 in FXII FnlI form 1 which is out of Trp53-Trp66 pocket in green circles.

4.3.0 Structural comparison of the FXII FnII and FnII homologues

Sequence alignment of FXII FnII domain with FnII domains from MMP2 and PDC109 shows that Trp53 and Trp66 of FXII plus other hydrophobic residues are conserved. The solvent exposed hydrophobic pocket made up of amino acid residues including conserved trptophans in FnII from FXII, MMP2 and PDC109 are also present in the Fibronectin FnII domain but made up of Trp-Phe. However, apart from Arg47 in loop 2 of FXII FnII, none of the other residues in loop 2 of FXII FnII is conserved when compared to FnII in MMP2 or Fibronectin. Arg47 and Arg368 in FXII FnII and MMP2 FnII, respectively are not conserved in PDC109 FnII and are replaced by a serine (Ser88), as shown in the sequence alignment below (Figure 4.21). From the sequence alignment, histidines (His29, His35, His40 and His44) are only present in FXII and these histidines are shown in the FXII FnII crystal structure (form 1 and form 2) to be involved in Zn²⁺ coordination. Although, FXII His29 is conserved in Fibronectin FnII, Zn²⁺ has never been reported to bind to Fibronectin FnII.

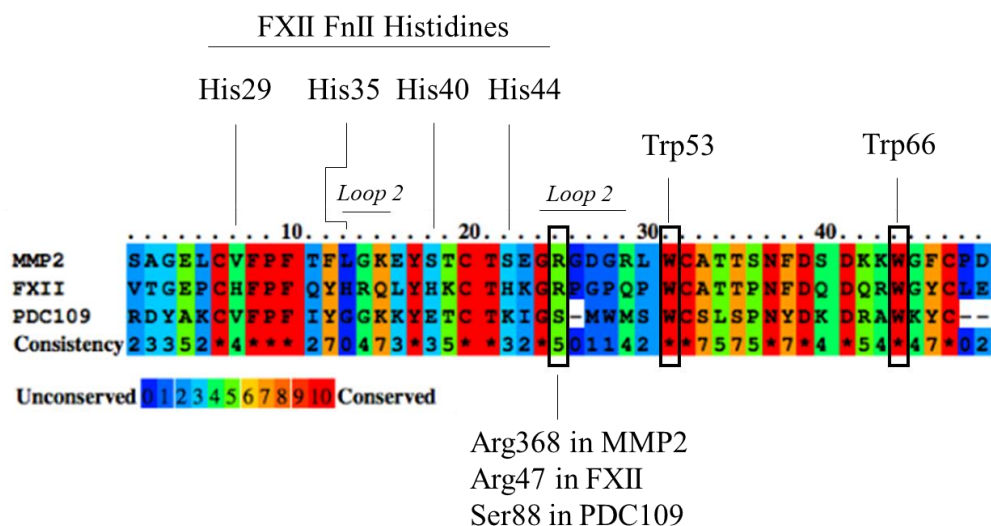


Figure 4.21: Amino acid sequence alignment of FXII FnII and FnII homologues. Amino acid sequence alignment shows conserved residues with 10 in red having 100% sequence identity and 0 in purple with no sequence conservation. Histidines in FXII FnII are also highlighted.

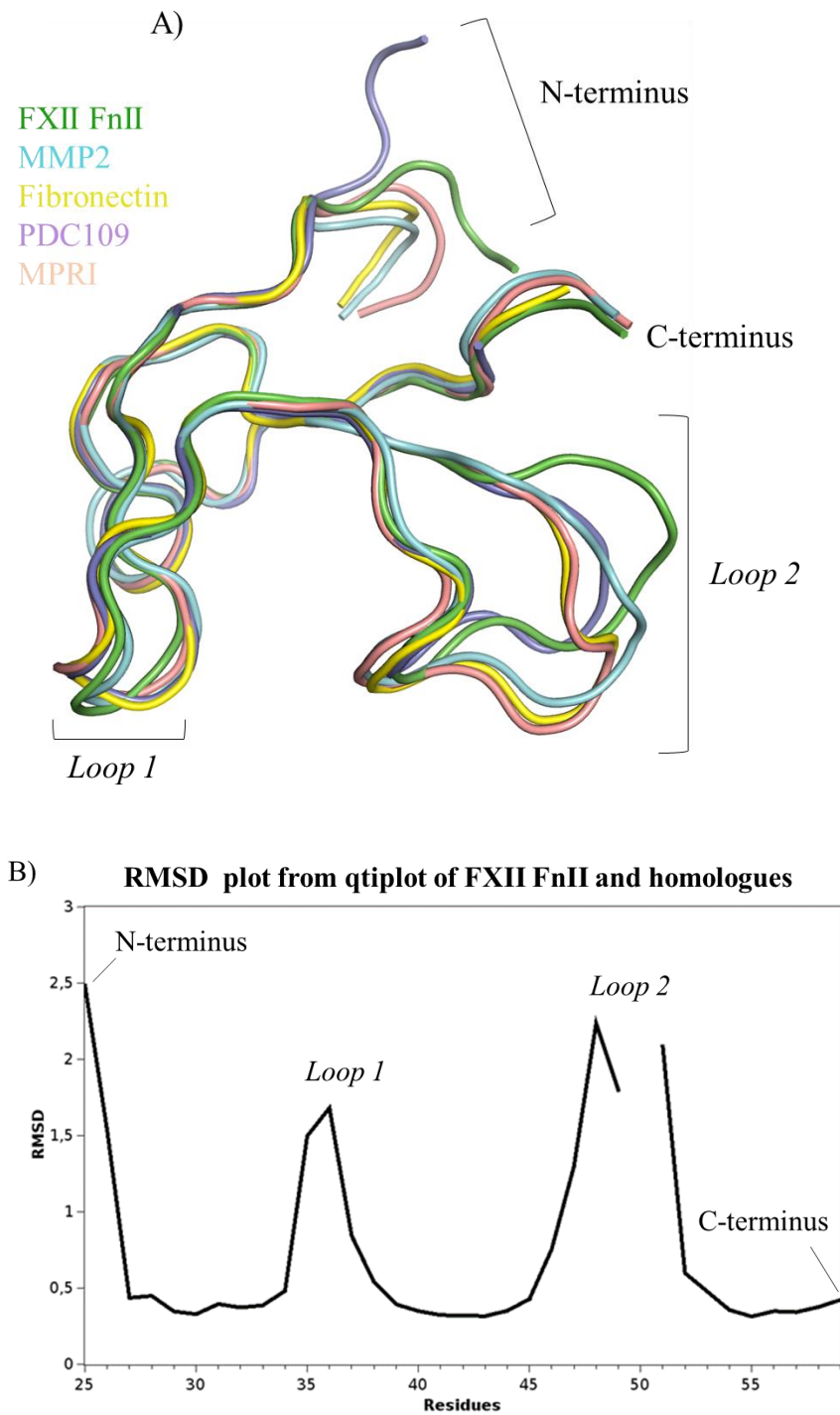


Figure 4.22: Structural overlay of FnlI in FXII and FnlI homologues A) Structural alignment showing differences in particularly loop 2. Loop 2 in FXII FnlI (Green) is shown to not superpose with the other FnlI homologues. B) Similarities and differences represented in RMSD are shown in the graph with loops 1 and 2 and the N-terminus showing high RMSD values.

Loops 1 and 2 are shown in the RMSD plot in Figure 4.22B to have high RMSD values, indicating differences in both loops for FXII FnII sequence overlaid with other FnII domains including MMP2, Fibronectin and PDC109. All the cysteines in FnII are conserved and form disulfide bonds as shown in the amino acid sequence alignment (Figure 4.21). In FXII FnII, the disulfide bonds formed seem to provide structural integrity as the N- and C-terminals are held in position, thus facilitating the formation of loop 2 and the Trp53-Trp66 pocket (Figure 4.23).

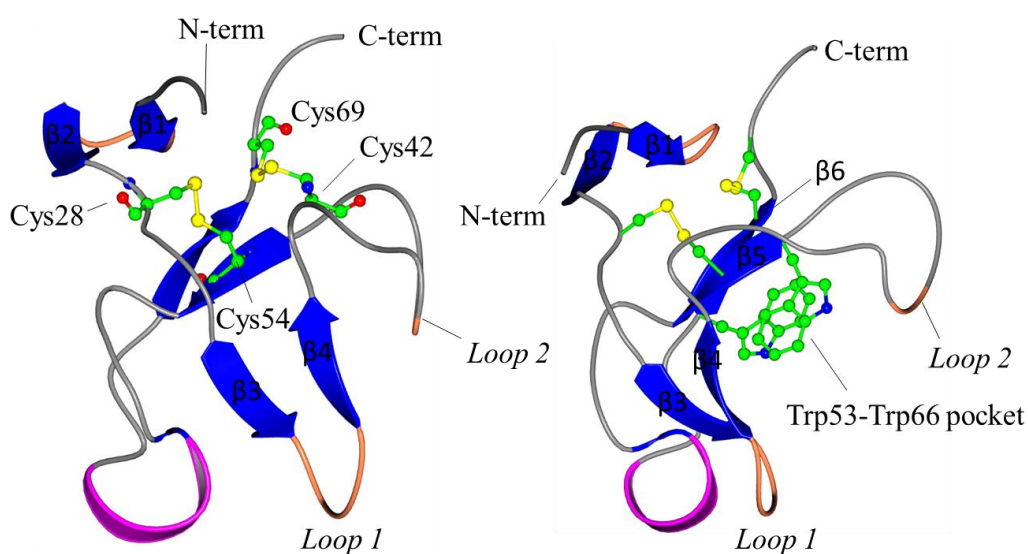


Figure 4.23: Disulfide bonds in FXII FnII form 1 with loop 2 and Trp53-Trp66. Both Trp53 and Trp66 sit at the base of $\beta 5$ and $\beta 6$, stabilised by Cys28-Cys54 formation, while loop 2 is stabilised and brought close to the Trp53-Trp66 pocket by Cys42-Cys69.

Comparative analysis of loop 2 and the hydrophobic pocket (Trp53-Trp66) in FXII, Fibronectin, Pro-MMP2 and PDC109 reveals similarities and differences in how the Trp-Trp or Trp-Phe (for Fibronectin FnII) pocket is either engaged or disengaged by residues from loop 2 in FXII and Fibronectin or by the Pro-domain in the case of Pro-MMP2.

The FXII FnII structures (form1 and form 3) were further compared to shed light on the Trp53-Trp66 pocket and its relationship with loop 2 (Figure 4.24). The Trp53-Trp66 pocket in form 3

adopts a close conformation in which the conserved Arg47 is out of the Trp53-Trp66 pocket, therefore facilitating Pro48 to sit in the Trp53-Trp66 pocket. Tyr68 holds Pro48 in place through Hydrogen bonding. In form 1, Arg47 sits in the Trp53-Trp66 pocket and forms a cation- π interaction with Trp66 (Figure 4.25).

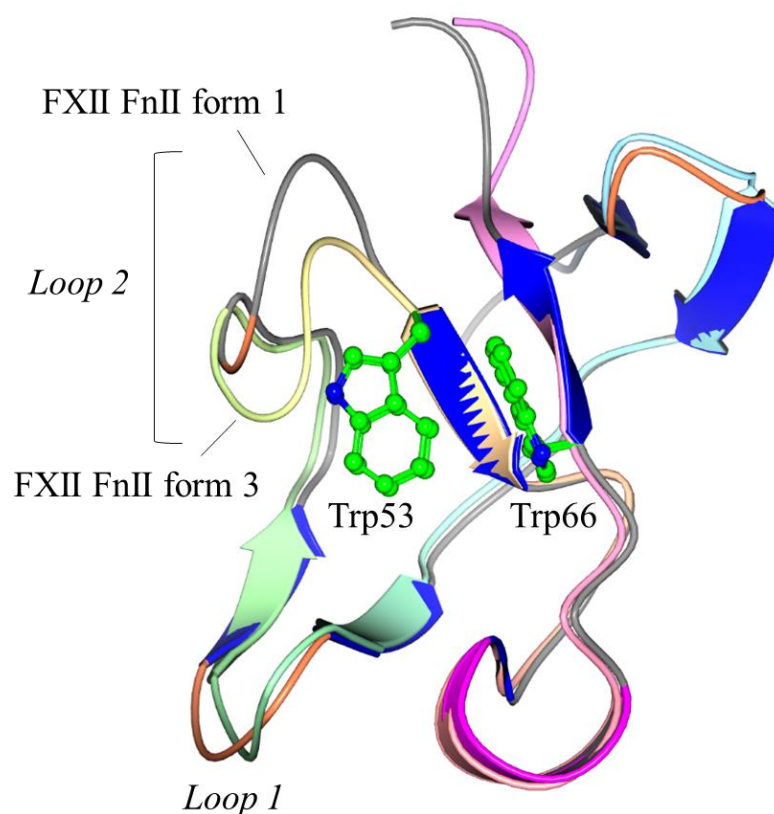


Figure 4.24: Structural overlay of FXII FnII structures (form 1 and form 3). Loop 2 and the Trp53-Trp66 pocket are shown with conformational changes in loop 2 upon superposition of FXII FnII form 1 and form 3. Conformational changes when FXII FnII binds to 1 or 3 Zn^{2+} for form 3 or form 1, respectively.

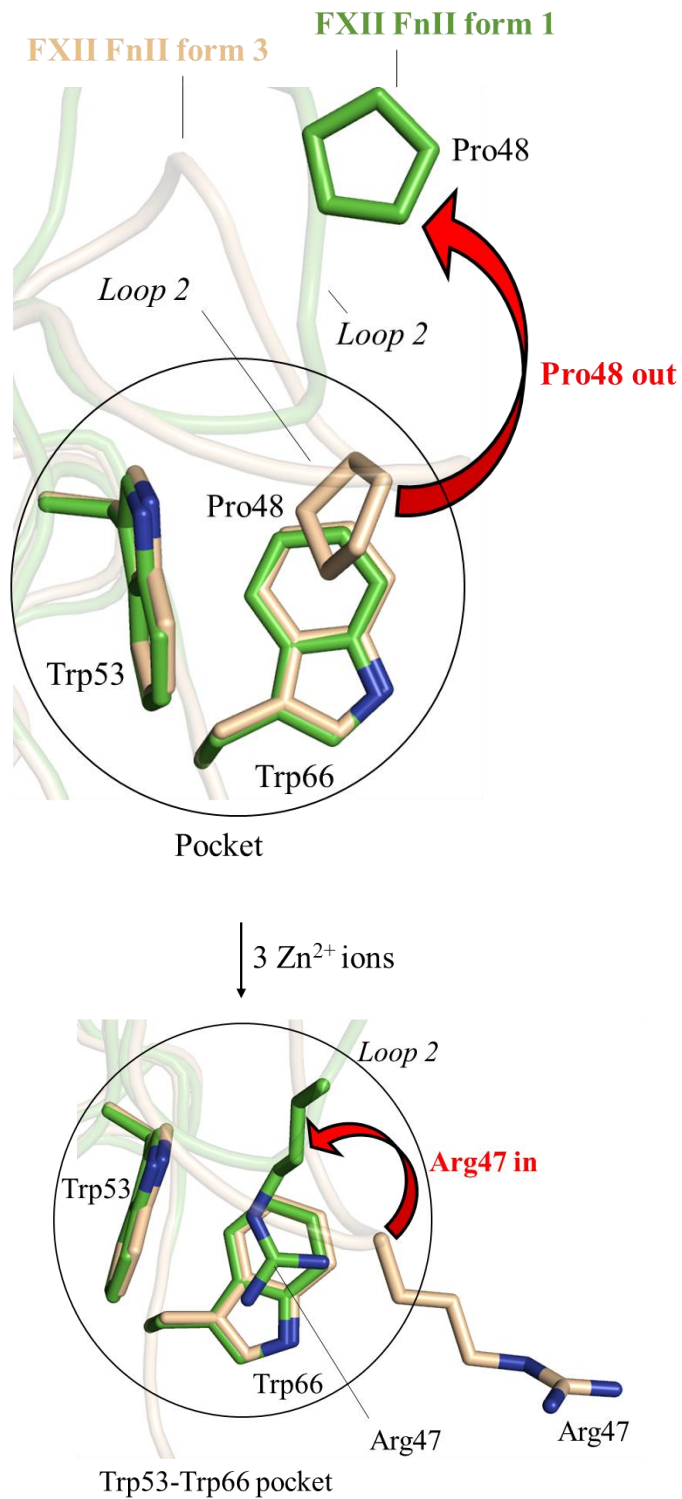


Figure 4.25: Conformational changes in loop 2 of FXII FnII form 1 and form 3. This shows the engagement of loop 2 by the Trp53-Trp66 pocket using Pro48 in FXII FnII for form 3 (wheat), while Arg47 in form 1 is inserted into the Trp53-Trp66 pocket. Arg47 is out and Pro48 in the Trp53-Trp66 pocket for form 3, while Pro48 is out and Arg47 in pocket for form 1.

The open conformation in the Trp53-Trp66 pocket observed for FXII F_{nII} form 1 is different to Pro-MMP2 F_{nII}; in that the conserved Arg368 in Pro-MMP2 is out of the Trp-Trp pocket and is occluded by hydrophobic residues Ile35 and Phe37. Pro-MMP2 Arg368 interacts with Asp40 of the Pro-domain (in magenta) of MMP2 (Figure 4.26).

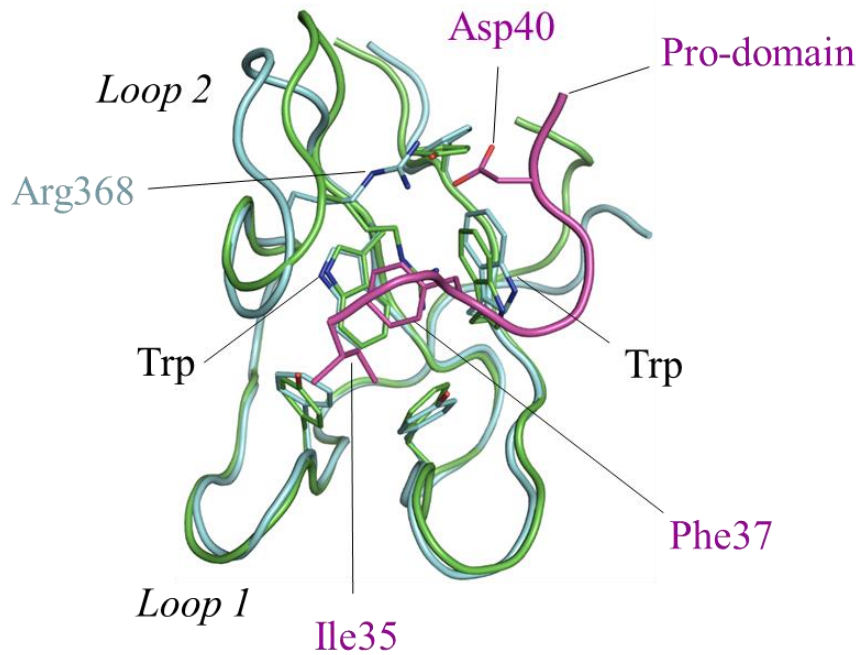


Figure 4.26: Structural overlay of F_{nII} in FXII and F_{nII} in Pro-MMP2 (plus Pro-domain). Trp-Trp pocket in Pro-MMP2 (Cyan) is shown to be occluded with hydrophobic residues Ile35 and Phe37 of the Prodomain (Purple), while Asp40 of the Prodomain holds Arg368 from loop 2 of Pro-MMP2 in the “up” position. FXII F_{nII} (Green) shows conserved Arg47 to sit in the Trp-Trp pocket and is in the “down” position in comparison to Arg368 in Pro-MMP2.

Interestingly, both Pro-MMP2 and FXII F_{nII} (form 3) seem to adopt a close conformation with their Arginines (Arg47 and Arg368) out of the Trp-Trp pocket. Furthermore, structural comparison for Fibronectin F_{nII} also shows its arginine (Arg439) out of its Trp-Phe pocket and is close to Asp441 as shown in the overlay with FXII F_{nII} (form 1) (Figure 4.27).

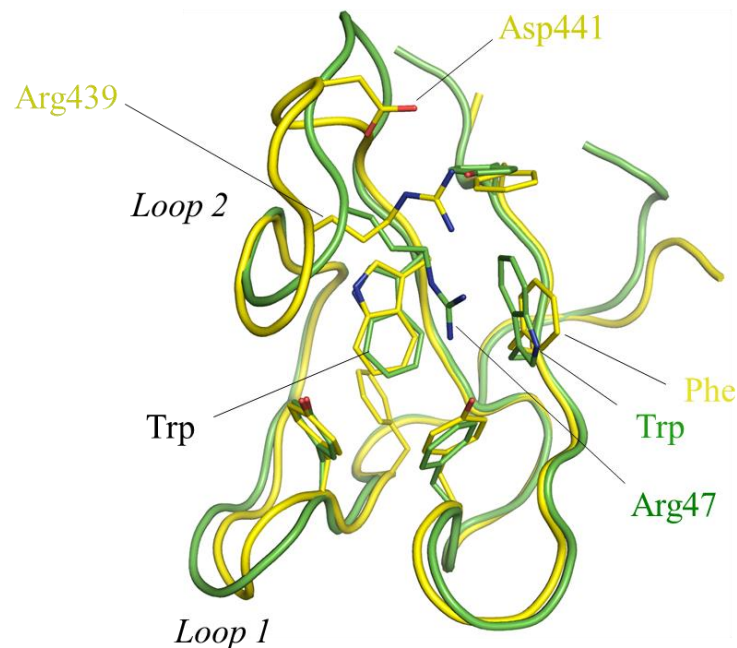
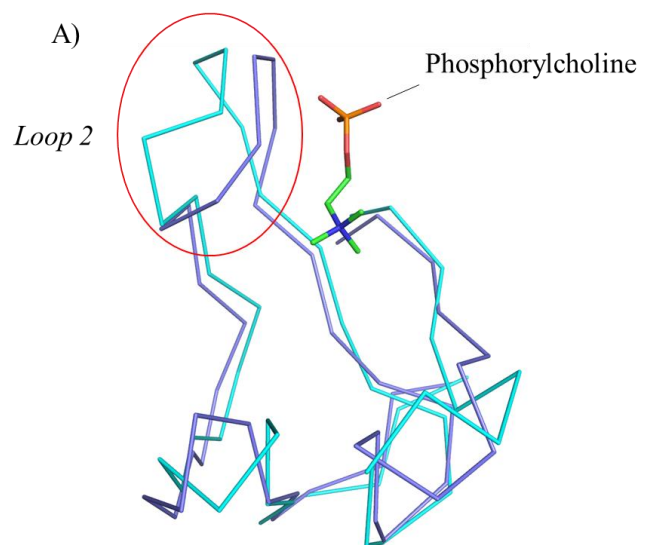
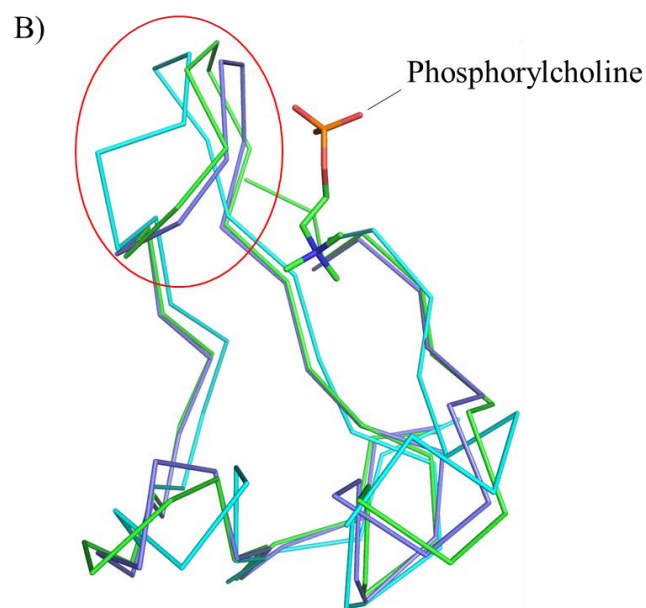


Figure 4.27: Structural overlay of FnlI in FXII and FnlI in Fibronectin. Arg439 from loop 2 of Fibronectin FnlI (Yellow) is shown to move upward, while the same arginine in FXII FnlI (Arg47) in green adopts a downward conformation to sit in the Trp53-Trp66 pocket.

Following careful analysis of the Trp-Trp pocket in FXII and in PDC109, the open and close conformations provide an interesting comparison in which hydrophobic residues in PDC109 unbound to phosphorylcholine decreases the Trp-Trp pockets' accessibility to the solvent. In the PDC109 bound to phosphorylcholine structure, the Trp-Trp pocket opens up, thus allowing phosphorylcholine to be accommodated in the Trp-Trp pocket, in a similar manner to what is observed for Arg47 in FXII by cation- π interaction. Ser88 of loop 2 in PDC109 interacts with the phosphate head of phosphorylcholine, while the ammonium group of the phosphorylcholine forms a cation- π interaction with a Trp93 in the Trp-Trp pocket (Figure 4.28 and 4.29).



PDC109 alone (Cyan)
 PDC109-Phosphorylcholine complex (Purple)



PDC109 alone (Cyan)
 PDC109-Phosphorylcholine complex (Purple)
 FXII FnII (Green)

Figure 4.28: Loop 2 in PDC109 and FXII FnII (form 1). A-B) Overlay of PDC109 unbound (Cyan) or bound (Purple) to phosphorylcholine and FXII FnII (form 1) in green showing similarities and differences in loop 2 as highlighted in red circle.

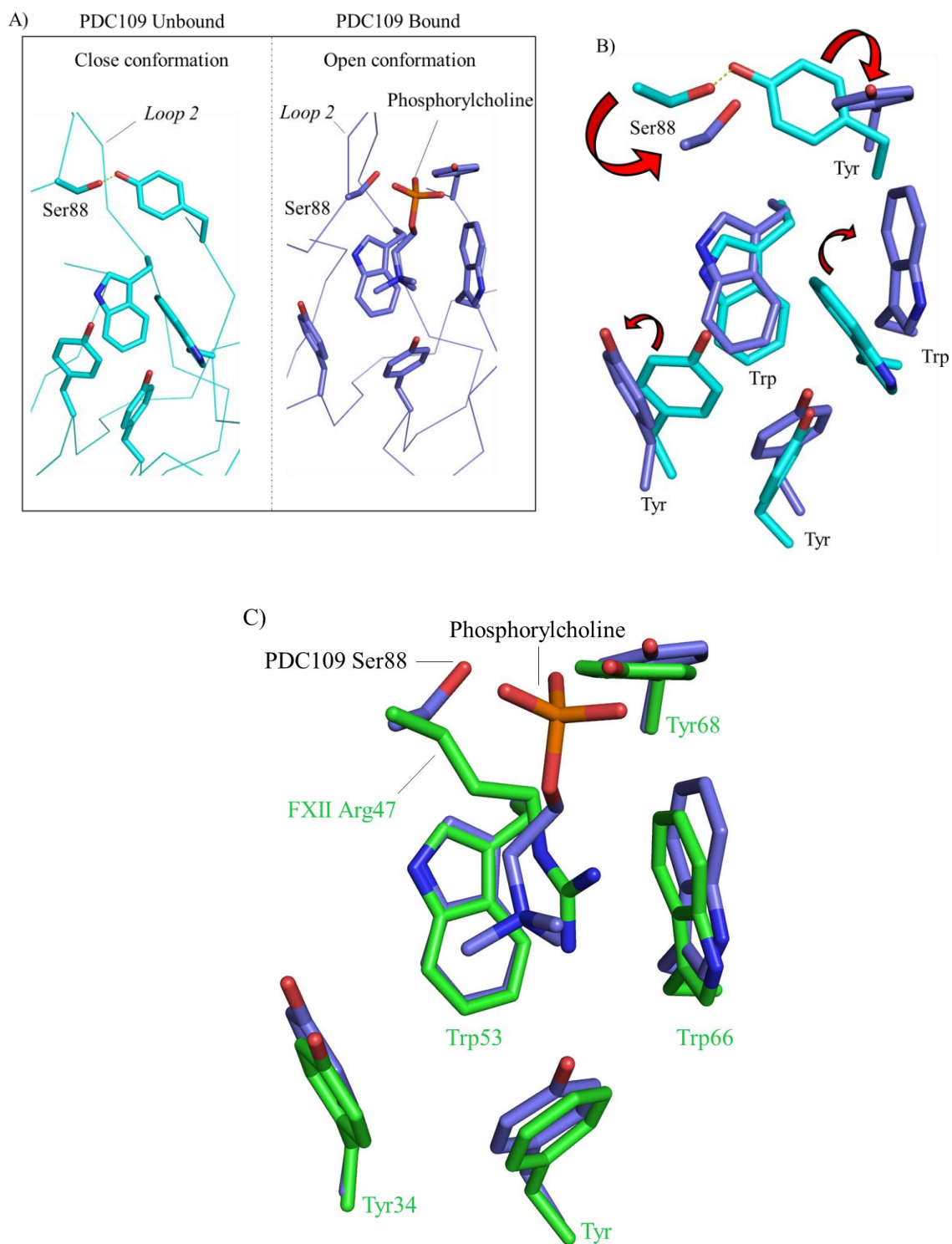


Figure 4.29: Stick representation of Trp-Trp pocket in PDC109 and FXII FnII (form 1). **A-B)** Open and close conformations of PDC109 unbound (Cyan) and bound to phosphorylcholine (Purple) with arrows showing changes of residues when phosphorylcholine is bound in the overlay. **C)** Overlay of FXII FnII (form 1) in green and PDC109 bound phosphorylcholine (Purple).

4.4.0 Discussion

4.4.1 Expression and purification of FXII FnII

Zn²⁺ has been documented to bind FXII and has been demonstrated to have a role in mediating FXII binding to negatively charged macromolecules. In line with the findings of FXII binding to Zn²⁺ ions, recombinant untagged FXII FnII and cleaved fusion of HisTrx-FXII FnII captured on Affinity (Zn²⁺) chromatography column therefore reinforces the capability of FXII to bind to Zn²⁺. Expression of untagged FXII FnII in insect cells and FXII FnII in Rosetta-gami2 cells showed no major difference on size exclusion chromatography, as both appeared to be folded in solution. This confirms that enhanced disulfide bond formation for correct folding in Rosetta-gami2 cells can produce high quality FXII FnII protein, although, no glycosylation is required for FXII FnII.

4.4.2 Structural effect of Zn²⁺ on FXII FnII

The FXII FnII structure provides the first molecular insight into FXII FnII binding to Zn²⁺ ions and the structural importance Zn²⁺ has on FXII FnII. Earlier studies have suggested residues 40-44 to theoretically have a Zn²⁺ locus⁽³⁰⁹⁾. Our FXII FnII structure bound to Zn²⁺ (form 1) therefore strengthens and expands on this by showing His40 and His44 to both have different Zn²⁺ loci. Additionally, the FXII FnII structure shows N-terminal His17 (not part of FnII domain), His29 and C-terminal Glu71, which have not been reported before to bind Zn²⁺. The exciting finding for FXII FnII bound to Zn²⁺ illustrates how amino acid residues (Gly46-Arg47-Pro48-Gly49-Pro50-Gln51-Pro52) in loop 2 rearranges upon binding to 1 Zn²⁺ ion for form 3 and 3 Zn²⁺ ions for form 1 to engage the Trp53-Trp66 pocket. This adds to the understanding of the relationship FXII has upon Zn²⁺ binding and therefore fits well with the structural comparisons made with FnII domains from Pro-MMP2, Fibronectin and PDC109.

Previous studies have shown four Zn^{2+} ions binding to zymogen FXII and three Zn^{2+} ions when activated to FXIIa, thus losing one Zn^{2+} site⁽³⁰⁹⁾. The same research group also suggested Zn^{2+} localisation within the FXII FnII and FXII EGF1, without any mention of how many Zn^{2+} ions each domain can bind to. Our current study provides new insight demonstrating only 3 Zn^{2+} ions can saturably bind FXII FnII at 10 or 200 mM $ZnCl_2$ and that undersaturation with 50 μ M $ZnCl_2$ only shows 1 Zn^{2+} ion bound to FXII FnII.

Determining the full length structure of FXII bound to Zn^{2+} or using a Zn^{2+} isotope to quantify the number of Zn^{2+} binding to various truncations within the heavy chain of FXII will certainly provide an in-depth structural insight on FXII binding to Zn^{2+} and will also reveal the structural effect Zn^{2+} might have on the whole FXII. However, the structural insight from the FXII FnII saturated with Zn^{2+} (Form 1) compared to under-saturated with Zn^{2+} (form 3) reveals that Zn^{2+} does induce conformational rearrangement within loop 2 of FXII FnII.

4.4.3 Structural similarities and differences in FXII FnII and FnII homologues

The structural data is corroborated by the comparative analysis made to understand the structural similarities and differences between FXII FnII and FnII in Pro-MMP2, Fibronectin or PDC109. Pro-MMP2 is the zymogen form of MMP2 and is proteolytically activated by thrombin. In Pro-MMP2, the solvent exposed hydrophobic Trp-Trp pocket in the third FnII domain structure delineates hydrophobic residues Ile35 and Phe37 within the Pro-domain of Pro-MMP2 to occlude the Trp-Trp pocket.

Furthermore, Asp40 of the Pro-domain is also shown to keep the conserved Arg368 in loop 2 of the Pro-MMP2 FnII in the “up” position and out of the Trp-Trp pocket, as opposed to the FXII FnII Arg47 displayed to be in the “down” position by sitting in the FXII Trp53-Trp66 pocket

(form 1). A similar conformational difference is observed with conserved Arg439 in loop2 of the Fibronectin FnII, in which its Arg439, similar to FnII Arg368 of Pro-MMP2 is flipped “out” of the Trp-Trp pocket and held up by interacting with Asp441.

Although, there are no structures published showing activated MMP2 Arg368 and Fibronectin Arg439 to suggest formation of cation- π interaction when inside their Trp-Trp pocket, Pro-MMP2 conversion to activated MMP2 has been reported to require cleavage of the Pro-domain. The Pro-domain interacts with the Trp-Trp pocket of FnII and the catalytic cleft of Pro-MMP2 to shield from water entering the cleft and hydrolyse the cysteine for Zn^{2+} coordination. For this to happen, the Pro-domain of Pro-MMP2 is broken down upon cleavage⁽³¹⁰⁾. Interestingly, the same Arg47, shown to occupy the FXII FnII Trp53-Trp66 pocket is in contrast to the same conserved Arginines in the Pro-MMP2 and Fibronectin observed to also move “out” of the FXII FnII Trp53-Trp66 pocket in FXII FnII form 3 structure. This displays useful similarities in the Trp-Trp pocket for FnII in FXII (form 3), Pro-MMP2 and Fibronectin.

Pro48 in the FXII FnII structure (form 3) is hydrogen bonding with Tyr68, reminiscent of how serine 88 (Ser88) in loop 2 of PDC109 FnII interacts with Tyr108 in the “closed” conformation of the Trp-Trp pocket in PDC109 in the absence of phosphorycholine. An overlay of FXII FnII (form 3) and FXII heavy chain structure unbound to Zn^{2+} (unpublished by Dr Chan Li and Prof Jonas Emsley) showed no difference at all and may therefore potentially shed light on FXII FnII zymogenicity when compared to FXII FnII (form 1).

In the FXII FnII form 3 structure, Zn^{2+} appears disordered with reduced occupancy. What is clear is that residues Gly46-Arg47-Pro48-Gly49-Pro50-Gln51 of loop 2 rearranges to facilitate Pro48 accommodation in the Trp53-Trp66 pocket in a similar manner to FXII heavy chain, while in FXII FnII form 1, the Pro48 is in the upward position. Partial display of electron density

map of Arg47 in the FXII FnII (form 3) indicates that Arg47 is mobile when FXII FnII is under-saturated with Zn²⁺.

Serine 88 (Ser88) in loop 2 and Trp-Trp pocket of PDC109 FnII structure unbound to phosphorycholine shows that the Trp-Trp pocket adopts a “close” conformation by closing in on itself to form hydrophobic interactions. The “open” conformation on the other hand, suggests that the Trp-Trp pocket undergoes a conformational change in order to increase the pocket area for phosphorycholine to fit into. Therefore, it is arguably reasonable to suggest for the FXII FnII (form 1) structure that Arg47 accommodated in the Trp53-Trp66 pocket is in the “open” conformation as cation- π interaction for Arg47 in FXII is similar to the ammonium group of the phosphorycholine ligand bound to the Trp-Trp pocket in PDC109 FnII. Furthermore, Pro48 in FXII FnII (form 3) structure, in the “close” conformation seems to block the top part of the Trp53-Trp66 pocket and is held in this position by Tyr68 and the same conserved Tyr108 in PDC109 FnII also contributes in the closing of the Trp-Trp pocket by forming a H-bond with Ser88.

I suspect in FXII activation, residues Pro48 and Arg47 within loop 2 of FXII FnII may switch to “in” and “out” state depending on the number of Zn²⁺ ions bound to FXII. This may facilitate how FXII is regulated prior and post adopting a conformation favourable for interactions with macromolecules such as polyphosphate and gC1q-R.

4.4.4 FXII FnII Cysteine 34 (Cys34) and Tenri deficiency

In addition to Trp53 and Trp66 in FXII FnII, other hydrophobic amino acid residues also contribute in forming the solvent exposed hydrophobic pocket, and interestingly, tyrosine 34 (Tyr34) has been clinically reported in a case study of a 71-year old Japanese woman with no measureable phenotype. In FXII hereditary deficiency, also known as Factor XII Tenri

deficiency, Tyr34 undergoes amino acid substitution to Cysteine 34 (Cys34) or Y34, and therefore results into disulfide bond formation of FXII with other proteins including α 1-microglobulin. As a result, this renders FXII Tenri inactive when compared to normal FXII, as conversion into the active form is obstructed ⁽³¹¹⁾.

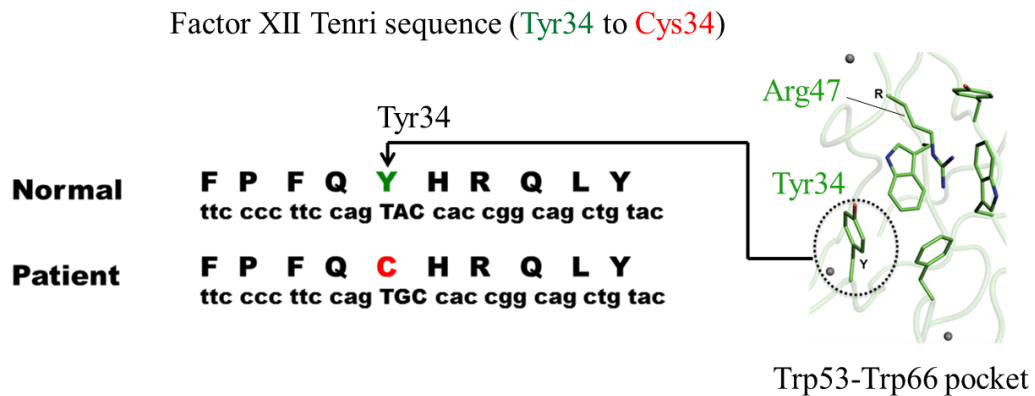


Figure 4.24: FXII Tenri deficiency as a result of amino acid mutation in Tyr34 to Cys34. Part of FXII F_{nII} sequence showing Tyr34 (Y in green) mutated to Cys34 (C in red). DNA sequence corresponding to the each amino acid is shown below. The Crystal structure in green also shows Tyr34 (dotted circle) to be part of the solvent exposed hydrophobic pocket in which Trp53 and Trp66 are also part of. Zn²⁺ ions are shown in grey.

It is unclear what this will do to the solvent expose hydrophobic pocket, although the structural integrity of FXII may be compromised, therefore retaining FXII inside cells as demonstrated *in vitro* by Fujihara N *et al.*, 2004.

CHAPTER 5.0

STRUCTURAL STUDIES OF THE FXII F_nII IN COMPLEX WITH gC1q-R

5.1.0 Structural determination of human FXII FnII in complex with complement receptor gC1q-R

5.1.1 Interaction between gC1q-R and FXII FnII

To shed light on the molecular insights delineating the relevance of Zn^{2+} in mediating FXII FnII (or possibly the whole FXII) binding to gC1q-R; I next sought to characterise the interaction of the human FXII FnII domain and complement receptor gC1q-R. FXII FnII has never been reported to interact with gC1q-R. Although, peptides corresponding to regions within FXII FnII have been shown to compete for binding to full-length human FXII on HUVEC thus leading to FXII and PK activation ⁽³¹²⁾.

Figure 5.1A shows a chromatograph of gC1q-R in the presence of FXII FnII with added 10 μ M Zn^{2+} in green and 50 μ M Zn^{2+} in red. In the presence of 10 μ M Zn^{2+} (green peak), no complex of gC1q-R and FXII FnII was formed therefore resulting into 2 peaks with gC1q-R eluting at 16.7 mL and FXII FnII at 20.2 mL. In black is gC1q-R alone and is overlaid with the green and the red peaks for comparison. FXII FnII alone is shown in the blue peak. The SDS-PAGE gel on Figure 5.1B confirms that no complex was formed as shown on lanes labelled complex 17 and complex 21.

To find out whether increasing the Zn^{2+} concentration to 50 μ M will drive complex formation, the fractions (17-22) from the green peaks were pooled and buffer exchanged in a running buffer containing 50 μ M Zn^{2+} , followed by isolation from S6 gel filtration column in 50 μ M Zn^{2+} running buffer. From this, the red peak shown in Figure 5.1A was produced and showed a slightly higher peak when compared to the first green peak eluting at 16.7 mL, although much of the second peak (FXII FnII) in red has disappeared. The red peak (gC1q-R and FXII FnII) had an absorbance (280 nm) of 61.5 mAU (Red peak) relative to 48.8 mAU for gC1q-R with no FXII FnII in 10 μ M Zn^{2+} (Green peak).

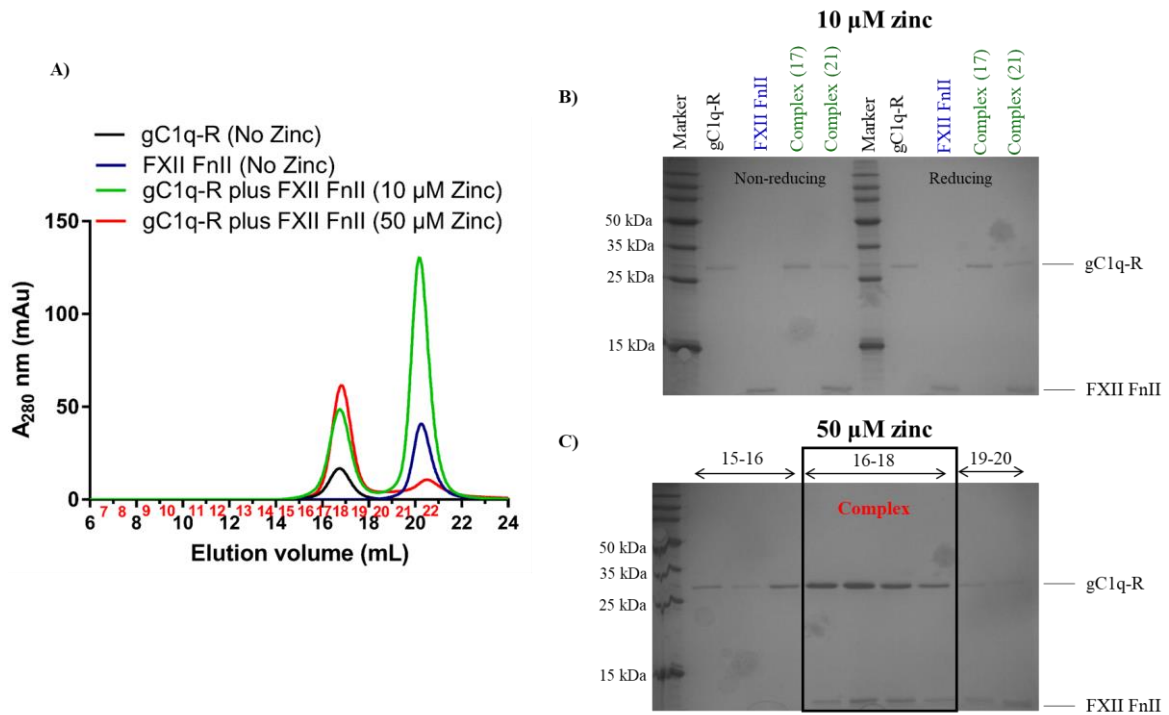


Figure 5.1: Interaction between gC1q-R and FXII FnII in 10 μM and 50 μM Zn^{2+} . **A)** For the size exclusion chromatography (gel filtration - S6 column), the mixture of gC1q-R and FXII FnII (1:2 molar ratio) containing 10 μM Zn^{2+} in the running buffer produced two peaks (green). Fractions from both peaks in green were pooled and buffer exchanged into running buffer containing 50 μM Zn^{2+} and isolated from the same column as shown as the red peaks. **B)** Fractions from the two peaks were analysed on SDS-PAGE gel showing no apparent complex formation at 10 μM Zn^{2+} concentration. **C)** SDS-PAGE gel shows complex formation from fractions of the red peak highlighted in the black box for running buffer containing 50 μM Zn^{2+} .

The SDS-PAGE gel (Figure 5.1C) from fractions of the red peak in running buffer containing 50 μM Zn^{2+} confirmed what is produced from the chromatographic peak and showed two bands corresponding to gC1q-R and FXII FnII on the same lane.

To further establish how many molecules of FXII FnII were bound to gC1q-R, more chromatographic experiments were performed in the presence of 50 μM Zn^{2+} .

Molar ratios of 1:1, 1:2 and 1:3 of gC1q-R to FXII FnII showed excess FXII FnII for ratios 1:2 and 1:3, indicating that one molecule of FXII FnII may interact with one gC1q-R trimer in solution. The fractions from their corresponding peaks show bands of gC1q-R and FXII FnII on the SDS-PAGE gel shown below at different binding ratios with excess FXII FnII shown for lanes 20 (1:2) and 20 and 21 (1:3).

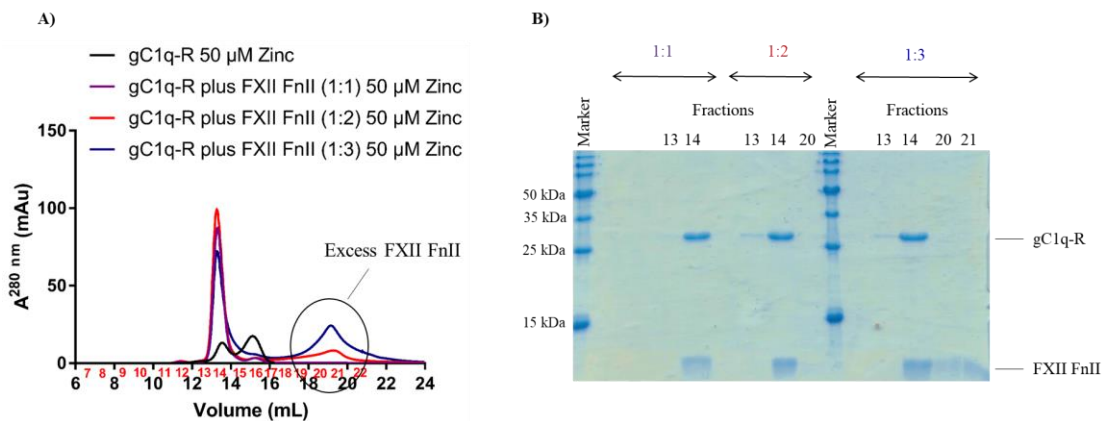


Figure 5.2: Interaction between gC1q-R and FXII FnII. **A)** gC1q-R-FXII FnII (1:1) in purple, gC1q-R-FXII FnII (1:2) in red and gC1q-R-FXII FnII (1:3) in blue with 50 μM Zn^{2+} in running buffer. Molar excess of FXII FnII in both red and blue are shown and highlighted with a black circle. **B)** Fractions for peaks eluted from the S6 column were subjected to SDS-PAGE gel showing the gC1q-R-FXII FnII complex and FXII FnII excess for molar ratios 1:2 and 1:3.

The solution studies in Figure 5.2 showing one molecule of FXII FnII interacting with one gC1q-R trimer was repeated to strengthen FXII FnII interaction to gC1q-R using the FXII FnII-EGF1 domain, which has an additional domain (EGF1) next to FnII. The interaction between gC1q-R and FXII FnII did not only demonstrate an interaction and reproducibility but also confirms that gC1q-R trimer can only interact with one molecule of FXII FnII or FXII FnII-EGF1 in the presence of 50 μM Zn^{2+} . The overlaid red and cyan peaks for gC1q-R bound to FXII FnII or

gC1q-R bound to FXII FnlI-EGF1 at molar ratio of 1:2 show excess for both peaks, as highlighted with the black circle (Figure 5.3A). Figure 5.3B shows fractions (15-19) from the cyan peak containing gC1q-R and FXII FnlI-EGF1 on the SDS-PAGE gel, shown highlighted in black box and labelled in cyan complex.

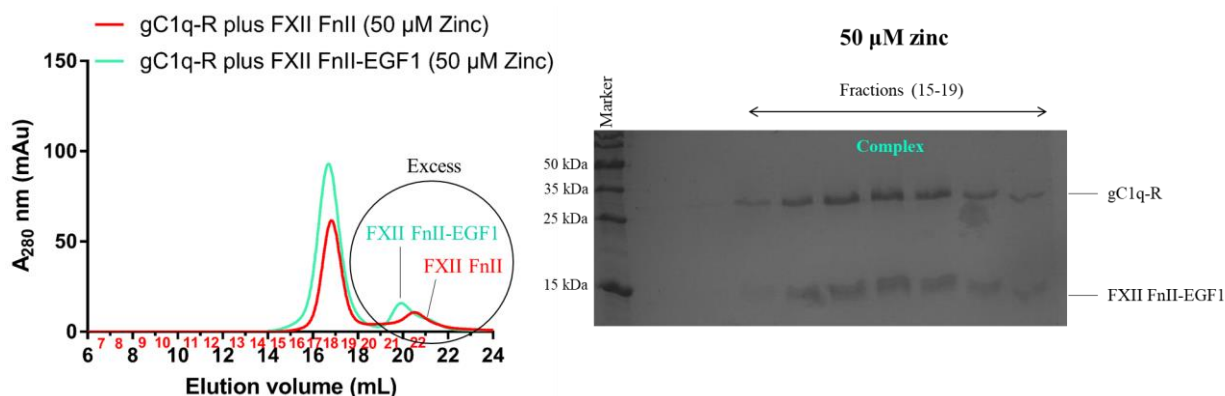


Figure 5.3: Interaction between gC1q-R and FXII FnlI-EGF1 in the presence of 50 $\mu\text{M Zn}^{2+}$. **A)** 1:2 molar ratio of gC1q-R-FXII FnlI-EGF1 complex (Cyan) formation in 50 $\mu\text{M Zn}^{2+}$ produced excess FXII FnlI-EGF1 (in cyan highlighted with a black line in a black circle) unbound to gC1q-R. The gC1q-R-FXII FnlI-EGF1 complex (Cyan) is overlaid with gC1q-R-FXII FnlI complex (Red) from a previous experiment showing excess FXII FnlI-EGF1 (Cyan) and FXII FnlI (Red). **B)** Fractions from the gC1q-R-FXII FnlI-EGF1 complex were subjected to SDS-PAGE gel analysis showing protein bands for both gC1q-R and FXII FnlI-EGF1 on the same lane (highlighted by an arrow showing fractions 15-19).

Preliminary data show that FXII FnlI competes with full length human FXII for gC1q-R binding and therefore strengthens the ability of FXII FnlI to interact with gC1q-R in the presence of 50 $\mu\text{M Zn}^{2+}$. Human gC1q-R is a trimer in solution and our data supports one FXII binds to a monomer of the gC1q-R trimer in solution leaving the remaining two gC1q-R monomers unoccupied. Dr Alexandre Slater demonstrated using gel filtration and Isothermal Titration Calorimetry (ITC) that gC1q-R is able to bind to two HK D5 domains (manuscript underway).

Furthermore, I have demonstrated that the FXII fusion (HisTrx-FXII FnII) also binds to gC1q-R in solution and that an excess of HisTrx-FXII FnII is shown unbound to gC1q-R (Figure 5.4) in a 1:2 molar ratio demonstrating that the other two gC1q-R monomers are unoccupied. This is similar to what was observed for FXII FnII and FXII FnII-EGF1 unbound (excess) to gC1q-R at a molar ratio of 1:2.

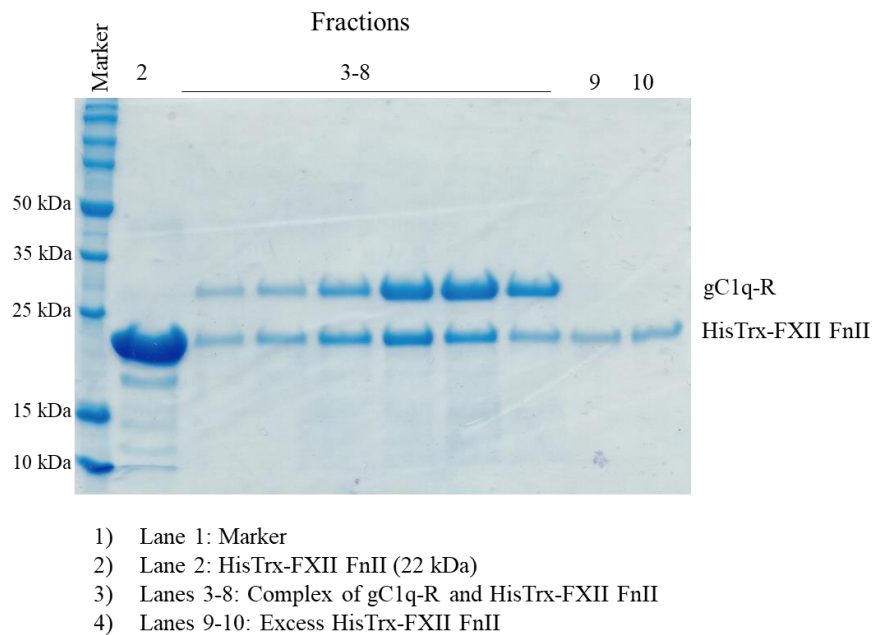


Figure 5.4: Interaction between gC1q-R and WT HisTrx-FXII FnII in the presence of 50 μ M Zn²⁺. A) SDS-PAGE gel of gC1q-R bound and unbound (excess) to HisTrx-FXII. The gel shows collected fractions of formed complex between gC1q-R and HisTrx-FXII FnII (1:2 molar ratio), as shown on lanes 3-8. Fractions on lanes 9 and 10 show unbound (excess) HisTrx-FXII FnII. Lane 2 shows HisTrx-FXII FnII alone next to the marker on lane 1.

5.1.2 Implications of gC1q-R bound to FXII FnII

Figure 5.5A shows an oligomeric peak eluting at 11.4 mL earlier than what was observed for one gC1q-R trimer bound to one FXII FnII at 13.3 mL. All the different ratios of gC1q-R bound to FXII FnII (1:1, 1:2 and 1:3) showed peaks eluting at 11.4 mL, while gC1q-R alone showed no peak eluted at 11.4 mL. As the peak height was not sufficient to run and analyse on SDS-PAGE gel, silver-staining analysis confirmed the presence of FXII FnII in the collected fraction peak (Figure 5.5B).

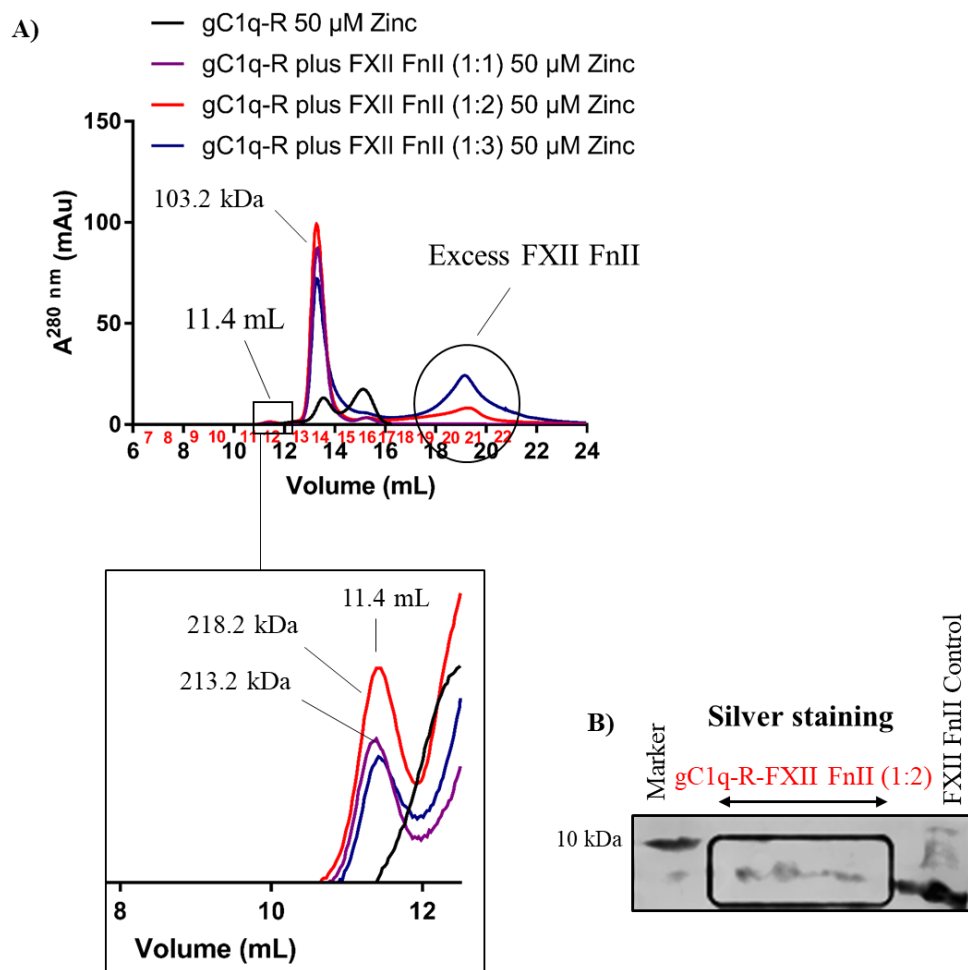


Figure 5.5. Oligomerisation of gC1q-R and FXII FnII. A) Oligomeric peak for gC1q-R and FXII FnII at molar ratios 1:1 and 1:2 is shown eluting earlier at 11.4 mL than the main peak (13.3 mL). B) Shows the presence of FXII FnII following silver staining analysis. FXII FnII on its own is shown on the last lane of the SDS-PAGE gel.

5.2.0 Crystallisation of gC1q-R with FXII FnII domain

5.2.1 Crystallisation of gel filtrated gC1q-R-FXII FnII-EGF1 or gC1q-R-FXII FnII

FXII FnII-EGF1 or FXII FnII in complex with gC1q-R in the presence of Zn^{2+} produced crystals in different crystallisation conditions. For the gC1q-R-FXII FnII (2.6 mg/mL), crystals (Figure 5.6A) were observed in the JCSG+ and Pi-PEG screens and diffracted at low resolution.

Although gC1q-R-FXII FnII crystals were optimised without observing any improvement in crystal quality, gel filtrated gC1q-R-FXII FnII-EGF1 at 5.6 mg/mL in the presence of Zn^{2+} improved crystal quality and produced a single crystals in a condition containing 0.1 M Calcium acetate, 0.1 M Sodium cacodylate pH 5.5, 12 % PEG 8000. From this condition, both gel filtrated gC1q-R-FXII FnII and gC1q-R-FXII FnII-EGF1 were optimised and produced more crystals (Figure 5.6B-F) in the following conditions (0.1 M Sodium acetate, 0.1 M Sodium cacodylate pH 5.3, 8 % PEG 8000) and (0.1 M Sodium acetate, 0.1 M Sodium cacodylate pH 5.7, 12 % PEG 8000).

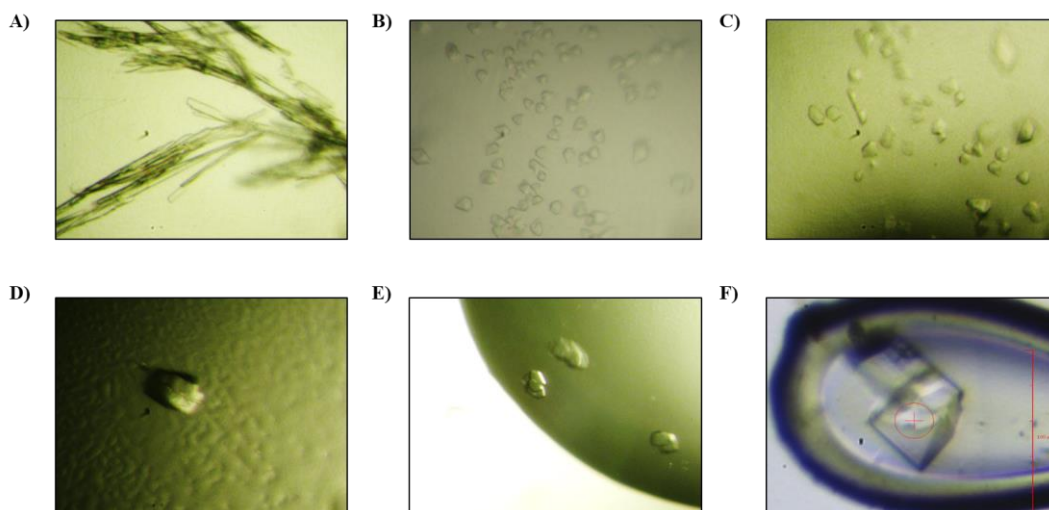


Figure 5.6: Crystals of gC1q-R bound FXII protein domains in the presence of Zn^{2+} . **A)** Crystals of gC1q-R and FXII FnII complex. **B-C)** Crystals of gC1q-R bound FXII FnII-EGF1 from the crystal trial. **D-F)** Optimised gC1q-R-FXII FnII-EGF1. Figure F shows crystals in loop ready to be exposed to X-ray beam from the diamond light source (DLS).

The gC1q-R-FXII FnII crystals again produced low resolution diffraction showing reflections (spots) for more than one crystal, while the gC1q-R-FXII FnII-EGF1 crystals diffracted at medium resolution. Two gC1q-R-FXII FnII-EGF1 crystals from the crystal trial (termed form 4) and optimised condition (termed form 5) diffracted to 3.14 Å and were assigned space groups I121 and C2221 for form 4 and form 5, respectively (Table 5.1).

Table 5.1. Crystallographic data collection statistics.

Sample	Form 4	Form 5
Data collection		
<i>Space group</i>	I121	C2221
<i>Cell dimensions</i>		
<i>a, b, c (Å)</i>	106.3, 71.5, 115.9	72.7, 123.5, 203.3
<i>α, β, γ (°)</i>	90, 110.6, 90	90, 90, 90
<i>Resolution (Å)*</i>	90.99-3.14	67.76-3.14
<i>R_{merge} † (%)*</i>	10.9(45.5)	14.6(56.1)
<i>Mean I / sigI*</i>	6.4(2.0)	10.7(4.0)
<i>Completeness (%)*</i>	99.9 (99.9)	100.0 (100.0)
<i>Redundancy*</i>	3.1(3.1)	5.8(5.7)
<i>CC1/2 †</i>	0.953(0.793)	0.992(0.829)

5.3.0 Crystal structure of gC1q-R bound to FXII FnII-EGF1

To solve the phase problem and find solutions for structure determination, both crystal structures of FXII FnII (unpublished) and gC1q-R (PDB code 1P32) used gave a molecular replacement solution values of LLG 6478 and TFZ score 8.7 for form 4, while form 5 gave a solution of LLG 3324 and TFZ score 17.3. The crystal structure of both forms (4 and 5) revealed a trimeric gC1q-R bound to one FXII FnII with no EGF1 in the asymmetric unit (A.S.U). FXII FnII sits on the surface of gC1q-R and is tethered to the 190-loop of gC1q-R chain C with only part of the 190-loop resolved for form 5 relative to form 4, which has an electron density map in blue for the 190-loop as shown in Figure 5.7A and Figure 5.7B.

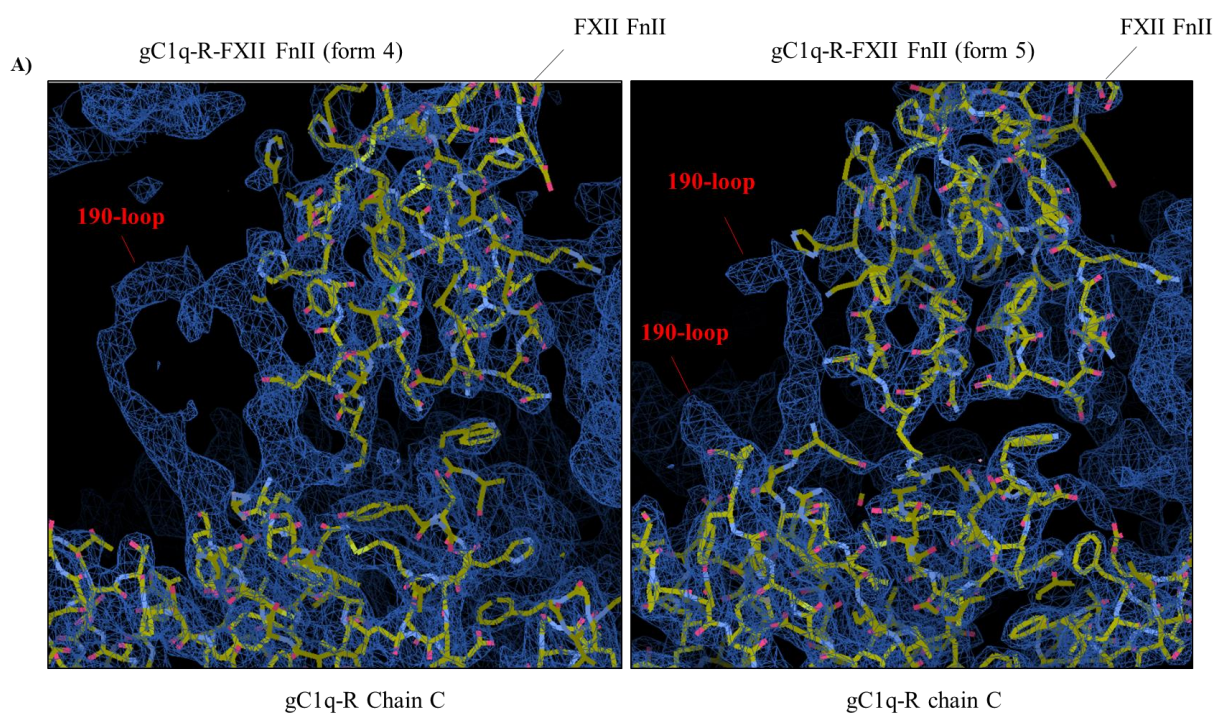


Figure 5.7A: Crystal structure of gC1q-R bound to FXII FnII. Shows electron density map (blue mesh) of gC1q-R chain C (monomer) with loop-190 shown without any residues (no yellow stick) next to FXII FnII. gC1q-R chain C and FXII FnII are represented in yellow stick and displayed to be inside the electron density map. Images were made using COOT.

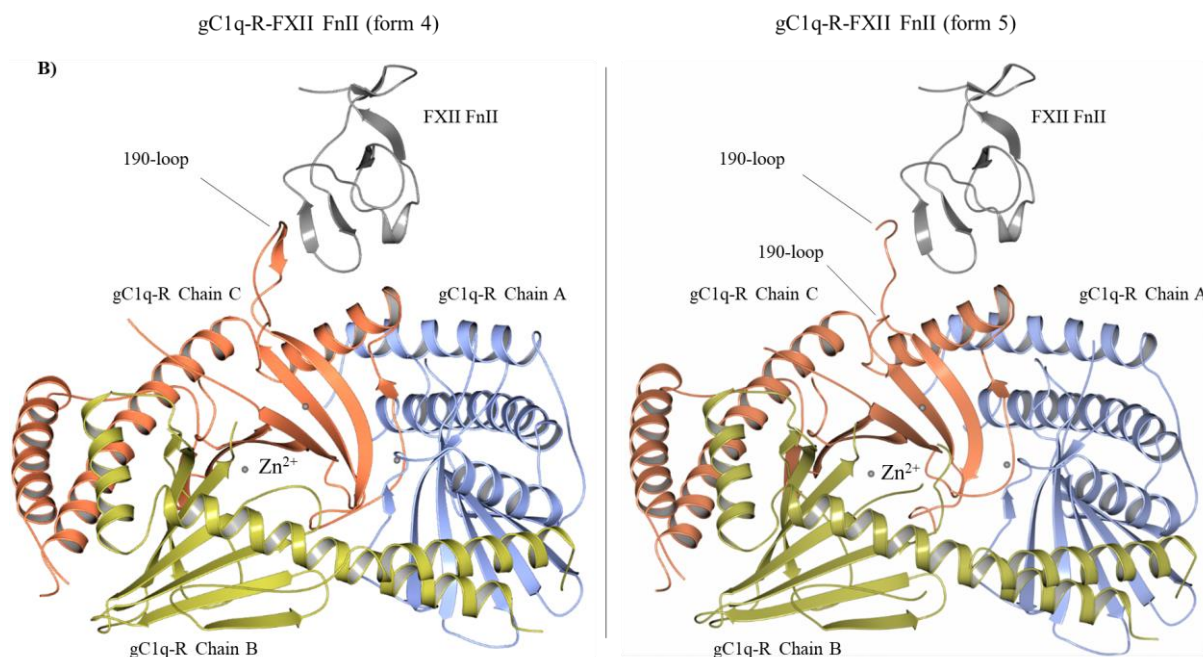


Figure 5.7B: Crystal structure of gC1q-R bound to FXII FnII. gC1q-R trimer made up of monomers A, B and C in ice blue, gold and coral, respectively shows gC1q-R chain C interacting with FXII FnII (grey). Also, in grey are 3 Zn²⁺ (sphere) with each gC1q-R monomer bound to one Zn²⁺. One of the FXII FnII binding sites on gC1q-R is the 190-loop shown with partial representation for form 5. Images were made using QtMG.

To confirm the differences between gC1q-R alone from the Protein Data Bank (PDB code 1P32) to gC1q-R bound FXII FnII (Form 4), structural comparative analysis using QtMG and PYMOL shows key differences in the structural overlay, as shown in Figure 5.8A. The major difference lies in the 190-loop, which in gC1q-R structure alone (cyan) is unresolved thus not present in the gC1q-R structure (PDB code 1P32). In the case of gC1q-R bound to FXII FnII or form 4 shown in cartoon (coral), the 190-loop (coral) is shown resolved and interacts with FXII FnII (grey).

Furthermore, a Zn²⁺ ion was observed bound to each gC1q-R monomer close to the G1 pocket at the base of the acidic 190-loop in strand β 5 with an anomalous difference Fourier showing

three high peaks in the map, whereas no Zn^{2+} ion was observed for gC1q-R alone (Figure 5.8B).

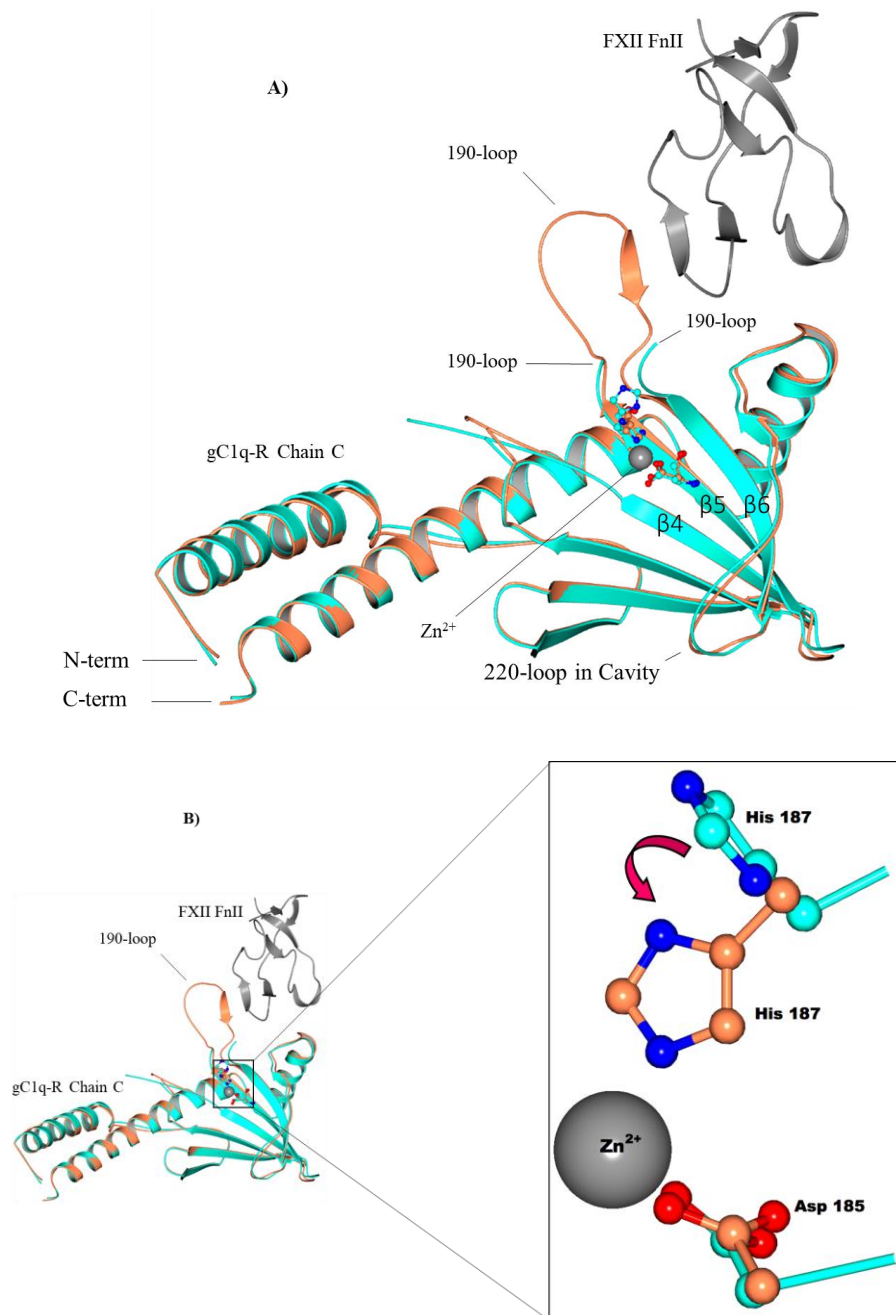


Figure 5.8: gC1q-R chain C showing 190-loop and Zn^{2+} site. A) Resolved 190-loop in gC1q-R-FXII FnlII coral for form 4 is shown while unresolved in gC1q-R alone (cyan). Zn^{2+} site is also shown in grey to be coordinated by His187 and Asp185 (circle in atom type). B) Circle atom type of His187 and Glu185 is shown in the presence of one Zn^{2+} (grey sphere). Full Zn^{2+} ion coordination was observed with H_2O (not shown). Images were made using QtMG.

No Zn^{2+} ion was observed bound to FXII F_{NI} in the gC1q-R-FXII F_{NI} structure, suggesting that FXII F_{NI} was unable to bind to Zn^{2+} when bound to gC1q-R. Comparing FXII F_{NI} alone (form 1) and FXII F_{NI} in the gC1q-R-FXII F_{NI} structure (form 4), no changes in Arg47 insertion into the Trp53-Trp66 pocket and loop 2 was observed for both structures. This leaves the amino acid sequence Pro48-Gly49-Pro50 unchanged as shown in the ball and stick representation in Figure 5.9B.

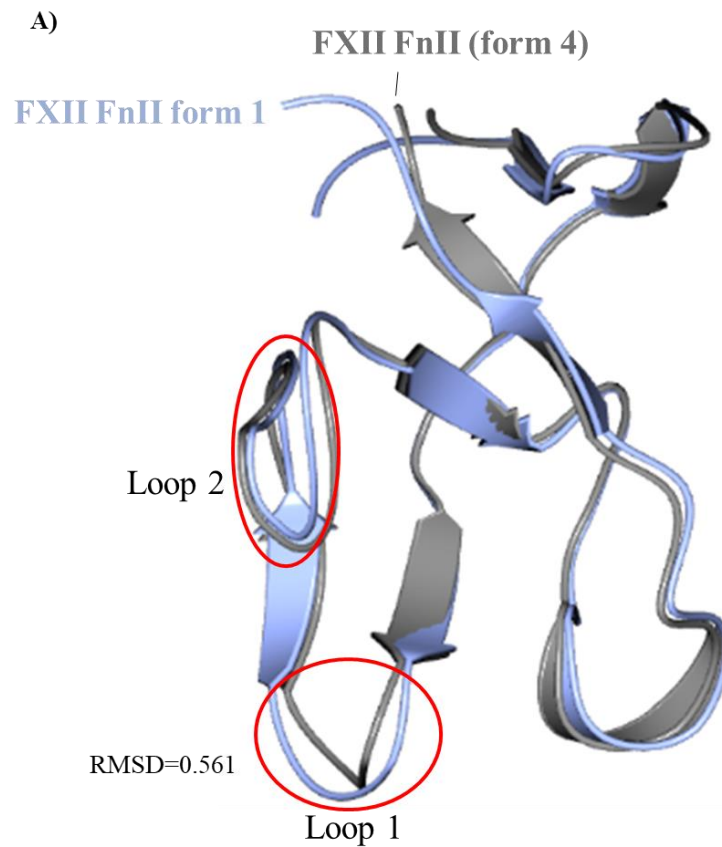


Figure 5.9A: Crystal structure of bound and unbound FXII FnII to gC1q-R. Shows an overlay of FXII FnII (grey) from form 4 and FXII FnII from form 1 (ice blue) and highlights differences in loop 1 and similarities in loop 2 (red circle). Zn^{2+} ions in FXII FnII form 1 are not shown as only loops 1 and 2 are subject to comparison.

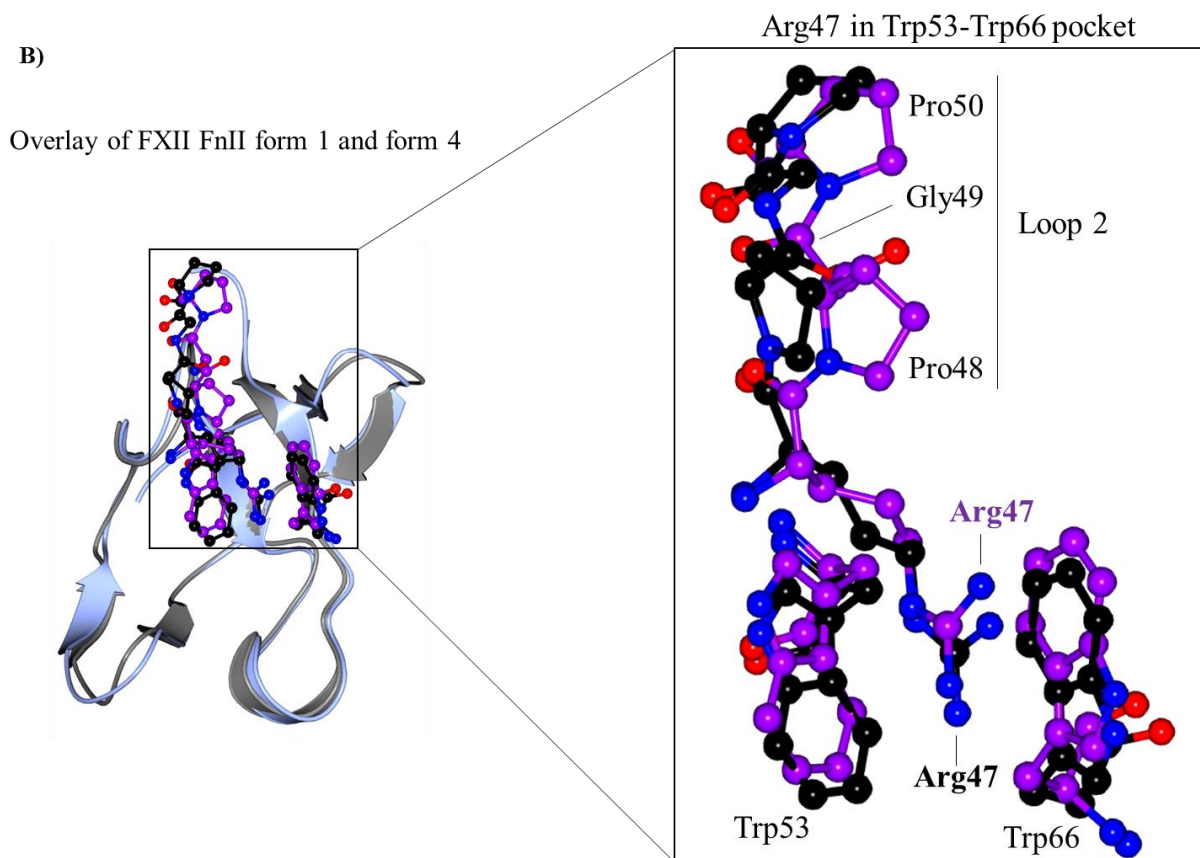


Figure 5.9B: Crystal structure of bound and unbound FXII F_nII to gC1q-R. Ball and stick representation of the Trp53-Trp66 pocket with part of loop 2 sequence Pro48-Gly49-Pro50 shown from the overlay. FXII F_nII form 4 is shown in black ball and stick while FXII F_nII form 1 in purple. Arg47 forms cation- π interaction with Trp66 in both structures.

However, differences in FXII F_nII bound form 4 and form 1 are observed in loop 1, located between strands β 3 and β 4, which contains conserved Arg36. His35 next to Arg36 is held in the 'up' position by Tyr34 in form 4 to avoid clash upon FXII F_nII interaction with gC1q-R. Strand β 4 of FXII F_nII forms hydrogen bonding with a β -strand donated by gC1q-R to form an anti-parallel β -sheet. Arg36 adopts a different conformation to sit on the surface of gC1q-R (Purple) in comparison to Arg36 in FXII F_nII form 1, shown in black ball and stick. Other changes include residues Gln37, His40 and Lys41 (Figure 5.10A). Furthermore, His17 is not

observed in the gC1q-R-FXII FnII structure and is not observed binding to any Zn^{2+} , as there is only electron density accounting for residues Val19-Val20-Leu21 but not His17-Thr18. Amino acid sequence Gln37-Leu38-Tyr39-His40-Lys41 of FXII FnII is shown interacting with the anionic 190-loop, while Arg36 sits on the surface of gC1q-R and occupies the G1 pocket (Figure 5.10B). Furthermore, Gln61 also sits on the surface to interact with Trp233. Trp233 of gC1q-R has been demonstrated to be important in FXII binding, as substituting W233 with Gly, significantly reduces the binding to FXII. Figure 5.10B shows the electrostatic charge surface of gC1q-R, thus demonstrating the negatively charge environment on the surface of gC1q-R.

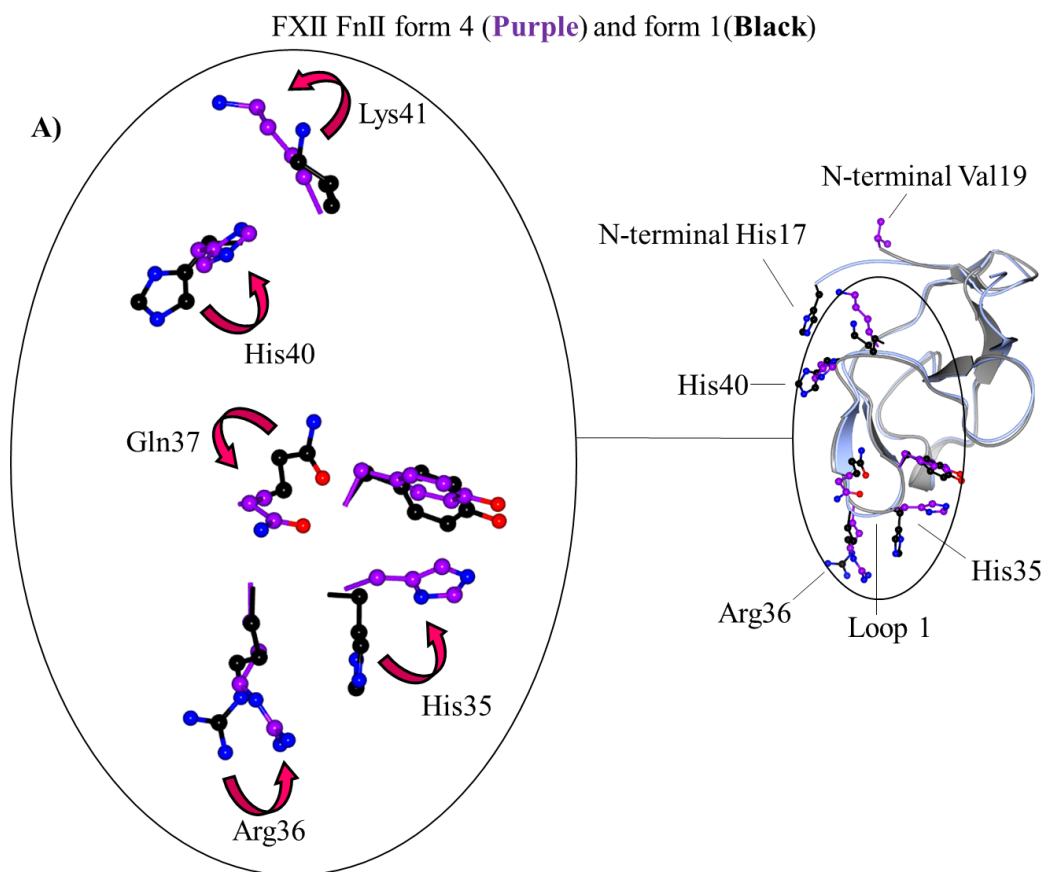


Figure 5.10A: FXII FnII bound to gC1q-R (form 4) showing anionic 190-loop and G1 pocket. An overlay of FXII FnII from form 4 (His35-Arg36-Gln37-Leu38-Tyr39-His40-Lys41) in purple and form 1 in Black.

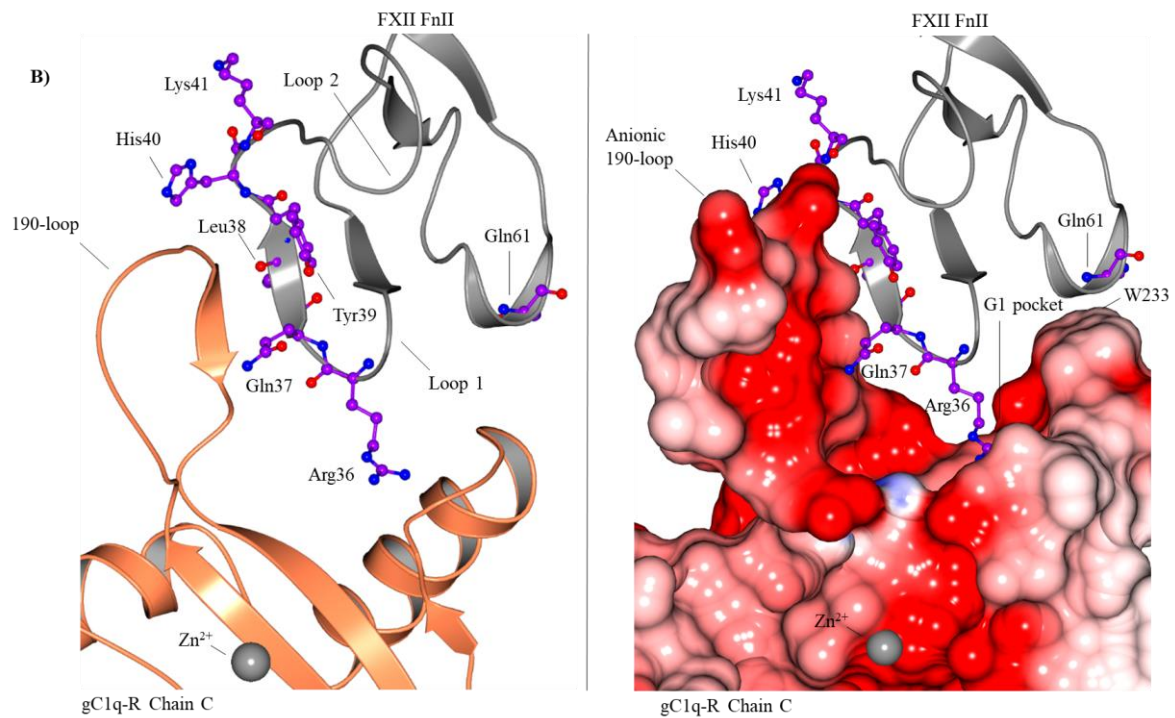


Figure 5.10B: FXII FnII bound to gC1q-R (form 4) showing anionic 190-loop and G1 pocket. Cartoon and surface representation of gC1q-R C chain negatively charged surface with the anionic 190-loop shown engaging FXII FnII residues Gln37-Leu38-Tyr39-His40-Lys41 within and close to β 4 strand, while Arg36 occupies the G1 pocket and Gln61 sits on Trp233 of gC1q-R chain C close to the G1 pocket.

5.4.0 Bridging of FXII FnII to two gC1q-R trimers

The crystal structure for gC1q-R-FXII FnII-EGF1 also revealed a symmetry related copy of gC1q-R trimer binding to FXII FnII using a different binding site from sites shown for the gC1q-R in the asymmetric unit (A.S.U). This is the first reported structure describing a potential second binding site for FXII FnII domain on gC1q-R (Figure 5.11). The aforementioned gel filtration data (refer to subsection 5.1.2) demonstrating the presence of FXII FnII in the oligomeric peak following silver staining and molecular weight calculation to contained two gC1q-R trimers and one FXII FnII in the presence of Zn^{2+} makes this very exciting.

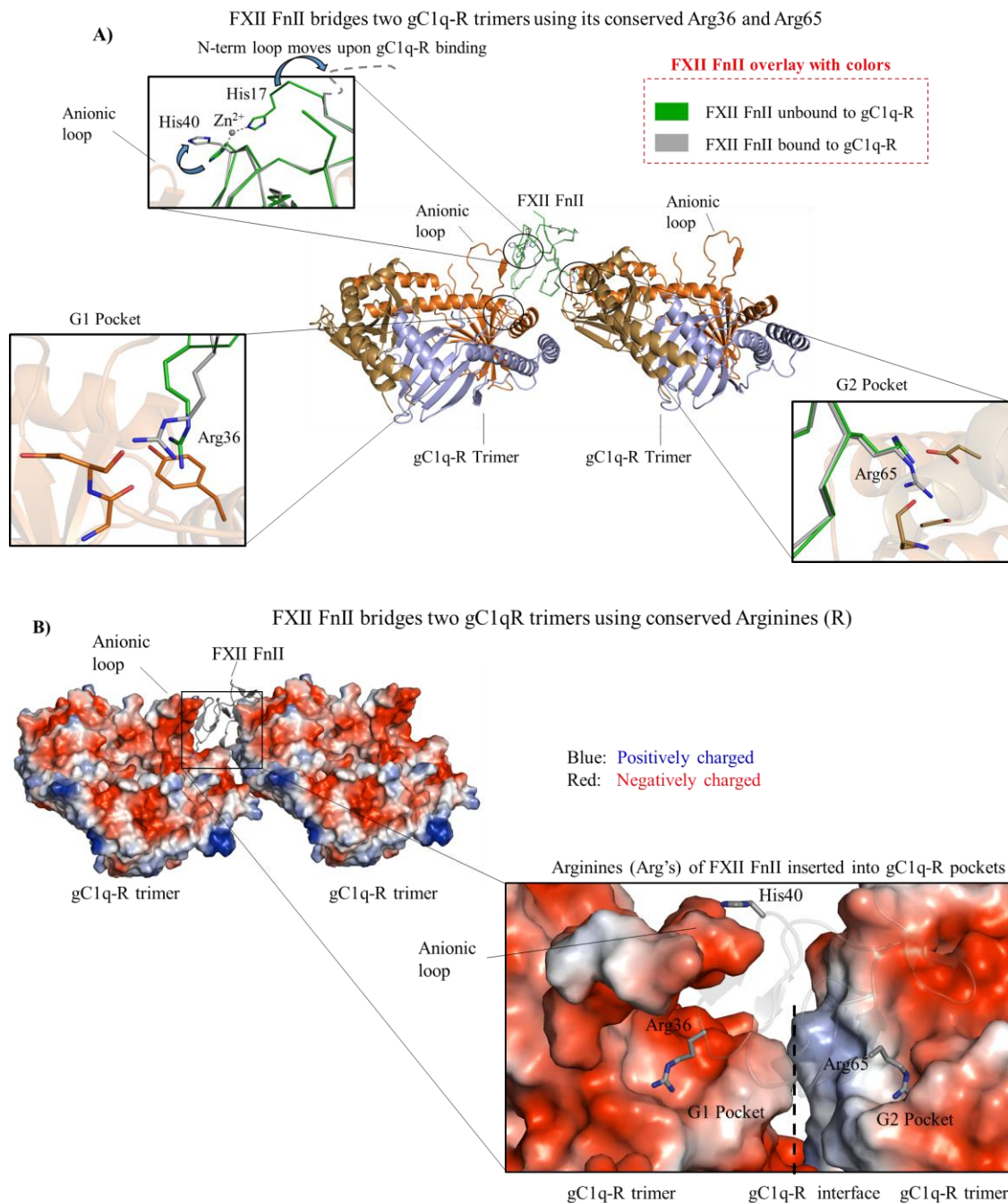


Figure 5.11: FXII FnII bridging two gC1q-R trimers. **A)** FXII FnII Arg36 and Arg65 are shown to sit in pockets G1 and G2 of gC1q-R, respectively. His17 within the N-terminal loop is not resolved in the FXII FnII form 4 (Grey), while in FXII FnII form 1 (Green) His17 and His40 are involved in Zn²⁺ binding. **B)** The anionic 190-loop, G1 and G2 pockets of gC1q-R are represented as electrostatic surface charge with the gC1q-R interface shown for two gC1q-R trimer.

5.5.0 Expression and purification of gC1q-R mutants

5.5.1 Binding kinetics between FXII FnII (or FXII FnII-EGF1) and gC1q-R

To validate and broaden the structural understanding gC1q-R has in binding to FXII and relate the binding to function, binding kinetics was performed using SPR. Figure 5.13A shows a concentration increase (25-250 nM) in FXII FnII binding to immobilised gC1q-R in the presence of Zn^{2+} , demonstrating non-saturable surface, therefore rendering kinetic parameters to not be determined (ND). Notably, a saturated surface following binding of FXII FnII with higher protein concentrations (200-1000 nM) produced 2 K_D values at 38 nM and 50.4 nM for site 1 and site 2, respectively (Figure 5.13B). This was repeated and showed reproducibility and consistency giving similar K_D values 37.7 nM and 64.5 nM (data not shown).

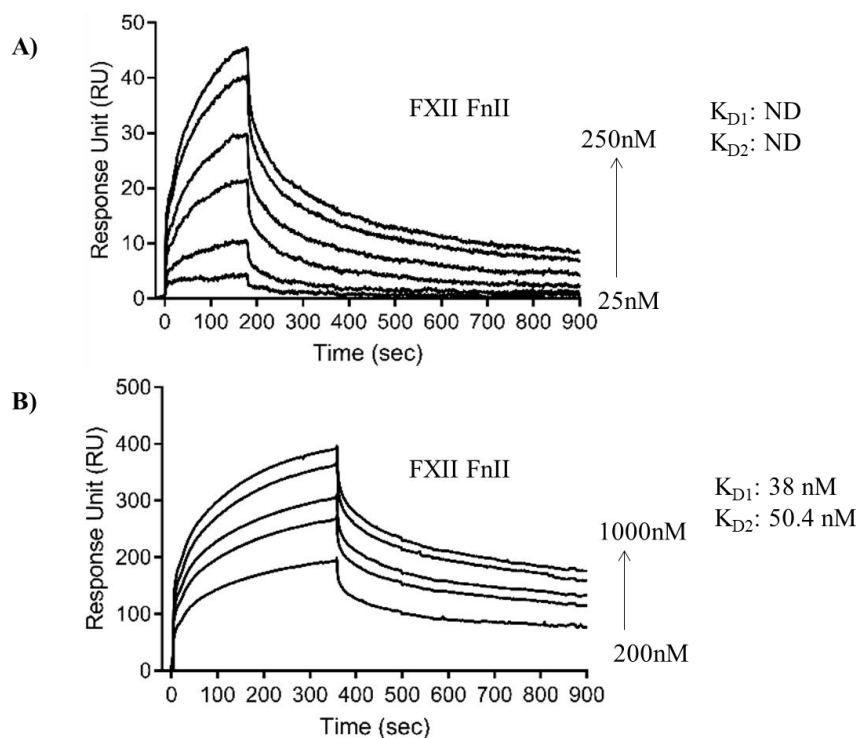


Figure 5.13: Sensogram of FXII FnII binding to immobilised gC1q-R. A) FXII FnII (25-250 nM) and B) FXII FnII (200-1000 nM) response unit following injection onto gC1q-R surface in the presence of Zn^{2+} . The K_D values (K_{D1} and K_{D2}) are displayed on the right. ND for not determined K_D .

Further assessments using the SensiQ Pioneer instrument to determine the K_D values of

FXII FnII and FXII FnII-EGF1 were also tested using a COOH2 (equivalent to CM5 chip) chip. Unlike the concentration series as demonstrated for the BIAcore3000 (Figure 5.13), K_D values were obtained from a single concentrated protein stock (OneStep injection) of either FXII FnII or FXII FnII-EGF1. Data analysis from Figure 5.14 showed consistency and reproducibility with K_D values of 122.1 nM (site 1) and 58.1 nM (site 2) for FXII FnII, while FXII FnII-EGF1 had K_D values of 104 nM for site 1 and 36 nM for site 2.

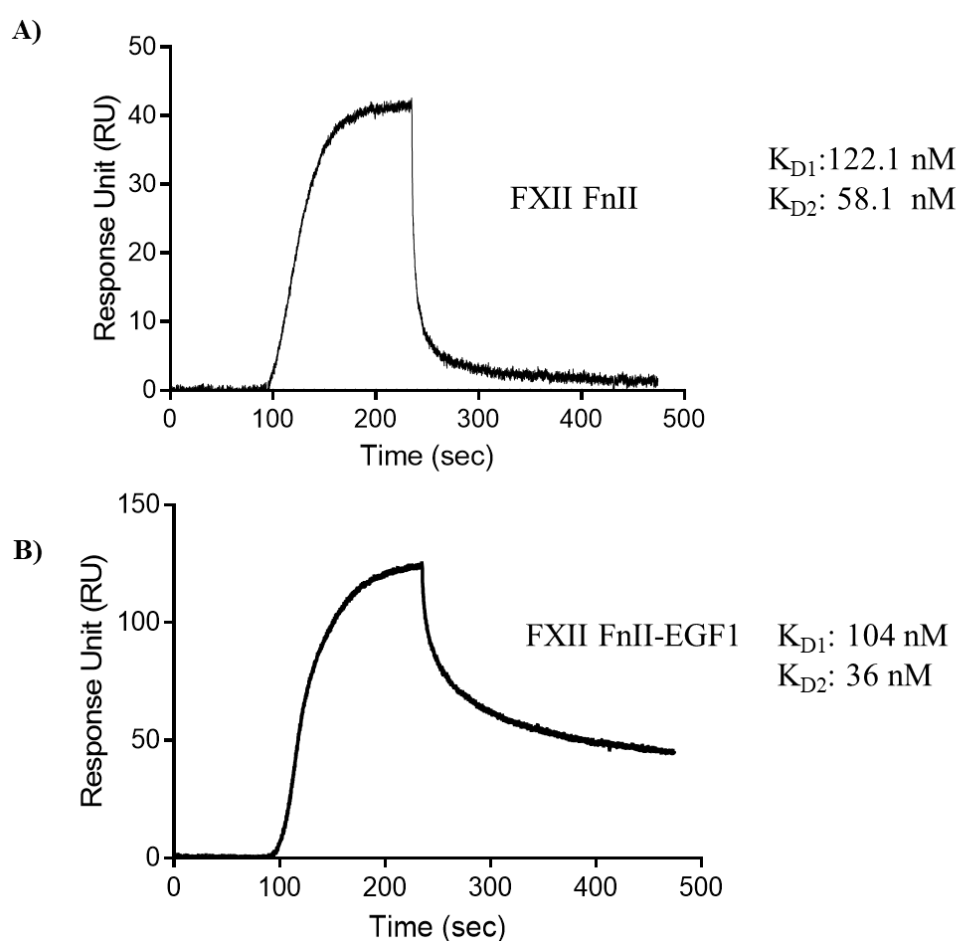


Figure 5.14: Sensogram of OneStep injection of FXII (FnII or FnII-EGF1) on immobilised gC1q-R. A) FXII FnII (1 μ M) and B) FXII FnII-EGF1 (1 μ M) injected onto immobilised gC1q-R on COOH2 chip in running buffer containing Zn^{2+} . K_D values (K_{D1} and K_{D2}) are displayed on the right.

Furthermore, a higher density chip (COOHV) on which gC1q-R is immobilised strengthens the notion of FXII FnII fitting to the 2-site model with K_D values below 200 nM. The data as shown in Figure 5.15A could not be fitted to the 1-site model, as demonstrated below with the red curve representing the model from the Qdat evaluation software and the experimental data in black. However, for Figure 5.15B, the red and black curves are shown to be in agreement as reflected in the low residual standard deviation (ResSD) and fitting with K_D values of $77.9 \pm 0.08 \text{ nM}$ for site 1 and $166.3 \pm 0.2 \text{ nM}$ for site 2. To have more confidence in the data fitting the same experiment was repeated at $50 \mu\text{L}/\text{min}$ and clearly fitted the 2-site model with K_D values (Figure 5.15C) similar to K_D values shown in Figure 5.15B.

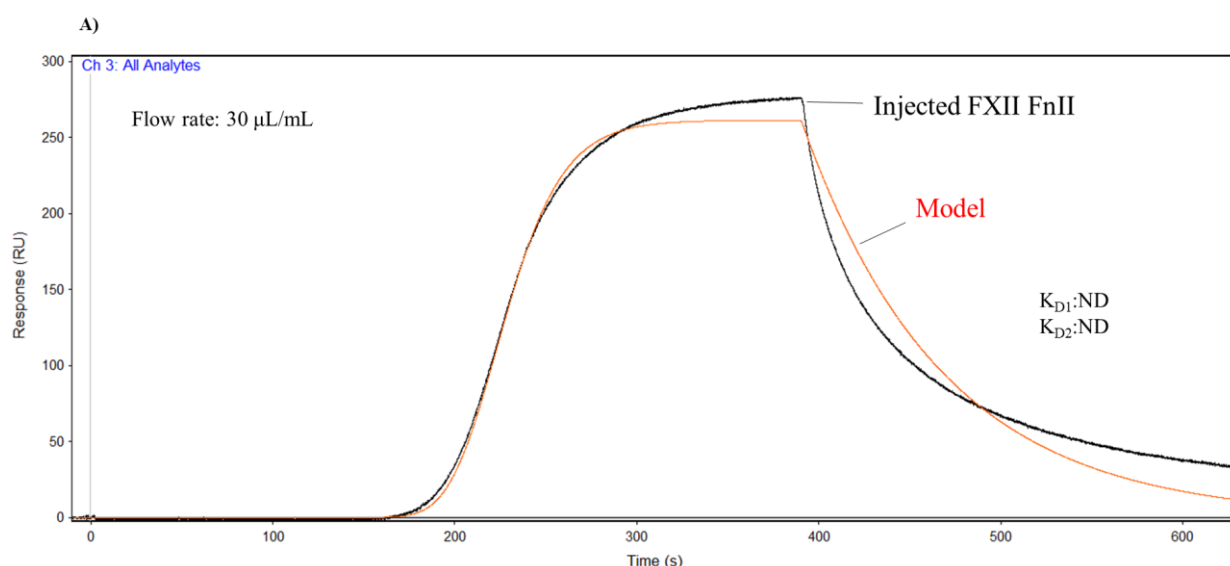


Figure 5.15A: Sensogram of OneStep of FXII FnII. Unfitted model of FXII FnII binding to immobilised gC1q-R with K_D values not determined (ND). Experimental data shown in black and model in red for the 1-site model.

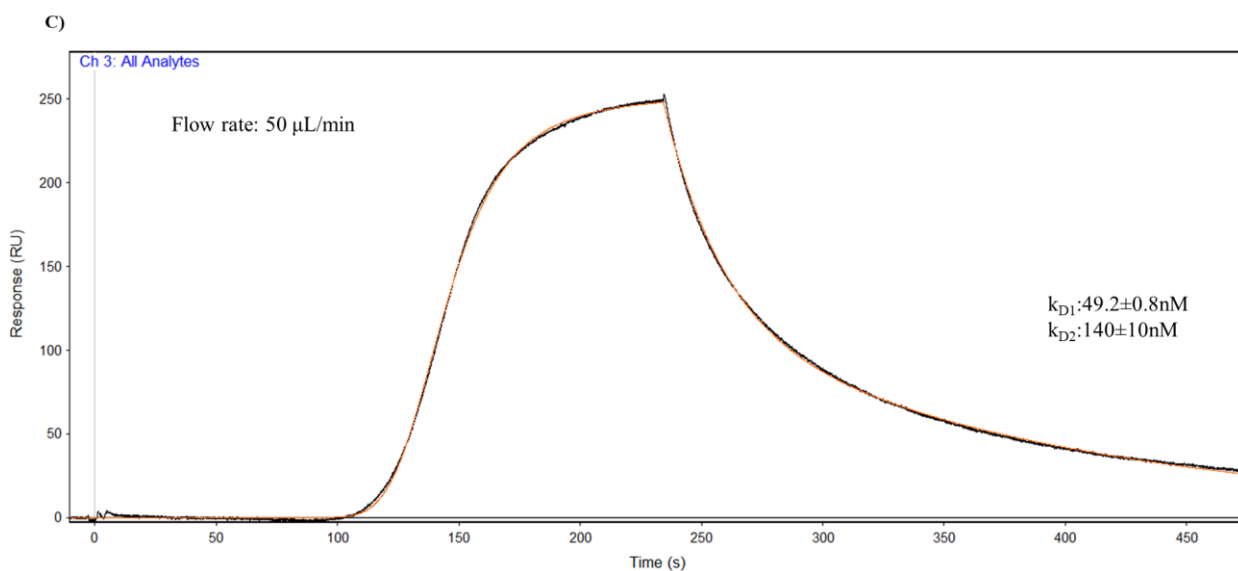
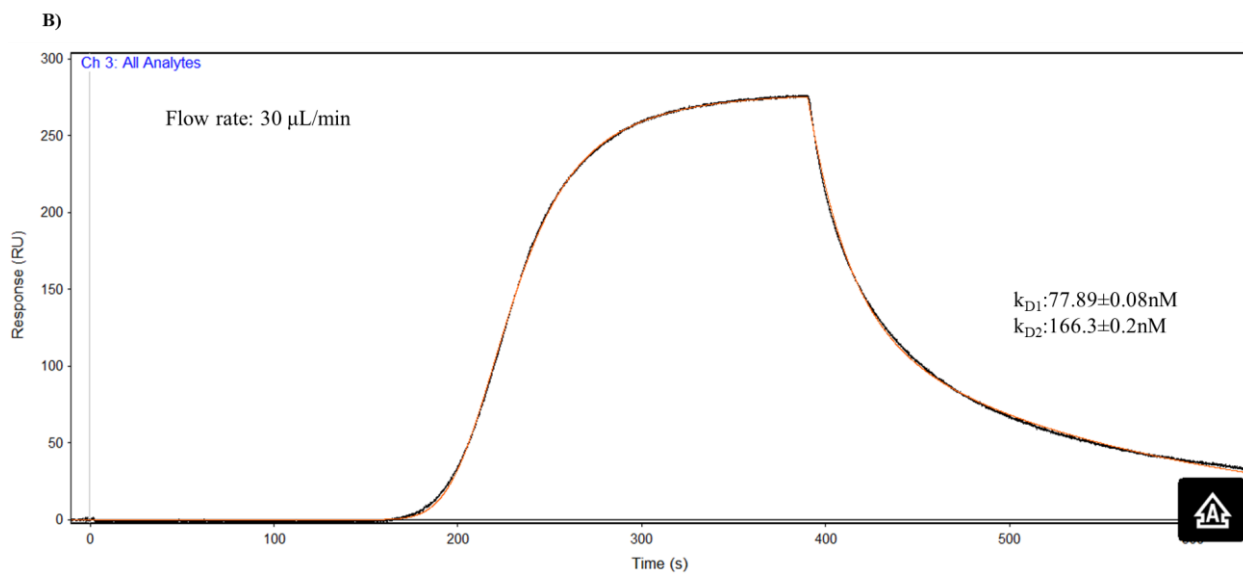


Figure 5.15B-C: Sensogram of OneStep of FXII FnlI. Fitted model of FXII FnlI binding to immobilised gC1q-R. Experimental data is shown in black, fitted to the 2-site model with the model in red shown in **B)** at a flow rate of 30 $\mu\text{L}/\text{min}$ and **C)** repeated at flow rate of 50 $\mu\text{L}/\text{min}$ with K_D for site 1 and 2 displayed.

5.5.2 Binding kinetics between HisTrx-FXII FnII and gC1q-R

HisTrx-FXII FnII fusion was also tested for binding to immobilised gC1q-R on COOH2 on the SensiQ Pioneer instrument and showed a similar binding kinetics to untagged FXII FnII upon analysis from the Qdat evaluation software. A 2-site binding was produced with K_D values of 47.9 ± 0.1 nM and 79.2 ± 0.6 nM for sites 1 and 2, respectively (Figure 5.16). This was repeated and showed reproducibility for both binding sites with K_D values of 48.8 ± 0.1 nM and 80.7 ± 0.6 nM (data not shown). The HisTrx alone was also tested and seem to show nonspecific binding to the sensor surface with K_D values more than $19 \mu\text{M}$ (Figure 5.16). Sucrose (3%) gradient in green is also shown, as it is needed for the diffusion coefficient in data fitting for the OneStep injection.

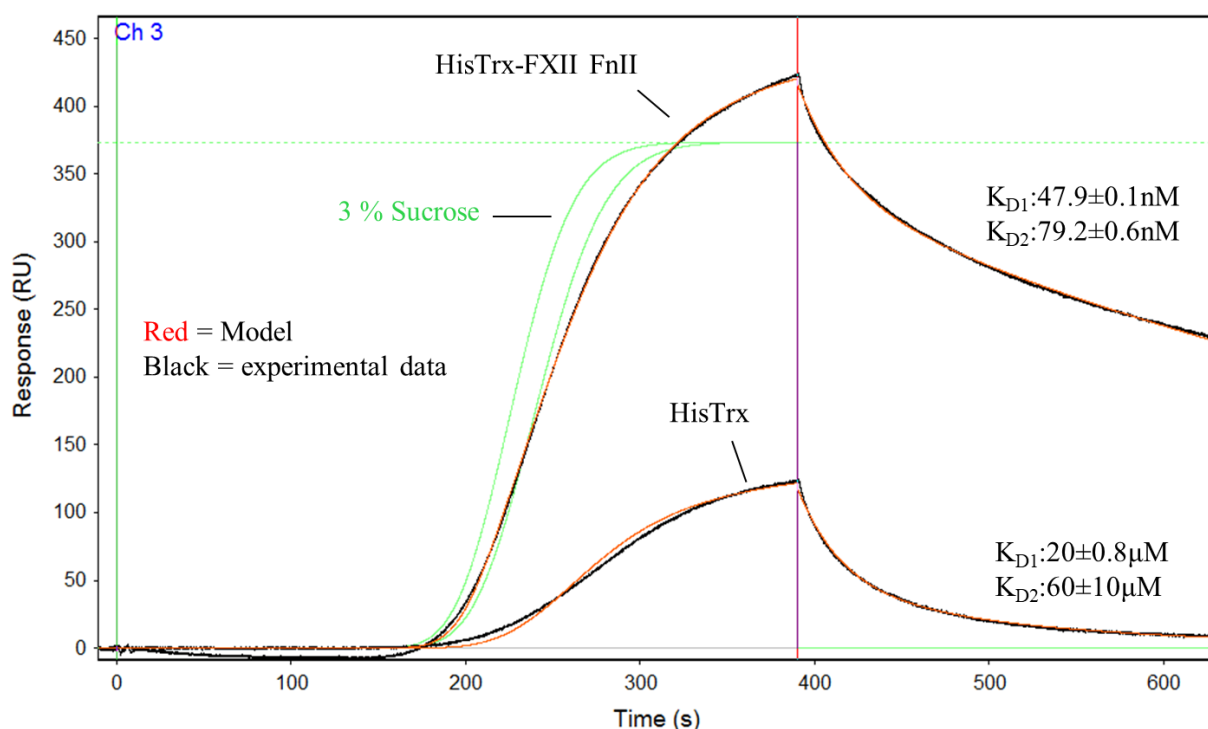


Figure 5.16: Sensogram of OneStep of HisTrx-FXII FnII and HisTrx (Control). Both analytes (WT-HisTrx-FXII FnII and HisTrx tag) were fitted to the 2-site model with model in red and experimental data shown in black. Sucrose (3%) gradient in green is also shown. Respective K_D values are shown on the right hand side next to each fitted curve.

To gain insight into the potential relevance of FXII FnII bridging two gC1q-R trimers in the gC1q-R bound FXII FnII structure, the FXII FnII fusion mutant (HisTrx-FXII FnII Asp63Ala-Gln64Ala-Arg65Ala) was assessed for binding to the G2 pocket of gC1q-R. Although, fusion FXII was used, interesting differences could be seen between for WT-HisTrx-FXII FnII and HisTrx-FXII FnII (Asp63Ala-Gln64Ala-Arg65Ala) mutant. WT-HisTrx-FXII FnII was fitted to the 2-site model, thus reproducing the two K_D values at $33.3 \pm 0.2 \text{ nM}$ for site 1 and $59 \pm 0.8 \text{ nM}$ for site 2. However, when the triple mutant in FXII FnII (HisTrx-FXII FnII Asp63Ala-Gln64Ala-Arg65Ala) was tested under the same condition as the WT-HisTrx-FXII FnII in the presence of Zn^{2+} , binding to immobilised gC1q-R was affected, as reflected in the kinetics parameters (i.e. k_D) following fitting to the 2-site model. The fitting could only produce one K_D at $280 \pm 20 \text{ nM}$ for site 1, while site 2 was unable to give any K_D value thus specified as “uncertain” (or ND) (Figure 5.17).

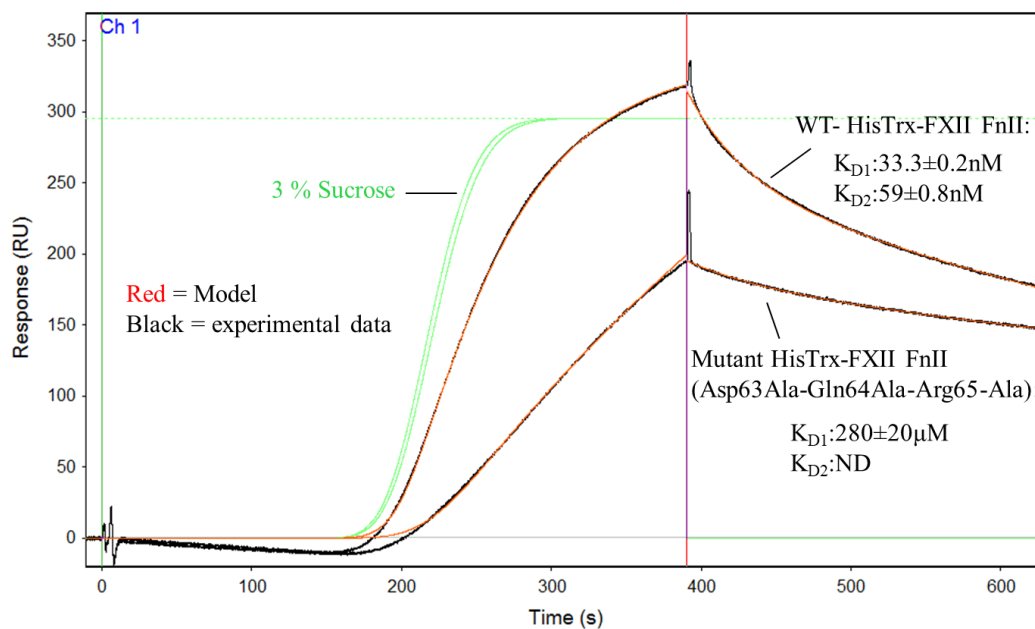


Figure 5.17: The effect of HisTrx-FXII FnII (Asp63Ala-Gln64Ala-Arg65Ala) mutant in binding to G2 pocket of gC1q-R. The K_D values following data fitting are shown for WT HisTrx-FXII FnII above the sensogram and for the HisTrx-FXII FnII (Asp63Ala-Gln64Ala-Arg65Ala) mutant shown below the sensogram.

5.5.3 Binding kinetics between full-length FXII and gC1q-R

To further validate the effect of FXII and gC1q-R binding, gC1q-R mutants were tested for binding to immobilised plasma FXII in the presence of Zn^{2+} . For WT gC1q-R binding to full-length FXII, the binding kinetics (i.e K_D) is reminiscent to gC1q-R binding to FXII F_{NI} and FXII F_{NI}-EGF1. The data reproduces the fitting to the 2-site model (Figure 5.18A) with 2 K_D values at 227 nM for site 1 and 26.4 nM for site 2 and a χ^2 value of 0.126 (Table 5.2) suggesting good fitting to the data.

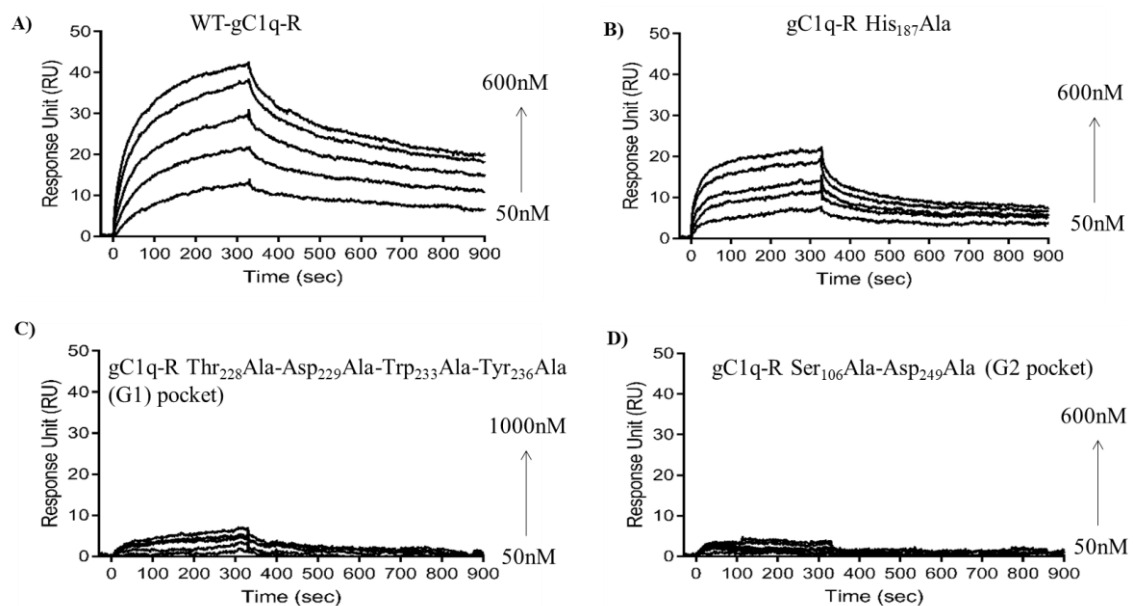


Figure 5.18: Binding of gC1q-R and immobilised FXII. A) WT-gC1q-R (50-600 nM). **B)** gC1q-R His187Ala mutant (50-600 nM). **C)** gC1q-R Thr228Ala-Asp229Ala-Trp233Ala-Tyr236Ala mutant (50-1000 nM). **D)** gC1q-R Ser106Ala-Asp249Ala (G2 pocket) mutant (50-600 nM).

To relate structure to function, a concentration series between 50-600 nM for gC1q-R His187Ala mutant appeared to not show much significant change in the binding, apart from reduced response unit compared to WT gC1q-R (Figure 5.18B). For the gC1q-R Thr₂₂₈Ala-Asp₂₂₉Ala-Trp₂₃₃Ala-Tyr₂₃₆Ala (or G1 pocket mutant) at concentrations of 50-1000 nM, binding to FXII was affected indicating that the G1 pocket in gC1q-R may play a role in FXII binding (Figure 5.18C). Furthermore, to reconcile the HisTrx-FXII FnII Asp₆₃Ala-Gln₆₄Ala-Arg₆₅Ala mutant binding to WT gC1q-R, gC1q-R Ser₁₀₆Ala-Asp₂₄₉Ala (G2 pocket) mutant binding to WT plasma FXII was studied and as shown in Figure 5.18D demonstrates significant reduction in SPR response unit and was unable to fit the model with K_D values not determined (ND).

Table 5.2. Kinetic constants determined at 25 °C (FXII with WT-gC1q-R and mutant gC1q-R).

<i>Biacore3000</i>		Heterogeneous ligand binding model			
<i>gC1q-R</i>		$K_a(M^{-1} s^{-1})$	$K_d (s^{-1})$	$K_D (M)$	Chi^2
WT-gC1q-R	Site 1	1.87×10^4	4.25×10^{-3}	227×10^{-9}	0.126
	Site 2	1.35×10^5	3.57×10^{-3}	26.4×10^{-9}	
gC1qR His187Ala	Site 1	2.46×10^5	3.30×10^{-3}	13.4×10^{-9}	0.178
	Site 2	2.61×10^4	7.23×10^{-3}	277×10^{-9}	
gC1q-R G1 mutant	Site 1	1.33×10^3	8.15×10^{-4}	613×10^{-9}	0.17
	Site 2	1.09×10^4	1.11×10^{-2}	1.02×10^{-6}	
gC1q-R G2 mutant	Site 1	ND	ND	ND	ND
	Site 2	ND	ND	ND	ND

k_a : Association rate constant; k_d : Dissociation rate constant; K_D : Dissociation constant. Numbers under Chi^2 represent the standard error in the model fitting. ND (not determined)

5.6.0 Binding kinetics between FXII and other substrates (PK and FXI)

FXII has been reported to interact with serine proteases including Prekallikrein (PK) and Factor XI (FXI). Kinetic data for binding of FXII to these substrates have not been reported previously; both PK and FXI were tested for binding to FXII using SPR. The figure in 5.19 shows full-length plasma PK binding to immobilised plasma FXII in a concentration dependent fashion. The sensogram analysis in prism Graphpad reports a K_D of 51.4 nM. Furthermore, Figure 5.19B-C maps PK binding site on FXII to be within the FXII FnII domain and not the N-terminal peptide in FXII, upstream of the FXII FnII domain. The N-terminal peptide alone does not bind to immobilised PK at concentrations of 100 nM, 500 nM and 1000 nM, while binding to immobilised PK is recorded for FXII FnII (plus 22mer N-terminal peptide) at minimum concentration of 25 nM (Figure 5.19C). The binding curves (sensogram) in Figure 5.19C is not saturated and cannot deduce any K_D values from it.

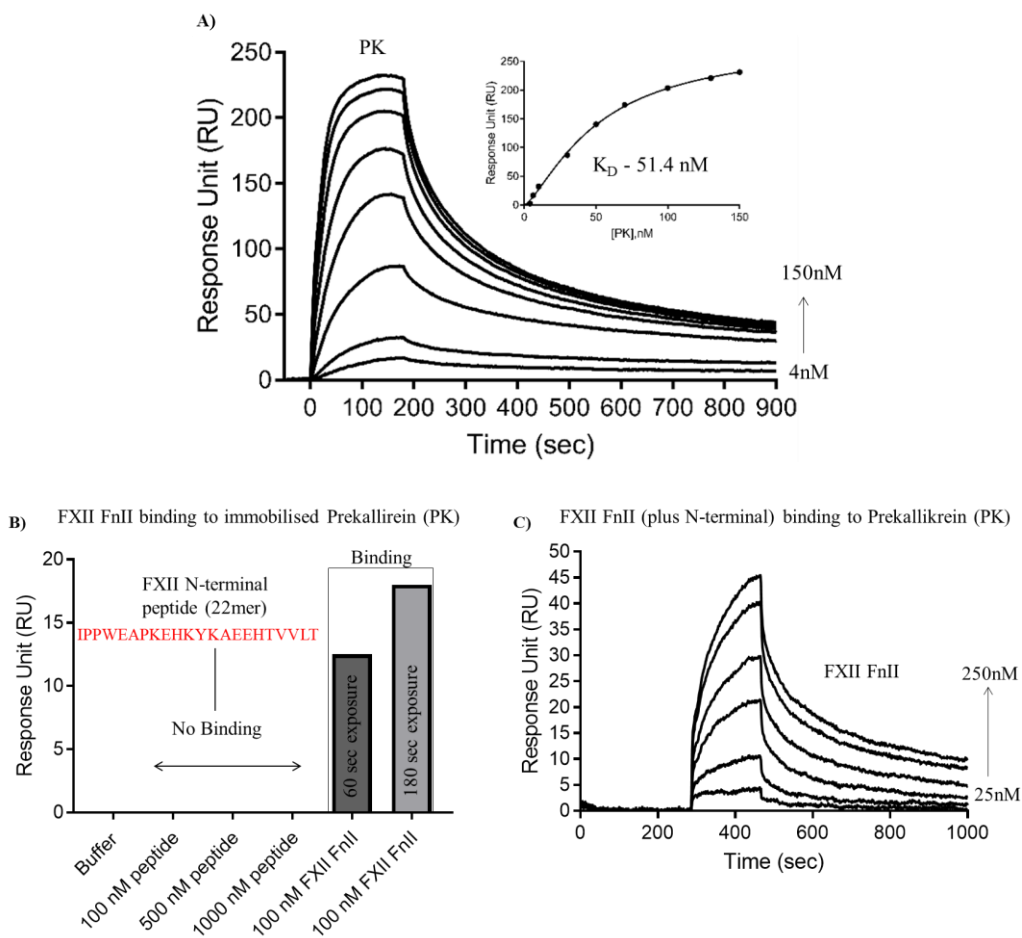


Figure 5.19: FXII binding to PK. **A)** Full-length PK binding to immobilised FXII on CM5 chip in a concentration dependent manner (4-150 nM) with a hill plot subsequently plotted to determine the binding. **B)** FXII FnII with FXII N-terminal peptide (22mer) showed binding, while the N-terminal peptide (22mer) alone showed no binding to immobilised PK. **C)** Unsaturated dose-dependent binding of FXII FnII to immobilised PK.

FXII FnII lacking or containing the N-terminal peptide (22mer) binding to immobilised Factor XI (FXI) was also studied and showed a consistent profile, in that the N-terminal peptide (22mer) was unable to bind both PK (Figure 5.19B) and FXI (Figure 5.20A). Figure 5.20B (for immobilised FXI), similar to immobilised PK (Figure 5.19B) was observed to bind to recombinant FXII FnII. This might not be surprising as FXI and PK have a similar domain organisation and share a 58 % homology.

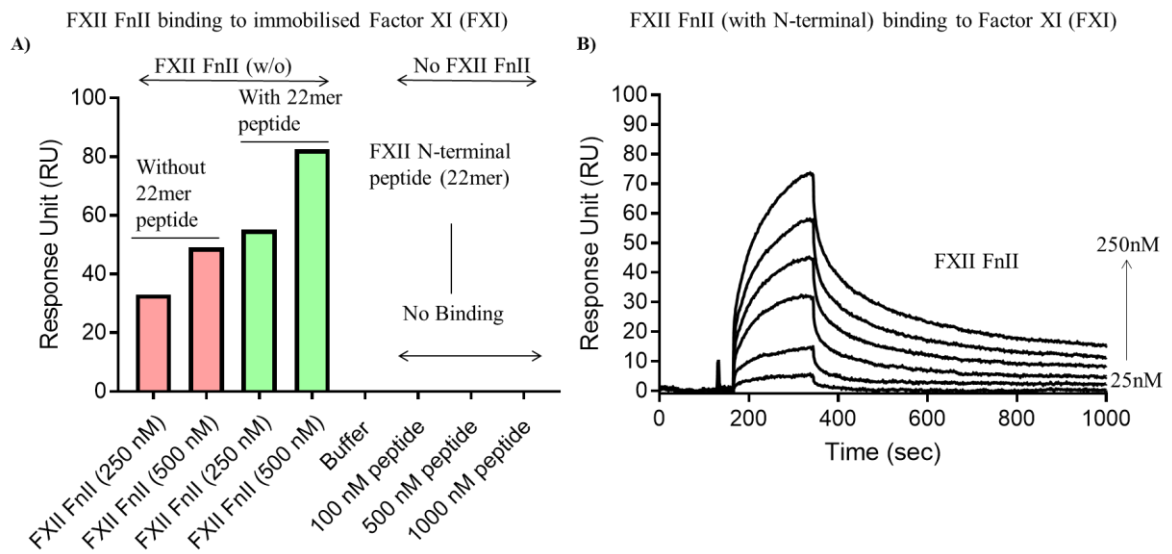


Figure 5.20: FXII binding to PK. A) FXII FnlI without N-terminal (22mer) peptide (in hot pick bar at 250 nM and 500 nM) and FXII FnlI with N-terminal (22mer) peptide (in Limegreen 250 nM and 500 nM), while N-terminal (22mer) peptide alone showed no binding at concentrations 100 nM, 500 nM and 1000 nM. **B)** Unsaturated dose-dependent binding of FXII FnlI with N-terminal (22mer) peptide to immobilised FXI.

5.7.0 Discussion

5.7.1 FXII binding to gC1q-R in the presence of Zn²⁺ using gel filtration

Previous studies from Kaplan has shown contact activation occurring in the presence of contact factors FXII and HK bound PK when gC1q-R and Zn²⁺ is added. However, the molecular assembly of the system is presently not reported in the literature. The analytical gel filtration analysis of gC1q-R in complex with full-length FXII isolates higher oligomers with calculated molecular weights of 396.2 kDa and 446.6 kDa for molar ratios of 1:1 and 2:1, respectively. Moreover, a preparation of gC1q-R bound to FXII F₁₁ with excess FXII F₁₁ produced a small peak eluting earlier than the main gC1q-R bound FXII F₁₁ peak. The small peak has a calculated molecular weight of 213.2 kDa and is approximately twice the size of the main peak eluting at 103 kDa. This indicates one molecule of gC1q-R bound to one FXII F₁₁ for the 103 kDa peak, while FXII F₁₁ could potentially bridge two gC1q-R trimers to give a hydrodynamic radius of 213.2 kDa.

This is the first in solution studies showing gC1q-R-FXII complexes in the presence of Zn²⁺, although Zn²⁺ concentration of 50 μM has been reportedly demonstrated to mediate binding of FXII to negatively charged macromolecules such as polyphosphates and gC1q-R in cell-based studies or ELISA. The data presented in this thesis confirmed that complex formation of gC1q-R and FXII F₁₁ with reduced Zn²⁺ concentration at 10 μM does not result into complex formation on gel filtration. This therefore supports and strengthens the notion of higher Zn²⁺ concentrations at 50 μM as a requirement for gC1q-R and FXII to form a complex in solution. In plasma, Zn²⁺ concentrations are relatively low at around 10-15 μM and free Zn²⁺ in plasma is less than 1 μM due to binding to albumin. However, collagen activated platelets have been demonstrated to release Zn²⁺ and support contact activation. Cells including endothelial cells

have also been reported to increase local Zn^{2+} concentrations. Concentrations of Zn^{2+} may play a role in regulating contact activation in the microenvironment to prevent premature triggering of the contact activation system.

5.7.2 Crystal structure of FXII FnII bound to gC1q-R

The crystal structure of FXII FnII bound to gC1q-R (FXII FnII-gC1q-R) in the presence of 1 Zn^{2+} ion bound to each monomer of gC1q-R and no Zn^{2+} ion bound to FXII FnII is the first complex structure providing an in-depth molecular insight into how FXII interacts with the complement receptor gC1q-R. Ghebrehiwet et al previously reported deletion of the anionic 190-loop (₁₉₆EDEAESD₂₀₂) and Trp233 mutant (Tryptophan 233 substituted to Glycine) for gC1q-R to have poor binding for FXII in a Solid-phase microplate binding assay. This is consistent with the unpublished FXII FnII-gC1q-R crystal structure, which also shows FXII FnII interacting with both the anionic 190-loop (₁₉₆EDEAESD₂₀₂) and Trp233 of gC1q-R ⁽²³¹⁾.

The anionic 190-loop for the gC1q-R structure alone (PDB code 1P32) ⁽²⁰⁷⁾ was not resolved and appeared to have been mobile thus not shown in the structure. However, binding of FXII to gC1q-R stabilises the anionic 190-loop and is therefore resolved; indicating that the 190-loop is flexible when unbound to FXII. Novel interactions observed for the FXII FnII-gC1q-R structure interestingly reveal FXII engagement by gC1q-R G1 and G2 pockets, with a Zn^{2+} binding site located beneath the G1 pocket. HK has been reported to bind to the anionic 190-loop (₁₉₆EDEAESD₂₀₂) and amino acid residues 204-218 on gC1q-R, located slightly beneath the Zn^{2+} binding site. The latter binding site was demonstrated by deleting 204-218 which renders the gC1q-R monomeric and therefore cannot provide any conclusive evidence for the relevance of this site in HK binding. Both HK and FXII cannot bind to the same anionic 190-

loop (₁₉₆EDEAESD₂₀₂) as this may contradict establishment of both contact factors (HK and FXII) being required for contact activation. Both the anionic 190-loop (₁₉₆EDEAESD₂₀₂) and 204-218 on β -strand 6 are systematically been shown to not bind to HK (unpublished data by Dr Alexander Slater - not shown).

Both HK and FXII have been reported to require Zn^{2+} for binding to gC1q-R and in the FXII FnII-gC1q-R crystal structure one Zn^{2+} ion is observed bound to each monomer of gC1q-R. This was confirmed by the anomalous difference Fourier map at a contour of 7.4 r.m.s and the bond distances between 2.0 to 2.2 Å for Zn^{2+} coordination in all three identical monomer were also observed. Although, Zn^{2+} binding to gC1q-R has previously not been reported in relation to contact activation, the FnII-gC1q-R complex structure reveals for the first time binding to gC1q-R but not for the gC1q-R structure alone. Spectrophotometric analysis of Zn^{2+} binding to gC1q-R has been reported to cause a conformational change in the C-terminus of gC1q-R, thereby exposing hydrophobic residues detected by a fluorescent dye at a given wavelength⁽³¹³⁾. Interestingly, FXII FnII uses basic amino acid residues to bind within the C-terminal part of gC1q-R.

Furthermore, human gC1q-R has been reported to bind to basic peptides such as Rubella capsid protein (RCP), Histone 4 (H4) and Lamin binding protein (LBP) in a Zn^{2+} independent fashion, while in the case of HK and FXII, Zn^{2+} is a requirement for binding.

Although Zn^{2+} is only seen binding to each monomer of gC1q-R and not FXII FnII in the FXII FnII-gC1q-R structure, it is plausible to suggest that FXII only requires Zn^{2+} at the initial stages to undergo a conformational change for binding to gC1q-R and no longer requires Zn^{2+} upon binding to gC1q-R. Upon comparing the FXII FnII structure (form 1) to the FXII FnII in the FXII

FnII-gC1q-R structure (form 4), a clear similarity was noted in the Trp53-Trp66 pocket and loop 2.

In both FXII FnII structures (form 1 and form 4), the Trp53-Trp66 pocket adopted an open conformation thus facilitating Arg47 to sit in the Trp53-Trp66 pocket. However, differences were observed in FXII FnII amino acid residues His35-Arg36-Qln37-Leu38-Tyr39-His40-Lys41 which interacts with the anionic 190-loop and the G1 pocket of gC1q-R. The N-terminal His17 shown in the FXII FnII structure (form 1) alongside His40 to coordinate Zn^{2+} 3 are no longer involved in creating the Zn^{2+} site as the N-terminal His17 in the FXII FnII-gC1q-R becomes mobile thus unresolved due to no electron density to account for it. His40 on the other hand is resolved and interacts with the anionic 190-loop of gC1q-R. This highlights the transition and dynamics FXII FnII underwent from being saturated with Zn^{2+} to interacting with gC1q-R.

Additionally, conserved FXII FnII residues (Asp63-Qln64-Arg65) never reported to interact with gC1q-R is observed to bridge gC1q-R by inserting its conserved Arg65 into the gC1q-R G2 acidic pocket, while Asp63 electrostatically interacts with conserved Arg122 of gC1q-R to strengthen the interaction.

As gC1q-R has been demonstrated to co-localise HK and FXII on the endothelial cell surface, I suspect the bridging effect observed in the FXII FnII-gC1q-R structure may broaden our understanding of whether gC1q-R trimers are brought together upon FXII or HK binding to create a larger surface area for effective contact activation. In other words, it is plausible to suggest whether size matters as it relates to having oligomers of gC1q-R providing FXII and HK bound PK a stable platform to dock and bring FXII and PK in close proximity with reasonable alignment for effective proteolysis.

This idea has been reported in the field by researchers including Coen Maas (University Medical Center Utrecht). Triggering contact activation using smaller polymer size of around 70-chain unit of polyphosphate or nanoparticle polyphosphates from platelets does certainly indicate that size does matter; as nanoparticle polyphosphate is significantly more potent in triggering contact activation. Although, gC1q-R is not a polymer but also a negatively charged macromolecule, similar to polyphosphate in providing a surface for contact activation for FXII and HK bound PK, a similar behaviour relating to size may be considered for gC1q-R. The recombinant gC1q-R oligomer isolated from gel filtration showed in the activation assay to have a measureable difference in substrate conversion relative to gel filtrated gC1q-R trimer in the presence of Zn^{2+} .

5.7.3 Binding studies of FXII FnII and gC1q-R

Validation to determine the binding constant of FXII FnII (or FXII) to gC1q-R in real time in the presence of Zn^{2+} complemented the aforementioned concept for the bridging effect suggested for the gC1q-R-FXII FnII structure and the 213.2 kDa eluant (two gC1q-R trimer and one FXII FnII) from the analytical gel filtration. The SPR data could only successfully fit into the 2-site model and therefore suggests FXII FnII bridging two immobilised gC1q-R on the sensor surface.

The model assumes that two independent sites on the immobilised gC1q-R are being engaged by FXII FnII and is therefore consistent and strengthens the initial hypothesis of molecular bridging between gC1q-R and FXII. FXII variants (FnII and FnII-EGF or HisTrxFXII FnII) consistently reproduced the K_D values for the 2-site model from BIAcore3000 and SensiQ Pioneer.

5.7.4 Binding studies of FXII to WT gC1q-R and gC1q-R mutants

To further relate the gC1q-R bound FXII F_nI₁ structure to function; immobilised full-length plasma zymogen FXII was tested for binding to WT gC1q-R and gC1q-R mutants. Interestingly, WT gC1q-R as analyte reproduced a similar binding kinetics to FXII F_nI₁ bound to immobilised WT gC1q-R and fitted into the heterogeneous ligand-binding model in which two independently distinct sites (2-sites) on immobilised FXII are able to recognise. This furthermore strengthens the reproducibility of the data under different conditions and most importantly, recapitulates the significance of the model being proposed for the molecular bridging of FXII and gC1q-R.

In line with the FXII and gC1q-R structure, gC1q-R G1 mutant (Thr228-Asp229-Trp233-Tyr236 substituted to Ala228-Ala229-Ala233-Ala236) validates the functional relevance of the G1 pocket in gC1q-R and its effect in FXII binding. The Zn²⁺ site on each monomer of the gC1q-R in the gC1q-R-FXII F_nI₁ structure may require further studies to establish its functional role in gC1q-R binding. The reason for this is because the gC1q-R mutant in which His187 is mutated to Ala showed no apparent change in binding to FXII when compared to WT gC1q-R. Furthermore, titration (using Isothermal Titration Calorimetry – ITC) of 800 μM ZnCl₂ into the cell containing 20 μM gC1q-R His187Ala mutant suggested that this mutant is capable of binding to Zn²⁺ with a K_D of 109 μM compared to 74.1 μM for WT gC1q-R.

Furthermore, complex formation of gC1q-R His187Ala mutant and WT HisTrx-FXII F_nI₁ fusion form a complex on gel filtration (data not shown) and confirmed on SDS-PAGE gel (data not shown) to have both FXII and gC1q-R band present, indicating that the His187Ala mutant is not really having any noticeable effect in the binding. The His187 displays no significant

molecular changes for gC1q-R alone overlaid to the gC1q-R-FXII FnII structure, even though the His187 undergoes a conformational change to facilitate Zn²⁺ binding. The molecular basis of Zn²⁺ mediating gC1q-R and FXII binding still remains unclear.

Another interesting gC1q-R mutant tested for the first time is gC1q-R G2 pocket (Ser106-Asp249 substituted to Ala106-Ala249 or Asp249 to Ala249), as this binding site was predicted by Prof. Emsley and myself that FXII utilises this pocket to bridge gC1q-R trimers. The binding response for the gC1q-R G2 pocket mutant was significantly reduced and unable to be fitted to the model.

Alternatively, SPR analysis and validation of the HisTrx-FXII FnII triple (Asp63Ala-Gln64Ala-Arg65Ala) mutant compared to the WT-HisTrx-FXII FnII seem to have a measurable effect in the binding to immobilised WT-gC1q-R with Zn²⁺ in the running buffer. WT-HisTrx-FXII FnII binding to immobilised gC1q-R reproduced two K_D values, while the mutant HisTrx-FXII FnII (Asp63Ala-Gln64Ala-Arg65Ala) could only produce a K_D value for site 1 with K_D for site 2 “uncertain” therefore not determined (ND). The K_Ds for WT-HisTrx-FXII FnII were consistent when compared to immobilised gC1q-R binding to insect expressed untagged FXII FnII or FXII FnII-EGF1. This may suggest that the observable difference in how WT-HisTrx-FXII FnII binds to immobilised gC1q-R relative to mutant HisTrx-FXII FnII (Asp63Ala-Gln64Ala-Arg65Ala) is therefore plausible and could demonstrate the relevance of the gC1q-R G2 pocket and the FXII Asp63-Gln64-Arg65 binding.

5.7.5 FXII and substrates Prekallikrein (PK) and Factor XI (FXI)

Although, binding of FXII to Prekallikrein (PK) is known ⁽³¹⁴⁾, this is the first binding studies showing the affinity of the binding using SPR. FXII binding to PK or FXI is important for activated FXII (FXIIa) to bind and activate substrates PK and FXI to impact thrombosis or

haemostasis, respectively. It has also been suggested that FXII heavy chain may bind to PK or FXI ⁽³¹⁴⁾ and the SPR data have shown a dose-dependent increase in FXII F_{nII} of FXII heavy chain binding to immobilised PK or FXI, although further characterisation is required to determine the strength of the binding.

Furthermore, the data indicates that the 22 amino acid peptide, upstream of FXII F_{nII} may not be involved in binding to PK or FXI as FXII N-terminal peptide (22mer) at concentrations of 100 nM, 500 nM and 1000 nM show no binding. This is contrary to a paper published in 1998 where Citarella F et al. report that amino acid residues 3-19 of the N-terminal peptide are important in binding to FXI upon deletion of this residue or using a synthetic peptide to compete with full length FXII for binding to FXI ⁽³¹⁴⁾. Whether both the N-terminal peptide (22mer) and FXII F_{nII} together contribute in binding to PK or FXI is yet to be explored. The FXII F_{nII} structure reveals that the N-terminal peptide (22mer) is highly disordered and using a synthetic peptide to characterise binding might not necessarily demonstrate binding even though disordered loops can be subject to stabilisation upon binding to proteins. However, our stable and folded FXII F_{nII} proteins (w/o) the N-terminal peptide does shed light on the capability of the FXII F_{nII} (without the 22mer) to bind to FXI.

CHAPTER 6.0

BINDING AND FUNCTIONAL STUDIES OF FXII, HK AND gC1q-R IN THE PRESENCE OF Zn²⁺ IONS

6.1.0 Interaction of FXII (or FXII and HK) to gC1q-R

6.1.1 Interaction between gC1q-R and mFXII in solution

To determine binding of gC1q-R and FXII in solution, a molar ratio of 1:1 and 1:2 of full-length mFXII to gC1q-R was made and isolated on an S200 10/300 column at 9.84 mL and 9.54 mL, respectively. This is the first reported complex formation of FXII and gC1q-R in solution in the presence of 50 μM Zn^{2+} and shows that excess gC1q-R in the 1:2 (Blue peak) molar ratio elutes at a higher molecular weight with increased absorbance when compared to a molar ratio of 1:1 (red peak), as shown in Figure 6.1. Controls of FXII alone (green) and gC1q-R trimer and dimer (black) give an indication of the shift on the left when a complex is formed.

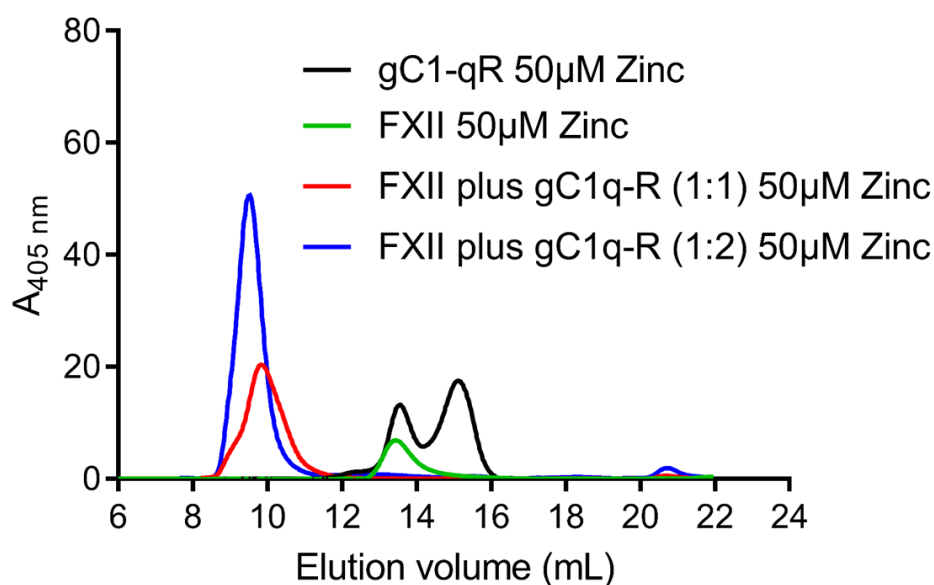


Figure 6.1: Complex formation of mFXII-gC1q-R in the presence of Zn^{2+} . Complex formation of mFXII and gC1q-R in solution in the presence of Zn^{2+} is shown. gC1q-R alone in black (trimer and dimer), FXII (in green), mFXII-gC1q-R complex (1:1) in red and mFXII-gC1q-R complex (1:2) in blue in running buffer containing 50 μM Zn^{2+} .

Furthermore, a heterogeneous mixture containing zymogen and activated mFXII (mFXII and mFXIIa) is shown demonstrating complete mFXII conversion to mFXIIa in the presence of gC1q-R and Zn²⁺ (Figure 6.2). Figure 6.2 shows a peak shift to the left with no excess mFXIIa observed at a molar ratio of 1:1 of gC1q-R to mFXII (mFXII/mFXIIa) in solution. The SDS-PAGE gel of the fractions shows heterogenous mixture of mFXII and mFXIIa on lane 2 next to the marker, while mFXIIa bound to gC1q-R produces two bands for mFXIIa (heavy chain and light chain), indicating mFXII activation under reducing condition. The gC1q-R may be in the same band as the mFXIIa light chain, as the band intensity increase from left to right unlike the mFXIIa heavy chain.

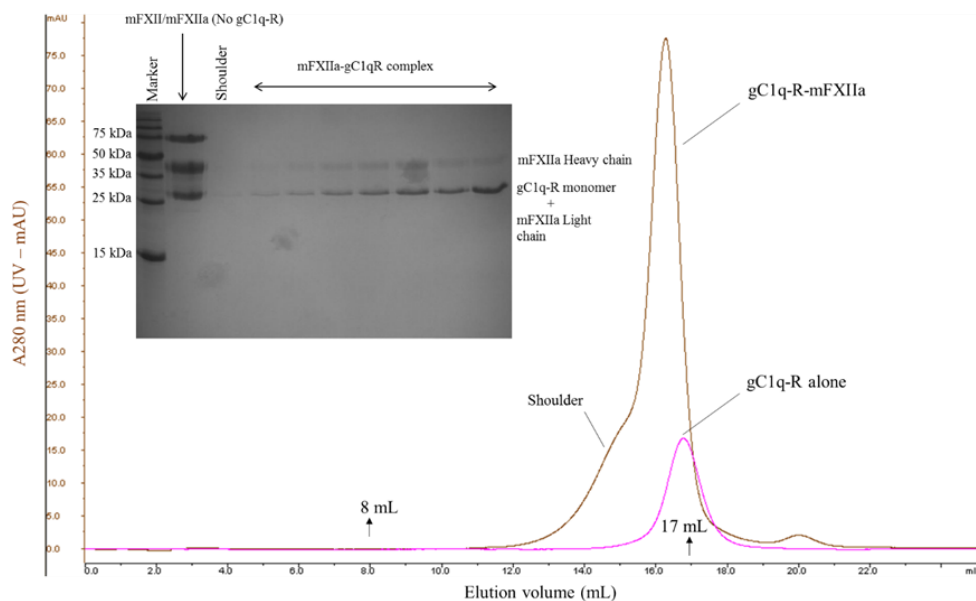
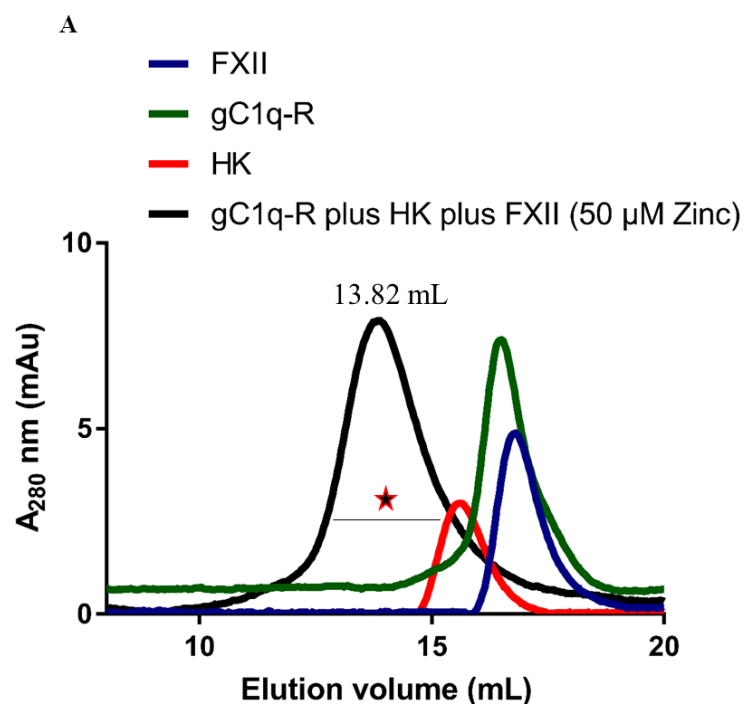


Figure 6.2: gC1q-R interaction with mFXII/mFXIIa mixture. A 1:1 molar ratio of gC1q-R and mFXII (mixture of mFXII/mFXIIa) was made in 50 μ M Zn²⁺, incubated and isolated on S6 column show a peak shift (Brown) relative to gC1q-R alone (Pink). A shoulder peak was observed, followed by a high and well-defined peak eluting around 16 mL. The fractions from the gC1q-R-mFXII peak were run on SDS-PAGE gel. This showed all zymogen mFXII to have been converted to active mFXIIa. gC1q-R (33 kDa) and FXII light chain (28-30 kDa) may migrate as one band thus showing no separation on this SDS-PAGE gel.

6.1.2 Interaction of human FXII and human HK to gC1q-R

FXII and HK have reportedly been demonstrated in the literature to compete for binding to gC1q-R, as HK has a much higher preference to bind gC1q-R with a K_D of 9 nM. Here, I show for the first time that FXII and HK can both simultaneously bind to gC1q-R in solution in the presence of Zn^{2+} . This supports the notion of contact activation being triggered when FXII and HK bound PK are present on a negatively charged surface, as a model having all components in close proximity for efficient proteolysis is plausible.

Figure 6.3A, shows a peak for gC1q-R, HK and FXII in the presence of Zn^{2+} and demonstrates that contrary to what has been suggested before that gC1q-R is capable of having both HK and FXII bound to it in solution. All the individual proteins as control (gC1q-R, HK and FXII) were also ran separately and all eluted at a much later elution volume compared to the gC1q-R-HK-FXII complex eluting at 13.82 mL. The relative calculated molecular weight for the gC1q-R-HK-FXII complex was 478.7 kDa.



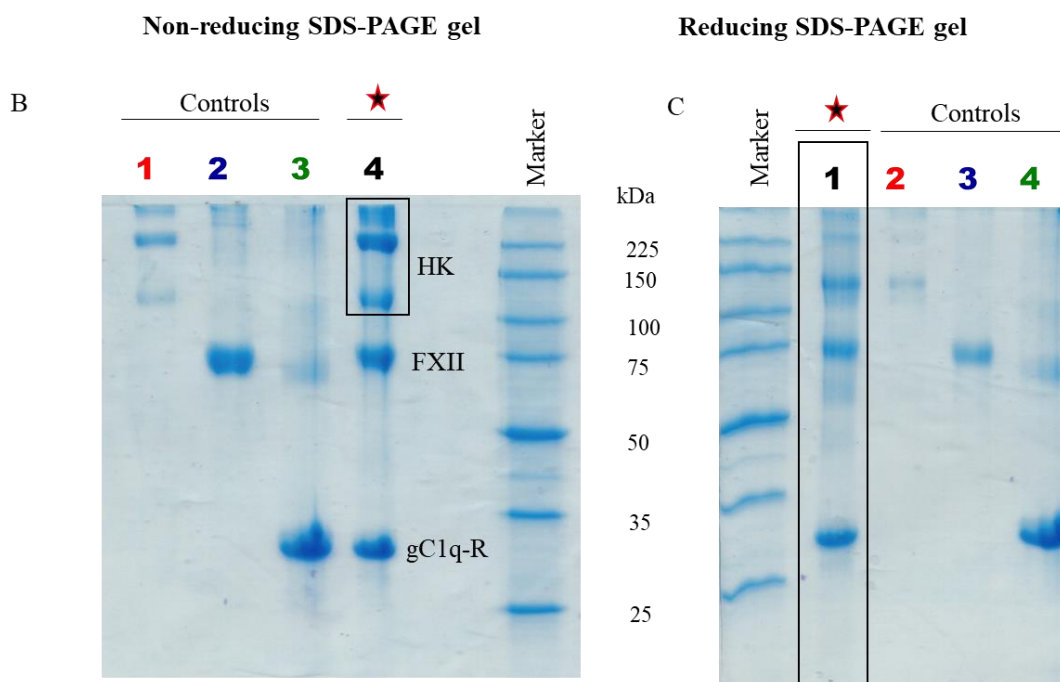


Figure 6.3: FXII-HK-gC1q-R complex formation in solution with Zn^{2+} added. A) FXII-HK-gC1q-R complex formation (in black) eluting at 13.82 mL. Individual controls (all human forms) for HK, gC1q-R and FXII in red, green and blue, respectively are also shown on the gel filtration column (S6 10/300) profile. The fractions under the peak (in black) highlighted with a black line and asterisk above it were subjected to SDS-PAGE gel under **B)** non-reducing and **C)** reducing conditions.

SDS-PAGE gel analysis of the gC1q-R-HK-FXII complex is shown under non-reducing (Figure 6.3B) and reducing (Figure 6.3C) condition. The SDS-PAGE gel shows the presence of all the three proteins (filled star – bands for HK, FXII and gC1q-R) on lane 4 and lane 1 under non-reducing and reducing condition, respectively. Also, the protein controls are shown with their respective colours to make comparison easier.

6.1.3 Interaction of mFXII and human HK to gC1q-R

In solution mFXII was also demonstrated to bind to gC1q-R in the presence of HK and Zn^{2+} (Figure 6.4A) and also elutes at a similar elution volume profile (elution volume 13.8 mL) to

gC1q-R-HK-hFXII complex (Figure 6.3), regardless of excess gC1q-R present. The gC1q-R-HK-mFXII complex peak eluting at 13.8 mL was shown to have bands corresponding to all three proteins (gC1q-R-HK-mFXII) on the SDS-PAGE gel under reducing condition (Figure 6.4B).

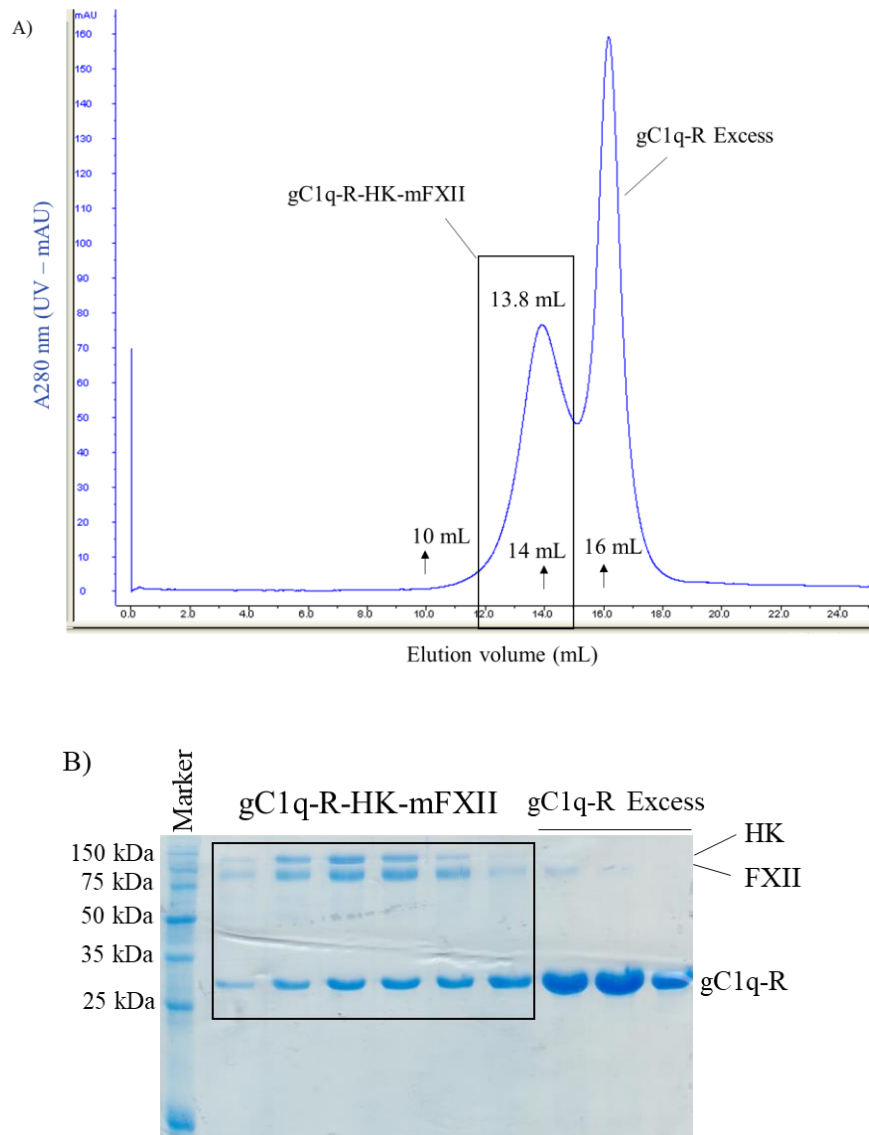


Figure 6.4: Complex formation of mFXII-HK-gC1q-R in solution in the presence Zn^{2+} . **A)** Two Peaks eluting at around 13.8 mL and 16.7 mL. **B)** On SDS-PAGE gel peak eluted at 13.8 mL shows bands for mFXII-HK-gC1q-R on same lane, while excess gC1q-R on the last three lanes.

HK and gC1q-R complex was also demonstrated to form in the absence of Zn^{2+} (Figure 6.5A-B) and is in line with what Dr Alexander Slater found and documented in his PhD thesis (unpublished data). The HK-gC1q-R complex produced two peaks a shoulder and a main peak eluting at 12.7 and 14.1 mL, respectively. The relative calculated molecular weight for the HK-gC1q-R complex is 401.6 kDa. This is reminiscent of what was aforementioned for mFXII-gC1q-R complex with respect to a shoulder forming in solution.

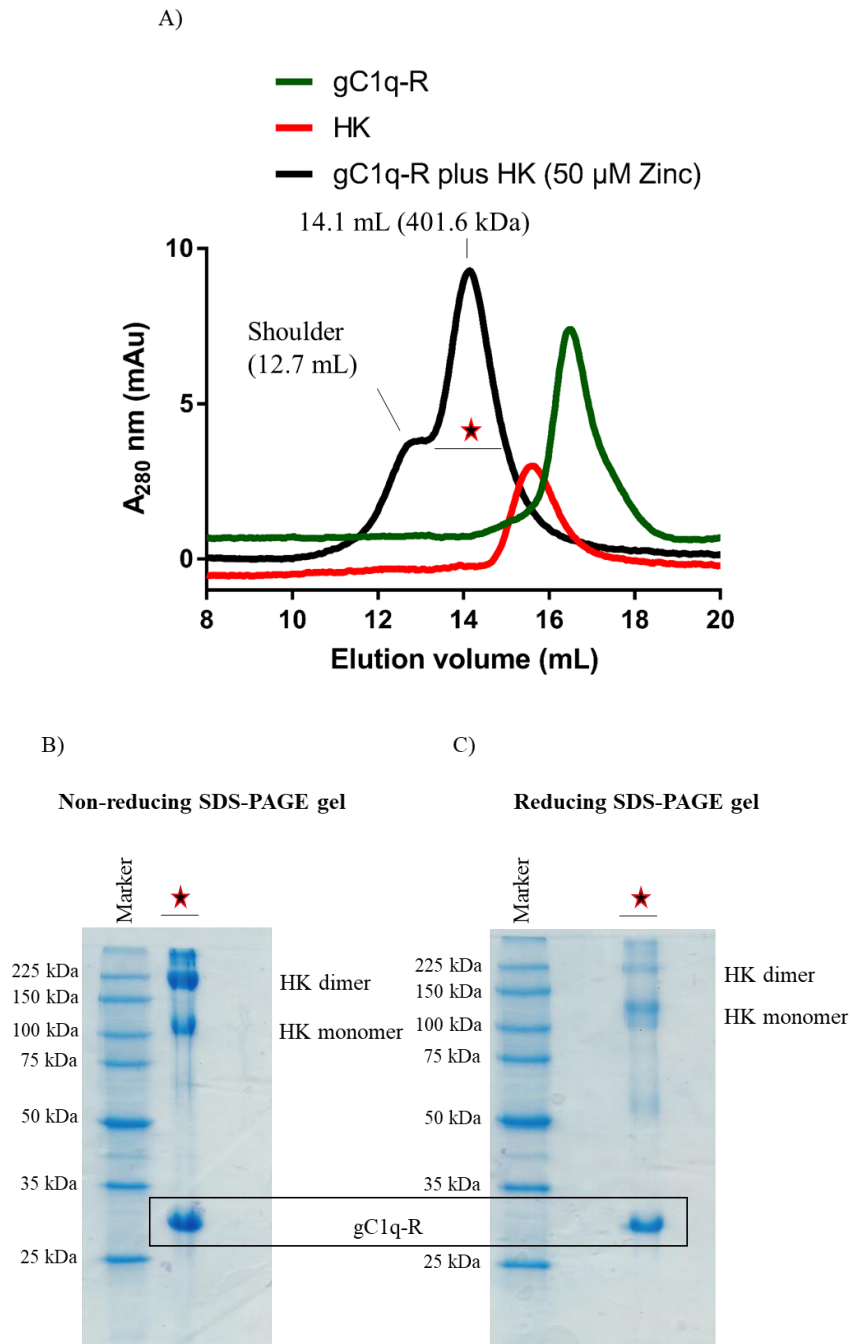


Figure 6.5: HK-gC1q-R complex formation in solution with Zn^{2+} added. A) A mixture of HK-gC1q-R was isolated from S6 10/300 column in HEPES buffer containing 50 μ M Zn^{2+} . HK-gC1q-R (in black) elutes at 14.1 mL with a shoulder peak eluting earlier at 12.7 mL. Individual controls HK (Red) and gC1q-R (Green) were separately ran on the column. Fractions (Black line with red and black asterisk) under the HK-gC1q-R complex peak were pooled and TCA precipitated and ran on a B) 12 % SDS-PAGE gel under both non-reducing and reducing conditions.

6.2.0 Contact activation assay for FXII and HK bound PK

To corroborate the complex formation of gC1q-R-FXII-HK into function, an enzyme activity assay was performed in the presence of Zn^{2+} . For Figure 6.6A, no activation was observed for gC1q-R alone and in the presence of gC1q-R and FXII (Figure 6.6B) or gC1q-R, HK and PK (Figure 6.6C) no activation of FXII or PK was observed either.

However, when the reaction contains gC1q-R, FXII, HK and PK plus Zn^{2+} , the FXIIa and PKa substrate (S-2302) is proteolytically cleaved to release pNA, which absorbs at 405 nm. This therefore indicates that both FXII and PK have become activated, as demonstrated by the increase pNA absorbance in Figure 6.6D. This data confirms what Kaplan *et al.* demonstrated for how the contact activation system (CAS) is triggered when all the contact factors (FXII, HK and PK) are present with added gC1q-R and Zn^{2+} .

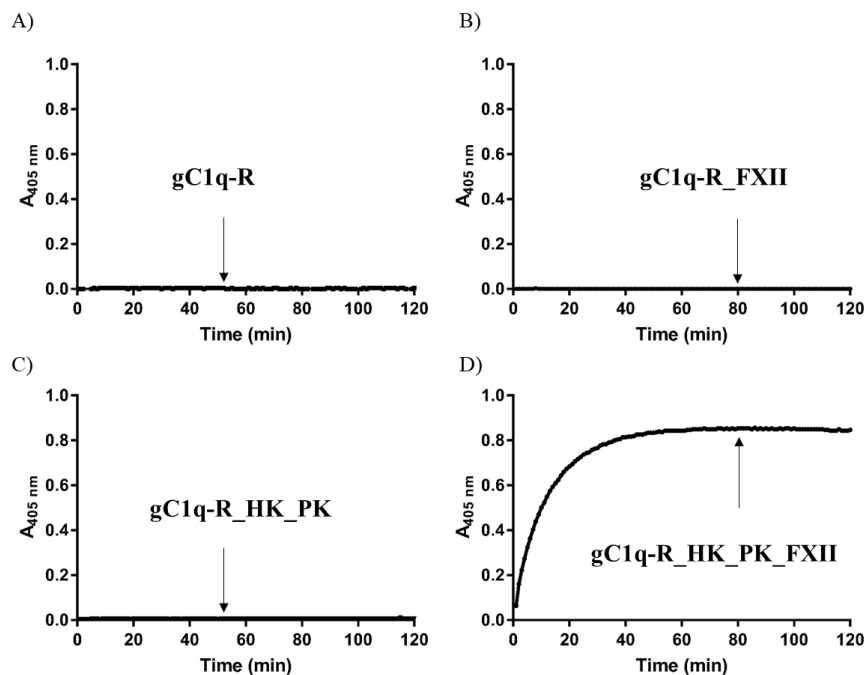


Figure 6.6: Contact activation assay. A) Recombinantly expressed WT gC1q-R alone. B) WT gC1q-R and FXII. C) WT gC1q-R in the presence of HK and PK. D) Activation in the presence of all contact factors (FXII, HK and PK) with added gC1q-R and $50\ \mu\text{M}\ Zn^{2+}$. S-2302 substrate is cleaved to release pNA, which is read at 405 nm every minute for 120 minutes.

6.3.0 Competition of FXII with FXII FnII in a contact activation assay

To demonstrate the involvement of FXII FnII and HKD5 in competing with full-length FXII and full-length HK, respectively in binding to gC1q-R, 200 nM of either FXII FnII or HKD5 in the reaction showed reduction in substrate cleavage and pNA turnover thus reflecting on how much pNA is absorbed with time (Figure 6.7).

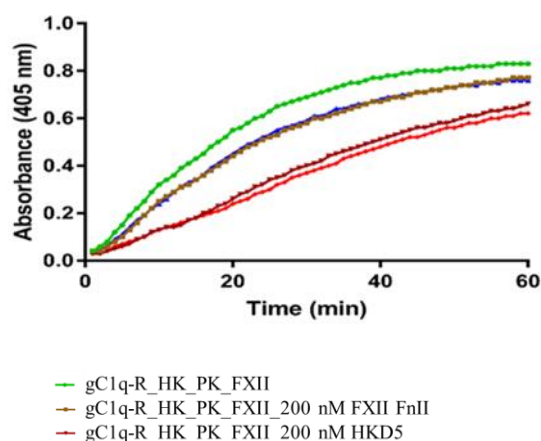


Figure 6.7: Displacement of FXII or HK binding to gC1q-R by FXII FnII or HKD5. 200 nM of FXII FnII or HKD5 competed for binding to WT gC1q-R and subsequently blocked full-length FXII and HK bound PK from to gC1q-R. This resulted in reduction of pNA product formation.

6.4.0 Contact activation assay using low and high molecular weight gC1q-R

Previous findings by Verhoef JJF *et al.* have shown nanoparticle polyphosphate to be more potent in triggering contact activation in the presence of FXII, HK and PK compared to soluble polyphosphate (polymer unit length of 70) ⁽³¹⁵⁾. Although, human gC1q-R has never been reported to form oligomers larger than the trimer in solution, recombinant gC1q-R trimer (90 kDa) and gC1q-R oligomer (>200 kDa) isolated from S200 increase 10/300 was used for contact activity assay.

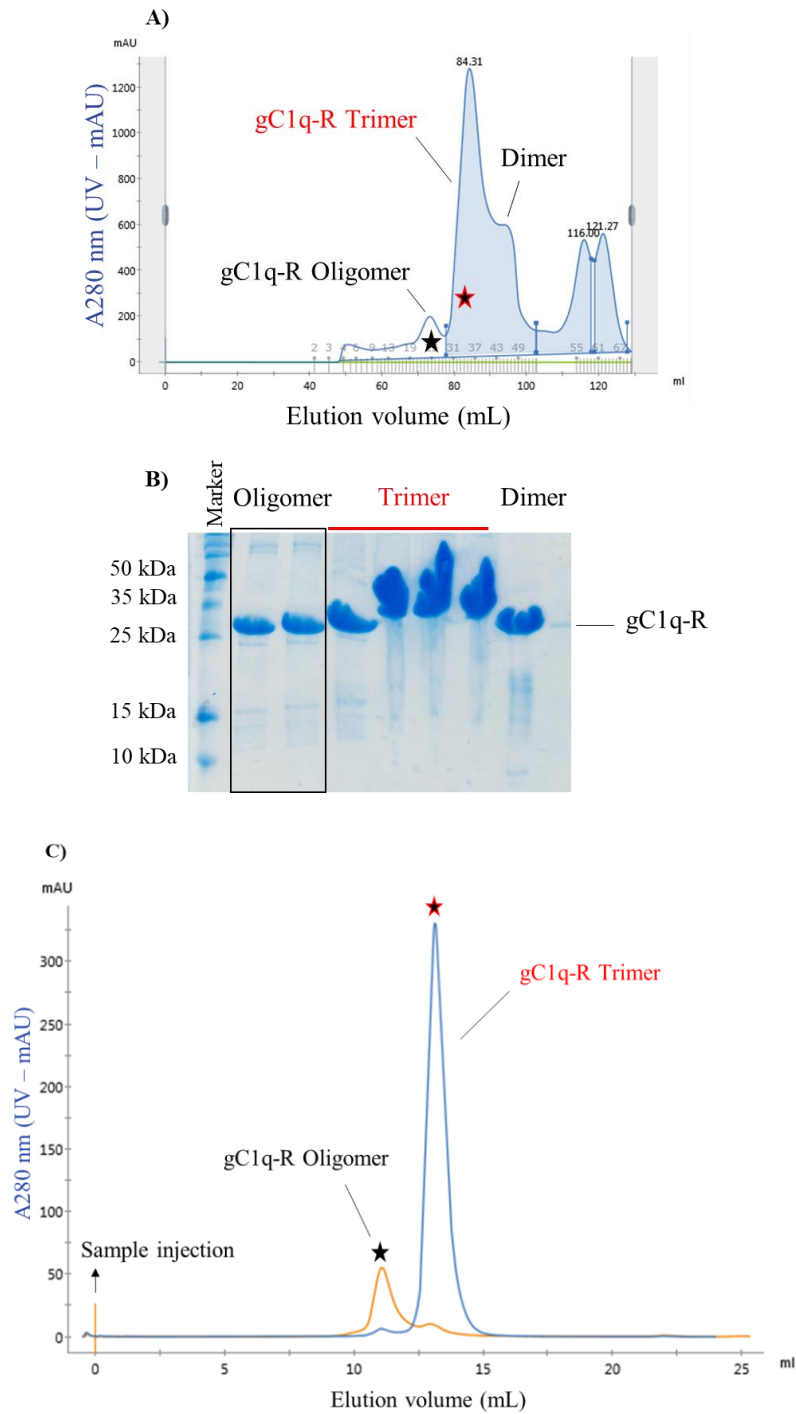


Figure 6.8: Forms of WT gC1q-R (oligomer and trimer). **A)** Captured and eluted gC1q-R (oligomer and trimer) using high NaCl on HiTrap-Q (5 mL) column. **B)** SDS-PAGE gel of the fractions for gC1q-R oligomer (in black box), WT gC1q-R trimer (in red) and gC1q-R dimer. **C)** gC1q-R oligomer and gC1q-R trimer were confirmed in solution using an analytical gel filtration column (S200 increase 10/300). The asterisk on the HiTrap-Q chromatograph highlights fractions taken and ran on the S200 increase 10/300 column.

Leaving WT gC1q-R trimer in the fridge for 2 days did not lead to oligomer formation and neither did the gC1q-R oligomer break down to trimer in 20 mM HEPES pH 7.4, 140 mM NaCl, confirming that the WT gC1q-R oligomer and trimer must have already been formed at equilibrium (data not shown).

Comparing the two forms of gC1q-R (trimer and oligomer) in contact activation in the presence of Zn^{2+} and contact factors (FXII, HK and PK) showed no difference for gC1q-R concentrations at 100 nM and 300 nM (Figure 6.9A-B), but at 600 nM, a slight difference between gC1q-R trimer and gC1q-R oligomer was observed with a *p-value* of 0.0345 (Figure 6.9C) from the initial rate of the reaction.

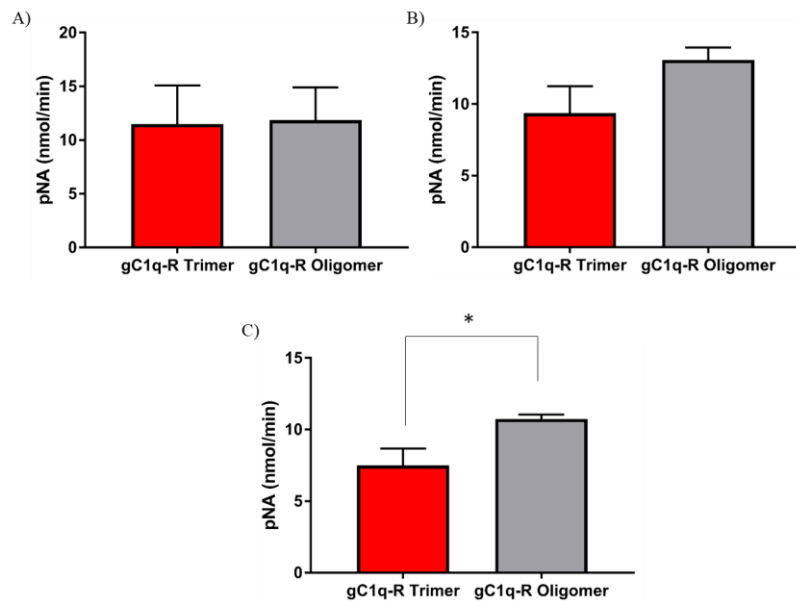


Figure 6.9: Contact activation assay for WT gC1q-R oligomer and gC1q-R trimer. A) 100 nM of gC1q-R (oligomer or trimer) B) 300 nM of gC1q-R (oligomer or trimer) and C) 600 nM of gC1q-R (oligomer or trimer). All reactions contained 50 μ M Zn^{2+} , 200 nM FXII, 10 nM HK, 10 nM PK and the reaction were incubated 37 °C for 15 minutes prior to addition of chromogenic S-2302 substrate (0.4 mM). Experiments were performed in triplicates and from which the initial rate of the reaction was generated. This was determined for the first 7 minutes of the reaction using a calibration curve of pNA only.

6.5.0 Contact activation assay in plasma with WT gC1q-R

To answer whether clotting time is shortened in the presence of WT gC1q-R in plasma, recombinant WT gC1q-R was sent to our collaborator (Dr Nicola Mutch – University of Aberdeen) to perform thrombin generation and clotting assays by using WT gC1q-R as an activator compared to no activator (no gC1q-R) in Figure 6.10A-D. This is the first plasma based assay for gC1q-R demonstrating that gC1q-R can act as an activator to facilitate clot induction, as shown in Figure 6.11. Increasing the concentration of gC1q-R in a dose-dependent fashion resulted to shorten clotting time and a significant difference is observed when compared to no gC1q-R (no activator) added in plasma.

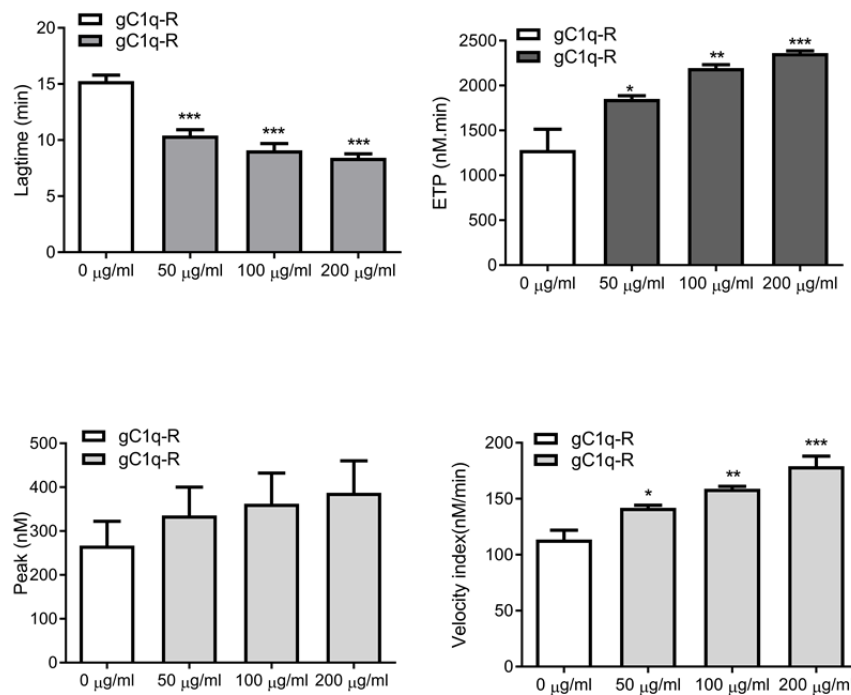


Figure 6.10: Plasma-based contact activation using WT gC1q-R as an activator. A-D) Thrombin generation and activity.

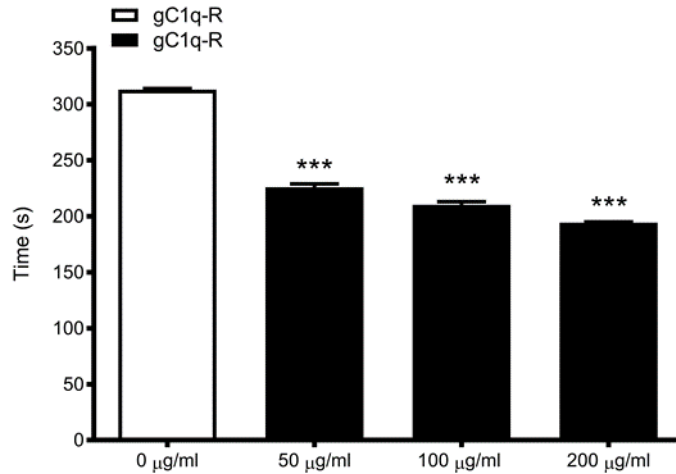


Figure 6.11: Clot formation using gC1q-R as an activator. Plasma proteases including FXII and HK bound PK were already present in plasma. A dose-dependent shortening of clotting time is observed for 50 μg/mL, 100 μg/mL and 200 μg/mL compared to no added gC1q-R (0 μg/mL).

The finding suggests that recombinant human WT gC1q-R is capable of activating the contact activation system in plasma and ultimately leading to thrombin generation. This demonstrates thrombin was being generated (Figure 6.10). FXII or FXI deficient plasma revealed interesting relevance of gC1q-R in clotting (data not shown). The lagtime, peak, ETP and velocity data (Figure 6.10A-D) demonstrates a thrombin peak in which the lagtime (Figure 6.10A) signifies how quickly thrombin is made and the concentration of thrombin (Figure 6.10B) represented as a peak (showing time of peak and peak height – data not shown). The ETP data in Figure 6.10C is generated from the area under the curve of the thrombin peak, while the velocity (Figure 6.10D) defines the rate at which thrombin is cleaving the substrate (usually a fluorescent substrate). Thrombin activity can convert fibrinogen to fibrin and ultimately leading to clot formation with time as shown in Figure 6.11 at different concentrations of gC1q-R.

6.6.0 Discussion

6.6.1 Molecular assembly of the contact factors on gC1q-R

The gC1q-R-FXII FnII crystal structure and the gel filtration data show only one FXII FnII bound to one gC1q-R trimer, and that two gC1q-R trimers may be bridged by FXII FnII using G1 and G2 pockets on gC1q-R. This therefore leaves vacant two unoccupied subunit on either sides of the two gC1q-R trimers bound to one FXII FnII. Effective contact activation with all contact factors in mind will require HK bound PK to occupy those vacant sites. Unpublished data by Dr Alexander Slater have demonstrated that two HKD5 bind to one gC1q-R trimer, thus opening the possibility of FXII to occupy the remaining site. The gel filtration data strengthens this position as it demonstrates a calculated molecular weight of 478.7 kDa for gC1q-R bound HK and FXII in the presence of Zn^{2+} .

This reinforces the notion of contact factor assembly and to have an effective proteolysis of FXII and PK on the gC1q-R surface, close proximity for activation of PK by FXIIa or FXII by PKa needs to be giving some consideration. It is clear that the activation assay aforementioned demonstrates the requirement of all contact factors to trigger contact activation, as missing one contact factor (FXII or HK bound PK) leads to no contact activation. All together, activation of FXII and HK bound PK or HK bound FXI can have a significant effect on thrombin generation and clot formation.

6.7.0 Conclusion

In conclusion my findings may shed light on the molecular mechanism FXII FnII binding to Zn^{2+} and the molecular changes in loops 2 upon under and supersaturation with Zn^{2+} in the crystals structure. Furthermore, the relationship between loop 2 and Trp-Trp pocket seems to play an important structural role in FXII FnII bound gC1q-R as mediated by Zn^{2+} . Although, attempts in crystallising full length FXII did not provide any structural information yet, FXII in

solution using analytical gel filtration and solid-phase characterisation have shown that FXII can form a complex with gC1q-R in the presence of HK and binds to gC1q-R with a strong affinity. FXII and HK bound PK in the presence of gC1q-R has established the capability of gC1q-R to provide the negatively charged surface for FXII and HK to dock on and perform proteolysis in plasma.

Lastly, FXII bridging two gC1q-R trimers is an interesting concept that may provide insight into oligomeric states of gC1q-R upon ligand binding to create a large docking platform for efficient proteolysis of FXII and PK in the presence of Zn^{2+} . Bridging of FXII to two gC1q-R trimers is confirmed by my gel filtration and SPR data.

6.8.0 Future prospects

Expanding the concept of contact factor assembly will be needed to further elucidate how FXII and HK bound PK are organised together on the gC1q-R surface. To do this, gC1q-R in complex with HK bound PK and FXII in the presence of Zn^{2+} will be prepared and subjected to Cryogenic electron microscopy (cryo-EM). This will provide a comprehensive structural insight of how both HK bound PK and FXII dock on gC1q-R and will certainly provide information that can be validated through mutagenesis and cell based assays coupled with *in vivo* studies to fully establish the physiological significance of the interaction.

CHAPTER 7.0

STUDIES OF FXII F_nII DIMERISATION IN THE PRESENCE OF Zn²⁺ IONS

7.1.0 Zn²⁺ mediated FXII FnII packing in the crystal lattice

The crystal structure of FXII FnII bound to 3 Zn²⁺ (form 1) reveals in its crystal packing 2 Zn²⁺ ions (termed Zn²⁺-1 and Zn²⁺-2) on opposite sides contributing in the mediation of the intermolecular bridging between the FXII FnII domains. Zn²⁺-1 coordinates with His44 and C-terminal Glu71 of the FXII FnII in the A.S.U with complete coordination in the presence of H₂O and His35 of the FXII FnII symmetry mate 1. The second Zn²⁺ (Zn²⁺-2) is coordinated with the same FXII FnII in the A.S.U through its N-terminal His29 and a Glu71 of the FXII FnII symmetry mate 2 (Figure 7.1).

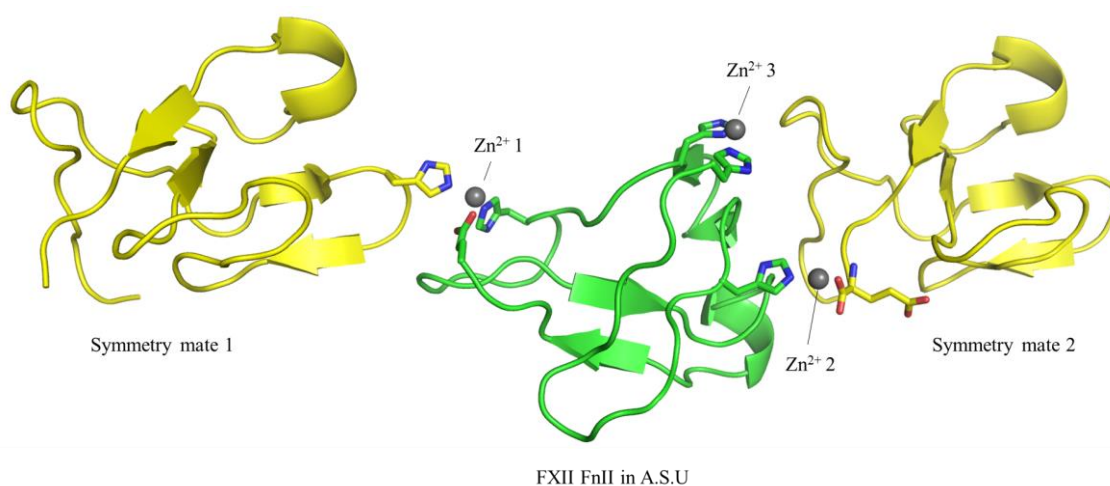


Figure 7.1: FXII FnII crystal packing with Zn²⁺ 1 and 2 in the interface. FXII FnII in green is bound to 3 Zn²⁺ (Zn²⁺ 1, Zn²⁺ 2 and Zn²⁺ 3) with coordination observed for Zn²⁺ 1 and Zn²⁺ 2 while Zn²⁺ 3 is only bound to FXII FnII in the asymmetric unit (A.S.U) in green.

Calculation of the solvent accessible surface area using AreaMol (CCP4 program) reveals that Zn²⁺-1 site on the FXII FnII structure to have reduced accessibility to the solvent in comparison to Zn²⁺ 2 site on FXII FnII. The values from the calculated surface area using AreaMol are 31 Å² for Zn²⁺ 2 site, while 4.7 Å² for Zn²⁺ 1 site, indicating less solvent accessibility for Zn²⁺ 1 site.

7.2.0 Dimerisation of FXII using Gel filtration

The crystal structure of human FXII F_nII revealed Zn²⁺ to be in the interface between FXII F_nII thus packing together in the crystal lattice and as a result I sought to verify whether Zn²⁺ played a role in FXII F_nII oligomerisation in solution using S200 increase 10/300. At pH 7.4 plus 50 μM Zn²⁺ or pH 7.4 plus 5 mM EDTA, the FXII F_nII peak eluted at almost 19 mL, but when the pH was lowered to 5.0 in the presence of 50 μM Zn²⁺, the FXII F_nII peak shifted towards the right by a volume of almost 2 mL thus eluting at around 21 mL (Figure 7.2A). Figure 7.2B shows migration of FXII F_nII from the gel filtrated peaks (in closed coloured stars) under both reducing and non-reducing condition with FXII F_nII having an estimated molecular weight of 10 kDa, although 8.5 kDa when calculated from expasy using FXII F_nII amino acid sequence.

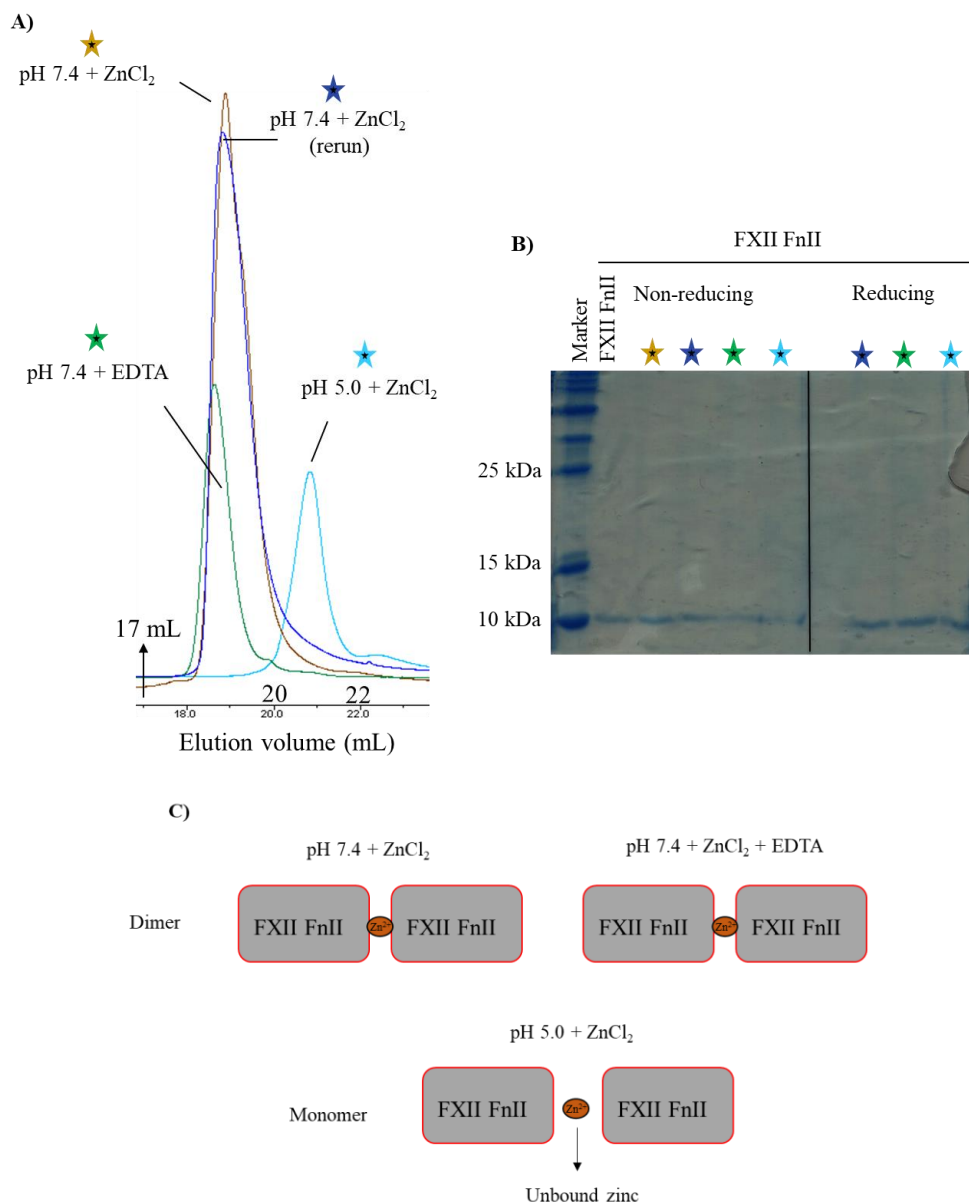


Figure 7.2: Zn^{2+} -induced FXII FnlI dimer formation in solution. **A)** Chromatographic analysis showing FXII FnlI in the presence of 50 μM Zn^{2+} or EDTA in HEPES buffer with pH 7.4 and 5. This shows that at pH 7.4 in HEPES buffer with EDTA the peak profile is similar to that of the peaks at pH 7.4 without EDTA. At pH 5.0 plus 50 μM Zn^{2+} , a lower molecular weight of FXII FnlI was observed thus demonstrating FXII FnlI being reduced to a monomer as shown in **B)** with SDS-PAGE gel of fractions from figure A showing all FXII FnlI to migrate at the same level as the FXII FnlI control on lane 2 next to the marker. **C)** Proposed diagrammatic representation showing FXII FnlI dimer and monomer at different pH in the presence of Zn^{2+} for dimer or EDTA for monomer.

On gel filtration FXII FnII monomer elutes at a calculated molecular weight of 5.8 kDa, while the dimer or oligomeric form of FXII FnII has a molecular weight of 20.4 kDa.

The FXII FnII crystal structure shows 2 Zn²⁺ ions contributing in bridging FXII FnII on either side of the FXII FnII in the asymmetric unit thus describing how FXII FnII packs in the crystal lattice (Figure 7.1). To confirm and strengthen the size exclusion chromatographic (gel filtration) data, binding studies using Surface Plasmon Resonance (SPR) was performed.

7.3.0 Binding analysis of FXII self-interaction in the presence of Zn²⁺

To determine whether FXII self-interacts in the presence of Zn²⁺, immobilised plasma human FXII was tested for binding using SPR. The binding analysis data (bar chart) shows that the same plasma FXII (1 µM) in solution was able to interact with immobilised plasma FXII in a running buffer containing 50 µM Zn²⁺.

Furthermore, recombinant human FXII FnII (5 µM) was also capable of interacting with immobilised plasma FXII in the presence of Zn²⁺ in the running buffer. WT gC1q-R (1 µM) was used as a positive control to demonstrate that it can interact with immobilised plasma FXII in the presence of 50 µM Zn²⁺ (Figure 7.3).

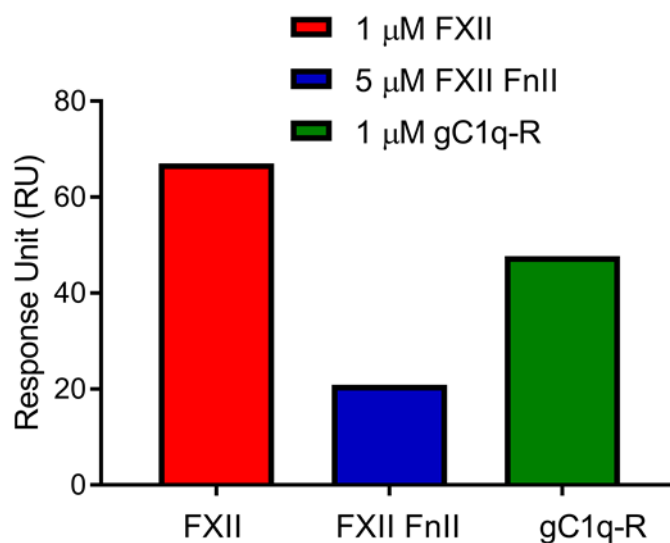


Figure 7.3: FXII and FXII FnII binding to immobilised FXII on CM5 chip. Protein samples were diluted in HEPES buffer containing 50 μM Zn²⁺. Plasma purified FXII (1 μM) in red, recombinant FXII FnII (5 μM) in blue and recombinant WT human gC1q-R (1 μM) in green.

7.4.0 SPR analysis of FXII FnII interaction with full length FXII

As binding was already observed for FXII FnII from the binding analysis, SPR analysis was performed in the presence of either 50 μM Zn²⁺ or 5 mM EDTA to gain insight into FXII self-interaction and the affinity for the interaction. Figure 7.4 shows FXII FnII (1-10 μM) plus Zn²⁺ to interact with immobilised plasma human FXII in a concentration dependent manner, with increased response unit (RU) for FXII FnII in 50 μM Zn²⁺ buffer. Comparison of FXII FnII (1-10 μM) plus Zn²⁺ to FXII FnII (1-10 μM) plus 5 mM EDTA showed a striking reduction in response unit (RU) observed for FXII FnII in the presence 5 mM EDTA. This suggests that Zn²⁺ might induce FXII to interact with itself.

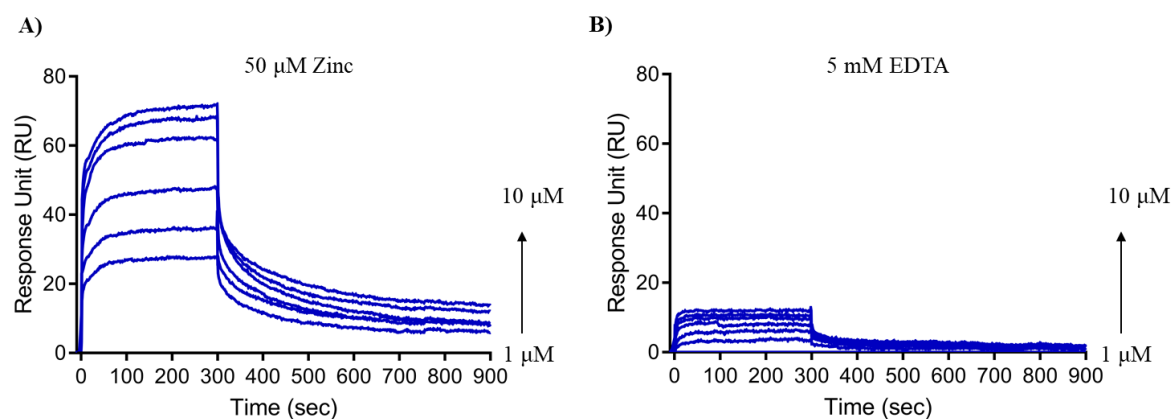


Figure 7.4: Binding studies showing FXII interacting to itself. A) Kinetics of FXII FnlI binding to immobilised plasma purified human FXII in HEPES buffer containing 50 μM Zn^{2+} or **B)** 5 mM EDTA with increase response unit (RU) for figure A and reduced response unit for figure B.

The binding curves for FXII FnlI in a concentration dependent manner were analysed and initially fitted to the 1:1 Langmuir binding model, which assumes that one molecule of FXII FnlI in solution binds to one molecule of immobilised plasma FXII. Data for FXII FnlI (plus Zn^{2+}) did not give a good fit to the 1:1 Langmuir binding model (Figure 7.5 A). However, the FXII FnlI (plus EDTA) on the other hand gave a good fit to the 1:1 Langmuir model as shown in Figure 7.5 B with the model curves shown in black and FXII FnlI in different colours.

Furthermore, the Chi^2 value at 0.0886 for FXII FnlI (plus EDTA) presented in table 7.1 was significantly low, indicating closeness in fitting to the experimental data to the 1:1 Langmuir binding model, with a K_D value of 0.106 μM for FXII FnlI binding (plus EDTA) to immobilised plasma FXII.

Although FXII FnlI (plus Zn^{2+}) was unable to fit to the 1:1 Langmuir binding, FXII FnlI (plus Zn^{2+}) gave a good fit to the heterogeneous ligand model. Fitting FXII FnlI (plus Zn^{2+}) to the heterogeneous ligand model produced a much better fit compared to the 1:1 Langmuir

binding model (Figure 7.5C). The heterogeneous ligand model generates two K_D values and for FXII FnlI (plus Zn^{2+}) the K_D values were 0.169 for site 1 and 0.0125 μM for site 2 (table 7.1). FXII FnlI (plus EDTA) was also fitted to the heterogeneous ligand model. Although a good fit to the heterogeneous ligand model (Figure 7.5D), the K_D values from the two sites for FXII FnlI (plus EDTA) remain unchanged at 0.105 μM . Both K_D values obtained for FXII FnlI (plus EDTA) from the 1:1 Langmuir binding and heterogeneous ligand model are similar. Furthermore, the k_D values (0.106 μM and 105 μM) for FXII FnlI (plus EDTA) is close to the k_D value FXII FnlI (plus Zn^{2+}) has for site 1 (0.169 μM) as shown in table 7.1.

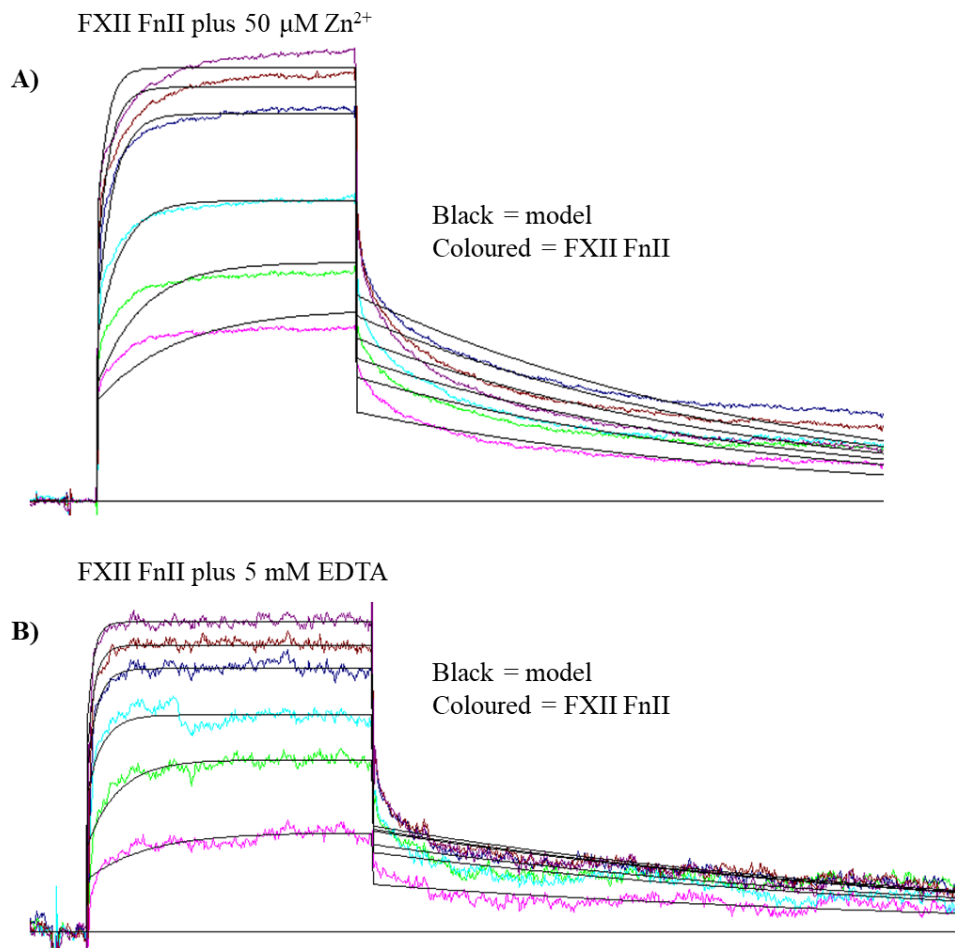


Figure 7.5A-B: Fitting of FXII FnlI (with or without Zn^{2+}) binding models. Experimental curves in colour are fitted to Langmuir binding model. **A)** FXII FnlI (plus Zn^{2+}) and **B)** FXII FnlI (plus EDTA).

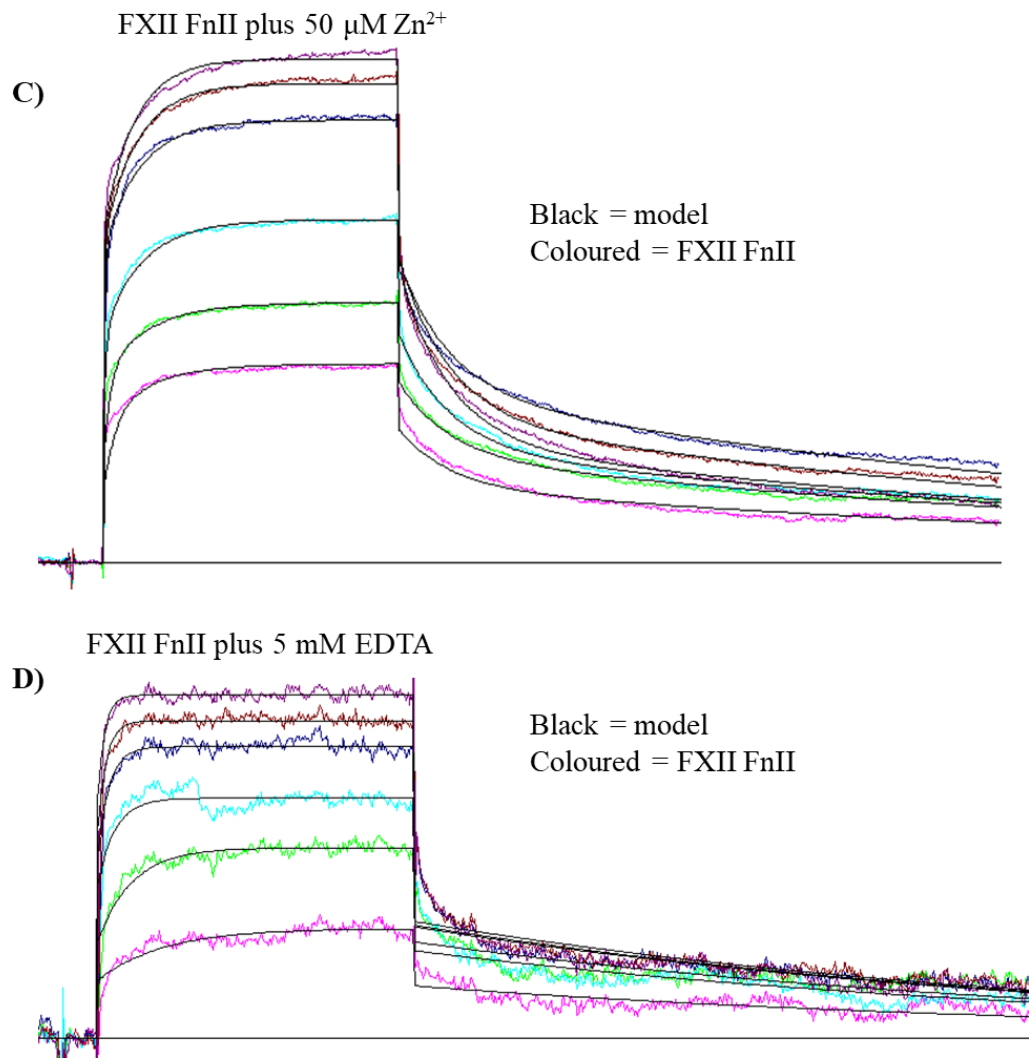


Figure 7.5C-D: Fitting of FXII F_nII (with or without Zn²⁺) binding models. Experimental curves in colour are fitted to heterogeneous ligand binding model. C) FXII F_nII (plus Zn²⁺) and D) FXII F_nII (plus EDTA).

Below are the binding kinetics parameters shown in table 7.1 from the fitting of FXII FnlI binding to immobilised plasma human FXII to the 1:1 Langmuir binding model and the 2:1 heterogeneous ligand-binding model.

(1:1) Langmuir binding model

	$k_a (M^{-1}s^{-1})$	$k_d (s^{-1})$	$K_D (\mu M)$	Chi ²
FXII FnlI (EDTA)	1.17E ⁺⁰³	1.98 E ⁻⁰²	0.106 (Site1)	0.0886
(2:1) Heterogeneous ligand-binding model				
FXII FnlI (Zn ²⁺)	1.17E ⁺⁰³	1.98 E ⁻⁰²	0.169 (Site1)	0.952
	8.77E ⁺⁰⁴	1.10E ⁻⁰³	0.0125 (Site2)	0.952
FXII FnlI (EDTA)	1.46E ⁺⁰⁴	1.54E ⁻⁰³	0.105 (Site1)	0.0887
	1.47E ⁺⁰⁴	1.54E ⁻⁰³	0.105 (Site2)	0.0887

Table 7.1: Parameters of binding kinetics of FXII FnlI binding to immobilised human FXII

7.5.0 Discussion

An earlier report published by Citarella F in 1998 demonstrated that a recombinant deletion mutant of amino acid residues 3-19 in human FXII (rFXII- Δ 19) was capable of binding to FXII, as well as negatively charged surfaces ⁽³¹⁴⁾. This is in agreement with our findings of plasma FXII binding to itself. It is well accepted that Zn^{2+} binds to FXII and from the gel filtration and SPR data, Zn^{2+} seems to play a role in FXII self-interaction as confirmed by the change in the hydrodynamic radius on gel filtration and reduced response unit from the SPR analysis in the presence of EDTA.

The structural and functional uniqueness of Zn^{2+} and its contribution to FXII dimerisation is unclear. However, this is the first reported data demonstrating that FXII F_{III} interacts with FXII, although which domain within FXII the FXII F_{III} interacts with is unknown. Despite the crystal structure of FXII F_{III} bound to Zn^{2+} and the gel filtration data demonstrating Zn^{2+} induced FXII F_{III}-FXII interaction, this does not explain any biological relevance.

The 3 tandem F_{III} domains from gelatinase A, also known as MMP2, have been demonstrated to all contribute to binding to gelatin with a much higher affinity than each individual F_{III} alone binding to gelatin ⁽³¹⁶⁾. Understandably, the question to consider is whether Zn^{2+} induced FXII self-interaction may serve to increase the binding affinity activated FXII (FXIIa) may have for some binding partners.

A possibility to consider is whether oligomerised FXII as a result of Zn^{2+} can increase the affinity FXII has to large physiologically relevant macromolecules including polyphosphate nanoparticle from platelets, amyloid- β implicated in Alzheimer's disease or dextran sulfate 500. Polyphosphate nanoparticle and amyloid- β have been reported to be more efficient in

binding and facilitating FXII activation in the presence of Zn^{2+} , than short chain polyphosphate (<70 unit) or monomeric amyloid- β . This is also true for dextran sulfate, as high molecular weight dextran sulfate 500 kDa is much more efficient in activating FXII when compared to low molecular weight dextran sulfate 5kDa, 15 kDa and 50 kDa.

7.6.0 Conclusion

In the FXII F_nII form 1 crystal structure, Zn^{2+} is seen to contribute in bridging the interface between 2 FXII F_nII. Structural analysis of the FXII F_nII crystal structure seem to suggest that this form of FXII F_nII is in its open conformation due to conformational changes in loop 2 and how this affects the Trp53-Trp66 pocket. Data from the in solution studies (gel filtration) showed a higher molecular weight peak corresponding to FXII F_nII dimer in pH 7.4 (Zn^{2+} or EDTA) as opposed to acidic pH 5.0 (plus Zn^{2+}), showing variation in hydrodynamic radius for FXII F_nII under acidic and basic pH.

Further characterisation of Zn^{2+} mediating FXII self-interaction was observed in the SPR data and revealed a much higher response unit (RU) in the sensogram of injected FXII onto the immobilised plasma human FXII. The response is significantly reduced when 5 mM EDTA is added to the running buffer, suggesting Zn^{2+} contribution in FXII self-interaction. So the question to consider is; whether Zn^{2+} can induce FXII self-interaction to increase increase the binding affinity FXII has for binding negatively charged surfaces, therefore increasing activity and efficiency for downstream molecular cascades in haemostasis and thrombosis.

7.7.0 Future prospects

Self-interaction of FXII upon binding to activators including dextran sulfate 500 induced by Zn^{2+} ions is worth looking into. Understanding the molecular insight of how FXII form oligomers upon contact with negatively charged surfaces to increase affinity and efficiency might help to broaden the molecular mechanism of FXII function under these conditions.

CHAPTER 8.0

**CRYSTALLISATION OF
MOUSE FXII (mFXII)**

8.1.0 Cloning of FXII for expression and purification

Figure 8.1 shows successful amplification of full-length mouse FXII (mFXII) from pCMV-SPORT6-mFXII template, producing a PCR product of 1.7 kb containing restriction enzyme sites (REs) BglII and MluI. Two DNA bands at 5.0 kb for pMT-PURO-His₆ and 1.7 kb for mFXII on the agarose gel confirmed that the cloning of mFXII into pMT-PURO worked following double digest. Site directed mutagenesis was also performed from WT mFXII to produce active site mutant mFXII S526A. DNA sequencing analysis confirmed correct cDNA sequence for both forms of mFXII.

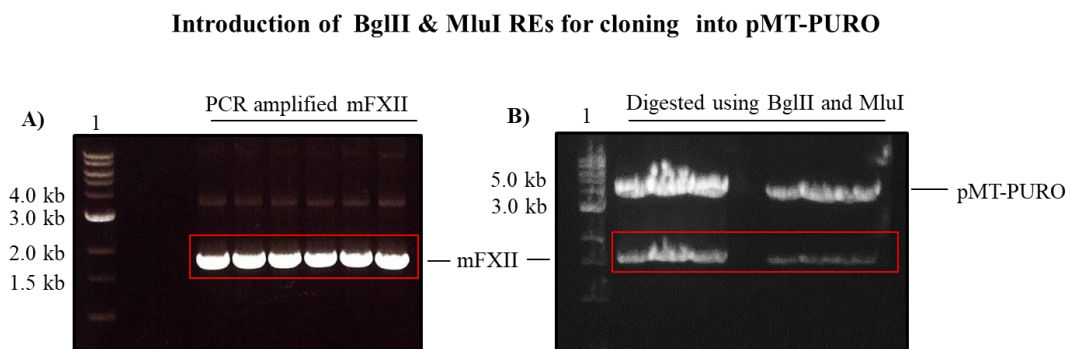


Figure 8.1: Agarose gel analysis of mFXII. **A)** Amplified full-length mouse FXII (mFXII) at 1.7 kilobase (kb) containing BglII and MluI restriction enzyme sites (REs) in lanes 4-9 as highlighted in red box. **B)** Restriction double digest of pMT-PURO-His₆ cloning vector containing mFXII insert with BglII and MluI REs shows two bands at 5.0 kb for pMT-PURO and 1.7 kb for mFXII.

8.2.0 Expression and purification of mFXII in drosophila S2 cells

Expression of WT mFXII and active site mutant S526A (1-596 amino acid residues) were confirmed by western blotting (using B7C9 mAb) in transient expression prior to selection with puromycin for stable cell line generation.

Large-scale (2-4 Litres) expression of His₆ tagged WT mFXII and mFXII S526A in stable drosophila S2 cells (puromycin selected) yielded soluble WT mFXII and mFXII S526A (Figure

8.2). Both forms of mFXII were secreted into the drosophila S2 cell media as a result of the signal peptide present on the pMT-PURO plasmid vector upstream of mFXII cDNA sequence. The S2 media was processed to obtain pure, soluble and monodisperse mFXII protein concentrations of 18.7 mg/mL for WT mFXII and 24.6 mg/mL for mFXII S526A. Mass spectrometry results confirmed expressed proteins to be that of mFXII.

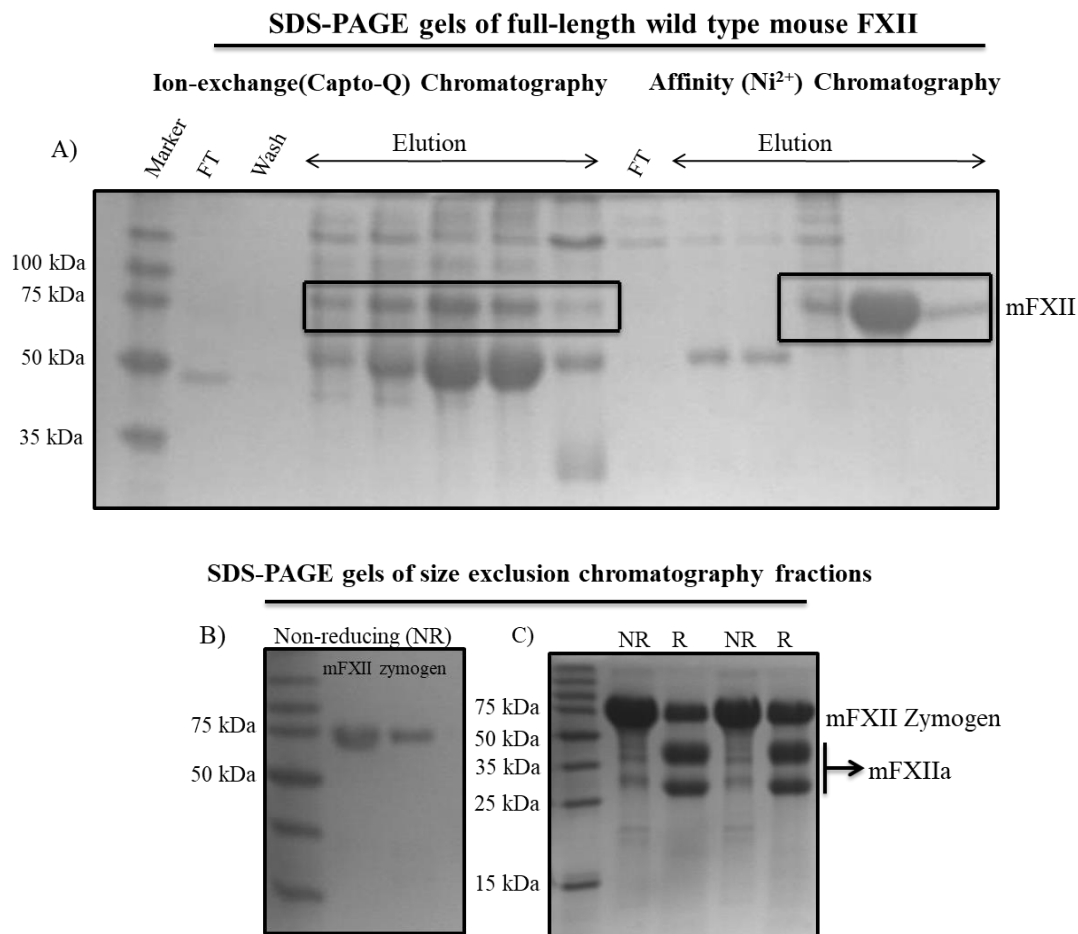


Figure 8.2A-C: SDS-PAGE gel analysis of mFXII purification. **A)** Fractions of eluted WT mFXII from Capto-Q column. Flow-through (FT) and wash are also shown in lanes 2 and 3, while mFXII is shown on lanes 4-8 (highlighted with a black box) under Ion-exchange (Capto-Q) chromatography. Eluted mFXII fractions from the Affinity (Ni²⁺) chromatography is shown highlighted black box under Affinity (Ni²⁺) chromatography. **B)** Pure WT mFXII was obtained after size exclusion chromatography. **C)** mFXII band under non-reducing (NR) and reducing (R) with 2-Mercaptoethanol.

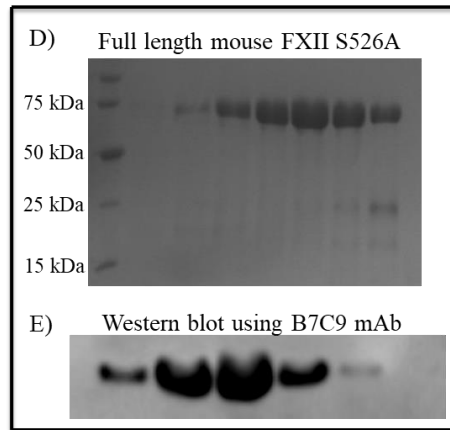


Figure 8.2D-E: SDS-PAGE gel and western blot analysis of mFXII S526A purification. D) Full length mFXII S526A. E) Western blot of mFXII S526A using mAb B7C9.

8.3.0 Mouse FXII S526A in the presence of Corn trypsin inhibitor (CTI)

Crystallisation trial with gel filtrated WT mFXII did not produce any crystals. As FXII autoactivates resulting into a heterogeneous mixture of the FXII zymogen and activated FXII as shown in Figure 8.3 C, the mFXII S526A was chosen over the WT mFXII because it is stable and should reduce sample heterogeneity.

This was further validated by forming a complex of mFXII S526A with corn trypsin inhibitor (selective inhibitor) and showed no binding on gel filtration and is also confirmed by the SDS-PAGE analysis (Figure 8.3). This confirms no activation of mFXII S526A. It has been established that CTI binds to β -FXIIa⁽³¹⁷⁾.

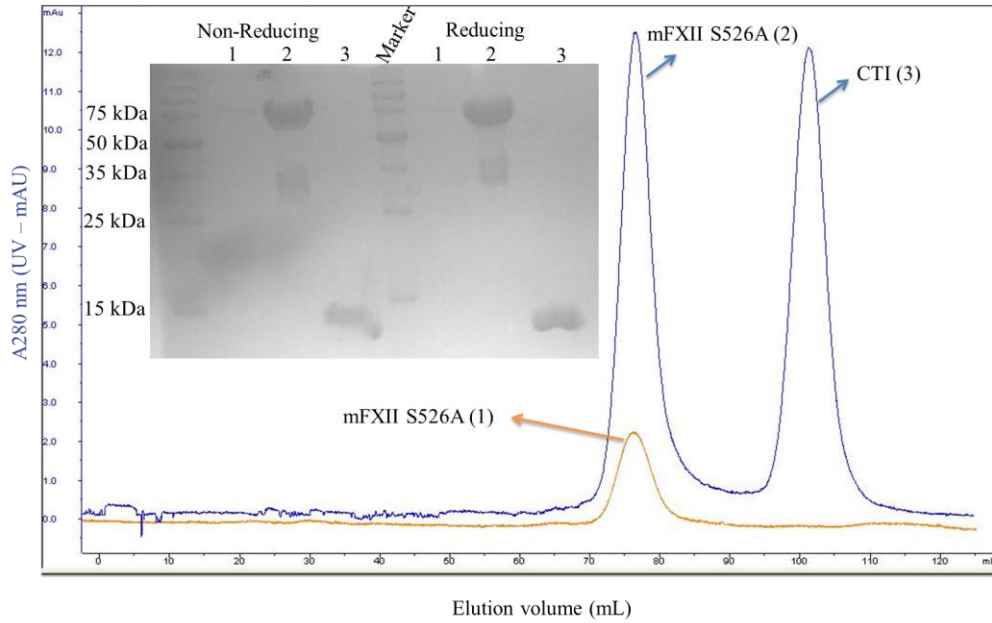


Figure 8.3: mFXII S526A in the presence of CTI. Blue peaks represent unbound mFXII S526A (2) and CTI (3), while in orange is mFXII S526A alone (1) as a control. Marker is shown with protein size on the side of the SDS-PAGE gel showing protein bands from isolated peaks from the gel filtration.

Figure 8.4 shows deglycosylation attempts of mFXII S526A, performed to reduce the heterogeneity of mFXII S526A and aid crystallisation. After 1-hour treatment with PNGase F, mFXII S526A was seen to reduce in molecular weight in comparison to no added PNGase F control (0 hour).

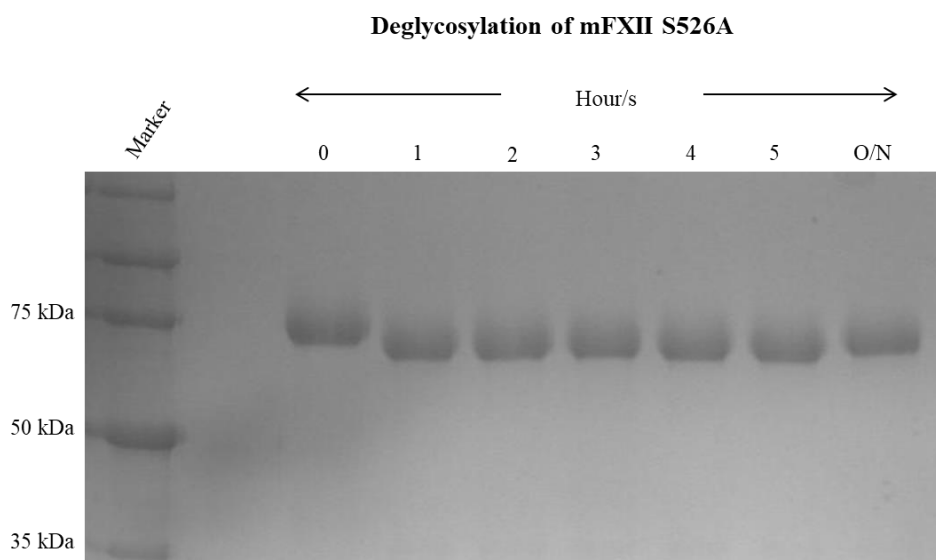


Figure 8.4: 15 % reducing SDS-PAGE gel showing mFXII S526A deglycosylation. A time course at times 0, 1, 2, 3, 4, 5 hours and overnight (O/N) shows an apparent band shift of mFXII S526A from higher for time 0 (no glycosylation) to lower bands following deglycosylation using PNGase F enzyme.

8.4.0 Crystallisation of WT mFXII in the presence of Dextran sulfate

Dextran sulfate has been reported to induce contact activation and Zn^{2+} has been demonstrated to play a role in mediating FXII interaction to dextran sulfate *in vitro*, although suggestions have been made that when Zn^{2+} is present, it prevents assembly of FXII and dextran sulfate.

A mixture of mFXII with 10 x molar excess of dextran sulfate produced crystals grown at 19°C and 10 °C. Crystals in Figure 8.5A grown at 19 °C produced oval crystals, while Figure 8.5B grown at 10 °C produced a different crystal morphologies (plate), although both crystal forms were produced in the following condition; 0.2M Sodium acetate, 0.1M Sodium citrate pH5.5, 10% PEG 4000 plus Zn^{2+} . Figure 8.5C optimised crystals grew at 10 °C with no Zn^{2+} added. Two crystal morphologies were observed for both 10 °C and 19 °C in the procomplex screen. Prof. David Gailani provided the mFXII proteins.

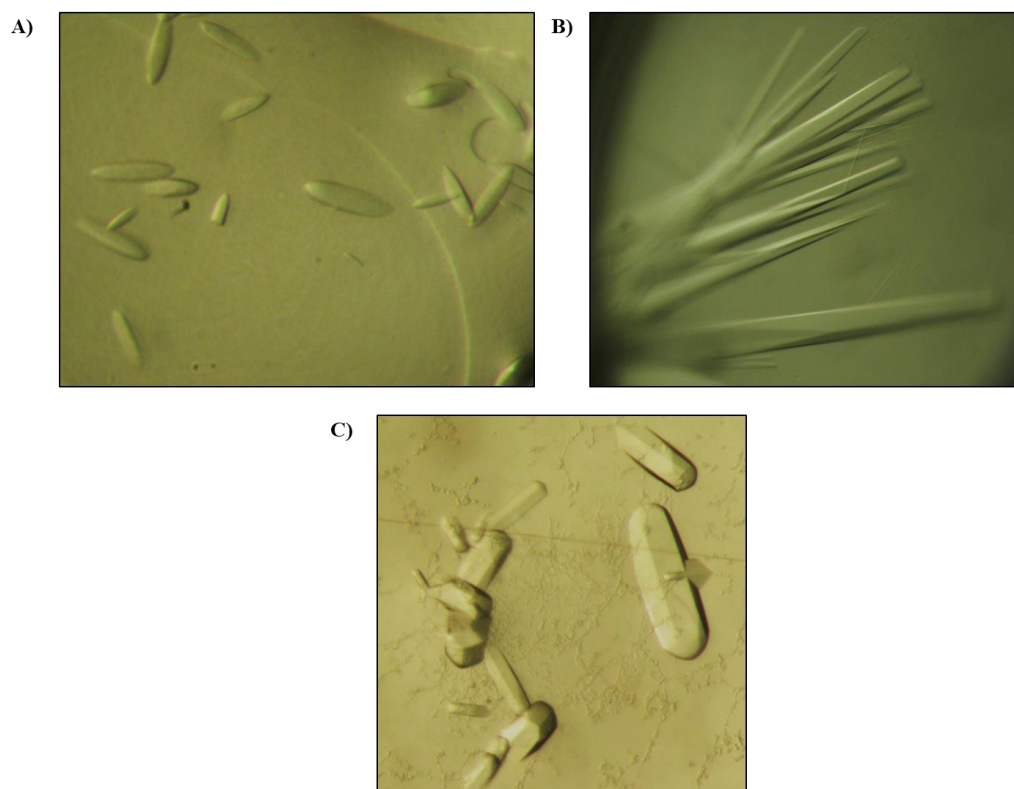


Figure 8.5: Crystals of WT mFXII in the presence of dextran sulfate 5 with and without Zn²⁺. Crystals of WT mFXII in the presence of dextran sulfate grew in the following conditions - **A)** [0.2 M Sodium acetate, 0.1 M Sodium citrate pH 5.5, 5 % PEG 4000 plus 50 μM Zn²⁺ at 19 °C]. **B)** [0.2 M Sodium acetate, 0.1 M Sodium citrate pH 5.5, 10 % PEG 4000 plus 50 μM Zn²⁺ at 10 °C]. **C)** Optimised crystals from figure B grew in 0.2 M Sodium acetate, 0.1 M Sodium citrate pH 5.5, 14 % PEG 4000 at 20 °C with no Zn²⁺ added.

Crystals from Figure 8.5A diffracted at around 20 Å, while Figures 8.6B-C diffracted to 8-6 Å as shown in Figure 8.6. This confirms that the crystals were that of protein and not salt due to diffraction recorded for the inner shell (or low resolution reflection). Salt crystals tend to have less reflection with high-resolution diffraction in the outer shell.

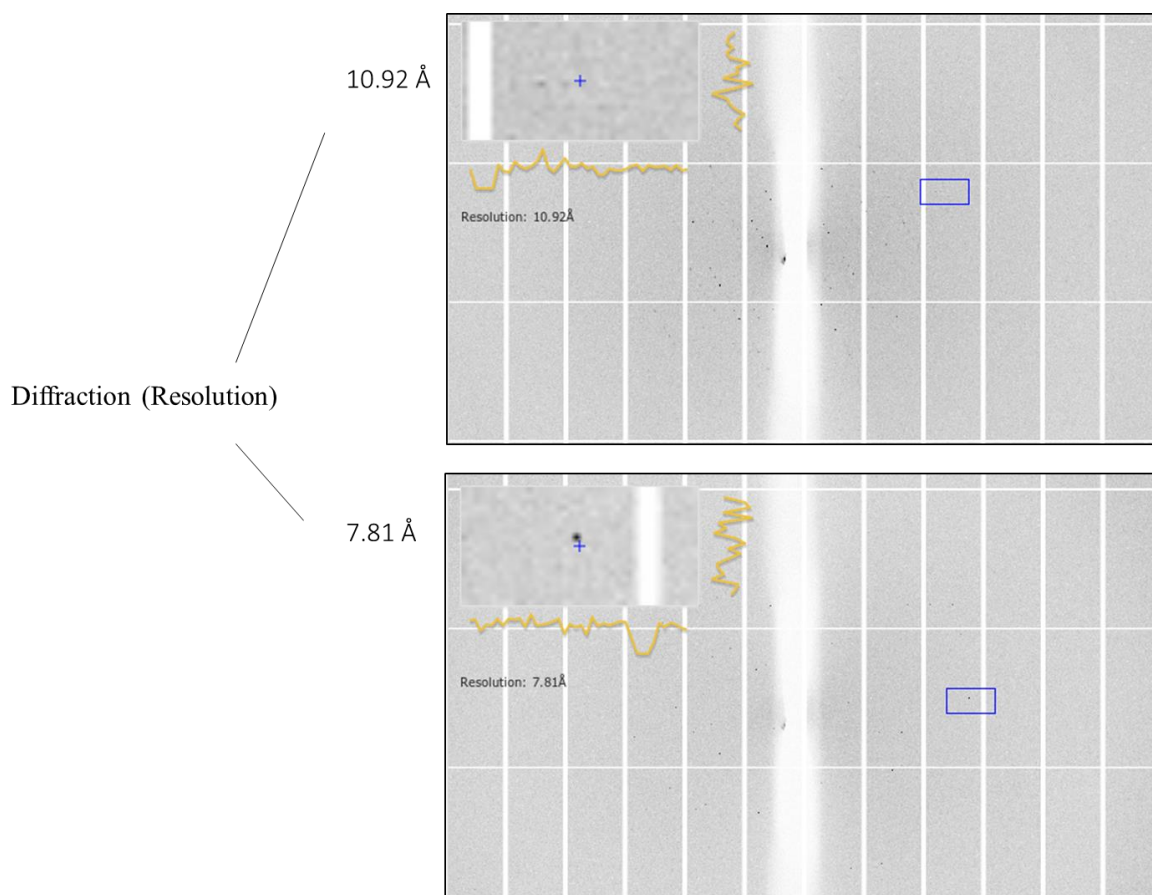


Figure 8.6: Diffraction of WT mFXII crystals. Crystals of mFXII in the presence of dextran sulfate diffracted and recorded showing low resolution at the edge of the diffraction image around 7.81 Å as shown on the upper left corner.

Other crystals of WT mFXII in the presence of dextran sulfate were sent to the Diamond Light Source (DLS) in Oxford and diffracted around 5.75 Å and 6 Å and images collected. However, the data was processed and the unit cell parameter calculated from Mathews (cell content analysis) suggested a big unit cell.

The calculated unit cell parameters suggested a cell length for a, b and c at 173.6 Å, 173.6 Å and 153.9 Å, respectively and angles of 90°, 90° and 120° for alpha, beta and gamma, respectively. Mathew's calculation suggested one molecule in the A.S.U with 47 % solvent content and a cell volume of 402,051.5 Daltons (402.1 kDa) suggesting 4 copies of mFXII in the unit cell with a space group of P321. To further optimised and improve on the crystal quality for data collection, additive screening (Ångstrom screen) was performed in the hope that the packing in the presence of added additive will help in the crystal packing thus improving on the resolution. Crystals have not been observed in the additive screening yet.

8.5.0 Crystallisation of gC1q-R in the presence of WT mFXII

FXII is activated by assembly on negatively charged surfaces such as gC1q-R, and since there is no reported structure of gC1q-R in complex with full length FXII; gel filtrated complex of mFXII and gC1q-R at concentrations 3.3 mg/mL and 6.6 mg/mL produced crystals from the procomplex screen (Figure 8.7). Diffraction data to 2.06 Å contained coordinates for only gC1q-R (PDB code 1P32) and no mFXII present.

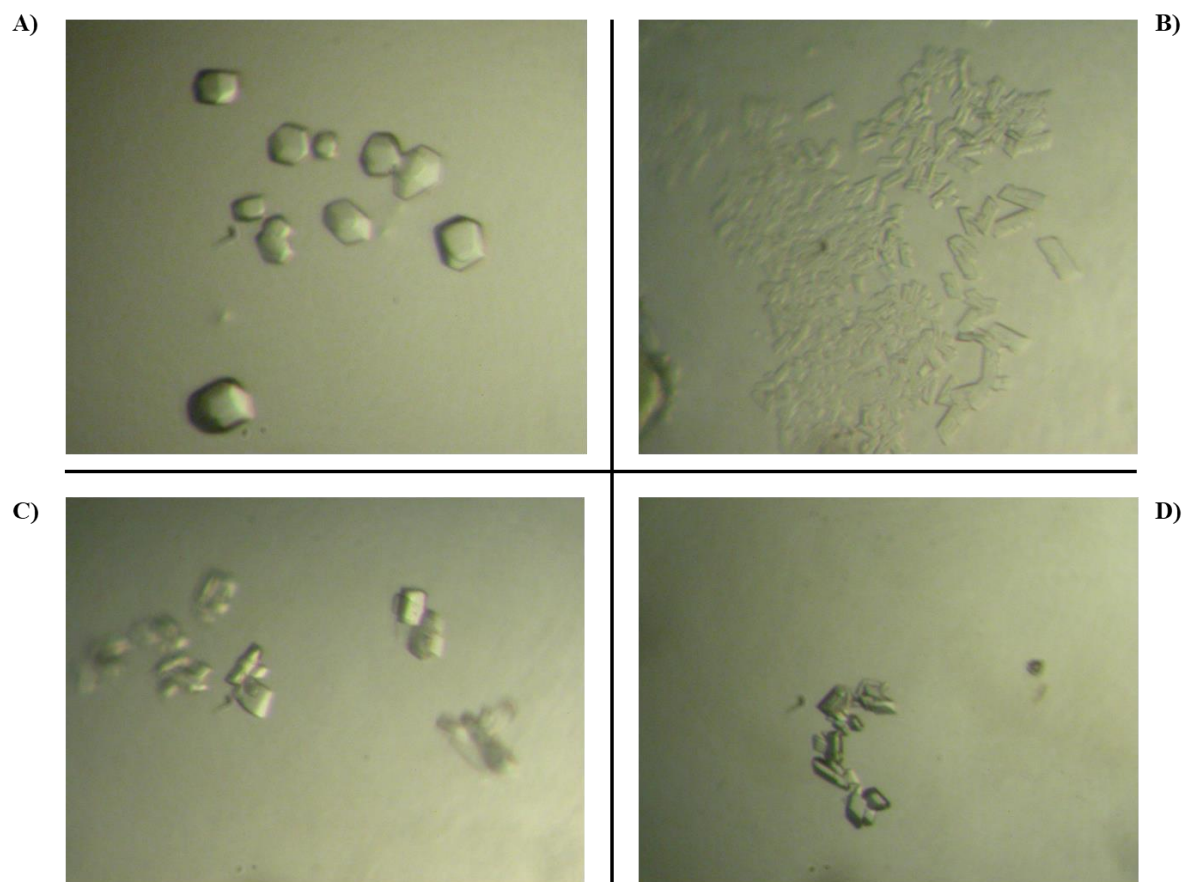


Figure 8.7: Crystals of mFXII in the presence of gC1q-R. Crystals the procomplex screen were obtained in conditions **A)** 0.1 M Sodium citrate pH 5.5, 15 % (w/v) PEG 6000 and **B)** 0.1 M Sodium acetate pH 5.0, 2 % (w/v) PEG 4000, 15 % (v/v) MPD at protein concentrations of 6.6 mg/mL for the crystal trial and 3.3 mg/mL for the optimised crystals from figure B reproducing crystals in figures **C)** (0.1 M Sodium acetate pH 5.0, 2 % (w/v) PEG 4000, 15 % (v/v) MPD) and **D)** (0.1 M Sodium acetate pH 5.0, 2 % (w/v) PEG 4000, 13 % (v/v) MPD).

8.6.0 Crystallisation of HK domain 5 (HKD5) in the presence of gC1q-R

Gel filtrated HKD5 domain (purified by Dr Alexandre Slater) and gC1q-R, in HEPES buffer containing 25 μM Zn^{2+} at a concentration of 6.7 mg/mL grew crystals in the proplex screen in conditions; 0.1 M MES pH 6.5, 10 % w/v PEG 5000 MME, 12 % v/v 1-propanol for Figure 8.8A and 0.2 M ammonium acetate, 0.1 M sodium acetate pH 4.0, 15 % w/v PEG 4000 for Figure 8.8B. Although other crystals smaller in size from the proplex screen were sent to the synchrotron facilities at the DLS and ESRF and no diffraction recorded, crystals in Figure 8.8, especially the big and single crystal in Figure 8.8 diffracted at a resolution of 7.27 Å and gave a space group of P2 with unit cell parameters of 95.1 Å, 55.0 Å and 134.8 Å for cell length a, b and c and respective angles at 90.0°, 95.2° and 90.0°.

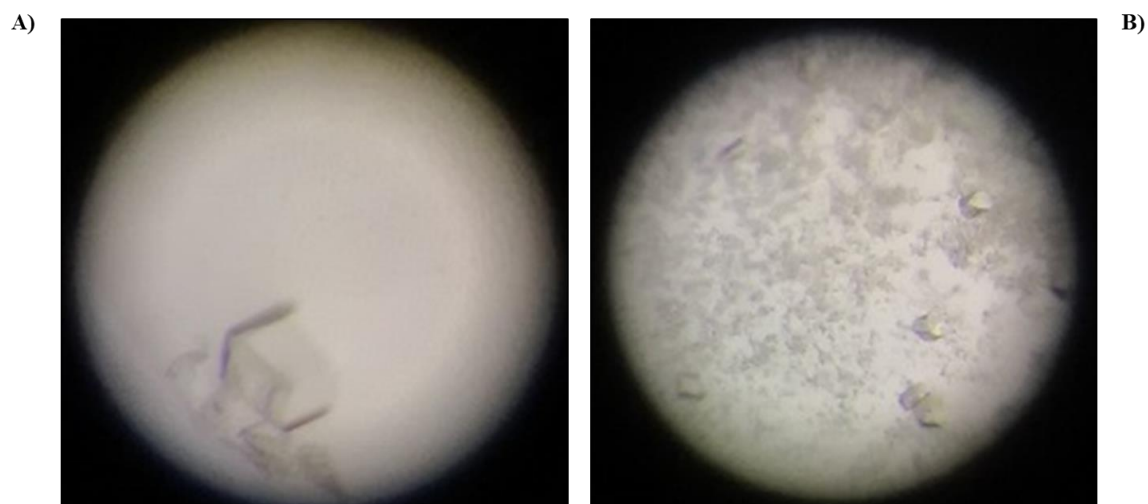


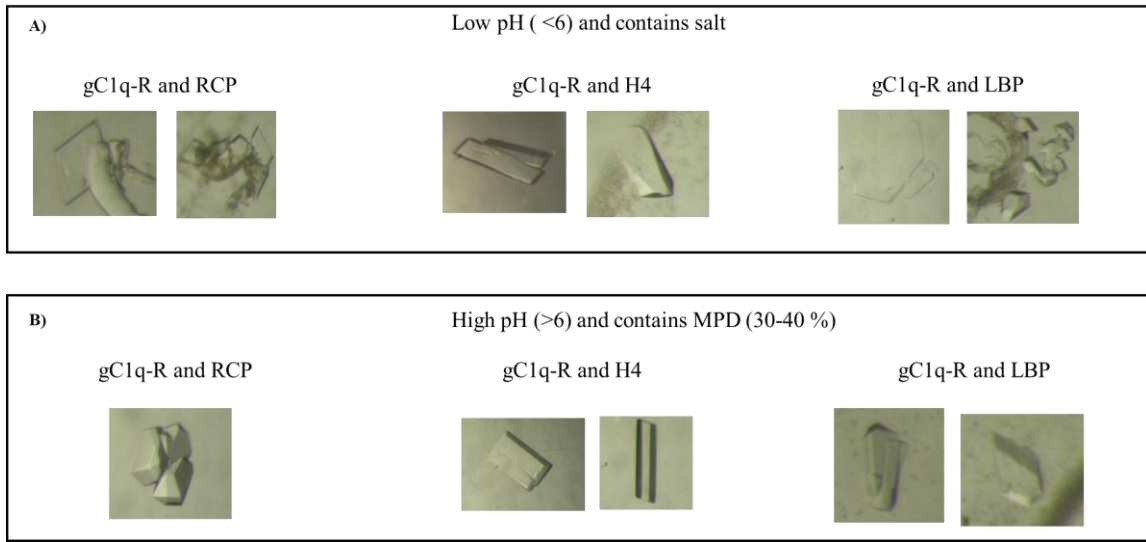
Figure 8.8: Crystals of gel filtrated gC1q-R in the presence of HK domain 5. A) shows single crystals with a big crystal in 0.1 M MES pH 6.5, 10 % w/v PEG 5000 MME, 12 % v/v 1-propanol and B) smaller crystals in 0.2 M ammonium acetate, 0.1 M sodium acetate pH 4.0, 15 % w/v PEG 4000.

8.7.0 Crystallisation of gC1q-R in the presence of peptides

A molar excess of 5-10 times peptide (RCP, H4 or LBP) was added to gC1q-R in the presence and absence of Zn^{2+} to allow gC1q-R and peptide complex formation for crystallisation. From this a number of crystals were observed in many different conditions, in low and high pH in buffers containing either salt or MPD.

Crystals obtained in the presence and absence of Zn^{2+} in a lower pH (less than 6) produced no complex formation of gC1q-R and peptides (RCP, H4 or LBP) as the solution after molecular replacement contained coordinates for gC1q-R but not for any of the peptides (RCP, H4 or LBP). Only 1 gC1q-R trimer was present in the A.S.U.

With a higher pH (more than 6), many crystals were observed to have similar crystal morphology but a bigger unit cell with 2 trimers of gC1q-R back to back in the A.S.U at a medium resolution of 3.7 Å. Optimisation is needed to improve the resolution and determine whether there is any peptide bound to gC1q-R (Figure 8.9).



C) Amino acid sequence of basic peptides

Histone 4(H4): SGRGKGGKGLGKGGAKRHRK

Lamin B receptor (LBR): PSRRRGSRSRSRSPGRP

Rubella Capsid protein (RCP): RDSGGPRRRRGNRGR

Figure 8.9: Crystals of gC1q-R in the presence of peptides (RCP, H4 or LBP). A) Crystals were obtained at low pH (<6) buffer containing different concentrations of salt (upper panel), while crystals in the B) lower panel - grew in conditions containing MPD and high pH (>6) buffer. C) Shows the amino acid sequence of the basic peptides used.

Further crystallisation experiments were performed in which all 3 peptides (H4, RCP and LBP) were incubated together with gC1q-R at 5 mg/mL with no Zn^{2+} and subjected to crystallisation in MPD and Proplex screens. Crystals were observed in both screens at different conditions with more crystals in the MPD screen.

8.8.0 Discussion

FXII has structurally been challenging to keep homogeneous as it autoactivates and therefore resulting to a mixture of FXII/FXIIa. This is not ideal for crystallisation as homogeneity is paramount to obtaining crystals. Aiding the remaining unactivated (FXII) to become activated (FXIIa), or adding inhibitors has proven to help in some instances to prevent FXII autoactivation/activation. Additionally, designing an active site mutant or removing sugars on the protein such as mFXII S526A can make tremendous difference in increasing the chances of producing crystals. However, the physical and chemical nature of crystallisation cannot be predicated and trial and error with different crystallisation conditions is a common practice. Crystallisation trials require a plethora of possibilities, as was done in my case without exhausting all possibilities. Complex formation of FXII and gC1q-R to bring about stabilisation produced crystals of just gC1q-R and it is not uncommon to have complexes dissociate during crystallisation. This is also true for gC1q-R in the presence of binding partners such as HKD5 or peptides from Histone 4 (H4), Lamin B receptor (LBP) and rubella capsid protein (RCP).

8.9.0 Conclusion

High yields of 14.83 mg/mL for WT mFXII and 28.1 mg/mL for mFXII S536A produced crystals that diffracted at 6 Å in crystallisation conditions with and without Zn^{2+} , in the presence and

absence of dextran sulfate. Although, additive screening was performed with no crystals obtained, further optimisation is required, and it will be useful to start screening around these conditions first in order to improve on data quality.

CHAPTER 9.0

Co-purification of mFXII and Graal₈₆₃₋₁₁₅₀

9.1.0 Mouse FXII co-purification with Graal₈₆₃₋₁₁₅₀

Heterologous expression of mFXII (mFXII; aa 1-596) in S2 insect cells showed an unexpected band (Band A) at a cell density around $4-5 \times 10^6$ cells/mL after 7 days of mFXII expression. Samples from the Ion-exchange (Capto-Q) chromatography show a protein band for mFXII on the SDS-PAGE gel analysis as highlighted in black box following elution, while samples from the Affinity (Ni^{2+}) chromatography showed a band for mFXII migrating at the expected size (Figure 9.1). However, an unknown band (Band A) is observed in the same lane as the mFXII band, seemingly co-purifying with mFXII following Affinity (Ni^{2+}) chromatography. Interestingly, band A was not present in the SDS-PAGE gel following Ion-exchange (Capto-Q) chromatography (Figure 9.1).

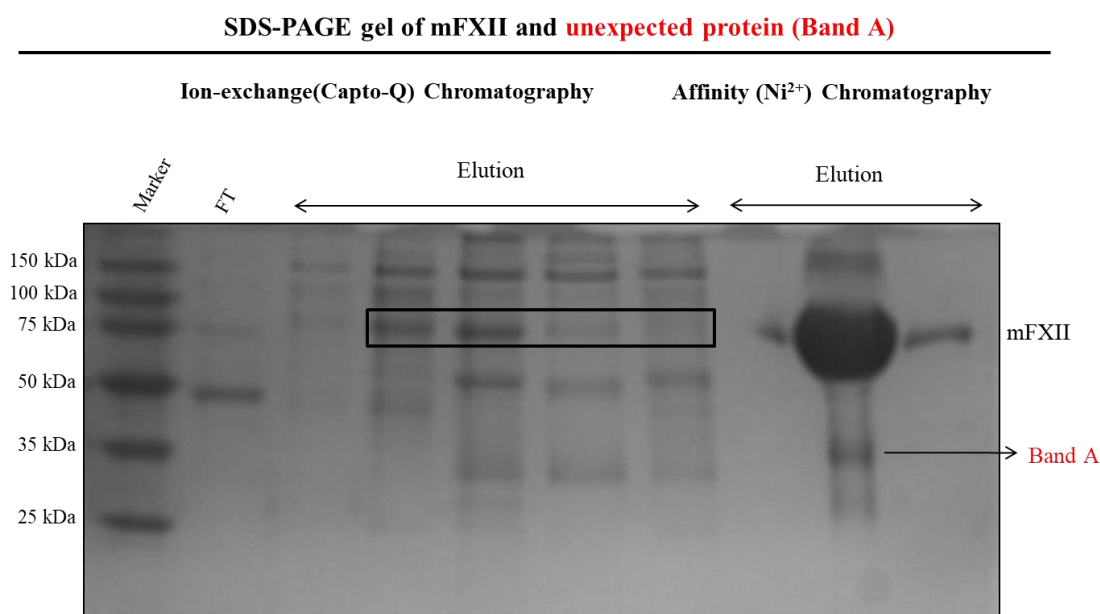


Figure 9.1: SDS-PAGE gel of mFXII expressed in S2 cells. Fractions of mFXII eluted from the Capto-Q column is shown on the SDS-PAGE gel migrating around 75 kDa (black box). Fractions of mFXII after Affinity (Ni^{2+}) chromatography purification is shown on the last three lanes of the SDS-PAGE gel. An expected protein band smaller than mFXII is also shown in red as band A. Protein marker (25-150 kDa) is shown on lane 1 and flow-through (FT) on lane 2.

Size exclusion chromatography in buffer (50 mM Tris-HCl pH 8.0, 150 mM NaCl) as the final purification step was also performed in the hope that band A will be separated from mFXII to obtain a pure homogeneous sample of mFXII. A narrow and sharp peak was observed (Figure 9.2A) and on the SDS-PAGE gel (Figure 9.2B) both mFXII and band A were present and therefore indicating both mFXII and band A to have co-eluted from the gel filtrated peak eluting at 14.9 mL (Figure 9.2A).

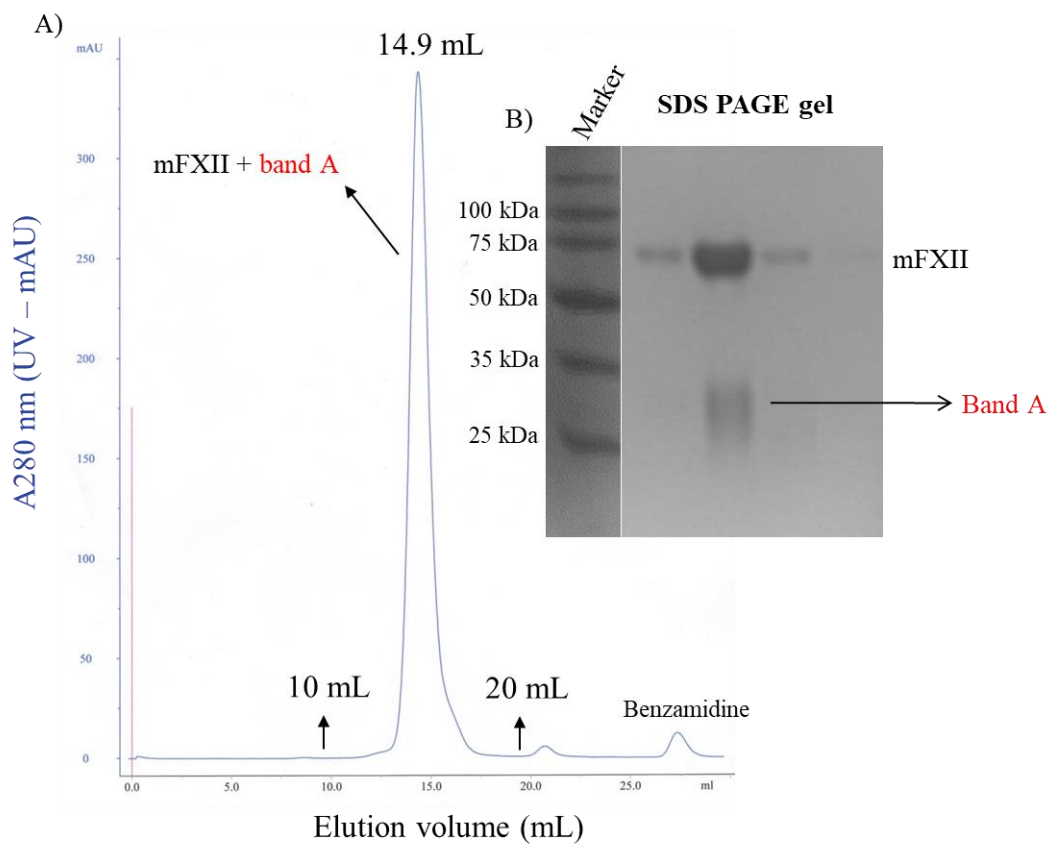


Figure 9.2: Analytical size exclusion chromatography and SDS-PAGE gel of mFXII expressed in S2 cells. **A)** Samples injected into a size exclusion chromatography (S200 10/200) column shows a high peak in the chromatograph eluting at 14.9 mL. **B)** The peak fractions are shown in a non-reducing SDS-PAGE gel and shows both mFXII and band A to be present on the same lane (middle lane), corresponding to the fraction from the middle part of the gel filtrated peak. Protein marker (25-150 kDa) is shown on lane 1.

As mFXII was not completely pure after size exclusion chromatography, and band A was still observed to have co-eluted with mFXII; a strong anion-exchange resin (Mono-Q) which has a high resolution separation capability was used to further separate Band A from mFXII based on charge. However, only a single sharp peak was observed eluting at a high NaCl concentration of around 0.82 M (820 mM) as shown in Figure 9.3A. Fractions collected are shown below the chromatograph in red from 1 to 19 with 11 and 12 ran on SDS-PAGE gel (Figure 9.3B).

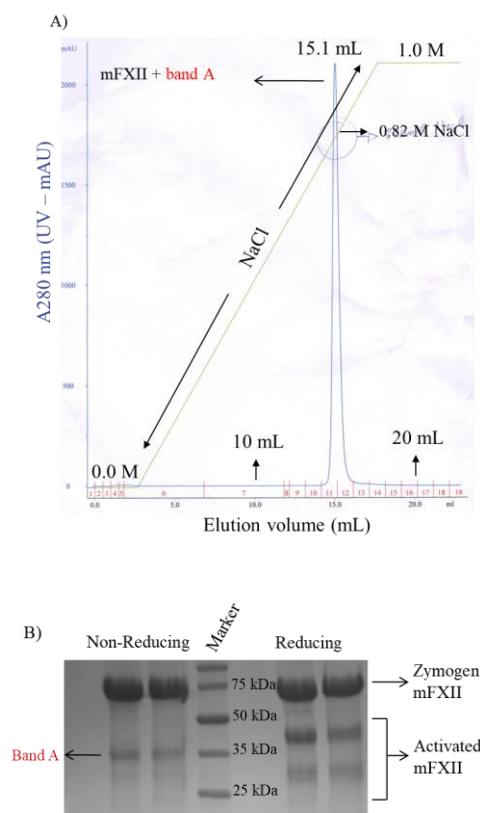


Figure 9.3: Ion-exchange chromatography and SDS-PAGE gel of mFXII expressed in S2 cells. A) Mono-Q column showed a sharp protein peak eluting at 0.82M NaCl concentration. **B)** The eluted peak fractions ran on the SDS-PAGE gel showed both mFXII and the band A under non-reducing condition but no band A under reducing condition although activated mFXII (mFXIIa) is shown. Protein marker (25-100 kDa) is shown on lane 1.

Band A protein was identified from mass spectrometry analysis as a serine protease, referred to as Graal1 (160 kDa). The mass spectrometry result revealed an isotopically averaged molecular weight of 31.7 kDa, which is close to the estimation observed on the SDS-PAGE gel (Figure 9.2). Below is an amino acid sequence of Graal1, highlighting the N-terminal signal peptide (Green), LDLR-CR and SRCR domains in bold black and red *italics*. Peptides generated from the mass spectrometry in-trypsin digest are shown bold black and red. The protease domain is underlined in black and cleavage site between Arg-Val (magenta) and catalytic triad in bold cyan also shown (Figure 9.4). The Graal1 domain organisation is also shown with Graal₈₆₃₋₁₁₅₀ highlighted.

```

MMAKWLLGLWLAILLVDVSVESLLIISNCRPGAKAYRSGSGYHSEQSEPVGLSATGNAHSSYGGDQQQPIYHRDSACPP
HFTGLVAYPHDCHRYVNCFDGSPITQTCSPGTLFNDRTQVCDHPSNVVCPAESASTRLGRLRQLDSEPKCQPGVNGLQ
PHPSDCSKFLNCANGQAFIMDCAPGTAFAFSPASLVCVHKDLAKCGSGTGAVRDTSGTDNRQSKSYETSGRDQFGNRYTT
RTTTTTRVIGDRWTDMMNQRPSGVGVEQNPHHHHHGYNPGWSGQETSIVQRGPTQSTLYVEGSLQPNRNYPTNKTPLAP
MAPNTNTGVVYGGPVEDKENVPSRQNYSRRIDYGSFPGNGWKMPPPLDPLGGQQPLNLDYSPHSPGAKEPQSQDSLPGQK
PINLDYDEEPIQYPHNGLPPYPGSPRPFYDQLPSGSKPIGRQQPVESRDATGFPDQQKPLDPNRLHGSKVPPRHS
PNPGYPLYNESNLYGGLLPPKPDSPVNTPTPTPNPSSSQAPTFLANRLHTFPYPPVDNKTSLRNP IQPHYSPSYAG
IAHSRDAFWAKVPTSTTPAQDPDPFNPELDEPFYDDVDPLSTTVRNVLVPPFDHKFYSQSTNPSINRNQASGSPNS
QAAIKKALKMLRPFYFNHSGNAQEQLAQQAESAIVSVISKPSTTTTTPRPTSKTPKTPDPDFDAELIKAGEQESLDSVD
DDYVFPDARETSRTEQLDPSSTTYASTNFQSRTRRAELDPDTLTATTMKTNWHAPGHSRDYHRRHPNLPDPFTEHHNS
SPHQHQHHRHPHEHSADFHLRHPGLPNPFFLKNETPQHQLNDDWDLNPSNAEEVTPKLATRSSFNTQCDFDCGNGQ
CLRKEICDGRKNCPNGKDEANCPPSDYEVRLSGGESPNMGRIEVKANGQWGYCDDRFGLKDADVVCRELGFQMGAE
VRGSSFYAPPNQDFNYLMDEVECHGNETKLGQCAFKGWGVNCGVDEAVGVTCKVVMKCPNNYWLCHTSKECIPPAFV
CDNTPDCADKSDECAAVCQAPVQYRLEGGRRNSNEGRLEVKHHGVWGSVCDDDFNLKSAQVACNSMGFFGPAKIEKNIFG
NSNGPIWLDQVMCFGNETSIDQCNHWNWGEHNCNHTEDVALHCSAGPPPRSQRYSQTQIKGGRSLGRETTPKTYSQIGL
WERSSKAVHTPRRCGIFKDDLTDEYAHREERVVRGNVAQRGRHPWQATIRTRGRGGISSHWCGAVVISKRHLLTAACHL
YGSPRGAYFVRVGDHYANIAESSEVDSFIENWYLHENFRKGTMMNNDIALVVLKTPPLKFSDYVQPICLPDKNAELVEDR
KCTISGWGSIKSGVSTPAQVLGSAELPLADHVCQSNVYGSAMSEGMFCAGSMDESVDACEGDSGGFLVCSDDDDGETL
YGLISWGQHCGFKNRPGVYVRVNHYIDWIYEKINESLLRF

```

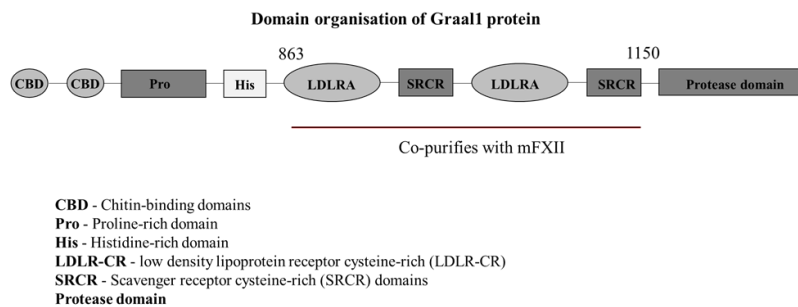


Figure 9.4: Amino acid sequence and domain organisation of Graal1. Amino acid sequence of Graal1 showing a signal peptide in green, LDLR and SRCR domains in black and red in *italics*. Peptides generated from the in-trypsin digest and subjected to mass spec is also in black and red with an isotopically averaged molecular weight of 31.7 kDa. Proteolysis to activate the serine protease takes place initially between Arg-Val (RV) in magenta and the catalytic triad in cyan within the protease domain underlined.

Graal has three isoforms with molecular weights of 160, 265 and 309 kDa in size for Graal1, Graal2 and Graal3, respectively. Figure 9.4 shows the Graal1 domain organisation, consisting of a chitin-binding domains (CBD), Histidine and Proline-rich domains, Scavenger receptor cysteine-rich (SRCR) domains, low density lipoprotein receptor cysteine-rich (LDLR-CR) domain and a serine protease domain. The mass spectrometry data revealed that the tandem LDLR-CR and SRCR domain (Graal₈₆₃₋₁₁₅₀) from Graal1 was co-purifying with mFXII on Affinity (Ni²⁺), size exclusion and strong anion-exchange (Mono-Q) columns suggesting a tightly bound complex. Both LDLR-CR and SRCR domains are rich in cysteines and form disulfide bonds. The disulphide bonds are reduced in the presence of 2-Mercaptoethanol (β ME), thus showing no Graal₈₆₃₋₁₁₅₀ band on a 15 % SDS-PAGE gel (Figure 9.3).

9.2.0 Preparation and expression of Graal₈₆₃₋₁₁₅₀ in S2 insect cells

A construct for Graal₈₆₃₋₁₁₅₀ gene (2x_LDLR-CR 2x_SRCR) was successfully amplified from pUC57-Graal1 template in which BglIII and MluI REs were already introduced. To confirm whether the Graal₈₆₃₋₁₁₅₀ gene was successfully subcloned into pMT-PURO, a double digest of pMT-PURO-Graal₈₆₃₋₁₁₅₀ was performed and showed a double band on a 1 % agarose gel (Figure 9.5) with Graal₈₆₃₋₁₁₅₀ migrating around 0.882 (lane 2) kb next to the 1 kb ladder band on lane 1. DNA sequencing results for pMT-PURO-Graal₈₆₃₋₁₁₅₀ sample shown on lane 2 was further confirmed to have no mutation and that the Graal₈₆₃₋₁₁₅₀ gene was correctly inserted into the pMT-PURO plasmid.

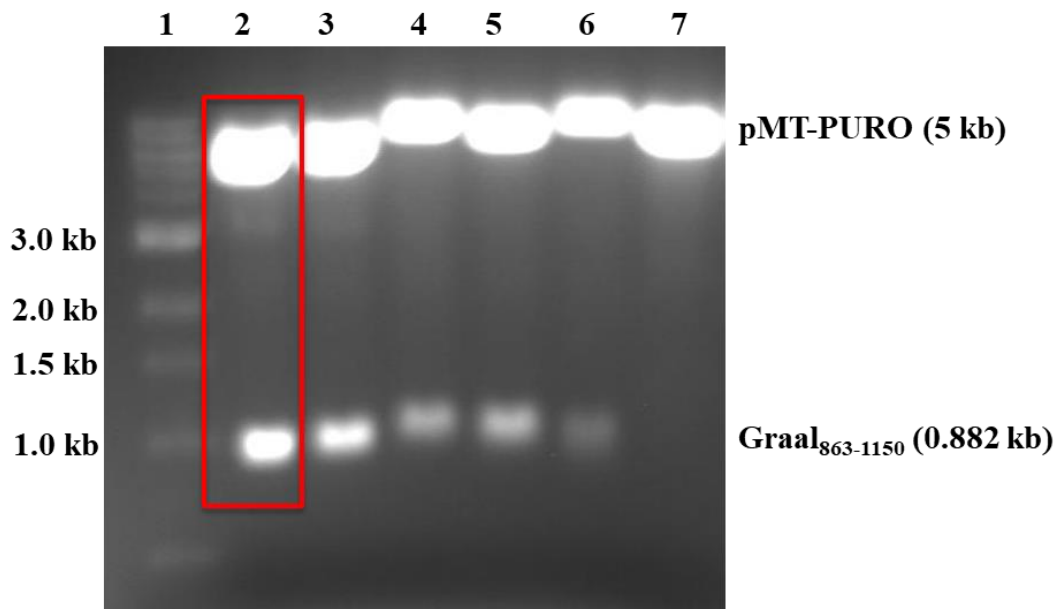


Figure 9.5: 1 % agarose gel analysis of double digested pMT-PURO- Graal₈₆₃₋₁₁₅₀ gene. 5 mL miniprep culture (novoblue cells) were double digested using BglIII and MluI. A 1 kb ladder was loaded first, followed by double digested pMT-PURO- Graal₈₆₃₋₁₁₅₀ gene and a double digested pMT-PURO alone on lane 7 (control). Lane 2 highlighted in red box shows digested pMT-PURO- Graal₈₆₃₋₁₁₅₀ producing pMT-PURO and Graal₈₆₃₋₁₁₅₀.

The highlighted Graal₈₆₃₋₁₁₅₀ protein bands in the red box for peak 2 were pooled and yielded a protein concentration of 13.8 mg/mL. This protein was used to perform binding studies with FXII using Surface Plasmon Resonance (SPR).

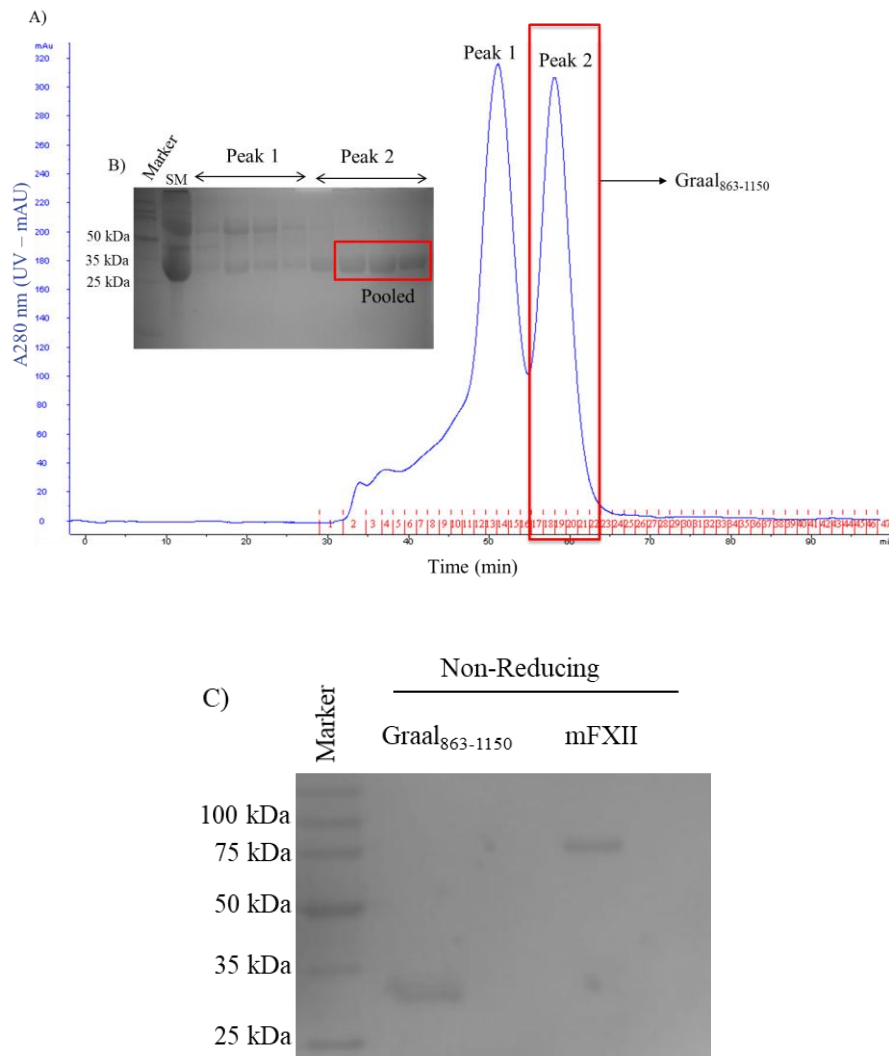


Figure 9.7: Size exclusion chromatography and SDS-PAGE gel analysis of Graal₈₆₃₋₁₁₅₀. A) Graal₈₆₃₋₁₁₅₀ protein isolation from size exclusion chromatography (S75 16/60 column). B) Peak 1 and peak 2 were ran on SDS-PAGE gel under non-reducing condition with the last 3 lanes of peak 2 showing pure Graal₈₆₃₋₁₁₅₀ protein bands migrating below the 35 kDa marker band. Starting material (SM) is shown next to the molecular weight marker (15-15 kDa). C) Shows pure bands of Graal₈₆₃₋₁₁₅₀ and mFXII under non-reducing conditions.

9.3.0 Binding analysis of Graal₈₆₃₋₁₁₅₀ and mFXII using SPR

Although, Graal has been suggested to may have a role in blood coagulation ⁽³¹⁸⁾ in hemolymph coagulation in horseshoe crabs ⁽³¹⁹⁾, there is no data characterising Graal binding to FXII. To confirm whether Graal₈₆₃₋₁₁₅₀ interacts with FXII, binding analysis of Graal₈₆₃₋₁₁₅₀ to immobilised mFXII S526A showed binding as recorded in response unit terms. Additionally, as human complement factor I (CFI) similar to Graal₈₆₃₋₁₁₅₀ contains 1 SRCR and 2 LDLR, it was also tested and showed binding for immobilised mFXII S536A in a buffer containing Zn²⁺. FXII substrates PK and FXI and FXII inhibitor corn trypsin inhibitor (CTI) were used as controls and they all as expected showed binding to immobilised mFXII S536A (Figure 9.8).

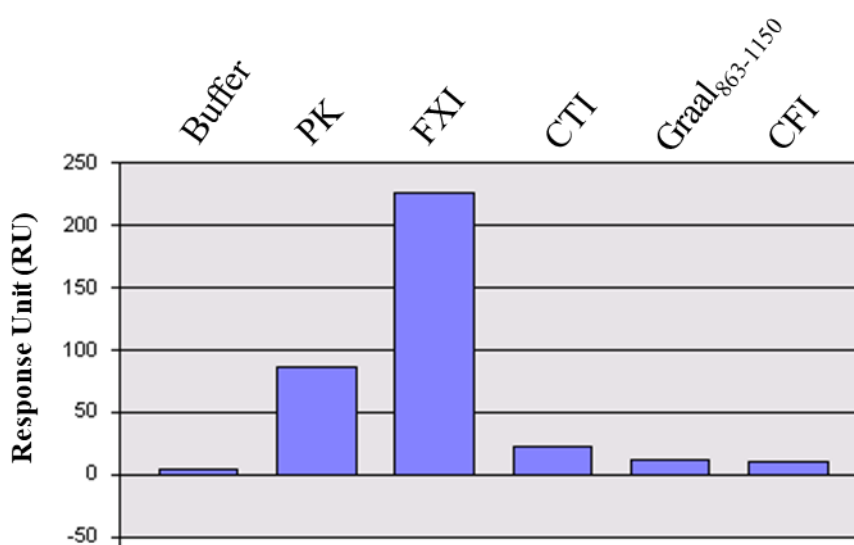


Figure 9.8: SPR binding analysis of immobilised mFXII S526A to Graal₈₆₃₋₁₁₅₀ and CFI. 300 nM Graal₈₆₃₋₁₁₅₀ and CFI binds to immobilised mFXII S526A. Controls of FXII substrates PK and FXI and FXII inhibitor CTI showed binding to FXII S526A. Buffer alone shown with background signal. Running buffer for samples contained Zn²⁺.

To determine whether FXII can bind to Graal₈₆₃₋₁₁₅₀, immobilised Graal₈₆₃₋₁₁₅₀ was also tested. Both mFXII S526A and human FXII FnII-EGF1 fused to MBP at 1000 nM were able to reproduce the binding to Graal₈₆₃₋₁₁₅₀ in a running buffer consisting of 20 mM Hepes pH 7.4, 140 mM NaCl, 0.005 % P20, 50 μ M Zn²⁺ (Figure 9.9).

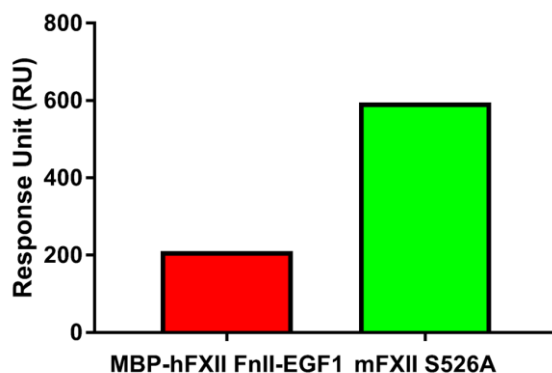


Figure 9.9: FXII binding to immobilised Graal₈₆₃₋₁₁₅₀ on CM5 sensor chip surface. 1000 nM of mFXII S526A and MBP-hFXII FnII-EGF1 binding to immobilised Graal₈₆₃₋₁₁₅₀ in red and green, respectively. Running buffer contained Zn²⁺.

The crystal structure of CFI⁽³²⁰⁾ shows 2 Ca²⁺ ions bound to each LDLR domain. As Ca²⁺ has been reported to play a structural role in CFI, adding 25 μ M Ca²⁺ and 25 μ M Zn²⁺ showed almost 3-fold increase in the SPR response unit (RU), compared to just 50 μ M Zn²⁺ for CFI binding to immobilised plasma FXIIa. With 25 μ M Ca²⁺, 300 nM of CFI was used, while almost 3 times the concentration (800 nM) of CFI used in the absence of Ca²⁺ gave lower RU (Figure 9.10).

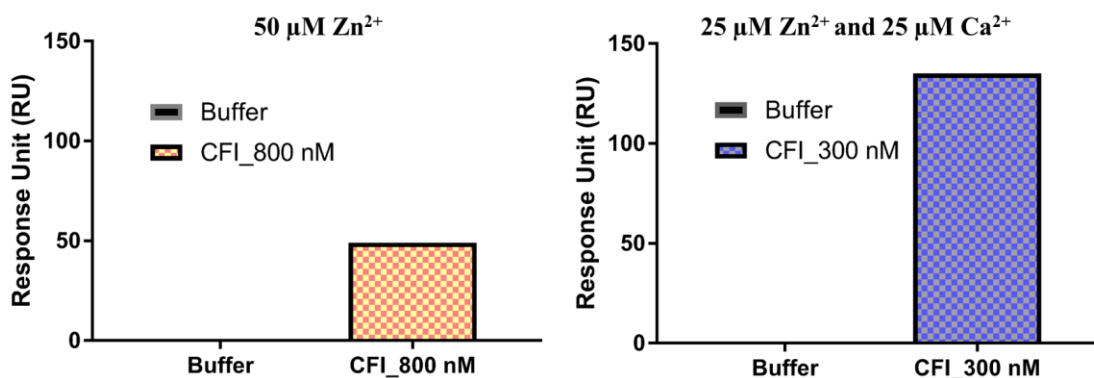


Figure 9.10: SPR binding analysis of CFI to immobilised human FXIIa in the presence and absence of Ca²⁺. Left panel – CFI (800 nM) with 50 µM Zn²⁺ and no Ca²⁺ in running buffer, while right panel in blue designed pattern represents CFI (300 nM) in the presence of 25 µM Zn²⁺ and 25 µM Ca²⁺.

Ca²⁺ ions clearly increased the RU of the sensogram with CFI in the presence of both Zn²⁺ and Ca²⁺ showing a much higher response than CFI at 800 nM without Ca²⁺. It appears that the structural role Ca²⁺ has for CFI improves the binding to immobilised plasma FXIIa.

9.3.1 Binding kinetics of Graal₈₆₃₋₁₁₅₀ to immobilised FXII

Graal₈₆₃₋₁₁₅₀ binding to immobilised mFXII S526A was further characterised to determine the K_D value of the interaction using SPR. A concentration increase (0.1-1 µM) in Graal₈₆₃₋₁₁₅₀ binding to immobilised mFXII S526A in the presence of 50 µM Zn²⁺ was assessed showing an association phase and dissociation phase. The sensogram also seem to suggest that the highest concentration (1 µM) for Graal₈₆₃₋₁₁₅₀ to saturate the surface.

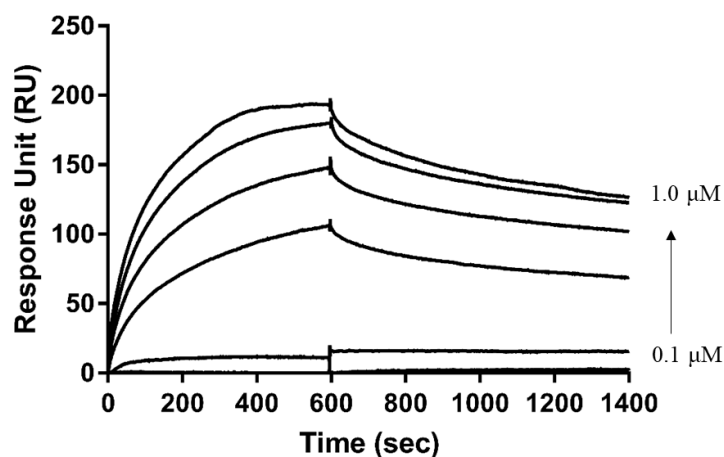


Figure 9.11: Binding curves of Graal₈₆₃₋₁₁₅₀ to immobilised mFXII S526A. Graal₈₆₃₋₁₁₅₀ was injected onto the CM surface on which mFXII S526A was immobilised. Binding was observed as shown in the association phase (0-600 seconds) followed by dissociation (600-1400 seconds). Running buffer contained 50 μM Zn^{2+} .

Lower concentrations of Graal₈₆₃₋₁₁₅₀ (50-400 nM) binding to immobilised plasma human FXIIa in a similar manner to CFI showed higher response unit (RU) in the presence of 25 μM Zn^{2+} and 25 μM Ca^{2+} . Comparing this to Figure 9.11 which had no Ca^{2+} ion in the running buffer, it therefore appears that 2.2-fold less concentration of Graal₈₆₃₋₁₁₅₀ can produce an RU of more than 250 or even more as the highest sensogram curve has not reached saturation (Figure 9.12). The wide gap between concentrations 200 nM and 300 nM is not ideal and therefore needs repeating to obtain correct K_D values.

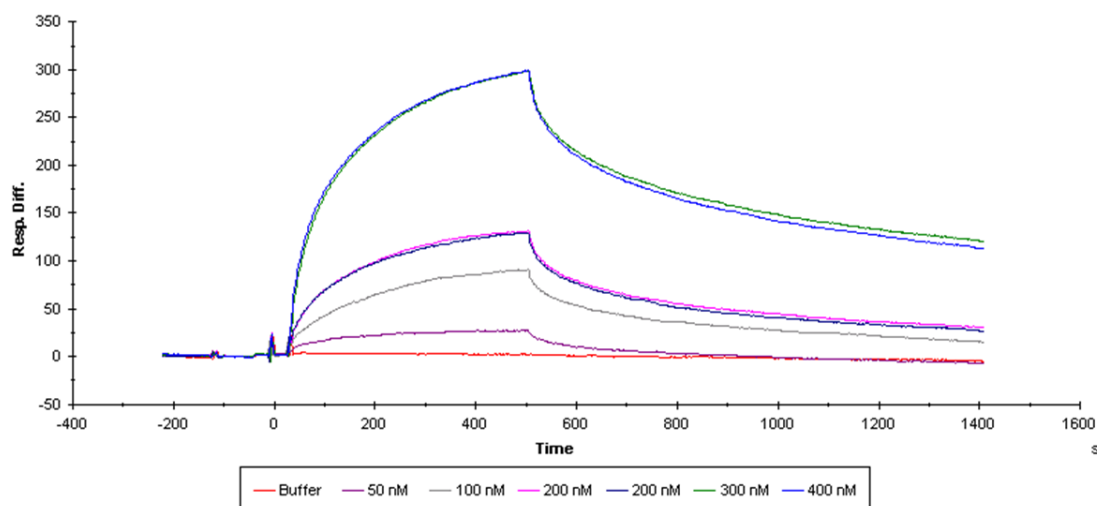


Figure 9.12: Binding curves of Graal₈₆₃₋₁₁₅₀ to immobilised human FXIIa. A concentration series of Graal₈₆₃₋₁₁₅₀ (50 – 400 nM) binding to immobilised human FXIIa in a running buffer containing 25 μM Zn^{2+} and 25 μM Ca^{2+} . Graal short at 200 nM was repeated as shown overlaid in pink and blue.

9.4.0 Binding kinetics of CFI to immobilised FXII

Following the binding analysis performed for CFI binding to immobilised plasma FXIIa at concentration of 300 nM in the presence of 25 μM Zn^{2+} and 25 μM Ca^{2+} , a concentration series of CFI (50-400 nM) again showed binding to immobilised plasma FXIIa thus reproducing the binding. Although the sensogram curves appear to reach equilibrium, optimisation with more concentration below 50 nM and a much stabler sensor surface as the 200 nM repeat (blue) does not seem to reproduce well enough (Figure 9.13)

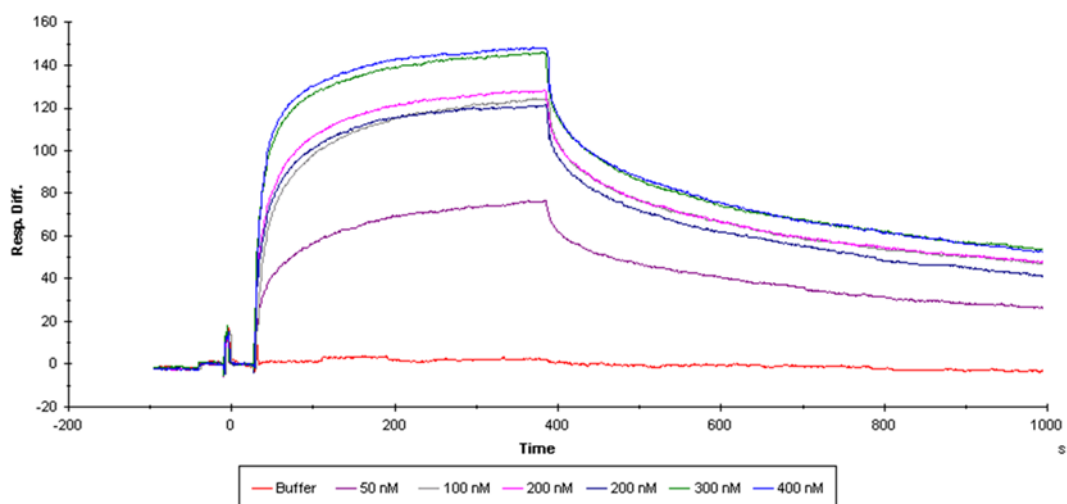


Figure 9.13: Binding curves of CFI to immobilised human FXIIa. A concentration series of Graal₈₆₃₋₁₁₅₀ (50 – 400 nM) binding to immobilised human FXIIa in a running buffer containing 25 μM Zn^{2+} and 25 μM Ca^{2+} . CFI at 200 nM was repeated as shown in pink and blue.

9.5.0 Plasma FXII activation in the presence of CFI

To find out whether FXII can be activated in the presence of CFI, human commercial zymogen FXII was assessed for activation in the presence of 50 μM Zn^{2+} and was observed to be converted from FXII to FXIIa following 10 minutes of incubation.

FXIIa was able to proteolytically cleave S-2302 substrate to produce pNA product thus having an absorbance of 1 at 405 nm (Figure 9.14). To determine whether FXII F_nII binds to CFI and compete for binding at the same site on CFI, 300 nM FXII F_nII was added. Interestingly, the absorbance at 405 after addition of S-2302 showed almost a similar readout as the buffer alone thus demonstrating that FXII F_nII interacts with CFI. The insect recombinant inhibitor, anophensin against FXII F_nII and HK domain 5 was also tested and showed a reduction in the absorbance of the pNA.

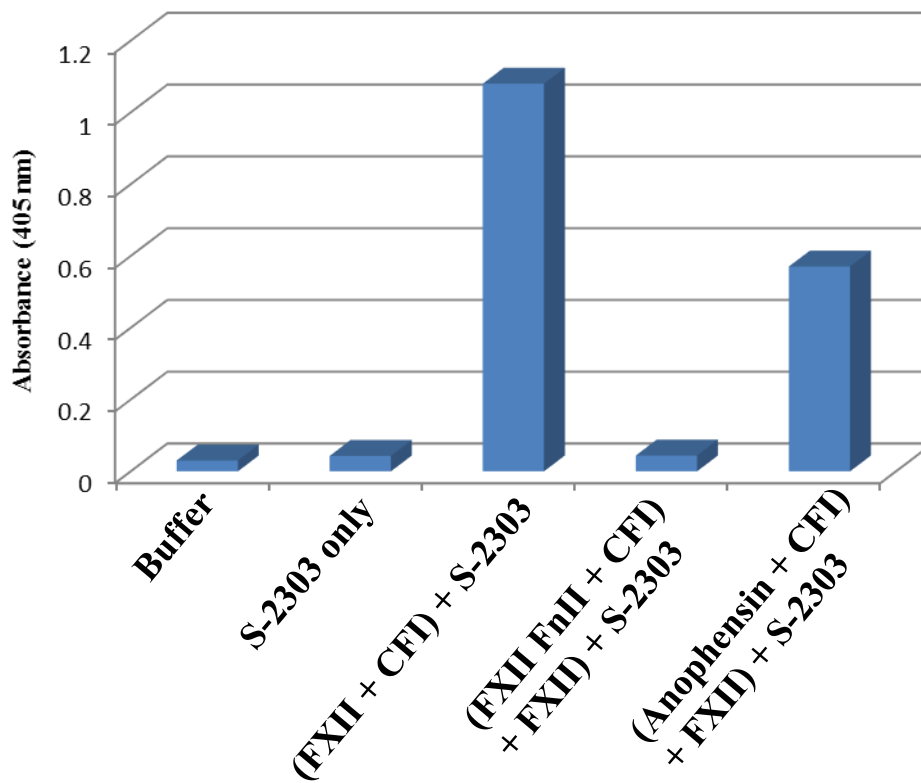


Figure 9.14: FXII cleavage of chromogenic substrate S-2302. FXII activity assay with activator (CFI) showing FXII conversion to FXIIa and subsequently cleaving the chromogenic substrate S-2302 to pNA to be read at 405 nm. FXII FnII competes with full length FXII for binding to CFI and shows no FXII activation. Addition of anophensin reduced the absorbance.

9.6.0 *Graal1* homologues and Molecular docking

Protein structure prediction with Phyre2 for Graal SRCR domain A and B predicts a model homologous to the crystal structure of human lysyl oxidase-like 2 (hLOXL2) and mouse MARCO (mMARCO) and are 44 % similar to Graal1 SRCR domain with 100 % confidence (Figure 9.15).

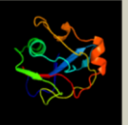
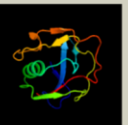
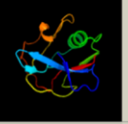
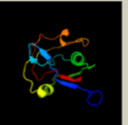
#	Template	Alignment Coverage	3D Model	Confidence	% I.d.	Template Information
1				100.0	44	PDB header: oxidoreductase Chain: B; PDB Molecule: lysyl oxidase homolog 2; PDBTitle: crystal structure of human lysyl oxidase-like 2 (hloxl2) in a2 precursor state
2				100.0	34	PDB header: endocytosis Chain: A; PDB Molecule: scavenger receptor cysteine-rich type 1 protein m130; PDBTitle: crystal structure of the scavenger receptor cysteine-rich domain 52 (srcr5) from porcine cd163
3				100.0	42	Fold: SRCR-like Superfamily: SRCR-like Family: Scavenger receptor cysteine-rich (SRCR) domain
4				100.0	44	PDB header: ligand binding protein Chain: A; PDB Molecule: macrophage receptor marco; PDBTitle: crystal structure analysis of the dimeric form of the srcr domain of 2 mouse marco
5				99.9	28	PDB header: immune system Chain: A; PDB Molecule: cell differentiation antigen cd6; PDBTitle: extracellular srcr domains of human cd6

Figure 9.15: Prediction of *Graal1* SRCR domain homologues using Phyre2. Numbers 1 (human lysyl oxidase-like 2 (hLOXL2) containing SRCR domain 4) and 2 (SRCR domain of mouse MARCO) showing their 3D structures from the Protein Data Bank (PDB), predicted to have a similar fold to the SRCR domain of *Graal1*.

9.7.0 Molecular docking of SRCR and FXII F_nII

Other human homologues including Hepsin and CFI also have the SRCR domain. From the SPR data, we know that CFI binds to immobilised human plasma FXII in the presence of divalent metal ions (Zn²⁺ and Ca²⁺). To understand the molecular interaction of SRCR domain in CFI,

mMARCO and hepsin to FXII, FXII FnII crystal structure (unpublished) and published SRCR domain for CFI, mMARCO and hepsin were studied *in silico* through molecular docking using CLUSPRO. In Figure 9.16 FXII FnII domain is shown docked to the SRCR domain of CFI (PDB code 2XRC). Under careful inspection FXII FnII Arg47 is noticed facing downward to sit on the surface of the SRCR domain containing negatively charged pocket. The docking data also indicated that Trp53-Trp66 pocket and Tyr68 to be involved in hydrophobic interactions with SRCR domain of CFI and mMarco (Figure 9.16A-B). For Hepsin SRCR domain interaction with FXII FnII, other residues including Tyr34, Lys45 and the Trp53-Trp66 from FXII FnII is seen to potentially be interacting with hepsin SRCR domain (Figure 9.16C). A zoomed in figure for FXII FnII Arg47 interaction with Gln10 of Hepsin SRCR domain is shown in Figure 9.16D-E.

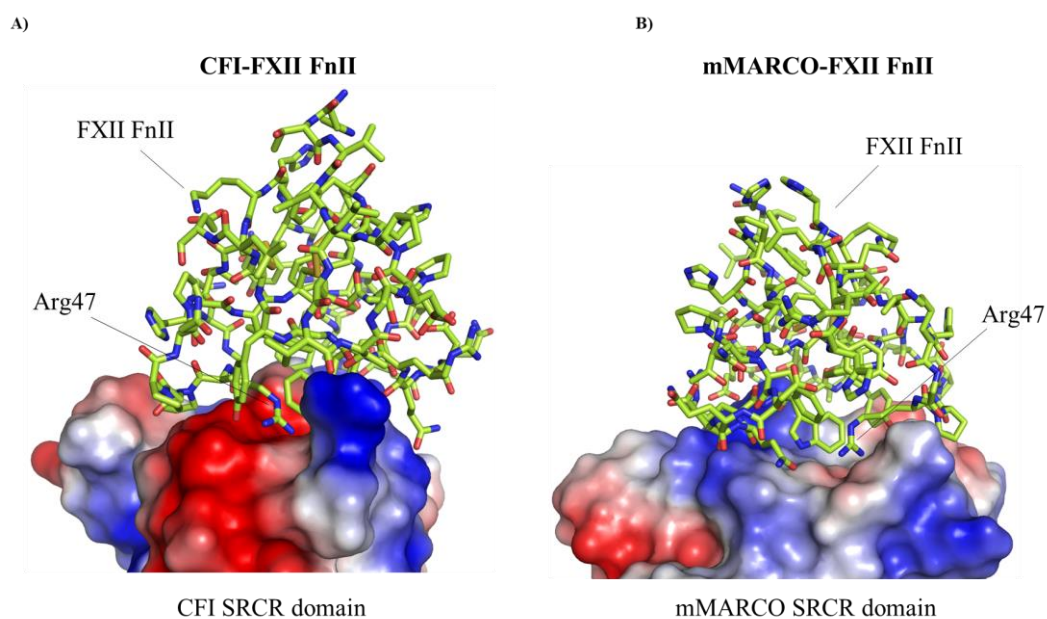


Figure 9.16A-B: Molecular docking of FXII FnII to SRCR domain from CFI and mMARCO. A) FXII FnII Arg47 is shown to sit on the surface of CFI SRCR domain (negatively charged surface). B) FXII FnII Arg47 interacts with a much reduced negatively charged surface on the mMARCO SRCR domain.

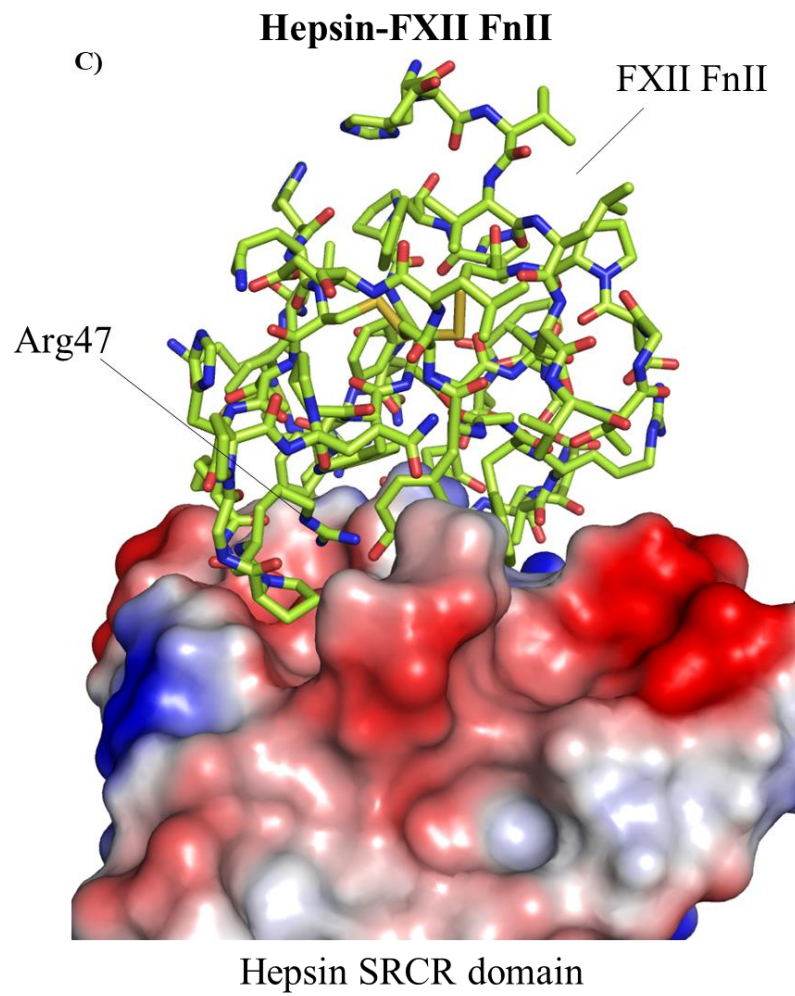


Figure 9.16C: Molecular docking of FXII FnII to the SRCR domain of Hepsin. FXII FnII Arg47 interacts with Gln10 of Hepsin SRCR domain.

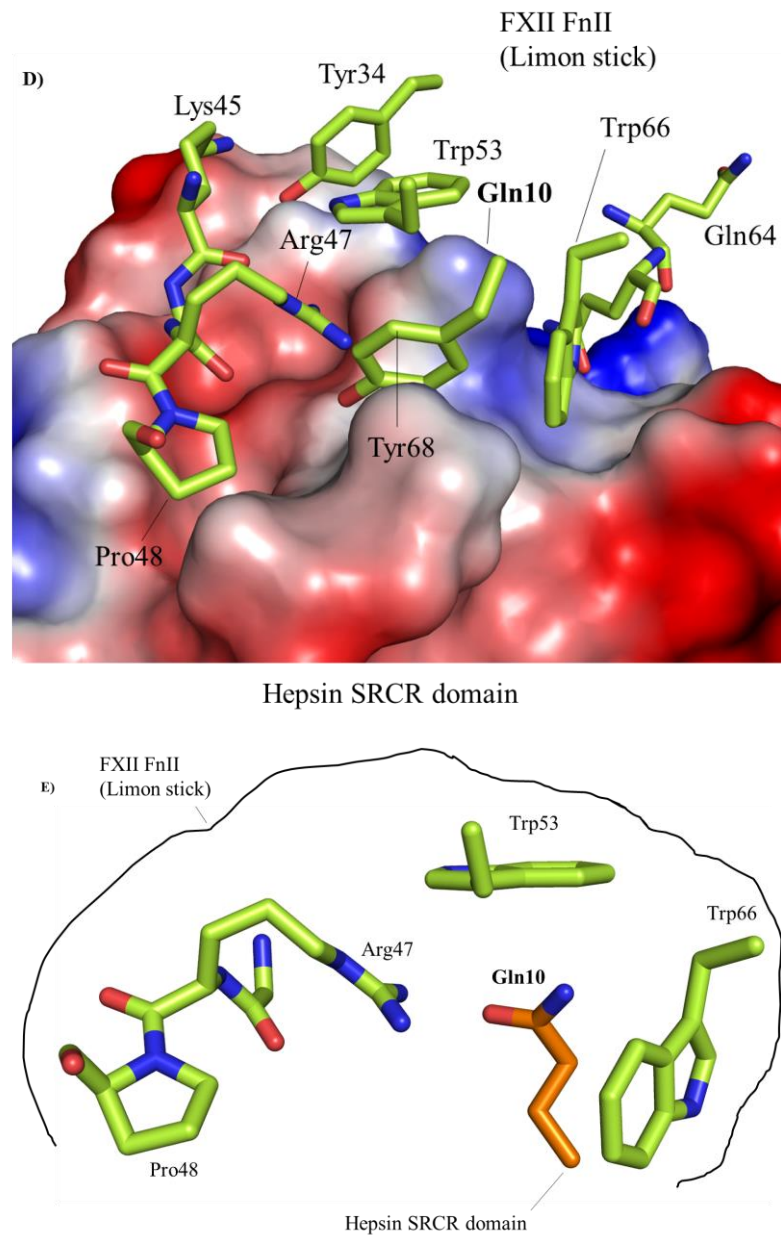


Figure 9.16D-E: Molecular docking of FXII FnII to the SRCR domain of Hepsin. Zooms in the interaction between FXII FnII and Hepsin SRCR domain showing Hepsin Gln10 interacting with Arg47 and is also in close proximity to Trp66 of FXII. FXII FnII is shown in limon stick, while the SRCR domains are represented with its electrostatic surface potential with red for negative charge, blue for positive charge and white/grey for neutral charge. Other residues in FXII FnII are also shown in the interaction with SRCR domains in all the figures (A-C).

9.10 Discussion

9.10.1 *Graal1 and CFI binding to FXII*

Graal1 (160 kDa) has been suggested to be autoactivated by bacteria and that it could have a role in blood clotting, in a similar manner to Limulus factor C zymogen ⁽³²¹⁾. Graal₈₆₃₋₁₁₅₀ from Graal1 interacts with FXII, as demonstrated from the co-purification of mFXII and Graal₈₆₃₋₁₁₅₀ without the remaining domains of Graal1 (including protease domain), suggesting that Graal1 was cleaved. The LDLR-CR and SRCR in proteins founds in humans have not previously been demonstrated to interact with FXII, so this opens the possibility of FXII binding to CFI, Hepsin or MARCO.

Whether, Graal1 was cleaved prior to or after binding to FXII in the media is rather unclear. However, the presence of a protein band (lanes 3-7) around 150 kDa and no Graal₈₆₃₋₁₁₅₀ (band A) from the Ion-change purification in Figure 9.1 seem to suggest no cleavage from the media. The Graal₈₆₃₋₁₁₅₀ band was observed in the affinity purification step, with no 150 kDa protein band present but a much smaller protein band migrating around 33 kDa corresponding to Graal₈₆₃₋₁₁₅₀. This may suggest Graal1 is cleaved after the Ion-change purification step, without ruling out FXIIa involvement in cleaving Graal1, as active FXIIa was present in the purification sample.

Graal1, similar to FXII is a serine protease but no Graal1 homologues in humans have previously not been reported to bind or cleave FXII to FXIIa or FXIIa binding and cleaving any Graal1 homologues. The reason why Graal1 has not retained its protease domain and other protein binding domains is unclear. What is clear is that Graal₈₆₃₋₁₁₅₀ bound tightly to mFXII/mFXIIa, as both Mono Q and gel filtration (size exclusion chromatography) were unable to separate mFXII from Graal₈₆₃₋₁₁₅₀, despite the charge and size difference.

In the binding analysis studies, Graal₈₆₃₋₁₁₅₀ and CFI showed binding to immobilised FXII S526A and therefore confirms Graal1 and CFI were able to bind FXII. However, it is unclear which domain whether the LDLR-CR or/and SRCR domains bind to FXII, although the SRCR domains in CFI and Hepsin contain negatively charged properties on their surfaces. Furthermore, hepsin has no LDLR-CR and it is therefore plausible to suggest that the SRCR domain may be involved in the binding. It is clear that the LDLR-CR domain helps to facilitate binding to FXII in the presence of Ca²⁺.

9.10.2 FXII activity assay in the presence of CFI

The activation of plasma FXII in the presence of CFI seems to indicate that CFI is contributing in zymogen FXII conversion to active FXII (FXIIa). Although, zymogen FXII or CFI alone were not tested for activation to rule out a false positive readout, the same result should have been reproduced in the presence of FXII FnII if FXII was already activated. Interestingly, abrogation of FXII activation was observed, suggesting that FXII FnII may compete with full-length FXII in binding to CFI and results into no conversion of FXII to FXIIa to assay the S-2302 substrate cleavage. Additionally, the Anophensin inhibition shows a clear indication that FXII-mediated S-2302 cleavage is affected as anophensin binds to the FXII FnII in the FXII (data not shown). All together, this may suggest that the FXII FnII may bind to CFI.

9.10.3 Binding of FXII FnII to SRCR domains

The molecular docking data for FXII FnII in complex with SRCR domains from CFI, MARCO and Hepsin are only predictions and may not necessarily reflect the true nature of such interaction, unless validated experimentally. What is observed to be a common trend in some of docked FXII FnII to SRCR domains from CFI, MARCO and Hepsin is that the conserved Arg47

in FXII FnII sits on the negatively charged surface of the SRCR domains shown. Interestingly, in the Hepsin SRCR-FXII FnII complex, the Trp53-Trp66 pocket in FXII FnII is shown accommodating Gln10 of Hepsin SRCR domain to interact with FXII FnII Arg47.

9.11.0 Conclusion

Scavenger receptor cysteine-rich (SRCR) protein domain is present in invertebrates (sponges) and vertebrates (mammals) ⁽²⁵⁰⁾ with reported function in host defence and immune response ⁽²⁵²⁾. My findings seem to suggest that FXII can interact with SRCR domains from insect (Gaal) and human CFI, with the activation assay for FXII demonstrating the capability of CFI to convert zymogen FXII to FXIIa.

Also, the FXII FnII may have a role in binding to CFI, as full-length FXII was displaced and prevented from binding to CFI in the competition assay. Furthermore, the molecular modelling predictions for SRCR domains in MARCO, CFI and Hepsin seem to all bind FXII FnII Arg47.

9.12.0 Future prospects

To validate the molecular docking data, site directed mutagenesis of key residues including Arg47 should be considered. Also, as Hepsin does not have any LDLR domain and has only one SRCR domain on its N-terminus and protease domain on its C-terminus, binding studies can provide useful insight into how FXII interacts with both SRCR and LDLR domains in CFI and MARCO in comparison to Hepsin. Unlike MARCO, both CFI and Hepsin are serine proteases and a cleavage or activity assay or a pull-down assay from plasma to verify complex formation of FXII with CFI or FXII bound to Hepsin or even MARCO depending on the design of the

experiment will add to the binding and molecular docking data. As all these three proteins are implicated in roles such as complement activation and the immune system with suggested roles in platelet function for CFI and Hepsin in blood clotting; the characterisation of FXII binding to SRCR domains might shed some light in FXII binding to new surface proteins (SRCR domains). As I am finishing my PhD, I intend to apply for funding to further characterise the molecular interaction of FXII to SRCR domains. This will involve the determination of how strongly FXII binds to recombinantly expressed SRCR domain in CFI, Hepsin and MARCO using analytical gel filtration, SPR and ITC. Furthermore, determination of the 3D crystal structure to deduce the binding at the molecular level. Translating the molecular interaction of FXII to SRCR domains using *in vitro* methods in plasma or plate reading following FXII activation upon stimulation by SRCR domains.

10.0 Appendices

Amino acid name	Three letter code	One letter code
Glycine	Gly	G
Alanine	Ala	A
Valine	Val	V
Leucine	Leu	L
Isoleucine	Ile	I
Threonine	Thr	T
Serine	Ser	S
Proline	Pro	P
Trptophan	Trp	W
Tyrosine	Tyr	Y
Phenylalanine	Phe	F
Cysteine	Cys	C
Methione	Met	M
Glutamine	Gln	Q
Asparagine	Asn	N
Glutamate	Glu	E
Aspartate	Asp	D
Arginine	Arg	R
Lysine	Lys	K
Histidine	His	H

Stock(10X) TBE	1 % Agarose for gel electrophoresis
107.8 g Tris 55 g Boric acid 5.8 g EDTA De-ionised water- Add to make up to 1 L	1 g of agarose powder in 100 mL of 1x TBE-buffer Make up 1x from 10x TBE to run gel.

Agar plates

Bacteriological Agar	7.5 g
NaCl	4 g
Trypton	5 g
Yeast extract	2.5 g

Antibiotics

Stock	Final
Ampicillin (30mg/mL)	30-50 µg/mL
Ampicillin (100mg/mL)	100 µg/mL
Chloramphenicol (30mg/mL)	30 µg/mL

Buffers for protein purification

Ion-exchange chromatography (Capto S)

Buffer A	Buffer B
20-50 mM MES pH 6.0	20-50 mM MES pH 6.0
	1 M NaCl

Ion-exchange chromatography (Capto Q)

Buffer A	Buffer B
20-50 mM Tris-HCl pH 8.0	20-50 mM Tris-HCl pH 8.0
	1 M NaCl

Affinity (Ni²⁺) chromatography

Column Lysis Buffer (Buffer A)	Elution Buffer (Buffer B)
50 mM Tris-HCl pH 8.0	50 mM Tris-HCl pH 8.0
200 mM NaCl	200 mM NaCl
20 mM Imidazole	1M Imidazole
1 complete tablet (Protease inhibitor-EDTA free)	1 complete tablet (Protease inhibitor)

Size exclusion chromatography

50 mM Tris-HCl, 100 mM NaCl pH 8.0

Sodium Dodecyl Sulfate-Polyacrylamide gel electrophoresis (SDS-PAGE)

Resolving Solution

	Resolving Solution			Stacking
	10%	15%	20%	4%
dH ₂ O	3.2 mL	1.8 mL	0.5 mL	3
Acrylamide (30%)	2.67 mL	4 mL	5.33 mL	0.67 mL
1.5 M Tris pH 8.8	2 mL	2 mL	2 mL	0 µL
0.5 M Tris pH 6.8	0 µL	0 µL	0 µL	1.25 mL
10 % SDS	80 µL	80 µL	80 µL	50 µL
10% APS	80 µL	80 µL	80 µL	50 µL
TEMED	8 µL	8 µL	8 µL	5 µL
Total volume (mL)	8 mL	8 mL	8 mL	5 mL

Western blot

10 X Stock	1X stock
30.3 g Tris base	100 mL 10X stock
144.1 g glycine	500 mL H ₂ O
Add dH ₂ O to make up 1 L	200 mL methanol
	Add dH ₂ O to make up 1 L

Volume	Blocking solution	Primary Antibody	Wash solution	Secondary Antibody HRP-conjugate
	1X PBS	1X PBS	1X PBS	1X PBS
	1 % BSA or 5 % semi-skimmed milk	1 % BSA or 5 % semi-skimmed milk		1 % BSA or 5 % semi-skimmed milk
	0.1 % v/v Tween 20	0.1 % v/v Tween 20	0.1 % v/v Tween 20	0.1 % v/v Tween 20
		1:1000 Antibody		1:2000 Antibody
Total volume	50 mL	10 mL	200 mL	10 mL

Developing solution

	Molecular weight (Mw)	Concentration	Volume	Developing Solution (Final)
p-Comaric acid (Solution A)	164.2	0.296 grams in 20 mL DMSO = 90 mM	22 µL	
Luminol (Solution B)	177.2	0.886g in 20 mL DMSO = 250 mM	50 µL	
				Add 22 µL of solution A, 50 µL of

				solution B and 3 μ L H_2O_2 in 10 mL of 0.1 M Tris pH 8.5
--	--	--	--	---

List of Primers:

Primers were purchased from both Sigma and Invitrogen

cDNA	Forward primer	Reverse primer
WT mFXII	gtcgagatctgctccaccatggaagactcc	cgacacgcgttgaagcaatatgcttctggatccaa
WT FXII FnII	attccaccttgggaagccccaaggagcataagt	acttatgctccttggggcttccaaggtggaat
FXII FnII Arg36Ala	ttgtggtacagctgcgcgtgtactggaaggg	ccctccagtaccacgcgcagctgtaccacaa
FXII FnII Arg65Ala	ctccaaacagtatccccatgcctggctctgatcaaagttg	caactttgatcaggaccaggcatggggatactgtttgga g
FXII FnII Arg36Ala/65Ala	ccaacacagtatccccatgcctgggctgatcaaagttg gg	caactttgatcaggaccaggcatggggatactgtttgga g
FXII FnII Asp63Ala/Gln64Ala/Arg 65Ala	gctccaaacagtatccccatgccgcgcctgatcaaag ttgggggtg	caccccaactttgatcaggccgcggcatggggatact gtttggagc
gC1q-R		
gC1q-R His187Ala	acctcatcctctggataagcacagtccaacacaagggc	gcccttgtgttggactgtgcttatccagaggatgaggt
gC1q-R Ser106Ala	ctcccaacctccagccatcttagggaggg	ccctccctaagatggctggaggtgggag
gC1q-R Asp229Ala	aggcccagccaaggaagctgtgttgagtataa	ttatacactcaacacagctccttggactgggcct
gC1q-R Asp249Ala	ctgcaaaagtgttggccaccctcggtcg	cgaccgaggggtggccaacacttttgcag

Protein expression of various construct of FXII

Constructs	Amino acid	Tag	Tag (kDa)	POI (kDa)	Vector	Host
FXII FnII	1-71	MBP	40	8.5	pMAL X(E)-MBP	<i>Escherichia Coli</i>
FXII FnII-EGF	1-109	MBP	40	12.9	pMAL X(E)-MBP	<i>Escherichia Coli</i>
WT FXII FnII	1-71	HisTrx	13	8.5	pOPIN-TRX	<i>Escherichia Coli</i>
FXII FnII-EGF	1-109	His-Trx	13	12.9	pOPIN-TRX	<i>Escherichia Coli</i>
FXII FnII Arg36Ala	1-71	His-Trx	13	8.3	pOPIN-TRX	<i>Escherichia Coli</i>
FXII FnII Arg65Ala	1-71	His-Trx	13	8.3	pOPIN-TRX	<i>Escherichia Coli</i>
FXII FnII Arg36Ala/Arg65Ala	1-71	His-Trx	13	8.2	pOPIN-TRX	<i>Escherichia Coli</i>
FXII FnII Asp63Ala/Gln64Ala/Arg65Ala	1-71	His-Trx	13	8.15	pOPIN-TRX	<i>Escherichia Coli</i>
WT mFXII	1-596	His	1	63.7	pMT-PURO	S2 cells (Insect)
FXII Ser526Ala	1-596	His	1	63.6	pMT-PURO	S2 cells (Insect)
FXII FnII	1-71	none	0	8.5	pMT-PURO	S2 cells (Insect)
FXII FnII-EGF	109	none	0	12.9	pMT-PURO	S2 cells (Insect)
WT gC1q-R	74-282	none	0	23.8	T7-pET	<i>Escherichia Coli</i>
gC1q-R His187Ala	74-282	none	0	23.7	T7-pET	<i>Escherichia Coli</i>
gC1q-R Thr228Ala/Asp229Ala/Tyr233Ala/Tyr236Ala (G1 pocket)	74-282	none	0	23.5	T7-pET	<i>Escherichia Coli</i>
gC1q-R Asp249Ala (G2 pocket)	74-282	none	0	23.7	T7-pET	<i>Escherichia Coli</i>
gC1q-R Ser106Ala/Asp249Ala (G2 pocket)	74-282	none	0	23.7	T7-pET	<i>Escherichia Coli</i>
Graal ₈₆₃₋₁₁₅₀	BglII/MluI	His	1		pMT-PURO	S2 cells (Insect)

Human and mouse FXII constructs showing residue boundaries, molecular weight of protein of interest (POI), expression vector, tag and expression host.

Amino acid sequence alignment of mouse FXII (mFXII) and human FXII (hFXII) – one letter code.

```

hFXII  IPPWEAPKEHKYKAEHTVVLTVTGEPCHFPPQYHRQLYHKCTHKGRPGQPWCATTPNF 60
mFXII  APPWKDSKKFKDAPDGPVVLVDGRLCHFPPQYHRQLHHKCIHKRRPGSRPWCAATTPNF 60
      *:*:*:*:*:*:*:*:*:*:*:*:*:*:*:*:*:*:*:*:*:*:*:*:*:*:*:*:*:*:*
hFXII  DQDQRWGYCLEPKKVKDHCSKHSPCQKGGTCVNMPSGPHCLCPQHLTGNHCQKEKCFEPQ 120
mFXII  DEDQQWGYCLEPKKVKDHCSKHNPCCHKGGTCINTPNGPHCLCPEHLTGKHCQKEKCFEPQ 120
      *:*:*:*:*:*:*:*:*:*:*:*:*:*:*:*:*:*:*:*:*:*:*:*:*:*:*:*:*:*
hFXII  LLRFFHKNEIWYRTEQAAVARCQCKGPDHCRLASQACRTNPCLHGGRCLEVEGHRLLCH 180
mFXII  LLKFFHENELWFRTPGGVARCECKGSEAHCKPVASQACSNPCLNGGSCLLVEDHPLCR 180
      *:*:*:*:*:*:*:*:*:*:*:*:*:*:*:*:*:*:*:*:*:*:*:*:*:*:*:*:*
hFXII  CPVGYTGAFCDVDTKASCYDGRGLSYRGLARTTLSGAPCQPWASEATYRNVTAEQARNWG 240
mFXII  CPTGYTGYFCDLWLWATCYEGRGLSYRQAGTTQSGAPCQRWTEATYRNMTKEQALSWG 240
      *:*:*:*:*:*:*:*:*:*:*:*:*:*:*:*:*:*:*:*:*:*:*:*:*:*:*:*
hFXII  LGGHAFCRNPNDIRPWCFLNDRDLSEWYCDLAQCQTPQAAPTPVSPRLHVPLMPAQ 300
mFXII  LGHHAFCRNPNDTRPWCVWVSGDRLSWDYCGLEQCQTPTFAPLVVPEEQEE----- 292
      *:*:*:*:*:*:*:*:*:*:*:*:*:*:*:*:*:*:*:*:*:*:*:*:*:*
hFXII  PAPPKQPTRTPPQSQTGALPAKREQPPSLTRNGPLSCGQRLRKSLSSMTRVVGGLVA 360
mFXII  --SPSQAPS-----L SHAP---NDSTDHQTSLKTNMTMCGGQRFKGLSSFMRVVGGLVA 342
      *:*:*:*:*:*:*:*:*:*:*:*:*:*:*:*:*:*:*:*:*:*:*:*:*:*
hFXII  LRGAHPYIAALYWGHSFCAGSLIAPCWVLTAAHCLQDRPAPEDLTVVLGQERRNHSCIPC 420
mFXII  LPGAHPYIAALYWGNNFCAGSLIAPCWVLTAAHCLQNRPAPEELTVVLGQDRHNQSCIEWC 402
      *:*:*:*:*:*:*:*:*:*:*:*:*:*:*:*:*:*:*:*:*:*:*:*:*:*
hFXII  QTLAVRSYRLHEAFSPVSYQHDLALLRLQEDADGSCALLSPYVQPVCLPSGAARPSETTL 480
mFXII  QTLAVRSYRLHEGFSSITYQHDLALLRLQESKTNSCAILSPHVQPVCLPSGAAPPSETVL 462
      *:*:*:*:*:*:*:*:*:*:*:*:*:*:*:*:*:*:*:*:*:*:*:*:*:*
hFXII  CQVAGWGHQFEGAEYASFLQEAQVPFLSLERCSPDVHGSSILPGMLCAGFLEGGTDAC 540
mFXII  CEVAGWGHQFEGAEYSTFLQEAQVPFIALDRCSNSNVHGDAILPGMLCAGFLEGGTDAC 522
      *:*:*:*:*:*:*:*:*:*:*:*:*:*:*:*:*:*:*:*:*:*:*:*:*:*
hFXII  QGDSGGPLVCEQAAERRLTLQGIISWGS GCGDRNKP G VYTDVAYYLAWI REHTVS 596
mFXII  QGDSGGPLVCEEGTAEHQLTLRGVISWGS GCGDRNKP G VYTDVANYLAWIQKH IAS 578
      *:*:*:*:*:*:*:*:*:*:*:*:*:*:*:*:*:*:*:*:*:*:*:*:*

```

Human gC1q-R – amino acid sequence

LHTDGDKAFVDFLSDEIKEERKIQKHKTLPKMSGGWELELNGTEAKLVRKVAGEKIT
VTFNINNSIPPTFDGEEEPSQGQKVEEQPELSTPNFVVEVIKNDDGKKALVLDCHYP
EDEVGQEDEAESDIFSIREVSFQSTGESEWKDTNYTLNTDSLWDALYDHLMDFLADR
GVDNTFADELVELSTALEHQEYITFLEDLKSFKSQ

HisTrx-FXII FnII construct – amino acid sequence

HisTrx

MAHHHHHSDKIIHLTDDSFDTDVLKADGAILVDFWAEWCGPCKMIAPILDEIADEY
QGKLTVAKLNIDQNPGTAPKYGIRGIPTLLLFKNGEVAATKVGALSCKGQLKEFLDAN
LASSGLEVLFGP

HRV 3C cleavage sequence

SSGLEVLFG/GP

FXII FnII AFTER CLEAVAGE

GPIPPWEAPKEHKYKAEHDTVLTVTGEPCHFQYHRQLYHKCTAKGRPGQPW
CATTPNFDQDQRWGYCLE

List of publications

- 1) Pathak M, **Kaira BG**, Slater A, Emsley J. Cell Receptor and Cofactor Interactions of the Contact Activation System and Factor XI. *Frontiers in medicine*. 2018;5:66. PubMed [PMID: 29619369](#). Pubmed Central PMCID: PMC5871670. Epub 2018/04/06. eng.
- 2) Monika Pathak*, Rosa Manna*, Chan Li, **Bubacarr G Kaira**, Badraddin Kareem Hamad, Benny Danilo Belviso, Camila R Bonturi, Ingrid Dreveny, Peter M Fischer, Lodewijk V Dekker, Maria Luiza Viela Oliva, and Jonas Emsley. Crystal structures of the recombinant β -Factor XIIa protease with bound Thr-Arg and Pro-Arg substrate mimetics. *Acta Crystallographica Section D*. (Accepted for publication in March 2019).

11.0 Reference:

1. Pugsley MK, Tabrizchi R. The vascular system. An overview of structure and function. *Journal of pharmacological and toxicological methods*. 2000 Sep-Oct;44(2):333-40. PubMed PMID: 11325577. Epub 2001/04/28. eng.
2. Gale AJ. Continuing education course #2: current understanding of hemostasis. *Toxicologic pathology*. 2011 Jan;39(1):273-80. PubMed PMID: 21119054. Pubmed Central PMCID: PMC3126677. Epub 2010/12/02. eng.
3. Versteeg HH, Heemskerk JW, Levi M, Reitsma PH. New fundamentals in hemostasis. *Physiol Rev*. 2013 Jan;93(1):327-58. PubMed PMID: 23303912. Epub 2013/01/11. eng.
4. de Laforcade A. Diseases associated with thrombosis. *Topics in companion animal medicine*. 2012 May;27(2):59-64. PubMed PMID: 23031457. Epub 2012/10/04. eng.
5. Javid M, Magee TR, Galland RB. Arterial thrombosis associated with malignant disease. *European journal of vascular and endovascular surgery : the official journal of the European Society for Vascular Surgery*. 2008 Jan;35(1):84-7. PubMed PMID: 17931915. Epub 2007/10/13. eng.
6. Margetic S. Inflammation and haemostasis. *Biochemia medica*. 2012;22(1):49-62. PubMed PMID: 22384519. Pubmed Central PMCID: PMC4062321. Epub 2012/03/06. eng.
7. Martin C, Morales LD, Cruz MA. Purified A2 domain of von Willebrand factor binds to the active conformation of von Willebrand factor and blocks the interaction with platelet glycoprotein Ibalpha. *Journal of thrombosis and haemostasis : JTH*. 2007 Jul;5(7):1363-70. PubMed PMID: 17389010. Epub 2007/03/29. eng.
8. Huizinga EG, Tsuji S, Romijn RA, Schiphorst ME, de Groot PG, Sixma JJ, et al. Structures of glycoprotein Ibalpha and its complex with von Willebrand factor A1 domain. *Science*. 2002 Aug 16;297(5584):1176-9. PubMed PMID: 12183630. Epub 2002/08/17. eng.
9. Doggett TA, Girdhar G, Lawshe A, Miller JL, Laurenzi IJ, Diamond SL, et al. Alterations in the intrinsic properties of the GPIbalpha-VWF tether bond define the kinetics of the platelet-type von Willebrand disease mutation, Gly233Val. *Blood*. 2003 Jul 1;102(1):152-60. PubMed PMID: 12637314. Epub 2003/03/15. eng.
10. Getz TM, Piatt R, Petrich BG, Monroe D, Mackman N, Bergmeier W. Novel mouse hemostasis model for real-time determination of bleeding time and hemostatic plug composition. *Journal of thrombosis and haemostasis : JTH*. 2015 Mar;13(3):417-25. PubMed PMID: 25442192. Pubmed Central PMCID: PMC4414118. Epub 2014/12/03. eng.
11. Shattil SJ, Newman PJ. Integrins: dynamic scaffolds for adhesion and signaling in platelets. *Blood*. 2004 Sep 15;104(6):1606-15. PubMed PMID: 15205259. Epub 2004/06/19. eng.
12. Furie B. Pathogenesis of thrombosis. *Hematology / the Education Program of the American Society of Hematology American Society of Hematology Education Program*. 2009:255-8. PubMed PMID: 20008207. Epub 2009/12/17. eng.
13. Hawiger J. Formation and regulation of platelet and fibrin hemostatic plug. *Human pathology*. 1987 Feb;18(2):111-22. PubMed PMID: 3804319. Epub 1987/02/01. eng.
14. McEver RP. Adhesive interactions of leukocytes, platelets, and the vessel wall during hemostasis and inflammation. *Thrombosis and haemostasis*. 2001 Sep;86(3):746-56. PubMed PMID: 11583304. Epub 2001/10/05. eng.
15. Bonar RA, Lippi G, Favaloro EJ. Overview of Hemostasis and Thrombosis and Contribution of Laboratory Testing to Diagnosis and Management of Hemostasis and Thrombosis Disorders. *Methods in molecular biology (Clifton, NJ)*. 2017;1646:3-27. PubMed PMID: 28804815. Epub 2017/08/15. eng.

16. Thomas DP, Roberts HR. Hypercoagulability in venous and arterial thrombosis. *Annals of internal medicine*. 1997 Apr 15;126(8):638-44. PubMed PMID: 9103132. Epub 1997/04/15. eng.
17. Nagareddy P, Smyth SS. Inflammation and thrombosis in cardiovascular disease. *Current opinion in hematology*. 2013;20(5):457-63. PubMed PMID: 23892572.
18. Koupenova M, Kehrel BE, Corkrey HA, Freedman JE. Thrombosis and platelets: an update. *European heart journal*. 2017 Mar 14;38(11):785-91. PubMed PMID: 28039338. Epub 2017/01/01. eng.
19. Scarvelis D, Wells PS. Diagnosis and treatment of deep-vein thrombosis. *CMAJ : Canadian Medical Association journal = journal de l'Association medicale canadienne*. 2006 Oct 24;175(9):1087-92. PubMed PMID: 17060659. Pubmed Central PMCID: PMC1609160. Epub 2006/10/25. eng.
20. Stubbs MJ, Mouyis M, Thomas M. Deep vein thrombosis. *BMJ (Clinical research ed)*. 2018 Feb 22;360:k351. PubMed PMID: 29472180. Epub 2018/02/24. eng.
21. Imberti D, Becattini C, Bernardi E, Camporese G, Cuccia C, Dentali F, et al. Multidisciplinary approach to the management of patients with pulmonary embolism and deep vein thrombosis: a consensus on diagnosis, traditional therapy and therapy with rivaroxaban. *Internal and emergency medicine*. 2018 Oct;13(7):1037-49. PubMed PMID: 29520700. Epub 2018/03/10. eng.
22. Schaefer JK, Jacobs B, Wakefield TW, Sood SL. New biomarkers and imaging approaches for the diagnosis of deep venous thrombosis. *Current opinion in hematology*. 2017 May;24(3):274-81. PubMed PMID: 28306666. Epub 2017/03/18. eng.
23. Ghozlan MF, Osman AA, Mahmoud HM, Eissa DG, Abuelela S. Comprehensive study on laboratory biomarkers for prediction and diagnosis of deep venous thrombosis. *Blood coagulation & fibrinolysis : an international journal in haemostasis and thrombosis*. 2015 Apr;26(3):255-60. PubMed PMID: 24991946. Epub 2014/07/06. eng.
24. Sexton T, Smyth SS. Novel mediators and biomarkers of thrombosis. *Journal of thrombosis and thrombolysis*. 2014 Jan;37(1):1-3. PubMed PMID: 24356857. Pubmed Central PMCID: PMC4086911. Epub 2013/12/21. eng.
25. Quinn C, Hill J, Hassouna H. A guide for diagnosis of patients with arterial and venous thrombosis. *Clinical laboratory science : journal of the American Society for Medical Technology*. 2000 Fall;13(4):229-38. PubMed PMID: 11586510. Epub 2001/10/06. eng.
26. Sharma M, Ramanathan S, Khalighi K. Development of New Deep Venous Thrombosis While on Apixaban. *Case reports in cardiology*. 2017;2017:2842935. PubMed PMID: 28713598. Pubmed Central PMCID: PMC5496103. Epub 2017/07/18. eng.
27. Nagalla S, Bray PF. Personalized medicine in thrombosis: back to the future. *Blood*. 2016 Jun 2;127(22):2665-71. PubMed PMID: 26847245. Pubmed Central PMCID: PMC4891951. Epub 2016/02/06. eng.
28. Wheeler AP, Gailani D. The Intrinsic Pathway of Coagulation as a Target for Antithrombotic Therapy. *Hematology/oncology clinics of North America*. 2016 Oct;30(5):1099-114. PubMed PMID: 27637310. Pubmed Central PMCID: PMC5028121. Epub 2016/09/18. eng.
29. Palta S, Saroa R, Palta A. Overview of the coagulation system. *Indian journal of anaesthesia*. 2014 Sep;58(5):515-23. PubMed PMID: 25535411. Pubmed Central PMCID: PMC4260295. Epub 2014/12/24. eng.
30. Peshkova AD, Le Minh G, Tutwiler V, Andrianova IA, Weisel JW, Litvinov RI. Activated Monocytes Enhance Platelet-Driven Contraction of Blood Clots via Tissue Factor Expression. *Scientific reports*. 2017 Jul 11;7(1):5149. PubMed PMID: 28698680. Pubmed Central PMCID: PMC5506001. Epub 2017/07/13. eng.

31. Kelley RF, Yang J, Eigenbrot C, Moran P, Peek M, Lipari MT, et al. Similar molecular interactions of factor VII and factor VIIa with the tissue factor region that allosterically regulates enzyme activity. *Biochemistry*. 2004 Feb 10;43(5):1223-9. PubMed PMID: 14756558. Epub 2004/02/06. eng.
32. Butenas S. Tissue factor structure and function. *Scientifica*. 2012;2012:964862. PubMed PMID: 24278763. Pubmed Central PMCID: PMC3820524. Epub 2012/01/01. eng.
33. Sichler K, Banner DW, D'Arcy A, Hopfner KP, Huber R, Bode W, et al. Crystal structures of uninhibited factor VIIa link its cofactor and substrate-assisted activation to specific interactions. *Journal of molecular biology*. 2002 Sep 20;322(3):591-603. PubMed PMID: 12225752. Epub 2002/09/13. eng.
34. Eigenbrot C, Kirchhofer D, Dennis MS, Santell L, Lazarus RA, Stamos J, et al. The factor VII zymogen structure reveals reregistration of beta strands during activation. *Structure (London, England : 1993)*. 2001 Jul 3;9(7):627-36. PubMed PMID: 11470437. Epub 2001/07/27. eng.
35. Renne T. The procoagulant and proinflammatory plasma contact system. *Seminars in immunopathology*. 2012 Jan;34(1):31-41. PubMed PMID: 21858560. Epub 2011/08/23. eng.
36. Colman RW, Schmaier AH. Contact system: a vascular biology modulator with anticoagulant, profibrinolytic, antiadhesive, and proinflammatory attributes. *Blood*. 1997 Nov 15;90(10):3819-43. PubMed PMID: 9354649. Epub 1997/11/14. eng.
37. van der Poll T, Herwald H. The coagulation system and its function in early immune defense. *Thrombosis and haemostasis*. 2014 Oct;112(4):640-8. PubMed PMID: 24696161. Epub 2014/04/04. eng.
38. Wu Y. Contact pathway of coagulation and inflammation. *Thrombosis journal*. 2015;13:17. PubMed PMID: 25949215. Pubmed Central PMCID: PMC4421925. Epub 2015/05/08. eng.
39. Oehmcke S, Herwald H. Contact system activation in severe infectious diseases. *Journal of molecular medicine (Berlin, Germany)*. 2010 Feb;88(2):121-6. PubMed PMID: 20232512. Epub 2010/03/17. eng.
40. Cochrane CG, Revak SD, Wuepper KD. Activation of Hageman factor in solid and fluid phases. A critical role of kallikrein. *The Journal of experimental medicine*. 1973 Dec 1;138(6):1564-83. PubMed PMID: 4271629. Pubmed Central PMCID: PMC2139466. Epub 1973/12/01. eng.
41. Goldsmith GH, Jr., Saito H, Ratnoff OS. The activation of plasminogen by Hageman factor (Factor XII) and Hageman factor fragments. *J Clin Invest*. 1978 Jul;62(1):54-60. PubMed PMID: 659637. Pubmed Central PMCID: PMC371736. Epub 1978/07/01. eng.
42. Gailani D, Renne T. The intrinsic pathway of coagulation: a target for treating thromboembolic disease? *Journal of thrombosis and haemostasis : JTH*. 2007 Jun;5(6):1106-12. PubMed PMID: 17388803. Epub 2007/03/29. eng.
43. Achneck HE, Sileshi B, Parikh A, Milano CA, Welsby IJ, Lawson JH. Pathophysiology of bleeding and clotting in the cardiac surgery patient: from vascular endothelium to circulatory assist device surface. *Circulation*. 2010 Nov 16;122(20):2068-77. PubMed PMID: 21098468.
44. Smith SA, Travers RJ, Morrissey JH. How it all starts: Initiation of the clotting cascade. *Critical reviews in biochemistry and molecular biology*. 2015;50(4):326-36. PubMed PMID: 26018600. Pubmed Central PMCID: PMC4826570. Epub 2015/05/29. eng.
45. Renne T, Schmaier AH, Nickel KF, Blomback M, Maas C. In vivo roles of factor XII. *Blood*. 2012 Nov 22;120(22):4296-303. PubMed PMID: WOS:000313111300010. English.
46. Schmaier AH. Physiologic activities of the contact activation system. *Thrombosis research*. 2014 May;133 Suppl 1:S41-4. PubMed PMID: 24759141. Pubmed Central PMCID: PMC4004333. Epub 2014/04/25. eng.

47. Schmaier AH. The elusive physiologic role of Factor XII. *J Clin Invest.* 2008 Sep;118(9):3006-9. PubMed PMID: 18725991. Pubmed Central PMCID: PMC2518076. Epub 2008/08/30. eng.
48. Colman RW, Schmaier AH. The contact activation system: biochemistry and interactions of these surface-mediated defense reactions. *Critical reviews in oncology/hematology.* 1986;5(1):57-85. PubMed PMID: 3633772. Epub 1986/01/01. eng.
49. Morrissey JH, Choi SH, Smith SA. Polyphosphate: an ancient molecule that links platelets, coagulation, and inflammation. *Blood.* 2012 Jun 21;119(25):5972-9. PubMed PMID: 22517894. Pubmed Central PMCID: PMC3383012. Epub 2012/04/21. eng.
50. Morrissey JH, Smith SA. Polyphosphate as modulator of hemostasis, thrombosis, and inflammation. *Journal of thrombosis and haemostasis : JTH.* 2015 Jun;13 Suppl 1:S92-7. PubMed PMID: 26149055. Pubmed Central PMCID: PMC4497372. Epub 2015/07/08. eng.
51. Morrissey JH. Polyphosphate: a link between platelets, coagulation and inflammation. *International journal of hematology.* 2012 Apr;95(4):346-52. PubMed PMID: 22477540. Pubmed Central PMCID: PMC3361507. Epub 2012/04/06. eng.
52. Joseph K, Shibayama Y, Ghebrehiwet B, Kaplan AP. Factor XII-dependent contact activation on endothelial cells and binding proteins gC1qR and cytokeratin 1. *Thrombosis and haemostasis.* 2001 Jan;85(1):119-24. PubMed PMID: 11204562. Epub 2001/02/24. eng.
53. Ghebrehiwet B, CebadaMora C, Tantral L, Jesty J, Peerschke EI. gC1qR/p33 serves as a molecular bridge between the complement and contact activation systems and is an important catalyst in inflammation. *Advances in experimental medicine and biology.* 2006;586:95-105. PubMed PMID: 16893067. Epub 2006/08/09. eng.
54. Matafonov A, Leung PY, Gailani AE, Grach SL, Puy C, Cheng Q, et al. Factor XII inhibition reduces thrombus formation in a primate thrombosis model. *Blood.* 2014 Mar 13;123(11):1739-46. PubMed PMID: 24408325. Pubmed Central PMCID: PMC3954054. Epub 2014/01/11. eng.
55. Simao F, Feener EP. The Effects of the Contact Activation System on Hemorrhage. *Frontiers in medicine.* 2017;4:121. PubMed PMID: 28824910. Pubmed Central PMCID: PMC5534673. Epub 2017/08/22. eng.
56. Gruber A. The role of the contact pathway in thrombus propagation. *Thrombosis research.* 2014 May;133 Suppl 1:S45-7. PubMed PMID: 24759142. Epub 2014/04/25. eng.
57. van Montfoort ML, Meijers JC. Recent insights into the role of the contact pathway in thrombo-inflammatory disorders. *Hematology / the Education Program of the American Society of Hematology American Society of Hematology Education Program.* 2014 Dec 5;2014(1):60-5. PubMed PMID: 25696835. Epub 2015/02/20. eng.
58. Samuel M, Pixley RA, Villanueva MA, Colman RW, Villanueva GB. Human factor XII (Hageman factor) autoactivation by dextran sulfate. Circular dichroism, fluorescence, and ultraviolet difference spectroscopic studies. *The Journal of biological chemistry.* 1992 Sep 25;267(27):19691-7. PubMed PMID: 1527088.
59. Silverberg M, Dunn JT, Garen L, Kaplan AP. Autoactivation of human Hageman factor. Demonstration utilizing a synthetic substrate. *The Journal of biological chemistry.* 1980 Aug 10;255(15):7281-6. PubMed PMID: 7391081. Epub 1980/08/10. eng.
60. Muller F, Gailani D, Renne T. Factor XI and XII as antithrombotic targets. *Current opinion in hematology.* 2011 Sep;18(5):349-55. PubMed PMID: 21730835. Pubmed Central PMCID: PMC4364027. Epub 2011/07/07. eng.
61. Engel R, Brain CM, Paget J, Lionikiene AS, Mutch NJ. Single-chain factor XII exhibits activity when complexed to polyphosphate. *Journal of thrombosis*

and haemostasis : JTH. 2014 Sep;12(9):1513-22. PubMed PMID: 25039405. Epub 2014/07/22. eng.

62. Weidmann H, Heikaus L, Long AT, Naudin C, Schluter H, Renne T. The plasma contact system, a protease cascade at the nexus of inflammation, coagulation and immunity. *Biochimica et biophysica acta Molecular cell research*. 2017 Nov;1864(11 Pt B):2118-27. PubMed PMID: 28743596. Epub 2017/07/27. eng.

63. Miyamoto A, Ishiguro S, Nishio A. Stimulation of bradykinin B2-receptors on endothelial cells induces relaxation and contraction in porcine basilar artery in vitro. *British journal of pharmacology*. 1999 Sep;128(1):241-7. PubMed PMID: 10498858. Pubmed Central PMCID: PMC1571616. Epub 1999/09/28. eng.

64. Sung CP, Arleth AJ, Shikano K, Berkowitz BA. Characterization and function of bradykinin receptors in vascular endothelial cells. *The Journal of pharmacology and experimental therapeutics*. 1988 Oct;247(1):8-13. PubMed PMID: 2902216. Epub 1988/10/01. eng.

65. Kaplan AP, Joseph K. Pathogenic mechanisms of bradykinin mediated diseases: dysregulation of an innate inflammatory pathway. *Advances in immunology*. 2014;121:41-89. PubMed PMID: 24388213. Epub 2014/01/07. eng.

66. Leeb-Lundberg LM, Marceau F, Muller-Esterl W, Pettibone DJ, Zuraw BL. International union of pharmacology. XLV. Classification of the kinin receptor family: from molecular mechanisms to pathophysiological consequences. *Pharmacological reviews*. 2005 Mar;57(1):27-77. PubMed PMID: 15734727. Epub 2005/03/01. eng.

67. Wu W, Sinha D, Shikov S, Yip CK, Walz T, Billings PC, et al. Factor XI homodimer structure is essential for normal proteolytic activation by factor XIIa, thrombin, and factor XIa. *The Journal of biological chemistry*. 2008 Jul 4;283(27):18655-64. PubMed PMID: 18441012. Pubmed Central PMCID: PMC2441546. Epub 2008/04/29. eng.

68. Pedicord DL, Seiffert D, Blat Y. Feedback activation of factor XI by thrombin does not occur in plasma. *Proceedings of the National Academy of Sciences of the United States of America*. 2007 Jul 31;104(31):12855-60. PubMed PMID: 17652512. Pubmed Central PMCID: PMC1937556. Epub 2007/07/27. eng.

69. Naito K, Fujikawa K. Activation of human blood coagulation factor XI independent of factor XII. Factor XI is activated by thrombin and factor XIa in the presence of negatively charged surfaces. *The Journal of biological chemistry*. 1991 Apr 25;266(12):7353-8. PubMed PMID: 2019570. Epub 1991/04/25. eng.

70. Gailani D, Broze GJ, Jr. Factor XI activation in a revised model of blood coagulation. *Science*. 1991 Aug 23;253(5022):909-12. PubMed PMID: 1652157. Epub 1991/09/02. eng.

71. Johne J, Blume C, Benz PM, Pozgajova M, Ullrich M, Schuh K, et al. Platelets promote coagulation factor XII-mediated proteolytic cascade systems in plasma. *Biological chemistry*. 2006 Feb;387(2):173-8. PubMed PMID: 16497149. Epub 2006/02/25. eng.

72. Gailani D, Geng Y, Verhamme I, Sun MF, Bajaj SP, Messer A, et al. The mechanism underlying activation of factor IX by factor XIa. *Thrombosis research*. 2014 May;133 Suppl 1:S48-51. PubMed PMID: 24759143. Pubmed Central PMCID: PMC4017667. Epub 2014/04/25. eng.

73. Brandstetter H, Bauer M, Huber R, Lollar P, Bode W. X-ray structure of clotting factor IXa: active site and module structure related to Xase activity and hemophilia B. *Proceedings of the National Academy of Sciences of the United States of America*. 1995 Oct 10;92(21):9796-800. PubMed PMID: 7568220. Pubmed Central PMCID: 40889.

74. Celie PH, Lenting PJ, Mertens K. Hydrophobic contact between the two epidermal growth factor-like domains of blood coagulation factor IX contributes to enzymatic activity. *The Journal of biological chemistry*. 2000 Jan 7;275(1):229-34. PubMed PMID: 10617609. Epub 2000/01/05. eng.
75. Kerschbaumer RJ, Riedrich K, Kral M, Varadi K, Dorner F, Rosing J, et al. An antibody specific for coagulation factor IX enhances the activity of the intrinsic factor X-activating complex. *The Journal of biological chemistry*. 2004 Sep 24;279(39):40445-50. PubMed PMID: 15265864. Epub 2004/07/22. eng.
76. Wolberg AS, Campbell RA. Thrombin generation, fibrin clot formation and hemostasis. *Transfusion and apheresis science : official journal of the World Apheresis Association : official journal of the European Society for Haemapheresis*. 2008 Feb;38(1):15-23. PubMed PMID: 18282807. Pubmed Central PMCID: 2408736.
77. Greenberg CS, Miraglia CC, Rickles FR, Shuman MA. Cleavage of Blood-Coagulation Factor-Xiii and Fibrinogen by Thrombin during Invitro Clotting. *J Clin Invest*. 1985;75(5):1463-70. PubMed PMID: WOS:A1985AHD4300009. English.
78. Konings J, Govers-Riemslog JW, Philippou H, Mutch NJ, Borissoff JI, Allan P, et al. Factor XIIa regulates the structure of the fibrin clot independently of thrombin generation through direct interaction with fibrin. *Blood*. 2011 Oct 6;118(14):3942-51. PubMed PMID: 21828145. Epub 2011/08/11. eng.
79. Konings J, Hoving LR, Ariens RS, Hethershaw EL, Ninivaggi M, Hardy LJ, et al. The role of activated coagulation factor XII in overall clot stability and fibrinolysis. *Thrombosis research*. 2015 Aug;136(2):474-80. PubMed PMID: 26153047. Epub 2015/07/15. eng.
80. Gailani D, Bane CE, Gruber A. Factor XI and contact activation as targets for antithrombotic therapy. *Journal of thrombosis and haemostasis : JTH*. 2015 Aug;13(8):1383-95. PubMed PMID: 25976012. Pubmed Central PMCID: PMC4516614. Epub 2015/05/16. eng.
81. Weitz JI. Factor XI and factor XII as targets for new anticoagulants. *Thrombosis research*. 2016 May;141 Suppl 2:S40-5. PubMed PMID: 27207423. Epub 2016/05/22. eng.
82. Labberton L, Kenne E, Long AT, Nickel KF, Di Gennaro A, Rigg RA, et al. Neutralizing blood-borne polyphosphate in vivo provides safe thromboprotection. *Nature communications*. 2016 Sep 6;7:12616. PubMed PMID: 27596064. Pubmed Central PMCID: PMC5025862. Epub 2016/09/07. eng.
83. Nickel KF, Labberton L, Long AT, Langer F, Fuchs TA, Stavrou EX, et al. The polyphosphate/factor XII pathway in cancer-associated thrombosis: novel perspectives for safe anticoagulation in patients with malignancies. *Thrombosis research*. 2016 May;141 Suppl 2:S4-7. PubMed PMID: 27207422. Epub 2016/05/22. eng.
84. Labberton L, Kenne E, Renne T. New agents for thromboprotection. A role for factor XII and XIIa inhibition. *Hamostaseologie*. 2015 Nov 4;35(4):338-50. PubMed PMID: 25609114. Epub 2015/01/23. eng.
85. Weisel JW, Litvinov RI. The biochemical and physical process of fibrinolysis and effects of clot structure and stability on the lysis rate. *Cardiovascular & hematological agents in medicinal chemistry*. 2008 Jul;6(3):161-80. PubMed PMID: 18673231. Epub 2008/08/05. eng.
86. Cortes-Canteli M, Zamolodchikov D, Ahn HJ, Strickland S, Norris EH. Fibrinogen and altered hemostasis in Alzheimer's disease. *Journal of Alzheimer's disease : JAD*. 2012;32(3):599-608. PubMed PMID: 22869464. Pubmed Central PMCID: PMC3683985. Epub 2012/08/08. eng.
87. Chapin JC, Hajjar KA. Fibrinolysis and the control of blood coagulation. *Blood reviews*. 2015 Jan;29(1):17-24. PubMed PMID: 25294122. Pubmed Central PMCID: PMC4314363. Epub 2014/10/09. eng.

88. Thompson WD, Harvey JA, Kazmi MA, Stout AJ. Fibrinolysis and angiogenesis in wound healing. *The Journal of pathology*. 1991 Dec;165(4):311-8. PubMed PMID: 1723752. Epub 1991/12/01. eng.
89. Laurens N, Koolwijk P, de Maat MP. Fibrin structure and wound healing. *Journal of thrombosis and haemostasis : JTH*. 2006 May;4(5):932-9. PubMed PMID: 16689737. Epub 2006/05/13. eng.
90. Medcalf RL. Fibrinolysis, inflammation, and regulation of the plasminogen activating system. *Journal of thrombosis and haemostasis : JTH*. 2007 Jul;5 Suppl 1:132-42. PubMed PMID: 17635719. Epub 2007/08/01. eng.
91. Vadivel K, Agah S, Messer AS, Cascio D, Bajaj MS, Krishnaswamy S, et al. Structural and functional studies of gamma-carboxyglutamic acid domains of factor VIIa and activated Protein C: role of magnesium at physiological calcium. *Journal of molecular biology*. 2013 Jun 12;425(11):1961-81. PubMed PMID: 23454357. Pubmed Central PMCID: PMC4017951. Epub 2013/03/05. eng.
92. Sun MF, Zhao M, Gailani D. Identification of amino acids in the factor XI apple 3 domain required for activation of factor IX. *The Journal of biological chemistry*. 1999 Dec 17;274(51):36373-8. PubMed PMID: 10593931. Epub 1999/12/14. eng.
93. Gailani D, Ho D, Sun MF, Cheng Q, Walsh PN. Model for a factor IX activation complex on blood platelets: dimeric conformation of factor XIa is essential. *Blood*. 2001 May 15;97(10):3117-22. PubMed PMID: 11342438. Epub 2001/05/09. eng.
94. Mandle RJ, Colman RW, Kaplan AP. Identification of prekallikrein and high-molecular-weight kininogen as a complex in human plasma. *Proceedings of the National Academy of Sciences of the United States of America*. 1976 Nov;73(11):4179-83. PubMed PMID: 1069308. Pubmed Central PMCID: PMC431375. Epub 1976/11/01. eng.
95. Tans G, Rosing J, Berrettini M, Lammle B, Griffin JH. Autoactivation of human plasma prekallikrein. *The Journal of biological chemistry*. 1987 Aug 15;262(23):11308-14. PubMed PMID: 2440889. Epub 1987/08/15. eng.
96. Mandle R, Jr., Kaplan AP. Hageman factor substrates. Human plasma prekallikrein: mechanism of activation by Hageman factor and participation in hageman factor-dependent fibrinolysis. *The Journal of biological chemistry*. 1977 Sep 10;252(17):6097-104. PubMed PMID: 408348. Epub 1977/09/10. eng.
97. Burger D, Schleuning WD, Schapira M. Human plasma prekallikrein. Immunoaffinity purification and activation to alpha- and beta-kallikrein. *The Journal of biological chemistry*. 1986 Jan 5;261(1):324-7. PubMed PMID: 2416749. Epub 1986/01/05. eng.
98. Cheng Q, Sun MF, Kravtsov DV, Aktimur A, Gailani D. Factor XI apple domains and protein dimerization. *Journal of thrombosis and haemostasis : JTH*. 2003 Nov;1(11):2340-7. PubMed PMID: 14629467. Epub 2003/11/25. eng.
99. Emsley J, McEwan PA, Gailani D. Structure and function of factor XI. *Blood*. 2010 Apr 1;115(13):2569-77. PubMed PMID: 20110423. Pubmed Central PMCID: PMC4828079. Epub 2010/01/30. eng.
100. Mohammed BM, Matafonov A, Ivanov I, Sun MF, Cheng Q, Dickeson SK, et al. An update on factor XI structure and function. *Thrombosis research*. 2018 Jan;161:94-105. PubMed PMID: 29223926. Pubmed Central PMCID: PMC5776729. Epub 2017/12/11. eng.
101. Donaldson VH, Glueck HI, Miller MA, Movat HZ, Habal F. Kininogen deficiency in Fitzgerald trait: role of high molecular weight kininogen in clotting and fibrinolysis. *The Journal of laboratory and clinical medicine*. 1976 Feb;87(2):327-37. PubMed PMID: 1245795. Epub 1976/02/01. eng.
102. Vogler EA, Siedlecki CA. Contact activation of blood-plasma coagulation. *Biomaterials*. 2009 Apr;30(10):1857-69. PubMed PMID: 19168215. Pubmed Central PMCID: PMC2705825. Epub 2009/01/27. eng.

103. Thompson RE, Mandle R, Jr., Kaplan AP. Characterization of human high molecular weight kininogen. Procoagulant activity associated with the light chain of kinin-free high molecular weight kininogen. *The Journal of experimental medicine*. 1978;147(2):488-99. PubMed PMID: 75240.
104. Weisel JW, Nagaswami C, Woodhead JL, DeLa Cadena RA, Page JD, Colman RW. The shape of high molecular weight kininogen. Organization into structural domains, changes with activation, and interactions with prekallikrein, as determined by electron microscopy. *The Journal of biological chemistry*. 1994 Apr 1;269(13):10100-6. PubMed PMID: 8144509. Epub 1994/04/01. eng.
105. Vogel R, Kaufmann J, Chung DW, Kellermann J, Muller-Esterl W. Mapping of the prekallikrein-binding site of human H-kininogen by ligand screening of lambda gt11 expression libraries. Mimicking of the predicted binding site by anti-idiotypic antibodies. *The Journal of biological chemistry*. 1990 Jul 25;265(21):12494-502. PubMed PMID: 1695630. Epub 1990/07/25. eng.
106. Thompson RE, Mandle R, Jr., Kaplan AP. Studies of binding of prekallikrein and Factor XI to high molecular weight kininogen and its light chain. *Proceedings of the National Academy of Sciences of the United States of America*. 1979 Oct;76(10):4862-6. PubMed PMID: 291905. Pubmed Central PMCID: PMC413037. Epub 1979/10/01. eng.
107. Wachtfogel YT, DeLa Cadena RA, Kunapuli SP, Rick L, Miller M, Schultze RL, et al. High molecular weight kininogen binds to Mac-1 on neutrophils by its heavy chain (domain 3) and its light chain (domain 5). *The Journal of biological chemistry*. 1994 Jul 29;269(30):19307-12. PubMed PMID: 8034694. Epub 1994/07/29. eng.
108. Hasan AA, Cines DB, Herwald H, Schmaier AH, Muller-Esterl W. Mapping the cell binding site on high molecular weight kininogen domain 5. *The Journal of biological chemistry*. 1995 Aug 18;270(33):19256-61. PubMed PMID: 7642598. Epub 1995/08/18. eng.
109. Herwald H, Morgelin M, Svensson HG, Sjobring U. Zinc-dependent conformational changes in domain D5 of high molecular mass kininogen modulate contact activation. *European journal of biochemistry / FEBS*. 2001 Jan;268(2):396-404. PubMed PMID: 11168375. Epub 2001/02/13. eng.
110. Scott CF, Silver LD, Purdon AD, Colman RW. Cleavage of human high molecular weight kininogen by factor XIa in vitro. Effect on structure and function. *The Journal of biological chemistry*. 1985 Sep 5;260(19):10856-63. PubMed PMID: 3875612. Epub 1985/09/05. eng.
111. Ratnoff OD, Margolius A, Jr. Hageman trait: an asymptomatic disorder of blood coagulation. *Transactions of the Association of American Physicians*. 1955;68:149-54. PubMed PMID: 13299324. Epub 1955/01/01. eng.
112. Ratnoff OD, Colopy JE. A familial hemorrhagic trait associated with a deficiency of a clot-promoting fraction of plasma. *J Clin Invest*. 1955 Apr;34(4):602-13. PubMed PMID: 14367514. Pubmed Central PMCID: PMC438666. Epub 1955/04/01. eng.
113. Ratnoff OD. The George M. Kober lecture. The legacy of John Hageman: new dividends. *Transactions of the Association of American Physicians*. 1985;98:cli-clxi. PubMed PMID: 3916033. Epub 1985/01/01. eng.
114. Caen J, Wu Q. Hageman factor, platelets and polyphosphates: early history and recent connection. *Journal of Thrombosis and Haemostasis*. 2010 Aug;8(8):1670-4. PubMed PMID: WOS:000280646300002. English.
115. Stavrou EX. Factor XII in inflammation and wound healing. *Current opinion in hematology*. 2018 Sep;25(5):403-9. PubMed PMID: 29994899. Epub 2018/07/12. eng.
116. Schloesser M, Zeerleder S, Lutze G, Halbmayer WM, Hofferbert S, Hinney B, et al. Mutations in the human factor XII gene. *Blood*. 1997 Nov 15;90(10):3967-77. PubMed PMID: 9354665. Epub 1997/11/14. eng.
117. Saito H, Hamilton SM, Tavill AS, Goodnough LT, Louis L, Angell A. Synthesis and release of Hageman factor (Factor XII) by the isolated perfused

- rat liver. *J Clin Invest.* 1983 Sep;72(3):948-54. PubMed PMID: 6411770. Pubmed Central PMCID: PMC1129260. Epub 1983/09/01. eng.
118. Citarella F, Misiti S, Felici A, Farsetti A, Pontecorvi A, Fantoni A. Estrogen induction and contact phase activation of human factor XII. *Steroids.* 1996 Apr;61(4):270-6. PubMed PMID: 8733013. Epub 1996/04/01. eng.
119. Gordon EM, Johnson TR, Ramos LP, Schmeidler-Sapiro KT. Enhanced expression of factor XII (Hageman factor) in isolated livers of estrogen- and prolactin-treated rats. *The Journal of laboratory and clinical medicine.* 1991 May;117(5):353-8. PubMed PMID: 2019789. Epub 1991/05/01. eng.
120. Shan J, Baguinon M, Zheng L, Krishnamoorthi R. Expression, refolding, and activation of the catalytic domain of human blood coagulation factor XII. *Protein expression and purification.* 2003 Jan;27(1):143-9. PubMed PMID: 12509996. Epub 2003/01/03. eng.
121. Reddigari SR, Shibayama Y, Brunnee T, Kaplan AP. Human Hageman factor (factor XII) and high molecular weight kininogen compete for the same binding site on human umbilical vein endothelial cells. *The Journal of biological chemistry.* 1993 Jun 5;268(16):11982-7. PubMed PMID: 8505323. Epub 1993/06/05. eng.
122. Shibayama Y, Brunnee T, Kaplan AP, Reddigari S. Activation of human Hageman factor (factor XII) in the presence of zinc and phosphate ions. *Brazilian journal of medical and biological research = Revista brasileira de pesquisas medicas e biologicas.* 1994 Aug;27(8):1817-28. PubMed PMID: 7749371. Epub 1994/08/01. eng.
123. Bernardo MM, Day DE, Olson ST, Shore JD. Surface-independent acceleration of factor XII activation by zinc ions. I. Kinetic characterization of the metal ion rate enhancement. *The Journal of biological chemistry.* 1993 Jun 15;268(17):12468-76. PubMed PMID: 8509386. Epub 1993/06/15. eng.
124. von Bruhl ML, Stark K, Steinhart A, Chandraratne S, Konrad I, Lorenz M, et al. Monocytes, neutrophils, and platelets cooperate to initiate and propagate venous thrombosis in mice in vivo. *The Journal of experimental medicine.* 2012 Apr 9;209(4):819-35. PubMed PMID: 22451716. Pubmed Central PMCID: PMC3328366. Epub 2012/03/28. eng.
125. van der Meijden PE, Munnix IC, Auger JM, Govers-Riemslog JW, Cosemans JM, Kuijpers MJ, et al. Dual role of collagen in factor XII-dependent thrombus formation. *Blood.* 2009 Jul 23;114(4):881-90. PubMed PMID: 19372258. Epub 2009/04/18. eng.
126. Sala-Cunill A, Bjorkqvist J, Senter R, Guilarte M, Cardona V, Labrador M, et al. Plasma contact system activation drives anaphylaxis in severe mast cell-mediated allergic reactions. *The Journal of allergy and clinical immunology.* 2015 Apr;135(4):1031-43 e6. PubMed PMID: 25240785. Epub 2014/09/23. eng.
127. Yang A, Chen F, He C, Zhou J, Lu Y, Dai J, et al. The Procoagulant Activity of Apoptotic Cells Is Mediated by Interaction with Factor XII. *Frontiers in immunology.* 2017;8:1188. PubMed PMID: 28993777. Pubmed Central PMCID: PMC5622377. Epub 2017/10/11. eng.
128. Kannemeier C, Shibamiya A, Nakazawa F, Trusheim H, Ruppert C, Markart P, et al. Extracellular RNA constitutes a natural procoagulant cofactor in blood coagulation. *Proceedings of the National Academy of Sciences of the United States of America.* 2007 Apr 10;104(15):6388-93. PubMed PMID: 17405864. Pubmed Central PMCID: PMC1851071. Epub 2007/04/05. eng.
129. Puy C, Tucker EI, Wong ZC, Gailani D, Smith SA, Choi SH, et al. Factor XII promotes blood coagulation independent of factor XI in the presence of long-chain polyphosphates. *Journal of thrombosis and haemostasis : JTH.* 2013 Jul;11(7):1341-52. PubMed PMID: 23659638. Pubmed Central PMCID: PMC3714337. Epub 2013/05/11. eng.
130. Mutch NJ, Waters EK, Morrissey JH. Immobilized transition metal ions stimulate contact activation and drive factor XII-mediated coagulation. *Journal*

- of Thrombosis and Haemostasis. 2012 Oct;10(10):2108-15. PubMed PMID: WOS:000309461900017. English.
131. Chatterjee K, Guo Z, Vogler EA, Siedlecki CA. Contributions of contact activation pathways of coagulation factor XII in plasma. *Journal of biomedical materials research Part A*. 2009 Jul;90(1):27-34. PubMed PMID: 18481791. Pubmed Central PMCID: PMC3598591. Epub 2008/05/17. eng.
132. Pathak M, Wilmann P, Awford J, Li C, Hamad BK, Fischer PM, et al. Coagulation factor XII protease domain crystal structure. *Journal of thrombosis and haemostasis : JTH*. 2015 Apr;13(4):580-91. PubMed PMID: 25604127. Pubmed Central PMCID: PMC4418343. Epub 2015/01/22. eng.
133. Stavrou E, Schmaier AH. Factor XII: what does it contribute to our understanding of the physiology and pathophysiology of hemostasis & thrombosis. *Thrombosis research*. 2010 Mar;125(3):210-5. PubMed PMID: 20022081. Pubmed Central PMCID: PMC2851158. Epub 2009/12/22. eng.
134. Bjorkqvist J, de Maat S, Lewandrowski U, Di Gennaro A, Oschatz C, Schonig K, et al. Defective glycosylation of coagulation factor XII underlies hereditary angioedema type III. *J Clin Invest*. 2015 Aug 3;125(8):3132-46. PubMed PMID: 26193639. Pubmed Central PMCID: PMC4563738. Epub 2015/07/21. eng.
135. de Maat S, Bjorkqvist J, Suffritti C, Wiesenekker CP, Nagtegaal W, Koekman A, et al. Plasmin is a natural trigger for bradykinin production in patients with hereditary angioedema with factor XII mutations. *The Journal of allergy and clinical immunology*. 2016 Nov;138(5):1414-23 e9. PubMed PMID: 27130860. Epub 2016/05/01. eng.
136. Bouillet L, Boccon-Gibod I, Gompel A, Floccard B, Martin L, Blanchard-Delaunay C, et al. Hereditary angioedema with normal C1 inhibitor: clinical characteristics and treatment response with plasma-derived human C1 inhibitor concentrate (Berinert((R))) in a French cohort. *European journal of dermatology : EJD*. 2017 Apr 1;27(2):155-9. PubMed PMID: 28251901. Epub 2017/03/03. eng.
137. Deroux A, Boccon-Gibod I, Fain O, Pralong P, Ollivier Y, Pagnier A, et al. Hereditary angioedema with normal C1 inhibitor and factor XII mutation: a series of 57 patients from the French National Center of Reference for Angioedema. *Clinical and experimental immunology*. 2016 Sep;185(3):332-7. PubMed PMID: 27271546. Pubmed Central PMCID: PMC4991515. Epub 2016/06/09. eng.
138. Canonica GW, Rossi O. Diagnosis and treatment of hereditary angioedema. *Panminerva medica*. 2012 Sep;54(3):241-53. PubMed PMID: 22801442. Epub 2012/07/18. eng.
139. Cool DE, Edgell CJ, Louie GV, Zoller MJ, Brayer GD, MacGillivray RT. Characterization of human blood coagulation factor XII cDNA. Prediction of the primary structure of factor XII and the tertiary structure of beta-factor XIIa. *The Journal of biological chemistry*. 1985 Nov 5;260(25):13666-76. PubMed PMID: 3877053.
140. Ivanov I, Matafonov A, Sun MF, Cheng Q, Dickeson SK, Verhamme IM, et al. Proteolytic properties of single-chain factor XII: a mechanism for triggering contact activation. *Blood*. 2017 Mar 16;129(11):1527-37. PubMed PMID: 28069606. Pubmed Central PMCID: PMC5356457. Epub 2017/01/11. eng.
141. Fujikawa K, McMullen BA. Amino acid sequence of human beta-factor XIIa. *The Journal of biological chemistry*. 1983 Sep 25;258(18):10924-33. PubMed PMID: 6604055. Epub 1983/09/25. eng.
142. McMullen BA, Fujikawa K. Amino acid sequence of the heavy chain of human alpha-factor XIIa (activated Hageman factor). *The Journal of biological chemistry*. 1985 May 10;260(9):5328-41. PubMed PMID: 3886654. Epub 1985/05/10. eng.
143. Clarke BJ, Cote HC, Cool DE, Clark-Lewis I, Saito H, Pixley RA, et al. Mapping of a putative surface-binding site of human coagulation factor XII. *The*

- Journal of biological chemistry. 1989 Jul 5;264(19):11497-502. PubMed PMID: 2472397. Epub 1989/07/05. eng.
144. Citarella F, Ravon DM, Pascucci B, Felici A, Fantoni A, Hack CE. Structure/function analysis of human factor XII using recombinant deletion mutants. Evidence for an additional region involved in the binding to negatively charged surfaces. *European journal of biochemistry / FEBS*. 1996 May 15;238(1):240-9. PubMed PMID: 8665943. Epub 1996/05/15. eng.
145. Pixley RA, Stumpo LG, Birkmeyer K, Silver L, Colman RW. A monoclonal antibody recognizing an icosapeptide sequence in the heavy chain of human factor XII inhibits surface-catalyzed activation. *The Journal of biological chemistry*. 1987 Jul 25;262(21):10140-5. PubMed PMID: 2440859. Epub 1987/07/25. eng.
146. Beringer DX, Kroon-Batenburg LM. The structure of the FnI-EGF-like tandem domain of coagulation factor XII solved using SIRAS. *Acta crystallographica Section F, Structural biology and crystallization communications*. 2013 Feb 1;69(Pt 2):94-102. PubMed PMID: 23385745. Pubmed Central PMCID: PMC3564606. Epub 2013/02/07. eng.
147. Isawa H, Orito Y, Iwanaga S, Jingushi N, Morita A, Chinzei Y, et al. Identification and characterization of a new kallikrein-kinin system inhibitor from the salivary glands of the malaria vector mosquito *Anopheles stephensi*. *Insect biochemistry and molecular biology*. 2007 May;37(5):466-77. PubMed PMID: 17456441. Epub 2007/04/26. eng.
148. Pankov R, Yamada KM. Fibronectin at a glance. *Journal of cell science*. 2002 Oct 15;115(Pt 20):3861-3. PubMed PMID: 12244123. Epub 2002/09/24. eng.
149. Gui L, Wojciechowski K, Gildner CD, Nedelkovska H, Hocking DC. Identification of the heparin-binding determinants within fibronectin repeat III1: role in cell spreading and growth. *The Journal of biological chemistry*. 2006 Nov 17;281(46):34816-25. PubMed PMID: 16982604. Epub 2006/09/20. eng.
150. Mao Y, Schwarzbauer JE. Fibronectin fibrillogenesis, a cell-mediated matrix assembly process. *Matrix biology : journal of the International Society for Matrix Biology*. 2005 Sep;24(6):389-99. PubMed PMID: 16061370. Epub 2005/08/03. eng.
151. Eigenbrot C, Ganesan R, Kirchhofer D. Hepatocyte growth factor activator (HGFA): molecular structure and interactions with HGFA inhibitor-1 (HAI-1). *The FEBS journal*. 2010 May;277(10):2215-22. PubMed PMID: 20402765. Epub 2010/04/21. eng.
152. Hornebeck W, Bellon G, Emonard H. Fibronectin type II (FnII)-like modules regulate gelatinase A activity. *Pathologie-biologie*. 2005 Sep;53(7):405-10. PubMed PMID: 16085117. Epub 2005/08/09. eng.
153. Briknarova K, Grishaev A, Banyai L, Tordai H, Patthy L, Llinas M. The second type II module from human matrix metalloproteinase 2: structure, function and dynamics. *Structure (London, England : 1993)*. 1999 Oct 15;7(10):1235-45. PubMed PMID: 10545322. Epub 1999/11/05. eng.
154. Scannevin RH, Alexander R, Haarlander TM, Burke SL, Singer M, Huo C, et al. Discovery of a highly selective chemical inhibitor of matrix metalloproteinase-9 (MMP-9) that allosterically inhibits zymogen activation. *The Journal of biological chemistry*. 2017 Oct 27;292(43):17963-74. PubMed PMID: 28860188. Pubmed Central PMCID: PMC5663893. Epub 2017/09/02. eng.
155. Greube A, Muller K, Topfer-Petersen E, Herrmann A, Muller P. Interaction of fibronectin type II proteins with membranes: the stallion seminal plasma protein SP-1/2. *Biochemistry*. 2004 Jan 20;43(2):464-72. PubMed PMID: 14717601. Epub 2004/01/14. eng.
156. Calvete JJ, Sanz L. Insights into structure-function correlations of ungulate seminal plasma proteins. *Society of Reproduction and Fertility*

- supplement. 2007;65:201-15. PubMed PMID: 17644963. Epub 2007/07/25. eng.
157. Citarella F, te Velthuis H, Helmer-Citterich M, Hack CE. Identification of a putative binding site for negatively charged surfaces in the fibronectin type II domain of human factor XII - An immunochemical and homology modeling approach. *Thrombosis and haemostasis*. 2000 Dec;84(6):1057-65. PubMed PMID: WOS:000166080600021. English.
158. Lupu F, Keshari RS, Lambris JD, Coggeshall KM. Crosstalk between the coagulation and complement systems in sepsis. *Thrombosis research*. 2014 May;133 Suppl 1:S28-31. PubMed PMID: 24759136. Pubmed Central PMCID: PMC4154483. Epub 2014/04/25. eng.
159. Pixley RA, De La Cadena R, Page JD, Kaufman N, Wyshock EG, Chang A, et al. The contact system contributes to hypotension but not disseminated intravascular coagulation in lethal bacteremia. In vivo use of a monoclonal anti-factor XII antibody to block contact activation in baboons. *J Clin Invest*. 1993 Jan;91(1):61-8. PubMed PMID: 7678610. Pubmed Central PMCID: PMC329995. Epub 1993/01/01. eng.
160. Morrison DC, Cochrane CG. Direct evidence for Hageman factor (factor XII) activation by bacterial lipopolysaccharides (endotoxins). *The Journal of experimental medicine*. 1974 Sep 1;140(3):797-811. PubMed PMID: 4378413. Pubmed Central PMCID: PMC2139619. Epub 1974/09/01. eng.
161. Antoniak S. The coagulation system in host defense. *Research and practice in thrombosis and haemostasis*. 2018 Jul;2(3):549-57. PubMed PMID: 30046760. Pubmed Central PMCID: PMC6046589. Epub 2018/07/27. eng.
162. Nickel KF, Renne T. Crosstalk of the plasma contact system with bacteria. *Thrombosis research*. 2012 Oct;130 Suppl 1:S78-83. PubMed PMID: 23026673. Epub 2012/10/03. eng.
163. Pixley RA, DeLa Cadena RA, Page JD, Kaufman N, Wyshock EG, Colman RW, et al. Activation of the contact system in lethal hypotensive bacteremia in a baboon model. *The American journal of pathology*. 1992 Apr;140(4):897-906. PubMed PMID: 1373271. Pubmed Central PMCID: PMC1886362. Epub 1992/04/11. eng.
164. Kalter ES, van Dijk WC, Timmerman A, Verhoef J, Bouma BN. Activation of purified human plasma prekallikrein triggered by cell wall fractions of *Escherichia coli* and *Staphylococcus aureus*. *The Journal of infectious diseases*. 1983 Oct;148(4):682-91. PubMed PMID: 6355312. Epub 1983/10/01. eng.
165. Smith SA, Choi SH, Davis-Harrison R, Huyck J, Boettcher J, Rienstra CM, et al. Polyphosphate exerts differential effects on blood clotting, depending on polymer size. *Blood*. 2010 Nov 18;116(20):4353-9. PubMed PMID: 20709905. Pubmed Central PMCID: PMC2993633. Epub 2010/08/17. eng.
166. Ben Nasr A, Olsen A, Sjobring U, Muller-Esterl W, Bjorck L. Assembly of human contact phase proteins and release of bradykinin at the surface of curli-expressing *Escherichia coli*. *Molecular microbiology*. 1996 Jun;20(5):927-35. PubMed PMID: 8809746. Epub 1996/06/01. eng.
167. Herwald H, Morgelin M, Olsen A, Rhen M, Dahlback B, Muller-Esterl W, et al. Activation of the contact-phase system on bacterial surfaces--a clue to serious complications in infectious diseases. *Nature medicine*. 1998 Mar;4(3):298-302. PubMed PMID: 9500602. Epub 1998/03/21. eng.
168. Yang A, Xie Z, Wang B, Colman RW, Dai J, Wu Y. An essential role of high-molecular-weight kininogen in endotoxemia. *The Journal of experimental medicine*. 2017 Sep 4;214(9):2649-70. PubMed PMID: 28794132. Pubmed Central PMCID: PMC5584120. Epub 2017/08/11. eng.
169. Gustafson EJ, Schmaier AH, Wachtfogel YT, Kaufman N, Kucich U, Colman RW. Human neutrophils contain and bind high molecular weight kininogen. *J Clin Invest*. 1989 Jul;84(1):28-35. PubMed PMID: 2738152. Pubmed Central PMCID: PMC303948. Epub 1989/07/01. eng.

170. Greengard JS, Griffin JH. Receptors for high molecular weight kininogen on stimulated washed human platelets. *Biochemistry*. 1984 Dec 18;23(26):6863-9. PubMed PMID: 6099145. Epub 1984/12/18. eng.
171. Fernando LP, Natesan S, Joseph K, Kaplan AP. High molecular weight kininogen and factor XII binding to endothelial cells and astrocytes. *Thrombosis and haemostasis*. 2003 Nov;90(5):787-95. PubMed PMID: 14597972. Epub 2003/11/05. eng.
172. Celi A, Lorenzet R, Furie B, Furie BC. Platelet-leukocyte-endothelial cell interaction on the blood vessel wall. *Seminars in hematology*. 1997 Oct;34(4):327-35. PubMed PMID: 9347583. Epub 1997/11/05. eng.
173. Engelmann B, Massberg S. Thrombosis as an intravascular effector of innate immunity. *Nature reviews Immunology*. 2013 Jan;13(1):34-45. PubMed PMID: 23222502. Epub 2012/12/12. eng.
174. Massberg S, Grahl L, von Bruehl ML, Manukyan D, Pfeiler S, Goosmann C, et al. Reciprocal coupling of coagulation and innate immunity via neutrophil serine proteases. *Nature medicine*. 2010 Aug;16(8):887-96. PubMed PMID: 20676107. Epub 2010/08/03. eng.
175. Baglia FA, Shrimpton CN, Emsley J, Kitagawa K, Ruggeri ZM, Lopez JA, et al. Factor XI interacts with the leucine-rich repeats of glycoprotein Ibalpha on the activated platelet. *The Journal of biological chemistry*. 2004 Nov 19;279(47):49323-9. PubMed PMID: 15375170. Epub 2004/09/18. eng.
176. Puri RN, Zhou F, Hu CJ, Colman RF, Colman RW. High molecular weight kininogen inhibits thrombin-induced platelet aggregation and cleavage of aggrecan by inhibiting binding of thrombin to platelets. *Blood*. 1991 Feb 1;77(3):500-7. PubMed PMID: 1846761. Epub 1991/02/01. eng.
177. Pfeiler S, Stark K, Massberg S, Engelmann B. Propagation of thrombosis by neutrophils and extracellular nucleosome networks. *Haematologica*. 2017 Feb;102(2):206-13. PubMed PMID: 27927771. Pubmed Central PMCID: PMC5286929. Epub 2016/12/09. eng.
178. Bradford HN, Dela Cadena RA, Kunapuli SP, Dong JF, Lopez JA, Colman RW. Human kininogens regulate thrombin binding to platelets through the glycoprotein Ib-IX-V complex. *Blood*. 1997 Aug 15;90(4):1508-15. PubMed PMID: 9269768. Epub 1997/08/15. eng.
179. Bradford HN, Pixley RA, Colman RW. Human factor XII binding to the glycoprotein Ib-IX-V complex inhibits thrombin-induced platelet aggregation. *The Journal of biological chemistry*. 2000 Jul 28;275(30):22756-63. PubMed PMID: 10801853. Epub 2000/05/10. eng.
180. Joseph K, Nakazawa Y, Bahou WF, Ghebrehiwet B, Kaplan AP. Platelet glycoprotein Ib: a zinc-dependent binding protein for the heavy chain of high-molecular-weight kininogen. *Molecular medicine (Cambridge, Mass)*. 1999 Aug;5(8):555-63. PubMed PMID: 10501658. Pubmed Central PMCID: PMC2230456. Epub 1999/09/29. eng.
181. Chavakis T, Santoso S, Clemetson KJ, Sachs UJ, Isordia-Salas I, Pixley RA, et al. High molecular weight kininogen regulates platelet-leukocyte interactions by bridging Mac-1 and glycoprotein Ib. *The Journal of biological chemistry*. 2003 Nov 14;278(46):45375-81. PubMed PMID: 12952972. Epub 2003/09/04. eng.
182. Henderson LM, Figueroa CD, Muller-Esterl W, Bhoola KD. Assembly of contact-phase factors on the surface of the human neutrophil membrane. *Blood*. 1994 Jul 15;84(2):474-82. PubMed PMID: 8025275. Epub 1994/07/15. eng.
183. Rebuck JW. The skin window as a monitor of leukocytic functions in contact activation factor deficiencies in man. *American journal of clinical pathology*. 1983 Apr;79(4):405-13. PubMed PMID: 6340459. Epub 1983/04/01. eng.
184. Wachtfogel YT, Pixley RA, Kucich U, Abrams W, Weinbaum G, Schapira M, et al. Purified plasma factor XIIa aggregates human neutrophils and causes

degranulation. *Blood*. 1986 Jun;67(6):1731-7. PubMed PMID: 3486686. Epub 1986/06/01. eng.

185. Stavrou EX, Fang C, Bane KL, Long AT, Naudin C, Kucukal E, et al. Factor XII and uPAR upregulate neutrophil functions to influence wound healing. *J Clin Invest*. 2018 Mar 1;128(3):944-59. PubMed PMID: 29376892. Pubmed Central PMCID: PMC5824869. Epub 2018/01/30. eng.

186. Joseph K, Ghebrehiwet B, Kaplan AP. Cytokeratin 1 and gC1qR mediate high molecular weight kininogen binding to endothelial cells. *Clinical immunology (Orlando, Fla)*. 1999 Sep;92(3):246-55. PubMed PMID: 10479529. Epub 1999/09/10. eng.

187. Pathak M, Kaira BG, Slater A, Emsley J. Cell Receptor and Cofactor Interactions of the Contact Activation System and Factor XI. *Frontiers in medicine*. 2018;5:66. PubMed PMID: 29619369. Pubmed Central PMCID: PMC5871670. Epub 2018/04/06. eng.

188. Dembitzer FR, Kinoshita Y, Burstein D, Phelps RG, Beasley MB, Garcia R, et al. gC1qR expression in normal and pathologic human tissues: differential expression in tissues of epithelial and mesenchymal origin. *The journal of histochemistry and cytochemistry : official journal of the Histochemistry Society*. 2012 Jun;60(6):467-74. PubMed PMID: 22638269. Pubmed Central PMCID: PMC3393077. Epub 2012/05/29. eng.

189. Guo WX, Ghebrehiwet B, Weksler B, Schweitzer K, Peerschke EI. Up-regulation of endothelial cell binding proteins/receptors for complement component C1q by inflammatory cytokines. *The Journal of laboratory and clinical medicine*. 1999 Jun;133(6):541-50. PubMed PMID: 10360628. Epub 1999/06/09. eng.

190. Peerschke EI, Minta JO, Zhou SZ, Bini A, Gotlieb A, Colman RW, et al. Expression of gC1q-R/p33 and its major ligands in human atherosclerotic lesions. *Molecular immunology*. 2004 Jul;41(8):759-66. PubMed PMID: 15234555. Epub 2004/07/06. eng.

191. Petersen-Mahrt SK, Estmer C, Ohrmalm C, Matthews DA, Russell WC, Akusjarvi G. The splicing factor-associated protein, p32, regulates RNA splicing by inhibiting ASF/SF2 RNA binding and phosphorylation. *The EMBO journal*. 1999 Feb 15;18(4):1014-24. PubMed PMID: 10022843. Pubmed Central PMCID: PMC1171193. Epub 1999/02/18. eng.

192. Kim KB, Kim BW, Choo HJ, Kwon YC, Ahn BY, Choi JS, et al. Proteome analysis of adipocyte lipid rafts reveals that gC1qR plays essential roles in adipogenesis and insulin signal transduction. *Proteomics*. 2009 May;9(9):2373-82. PubMed PMID: 19402044. Epub 2009/04/30. eng.

193. Ghebrehiwet B, Ji Y, Valentino A, Pednekar L, Ramadass M, Habel D, et al. Soluble gC1qR is an autocrine signal that induces B1R expression on endothelial cells. *Journal of immunology (Baltimore, Md : 1950)*. 2014 Jan 1;192(1):377-84. PubMed PMID: 24319267. Pubmed Central PMCID: PMC3876932. Epub 2013/12/10. eng.

194. Ghebrehiwet B, Lim BL, Kumar R, Feng X, Peerschke EI. gC1q-R/p33, a member of a new class of multifunctional and multicompartmental cellular proteins, is involved in inflammation and infection. *Immunological reviews*. 2001 Apr;180:65-77. PubMed PMID: 11414365. Epub 2001/06/21. eng.

195. Ghebrehiwet B, Lim BL, Peerschke EI, Willis AC, Reid KB. Isolation, cDNA cloning, and overexpression of a 33-kD cell surface glycoprotein that binds to the globular "heads" of C1q. *The Journal of experimental medicine*. 1994 Jun 1;179(6):1809-21. PubMed PMID: 8195709. Pubmed Central PMCID: PMC2191527. Epub 1994/06/01. eng.

196. Ghebrehiwet B, Kew RR, Gruber BL, Marchese MJ, Peerschke EI, Reid KB. Murine mast cells express two types of C1q receptors that are involved in the induction of chemotaxis and chemokinesis. *Journal of immunology (Baltimore, Md : 1950)*. 1995 Sep 1;155(5):2614-9. PubMed PMID: 7650391. Epub 1995/09/01. eng.

197. Eggleton P, Ghebrehiwet B, Sastry KN, Coburn JP, Zaner KS, Reid KB, et al. Identification of a gC1q-binding protein (gC1q-R) on the surface of human neutrophils. Subcellular localization and binding properties in comparison with the cC1q-R. *J Clin Invest*. 1995 Apr;95(4):1569-78. PubMed PMID: 7706463. Pubmed Central PMCID: PMC295648. Epub 1995/04/01. eng.
198. Peerschke EI, Reid KB, Ghebrehiwet B. Identification of a novel 33-kDa C1q-binding site on human blood platelets. *Journal of immunology (Baltimore, Md : 1950)*. 1994 Jun 15;152(12):5896-901. PubMed PMID: 8207215. Epub 1994/06/15. eng.
199. Ghebrehiwet B, Jesty J, Peerschke EI. gC1q-R/p33: structure-function predictions from the crystal structure. *Immunobiology*. 2002 Sep;205(4-5):421-32. PubMed PMID: 12396004. Epub 2002/10/25. eng.
200. Ghebrehiwet B, Lu PD, Zhang W, Lim BL, Eggleton P, Leigh LE, et al. Identification of functional domains on gC1Q-R, a cell surface protein that binds to the globular "heads" of C1Q, using monoclonal antibodies and synthetic peptides. *Hybridoma*. 1996 Oct;15(5):333-42. PubMed PMID: 8913782. Epub 1996/10/01. eng.
201. Ghebrehiwet B, Lu PD, Zhang W, Keilbaugh SA, Leigh LE, Eggleton P, et al. Evidence that the two C1q binding membrane proteins, gC1q-R and cC1q-R, associate to form a complex. *Journal of immunology (Baltimore, Md : 1950)*. 1997 Aug 1;159(3):1429-36. PubMed PMID: 9233640. Epub 1997/08/01. eng.
202. Lim BL, Reid KB, Ghebrehiwet B, Peerschke EI, Leigh LA, Preissner KT. The binding protein for globular heads of complement C1q, gC1qR. Functional expression and characterization as a novel vitronectin binding factor. *The Journal of biological chemistry*. 1996 Oct 25;271(43):26739-44. PubMed PMID: 8900153. Epub 1996/10/25. eng.
203. Pixley RA, Espinola RG, Ghebrehiwet B, Joseph K, Kao A, Bdeir K, et al. Interaction of high-molecular-weight kininogen with endothelial cell binding proteins suPAR, gC1qR and cytokeratin 1 determined by surface plasmon resonance (BiaCore). *Thrombosis and haemostasis*. 2011 Jun;105(6):1053-9. PubMed PMID: 21544310. Pubmed Central PMCID: PMC3149827. Epub 2011/05/06. eng.
204. Ghebrehiwet B, Peerschke EI. Structure and function of gC1q-R: a multiligand binding cellular protein. *Immunobiology*. 1998 Aug;199(2):225-38. PubMed PMID: 9777408. Epub 1998/10/20. eng.
205. Ye T, Huang X, Wang XW, Shi YR, Hui KM, Ren Q. Characterization of a gC1qR from the giant freshwater prawn, *Macrobrachium rosenbergii*. *Fish & shellfish immunology*. 2015 Mar;43(1):200-8. PubMed PMID: 25555810. Epub 2015/01/04. eng.
206. Sprehe M, Fisk JC, McEvoy SM, Read LK, Schumacher MA. Structure of the *Trypanosoma brucei* p22 protein, a cytochrome oxidase subunit II-specific RNA-editing accessory factor. *The Journal of biological chemistry*. 2010 Jun 11;285(24):18899-908. PubMed PMID: 20392699. Pubmed Central PMCID: PMC2881812. Epub 2010/04/16. eng.
207. Jiang J, Zhang Y, Krainer AR, Xu RM. Crystal structure of human p32, a doughnut-shaped acidic mitochondrial matrix protein. *Proceedings of the National Academy of Sciences of the United States of America*. 1999 Mar 30;96(7):3572-7. PubMed PMID: 10097078. Pubmed Central PMCID: PMC22335. Epub 1999/03/31. eng.
208. Lim BL, White RA, Hummel GS, Schwaeble W, Lynch NJ, Peerschke EI, et al. Characterization of the murine gene of gC1qBP, a novel cell protein that binds the globular heads of C1q, vitronectin, high molecular weight kininogen and factor XII. *Gene*. 1998 Mar 16;209(1-2):229-37. PubMed PMID: 9524273. Epub 1998/05/16. eng.
209. Feng X, Tonnesen MG, Peerschke EI, Ghebrehiwet B. Cooperation of C1q receptors and integrins in C1q-mediated endothelial cell adhesion and

spreading. *Journal of immunology* (Baltimore, Md : 1950). 2002 Mar 1;168(5):2441-8. PubMed PMID: 11859136. Epub 2002/02/23. eng.

210. Hosszu KK, Valentino A, Vinayagasundaram U, Vinayagasundaram R, Joyce MG, Ji Y, et al. DC-SIGN, C1q, and gC1qR form a trimolecular receptor complex on the surface of monocyte-derived immature dendritic cells. *Blood*. 2012 Aug 9;120(6):1228-36. PubMed PMID: 22700724. Pubmed Central PMCID: PMC3418718. Epub 2012/06/16. eng.

211. Beatch MD, Everitt JC, Law LJ, Hobman TC. Interactions between rubella virus capsid and host protein p32 are important for virus replication. *Journal of virology*. 2005 Aug;79(16):10807-20. PubMed PMID: 16051872. Pubmed Central PMCID: PMC1182682. Epub 2005/07/30. eng.

212. Beatch MD, Hobman TC. Rubella virus capsid associates with host cell protein p32 and localizes to mitochondria. *Journal of virology*. 2000 Jun;74(12):5569-76. PubMed PMID: 10823864. Pubmed Central PMCID: PMC112044. Epub 2000/05/24. eng.

213. Luo Y, Yu H, Peterlin BM. Cellular protein modulates effects of human immunodeficiency virus type 1 Rev. *Journal of virology*. 1994 Jun;68(6):3850-6. PubMed PMID: 8189522. Pubmed Central PMCID: PMC236890. Epub 1994/06/01. eng.

214. Yu L, Loewenstein PM, Zhang Z, Green M. In vitro interaction of the human immunodeficiency virus type 1 Tat transactivator and the general transcription factor TFIIB with the cellular protein TAP. *Journal of virology*. 1995 May;69(5):3017-23. PubMed PMID: 7707528. Pubmed Central PMCID: PMC189001. Epub 1995/05/01. eng.

215. Wang Y, Finan JE, Middeldorp JM, Hayward SD. P32/TAP, a cellular protein that interacts with EBNA-1 of Epstein-Barr virus. *Virology*. 1997 Sep 15;236(1):18-29. PubMed PMID: 9299613. Epub 1997/09/23. eng.

216. Matthews DA, Russell WC. Adenovirus core protein V interacts with p32-- a protein which is associated with both the mitochondria and the nucleus. *The Journal of general virology*. 1998 Jul;79 (Pt 7):1677-85. PubMed PMID: 9680131. Epub 1998/07/29. eng.

217. Kittlesen DJ, Chianese-Bullock KA, Yao ZQ, Braciale TJ, Hahn YS. Interaction between complement receptor gC1qR and hepatitis C virus core protein inhibits T-lymphocyte proliferation. *J Clin Invest*. 2000 Nov;106(10):1239-49. PubMed PMID: 11086025. Pubmed Central PMCID: PMC381434. Epub 2000/11/22. eng.

218. Mohan KV, Ghebrehiwet B, Atreya CD. The N-terminal conserved domain of rubella virus capsid interacts with the C-terminal region of cellular p32 and overexpression of p32 enhances the viral infectivity. *Virus research*. 2002 May 10;85(2):151-61. PubMed PMID: 12034482. Epub 2002/05/30. eng.

219. Westman J, Smeds E, Johansson L, Morgelin M, Olin AI, Malmstrom E, et al. Treatment with p33 curtails morbidity and mortality in a histone-induced murine shock model. *Journal of innate immunity*. 2014;6(6):819-30. PubMed PMID: 24942226. Epub 2014/06/20. eng.

220. Olins AL, Rhodes G, Welch DB, Zwerger M, Olins DE. Lamin B receptor: multi-tasking at the nuclear envelope. *Nucleus (Austin, Tex)*. 2010 Jan-Feb;1(1):53-70. PubMed PMID: 21327105. Pubmed Central PMCID: PMC3035127. Epub 2011/02/18. eng.

221. Duband-Goulet I, Courvalin JC, Buendia B. LBR, a chromatin and lamin binding protein from the inner nuclear membrane, is proteolyzed at late stages of apoptosis. *Journal of cell science*. 1998 May;111 (Pt 10):1441-51. PubMed PMID: 9570761. Epub 1998/05/07. eng.

222. Mylonis I, Drosou V, Brancorsini S, Nikolakaki E, Sassone-Corsi P, Giannakouros T. Temporal association of protamine 1 with the inner nuclear membrane protein lamin B receptor during spermiogenesis. *The Journal of biological chemistry*. 2004 Mar 19;279(12):11626-31. PubMed PMID: 14701833. Epub 2004/01/01. eng.

223. Milbradt J, Auerochs S, Sticht H, Marschall M. Cytomegaloviral proteins that associate with the nuclear lamina: components of a postulated nuclear egress complex. *The Journal of general virology*. 2009 Mar;90(Pt 3):579-90. PubMed PMID: 19218202. Epub 2009/02/17. eng.
224. Peerschke EI, Ghebrehiwet B. cC1qR/CR and gC1qR/p33: observations in cancer. *Molecular immunology*. 2014 Oct;61(2):100-9. PubMed PMID: 25044096. Epub 2014/07/22. eng.
225. Wang Y, Fu D, Su J, Chen Y, Qi C, Sun Y, et al. C1QBP suppresses cell adhesion and metastasis of renal carcinoma cells. *Scientific reports*. 2017 Apr 20;7(1):999. PubMed PMID: 28428626. Pubmed Central PMCID: PMC5430506. Epub 2017/04/22. eng.
226. Zhang X, Zhang F, Guo L, Wang Y, Zhang P, Wang R, et al. Interactome analysis reveals that C1QBP (complement component 1, q subcomponent binding protein) is associated with cancer cell chemotaxis and metastasis. *Molecular & cellular proteomics : MCP*. 2013 Nov;12(11):3199-209. PubMed PMID: 23924515. Pubmed Central PMCID: PMC3820933. Epub 2013/08/09. eng.
227. Fogal V, Zhang L, Krajewski S, Ruoslahti E. Mitochondrial/cell-surface protein p32/gC1qR as a molecular target in tumor cells and tumor stroma. *Cancer research*. 2008 Sep 1;68(17):7210-8. PubMed PMID: 18757437. Pubmed Central PMCID: PMC2562323. Epub 2008/09/02. eng.
228. Hunt H, Simon-Gracia L, Tobi A, Kotamraju VR, Sharma S, Nigul M, et al. Targeting of p32 in peritoneal carcinomatosis with intraperitoneal linTT1 peptide-guided pro-apoptotic nanoparticles. *Journal of controlled release : official journal of the Controlled Release Society*. 2017 Aug 28;260:142-53. PubMed PMID: 28603028. Pubmed Central PMCID: PMC6129970. Epub 2017/06/13. eng.
229. Paasonen L, Sharma S, Braun GB, Kotamraju VR, Chung TD, She ZG, et al. New p32/gC1qR Ligands for Targeted Tumor Drug Delivery. *Chembiochem : a European journal of chemical biology*. 2016 Apr 1;17(7):570-5. PubMed PMID: 26895508. Pubmed Central PMCID: PMC5433940. Epub 2016/02/20. eng.
230. Shibayama Y, Reddigari SR, Teruya M, Nakamura K, Fukunaga Y, Ienaga K, et al. Effect of neurotrophin on the binding of high molecular weight kininogen and Hageman factor to human umbilical vein endothelial cells and the autoactivation of bound Hageman factor. *Biochemical pharmacology*. 1998 Apr 15;55(8):1175-80. PubMed PMID: 9719471. Epub 1998/08/27. eng.
231. Ghebrehiwet B, Jesty J, Xu S, Vinayagasundaram R, Vinayagasundaram U, Ji Y, et al. Structure-function studies using deletion mutants identify domains of gC1qR/p33 as potential therapeutic targets for vascular permeability and inflammation. *Frontiers in immunology*. 2011 Nov 1;2. PubMed PMID: 22282702. Pubmed Central PMCID: PMC3265123. Epub 2012/01/28. eng.
232. Peerschke EI, Murphy TK, Ghebrehiwet B. Activation-dependent surface expression of gC1qR/p33 on human blood platelets. *Thrombosis and haemostasis*. 2003 Feb;89(2):331-9. PubMed PMID: 12574814. Epub 2003/02/08. eng.
233. Yagi M, Uchiumi T, Takazaki S, Okuno B, Nomura M, Yoshida S, et al. p32/gC1qR is indispensable for fetal development and mitochondrial translation: importance of its RNA-binding ability. *Nucleic acids research*. 2012 Oct;40(19):9717-37. PubMed PMID: 22904065. Pubmed Central PMCID: PMC3479211. Epub 2012/08/21. eng.
234. Amara U, Rittirsch D, Flierl M, Bruckner U, Klos A, Gebhard F, et al. Interaction between the coagulation and complement system. *Advances in experimental medicine and biology*. 2008;632:71-9. PubMed PMID: 19025115. Pubmed Central PMCID: PMC2713875. Epub 2008/11/26. eng.
235. Huber-Lang M, Sarma JV, Zetoune FS, Rittirsch D, Neff TA, McGuire SR, et al. Generation of C5a in the absence of C3: a new complement activation

pathway. *Nature medicine*. 2006 Jun;12(6):682-7. PubMed PMID: 16715088. Epub 2006/05/23. eng.

236. Krisinger MJ, Goebeler V, Lu Z, Meixner SC, Myles T, Pryzdial EL, et al. Thrombin generates previously unidentified C5 products that support the terminal complement activation pathway. *Blood*. 2012 Aug 23;120(8):1717-25. PubMed PMID: 22802338. Epub 2012/07/18. eng.

237. Mizuno T, Yoshioka K, Mizuno M, Shimizu M, Nagano F, Okuda T, et al. Complement component 5 promotes lethal thrombosis. *Scientific reports*. 2017 Feb 16;7:42714. PubMed PMID: 28205538. Pubmed Central PMCID: PMC5311936. Epub 2017/02/17. eng.

238. DiScipio RG. The activation of the alternative pathway C3 convertase by human plasma kallikrein. *Immunology*. 1982 Mar;45(3):587-95. PubMed PMID: 6916710. Pubmed Central PMCID: PMC1555245. Epub 1982/03/01. eng.

239. Irmischer S, Doring N, Halder LD, Jo EAH, Kopka I, Dunker C, et al. Kallikrein Cleaves C3 and Activates Complement. *Journal of innate immunity*. 2018;10(2):94-105. PubMed PMID: 29237166. Epub 2017/12/14. eng.

240. Ghebrehiwet B, Randazzo BP, Dunn JT, Silverberg M, Kaplan AP. Mechanisms of activation of the classical pathway of complement by Hageman factor fragment. *J Clin Invest*. 1983 May;71(5):1450-6. PubMed PMID: 6304147. Pubmed Central PMCID: PMC437009. Epub 1983/05/01. eng.

241. Kishimoto TK, Viswanathan K, Ganguly T, Elankumaran S, Smith S, Pelzer K, et al. Contaminated heparin associated with adverse clinical events and activation of the contact system. *The New England journal of medicine*. 2008 Jun 5;358(23):2457-67. PubMed PMID: 18434646. Pubmed Central PMCID: PMC3778681. Epub 2008/04/25. eng.

242. Rodamilans B, Munoz IG, Bragado-Nilsson E, Sarrias MR, Padilla O, Blanco FJ, et al. Crystal structure of the third extracellular domain of CD5 reveals the fold of a group B scavenger cysteine-rich receptor domain. *The Journal of biological chemistry*. 2007 Apr 27;282(17):12669-77. PubMed PMID: 17322294. Epub 2007/02/27. eng.

243. Kazama Y, Hamamoto T, Foster DC, Kisiel W. Hepsin, a putative membrane-associated serine protease, activates human factor VII and initiates a pathway of blood coagulation on the cell surface leading to thrombin formation. *The Journal of biological chemistry*. 1995 Jan 6;270(1):66-72. PubMed PMID: 7814421. Epub 1995/01/06. eng.

244. Somoza JR, Ho JD, Luong C, Ghate M, Sprengeler PA, Mortara K, et al. The structure of the extracellular region of human hepsin reveals a serine protease domain and a novel scavenger receptor cysteine-rich (SRCR) domain. *Structure (London, England : 1993)*. 2003 Sep;11(9):1123-31. PubMed PMID: 12962630. Epub 2003/09/10. eng.

245. Alba-Dominguez M, Lopez-Lera A, Garrido S, Nozal P, Gonzalez-Granado I, Melero J, et al. Complement factor I deficiency: a not so rare immune defect: characterization of new mutations and the first large gene deletion. *Orphanet journal of rare diseases*. 2012 Jun 18;7:42. PubMed PMID: 22710145. Pubmed Central PMCID: PMC3458969. Epub 2012/06/20. eng.

246. Le Quintrec M, Lionet A, Kamar N, Karras A, Barbier S, Buchler M, et al. Complement mutation-associated de novo thrombotic microangiopathy following kidney transplantation. *American journal of transplantation : official journal of the American Society of Transplantation and the American Society of Transplant Surgeons*. 2008 Aug;8(8):1694-701. PubMed PMID: 18557729. Epub 2008/06/19. eng.

247. Arredouani MS, Palecanda A, Koziel H, Huang YC, Imrich A, Sulahian TH, et al. MARCO is the major binding receptor for unopsonized particles and bacteria on human alveolar macrophages. *Journal of immunology (Baltimore, Md : 1950)*. 2005 Nov 1;175(9):6058-64. PubMed PMID: 16237101. Epub 2005/10/21. eng.

248. Hohenester E, Sasaki T, Timpl R. Crystal structure of a scavenger receptor cysteine-rich domain sheds light on an ancient superfamily. *Nature structural biology*. 1999 Mar;6(3):228-32. PubMed PMID: 10074941. Epub 1999/03/13. eng.
249. Resnick D, Pearson A, Krieger M. The SRCR superfamily: a family reminiscent of the Ig superfamily. *Trends in biochemical sciences*. 1994 Jan;19(1):5-8. PubMed PMID: 8140623. Epub 1994/01/01. eng.
250. Sarrias MR, Gronlund J, Padilla O, Madsen J, Holmskov U, Lozano F. The Scavenger Receptor Cysteine-Rich (SRCR) domain: an ancient and highly conserved protein module of the innate immune system. *Critical reviews in immunology*. 2004;24(1):1-37. PubMed PMID: 14995912. Epub 2004/03/05. eng.
251. Huang FL, Shiao YJ, Hou SJ, Yang CN, Chen YJ, Lin CH, et al. Cysteine-rich domain of scavenger receptor AI modulates the efficacy of surface targeting and mediates oligomeric Abeta internalization. *Journal of biomedical science*. 2013 Aug 2;20:54. PubMed PMID: 23915271. Pubmed Central PMCID: PMC3750411. Epub 2013/08/07. eng.
252. Martinez VG, Moestrup SK, Holmskov U, Mollenhauer J, Lozano F. The conserved scavenger receptor cysteine-rich superfamily in therapy and diagnosis. *Pharmacological reviews*. 2011 Dec;63(4):967-1000. PubMed PMID: 21880988. Epub 2011/09/02. eng.
253. Coskun O. Separation techniques: Chromatography. *Northern clinics of Istanbul*. 2016;3(2):156-60. PubMed PMID: 28058406.
254. Cummins PM, Rochfort KD, O'Connor BF. Ion-Exchange Chromatography: Basic Principles and Application. *Methods in molecular biology (Clifton, NJ)*. 2017;1485:209-23. PubMed PMID: 27730555. Epub 2016/10/13. eng.
255. Darcy E, Leonard P, Fitzgerald J, Danaher M, Ma H, O'Kennedy R. Purification of Antibodies Using Affinity Chromatography. *Methods in molecular biology (Clifton, NJ)*. 2017;1485:305-18. PubMed PMID: 27730559. Epub 2016/10/13. eng.
256. Urh M, Simpson D, Zhao K. Affinity chromatography: general methods. *Methods in enzymology*. 2009;463:417-38. PubMed PMID: 19892186. Epub 2009/11/07. eng.
257. Bornhorst JA, Falke JJ. Purification of proteins using polyhistidine affinity tags. *Methods in enzymology*. 2000;326:245-54. PubMed PMID: 11036646.
258. Kimple ME, Brill AL, Pasker RL. Overview of affinity tags for protein purification. *Current protocols in protein science*. 2013;73:Unit-9. PubMed PMID: 24510596.
259. Irvine GB. Determination of molecular size by size-exclusion chromatography (gel filtration). *Current protocols in cell biology*. 2001 May;Chapter 5:Unit 5 PubMed PMID: 18228373. Epub 2008/01/30. eng.
260. Duong-Ly KC, Gabelli SB. Gel filtration chromatography (size exclusion chromatography) of proteins. *Methods in enzymology*. 2014;541:105-14. PubMed PMID: 24674066. Epub 2014/03/29. eng.
261. Hagel L. Gel-filtration chromatography. *Current protocols in molecular biology*. 2001 May;Chapter 10:Unit 10 9. PubMed PMID: 18265066. Epub 2008/02/12. eng.
262. Darweesh AA, Bauman SJ, Debu DT, Herzog JB. The Role of Rayleigh-Wood Anomalies and Surface Plasmons in Optical Enhancement for Nano-Gratings. *Nanomaterials (Basel, Switzerland)*. 2018;8(10):809. PubMed PMID: 30304809.
263. Prabowo BA, Purwidyantri A, Liu KC. Surface Plasmon Resonance Optical Sensor: A Review on Light Source Technology. *Biosensors*. 2018 Aug 26;8(3). PubMed PMID: 30149679. Pubmed Central PMCID: PMC6163427. Epub 2018/08/29. eng.
264. Daghestani HN, Day BW. Theory and applications of surface plasmon resonance, resonant mirror, resonant waveguide grating, and dual polarization

interferometry biosensors. *Sensors (Basel, Switzerland)*. 2010;10(11):9630-46. PubMed PMID: 22163431. Pubmed Central PMCID: PMC3230998. Epub 2010/01/01. eng.

265. Lakowicz JR. Radiative decay engineering 3. Surface plasmon-coupled directional emission. *Analytical biochemistry*. 2004 Jan 15;324(2):153-69. PubMed PMID: 14690679. Pubmed Central PMCID: PMC2737403. Epub 2003/12/24. eng.

266. Sahoo PR, Swain P, Nayak SM, Bag S, Mishra SR. Surface plasmon resonance based biosensor: A new platform for rapid diagnosis of livestock diseases. *Veterinary world*. 2016 Dec;9(12):1338-42. PubMed PMID: 28096602. Pubmed Central PMCID: PMC5234044. Epub 2017/01/18. eng.

267. Piliarik M, Vaisocherova H, Homola J. Surface plasmon resonance biosensing. *Methods in molecular biology (Clifton, NJ)*. 2009;503:65-88. PubMed PMID: 19151937. Epub 2009/01/20. eng.

268. Drescher DG, Ramakrishnan NA, Drescher MJ. Surface plasmon resonance (SPR) analysis of binding interactions of proteins in inner-ear sensory epithelia. *Methods in molecular biology (Clifton, NJ)*. 2009;493:323-43. PubMed PMID: 18839357. Pubmed Central PMCID: PMC2864718. Epub 2008/10/08. eng.

269. Douzi B. Protein-Protein Interactions: Surface Plasmon Resonance. *Methods in molecular biology (Clifton, NJ)*. 2017;1615:257-75. PubMed PMID: 28667619. Epub 2017/07/02. eng.

270. Fischer MJ. Amine coupling through EDC/NHS: a practical approach. *Methods in molecular biology (Clifton, NJ)*. 2010;627:55-73. PubMed PMID: 20217613. Epub 2010/03/11. eng.

271. Andersson K, Areskoug D, Hardenborg E. Exploring buffer space for molecular interactions. *Journal of molecular recognition : JMR*. 1999 Sep-Oct;12(5):310-5. PubMed PMID: 10556879. Epub 1999/11/11. eng.

272. Onell A, Andersson K. Kinetic determinations of molecular interactions using Biacore--minimum data requirements for efficient experimental design. *Journal of molecular recognition : JMR*. 2005 Jul-Aug;18(4):307-17. PubMed PMID: 15952219. Epub 2005/06/14. eng.

273. O'Shannessy DJ, Brigham-Burke M, Soneson KK, Hensley P, Brooks I. Determination of rate and equilibrium binding constants for macromolecular interactions using surface plasmon resonance: use of nonlinear least squares analysis methods. *Analytical biochemistry*. 1993 Aug 1;212(2):457-68. PubMed PMID: 8214588. Epub 1993/08/01. eng.

274. Gelinsky-Wersing D, Wersing W, Pompe W. Bivalent kinetic binding model to surface plasmon resonance studies of antigen-antibody displacement reactions. *Analytical biochemistry*. 2017 Feb 1;518:110-25. PubMed PMID: 27888099. Epub 2016/11/27. eng.

275. Ward AB, Sali A, Wilson IA. Biochemistry. Integrative structural biology. *Science*. 2013 Feb 22;339(6122):913-5. PubMed PMID: 23430643. Pubmed Central PMCID: PMC3633482. Epub 2013/02/23. eng.

276. Ennifar E. X-ray crystallography as a tool for mechanism-of-action studies and drug discovery. *Current pharmaceutical biotechnology*. 2013;14(5):537-50. PubMed PMID: 22429136. Epub 2012/03/21. eng.

277. Milo R. What is the total number of protein molecules per cell volume? A call to rethink some published values. *BioEssays : news and reviews in molecular, cellular and developmental biology*. 2013 Dec;35(12):1050-5. PubMed PMID: 24114984. Pubmed Central PMCID: PMC3910158. Epub 2013/10/12. eng.

278. Su XD, Zhang H, Terwilliger TC, Liljas A, Xiao J, Dong Y. Protein Crystallography from the Perspective of Technology Developments. *Crystallography reviews*. 2015;21(1-2):122-53. PubMed PMID: 25983389. Pubmed Central PMCID: PMC4430849. Epub 2015/05/20. eng.

279. McPherson A, Gavira JA. Introduction to protein crystallization. *Acta crystallographica Section F, Structural biology communications*. 2014 Jan;70(Pt

- 1):2-20. PubMed PMID: 24419610. Pubmed Central PMCID: PMC3943105. Epub 2014/01/15. eng.
280. Dessau MA, Modis Y. Protein crystallization for X-ray crystallography. *Journal of visualized experiments : JoVE*. 2011 Jan 16(47). PubMed PMID: 21304455. Pubmed Central PMCID: PMC3182643. Epub 2011/02/10. eng.
281. Chernov AA. Protein crystals and their growth. *Journal of structural biology*. 2003 Apr;142(1):3-21. PubMed PMID: 12718915. Epub 2003/04/30. eng.
282. Ilari A, Savino C. Protein structure determination by x-ray crystallography. *Methods in molecular biology (Clifton, NJ)*. 2008;452:63-87. PubMed PMID: 18563369. Epub 2008/06/20. eng.
283. Russo Krauss I, Merlino A, Vergara A, Sica F. An overview of biological macromolecule crystallization. *International journal of molecular sciences*. 2013 May 31;14(6):11643-91. PubMed PMID: 23727935. Pubmed Central PMCID: PMC3709751. Epub 2013/06/04. eng.
284. Forsythe EL, Maxwell DL, Pusey M. Vapor diffusion, nucleation rates and the reservoir to crystallization volume ratio. *Acta crystallographica Section D, Biological crystallography*. 2002 Oct;58(Pt 10 Pt 1):1601-5. PubMed PMID: 12351870. Epub 2002/09/28. eng.
285. Salemme FR. Protein crystallization by free interface diffusion. *Methods in enzymology*. 1985;114:140-1. PubMed PMID: 4079761. Epub 1985/01/01. eng.
286. Garman EF, Owen RL. Cryocooling and radiation damage in macromolecular crystallography. *Acta crystallographica Section D, Biological crystallography*. 2006 Jan;62(Pt 1):32-47. PubMed PMID: 16369092. Epub 2005/12/22. eng.
287. Garman E. 'Cool' crystals: macromolecular cryocrystallography and radiation damage. *Current opinion in structural biology*. 2003 Oct;13(5):545-51. PubMed PMID: 14568608. Epub 2003/10/22. eng.
288. Altan I, Charbonneau P, Snell EH. Computational crystallization. *Archives of biochemistry and biophysics*. 2016 Jul 15;602:12-20. PubMed PMID: 26792536. Pubmed Central PMCID: PMC4909510. Epub 2016/01/23. eng.
289. Rubinson KA, Ladner JE, Tordova M, Gilliland GL. Cryosalts: suppression of ice formation in macromolecular crystallography. *Acta crystallographica Section D, Biological crystallography*. 2000 Aug;56(Pt 8):996-1001. PubMed PMID: 10944336. Epub 2000/08/16. eng.
290. Juers DH, Matthews BW. Cryo-cooling in macromolecular crystallography: advantages, disadvantages and optimization. *Quarterly reviews of biophysics*. 2004 May;37(2):105-19. PubMed PMID: 15999418. Epub 2005/07/08. eng.
291. Ilari A, Savino C. A Practical Approach to Protein Crystallography. *Methods in molecular biology (Clifton, NJ)*. 2017;1525:47-78. PubMed PMID: 27896717. Epub 2016/11/30. eng.
292. Tubiana M. [Wilhelm Conrad Rontgen and the discovery of X-rays]. *Bulletin de l'Academie nationale de medecine*. 1996 Jan;180(1):97-108. PubMed PMID: 8696882. Epub 1996/01/01. Wilhelm Conrad Rontgen et la decouverte des rayons X. fre.
293. Wlodawer A, Minor W, Dauter Z, Jaskolski M. Protein crystallography for aspiring crystallographers or how to avoid pitfalls and traps in macromolecular structure determination. *The FEBS journal*. 2013 Nov;280(22):5705-36. PubMed PMID: 24034303. Pubmed Central PMCID: PMC4080831. Epub 2013/09/17. eng.
294. Kendrew JC, Bodo G, Dintzis HM, Parrish RG, Wyckoff H, Phillips DC. A three-dimensional model of the myoglobin molecule obtained by x-ray analysis. *Nature*. 1958 Mar 8;181(4610):662-6. PubMed PMID: 13517261. Epub 1958/03/08. eng.
295. Skarzynski T. Collecting data in the home laboratory: evolution of X-ray sources, detectors and working practices. *Acta crystallographica Section D,*

Biological crystallography. 2013 Jul;69(Pt 7):1283-8. PubMed PMID: 23793154. Pubmed Central PMCID: PMC3689531. Epub 2013/06/26. eng.

296. Powell HR, Johnson O, Leslie AG. Autoindexing diffraction images with iMosflm. *Acta crystallographica Section D, Biological crystallography*. 2013 Jul;69(Pt 7):1195-203. PubMed PMID: 23793145. Pubmed Central PMCID: PMC3689522. Epub 2013/06/26. eng.

297. Winn MD, Ballard CC, Cowtan KD, Dodson EJ, Emsley P, Evans PR, et al. Overview of the CCP4 suite and current developments. *Acta crystallographica Section D, Biological crystallography*. 2011 Apr;67(Pt 4):235-42. PubMed PMID: 21460441. Pubmed Central PMCID: PMC3069738. Epub 2011/04/05. eng.

298. Powell HR. X-ray data processing. *Bioscience reports*. 2017 Oct 31;37(5). PubMed PMID: 28899925. Pubmed Central PMCID: PMC5629563. Epub 2017/09/14. eng.

299. Evans PR, Murshudov GN. How good are my data and what is the resolution? *Acta crystallographica Section D, Biological crystallography*. 2013 Jul;69(Pt 7):1204-14. PubMed PMID: 23793146. Pubmed Central PMCID: PMC3689523. Epub 2013/06/26. eng.

300. Wlodawer A, Minor W, Dauter Z, Jaskolski M. Protein crystallography for non-crystallographers, or how to get the best (but not more) from published macromolecular structures. *The FEBS journal*. 2008 Jan;275(1):1-21. PubMed PMID: 18034855. Pubmed Central PMCID: PMC4465431. Epub 2007/11/24. eng.

301. Evans PR. An introduction to data reduction: space-group determination, scaling and intensity statistics. *Acta crystallographica Section D, Biological crystallography*. 2011;67(Pt 4):282-92. PubMed PMID: 21460446. Epub 03/18.

302. Taylor GL. Introduction to phasing. *Acta crystallographica Section D, Biological crystallography*. 2010 Apr;66(Pt 4):325-38. PubMed PMID: 20382985. Pubmed Central PMCID: PMC2852296. Epub 2010/04/13. eng.

303. Evans P, McCoy A. An introduction to molecular replacement. *Acta crystallographica Section D, Biological crystallography*. 2008 Jan;64(Pt 1):1-10. PubMed PMID: 18094461. Pubmed Central PMCID: PMC2394790. Epub 2007/12/21. eng.

304. Read RJ, McCoy AJ. A log-likelihood-gain intensity target for crystallographic phasing that accounts for experimental error. *Acta crystallographica Section D, Structural biology*. 2016;72(Pt 3):375-87. PubMed PMID: 26960124.

305. Das R, Baker D. Prospects for de novo phasing with de novo protein models. *Acta crystallographica Section D, Biological crystallography*. 2009;65(Pt 2):169-75. PubMed PMID: 19171972. Epub 01/20.

306. Steiner RA, Rupp B. Model building, refinement and validation. *Acta crystallographica Section D, Biological crystallography*. 2012;68(Pt 4):325-7. PubMed PMID: 22505252. Epub 03/16.

307. Richardson JS, Bryan WA, 3rd, Richardson DC. New tools and data for improving structures, using all-atom contacts. *Methods in enzymology*. 2003;374:385-412. PubMed PMID: 14696383. Epub 2003/12/31. eng.

308. Wlodawer A. Stereochemistry and Validation of Macromolecular Structures. *Methods in molecular biology (Clifton, NJ)*. 2017;1607:595-610. PubMed PMID: 28573590. Pubmed Central PMCID: PMC5560084. Epub 2017/06/03. eng.

309. Rojkaer R, Schousboe I. Partial identification of the Zn²⁺-binding sites in factor XII and its activation derivatives. *European journal of biochemistry / FEBS*. 1997 Jul 15;247(2):491-6. PubMed PMID: 9266689. Epub 1997/07/15. eng.

310. Morgunova E, Tuuttila A, Bergmann U, Isupov M, Lindqvist Y, Schneider G, et al. Structure of human pro-matrix metalloproteinase-2: activation mechanism revealed. *Science*. 1999 Jun 4;284(5420):1667-70. PubMed PMID: 10356396. Epub 1999/06/05. eng.

311. Fujihara N, Tozuka M, Yamauchi K, Ueno I, Urasawa N, Ishikawa S, et al. Characterization of factor XII Tenri, a rare CRM-negative factor XII deficiency. *Annals of clinical and laboratory science*. 2004 Spring;34(2):218-25. PubMed PMID: 15228238. Epub 2004/07/02. eng.
312. Mahdi F, Madar ZS, Figueroa CD, Schmaier AH. Factor XII interacts with the multiprotein assembly of urokinase plasminogen activator receptor, gC1qR, and cytokeratin 1 on endothelial cell membranes. *Blood*. 2002 May 15;99(10):3585-96. PubMed PMID: 11986212. Epub 2002/05/03. eng.
313. Kumar R, Peerschke EI, Ghebrehiwet B. Zinc induces exposure of hydrophobic sites in the C-terminal domain of gC1q-R/p33. *Molecular immunology*. 2002 Sep;39(1-2):69-75. PubMed PMID: 12213329. Epub 2002/09/06. eng.
314. Citarella F, Fedele G, Roem D, Fantoni A, Hack CE. The second exon-encoded factor XII region is involved in the interaction of factor XII with factor XI and does not contribute to the binding site for negatively charged surfaces. *Blood*. 1998 Dec 1;92(11):4198-206. PubMed PMID: 9834224. Epub 1998/12/03. eng.
315. Verhoef JJ, Barendrecht AD, Nickel KF, Dijkxhoorn K, Kenne E, Labberton L, et al. Polyphosphate nanoparticles on the platelet surface trigger contact system activation. *Blood*. 2017 Mar 23;129(12):1707-17. PubMed PMID: 28049643. Pubmed Central PMCID: PMC5364341. Epub 2017/01/05. eng.
316. Banyai L, Tordai H, Pathty L. Structure and domain-domain interactions of the gelatin binding site of human 72-kilodalton type IV collagenase (gelatinase A, matrix metalloproteinase 2). *The Journal of biological chemistry*. 1996 May 17;271(20):12003-8. PubMed PMID: 8662603. Epub 1996/05/17. eng.
317. Hamad BK, Pathak M, Manna R, Fischer PM, Emsley J, Dekker LV. Assessment of the protein interaction between coagulation factor XII and corn trypsin inhibitor by molecular docking and biochemical validation. *Journal of thrombosis and haemostasis : JTH*. 2017 Sep;15(9):1818-28. PubMed PMID: 28688220. Pubmed Central PMCID: PMC5638086. Epub 2017/07/09. eng.
318. Danielli A, Loukeris TG, Lagueux M, Muller HM, Richman A, Kafatos FC. A modular chitin-binding protease associated with hemocytes and hemolymph in the mosquito *Anopheles gambiae*. *Proceedings of the National Academy of Sciences of the United States of America*. 2000 Jun 20;97(13):7136-41. PubMed PMID: 10860981. Pubmed Central PMCID: PMC16512. Epub 2000/06/22. eng.
319. Kanost MR, Jiang H. Clip-domain serine proteases as immune factors in insect hemolymph. *Current opinion in insect science*. 2015 Oct 1;11:47-55. PubMed PMID: 26688791. Pubmed Central PMCID: PMC4680995. Epub 2015/12/22. eng.
320. Roversi P, Johnson S, Caesar JJ, McLean F, Leath KJ, Tsiftoglou SA, et al. Structural basis for complement factor I control and its disease-associated sequence polymorphisms. *Proceedings of the National Academy of Sciences of the United States of America*. 2011 Aug 2;108(31):12839-44. PubMed PMID: 21768352. Pubmed Central PMCID: PMC3150940. Epub 2011/07/20. eng.
321. Munier AI, Medzhitov R, Janeway CA, Jr., Doucet D, Capovilla M, Lagueux M. graal: a *Drosophila* gene coding for several mosaic serine proteases. *Insect biochemistry and molecular biology*. 2004 Oct;34(10):1025-35. PubMed PMID: 15475297. Epub 2004/10/12. eng.